The Effect of Zeolite Type on the Hydrocracking of Long n-Paraffins

Ross S. Kukard

Submitted in partial fulfilment of the requirements
of the degree of Master of Science in Chemical Engineering

December 2008

Centre for Catalysis Research
Department of Chemical Engineering
University of Cape Town
Cape Town
South Africa

Acknowledgements

The author would like to gratefully acknowledge the efforts and support of all of the individuals and organisations involved in the development of this research endeavour, specifically:

Prof. Jack C.Q. Fletcher for the opportunity to conduct this research, support in determining the direction and focus for this endeavour, and guidance in the development of this report.

Mr Walter Böhringer for help in the analysis of results and guidance in the development of this report.

Mr Stephen Roberts for the extraordinary amount of assistance with regards to the design, construction and troubleshooting of the rig itself, in the development of a GC analysis programme, the plethora of insightful input along the way and the seemingly endless supply of comedic relief

Mr Marc Wüst for his time and assistance in all rig and laboratory related matters, from the design and construction of the apparatus and daily insights into operating procedures to keeping the laboratory running as efficiently and safely as possible

Mr Hermann Botha and the many other gentlemen in the workshop for all their effort and assistance with the design and construction of the apparatus

Johnson Matthey for their supply of the supported metal catalyst and silica diluent

Süd-Chemie for their supply of many of the zeolites utilised in this investigation

The University of Cape Town and in particular the Department of Chemical Engineering for financial support and the use of their facilities and other resources

The National Research Foundation of South Africa (NRF) for financial support, with the opinions expressed and the conclusions arrived at in this work being those of the author and not necessarily attributable to the NRF

And finally, the author would like to thank all those in the Centre for Catalysis Research who made day to day life at UCT so enjoyable. There was never a dull moment in the office!

Declaration

I, the undersigned, hereby certify that this thesis contains work that is my own research and interpretation completed with the assistance of my supervisors (indicated on the title page). Any information which is not my own has been indicated as such and referenced in accordance with the Harvard referencing system.

Signed: ______________________________

Name: ______________________________

Date: ______________________________

Synopsis

Although it is debatable as to the lifetime of the planet's crude oil reserves, it is indisputable that they are finite and will, eventually, become exhausted. As such it is desired to devise methods whereby currently available non-crude oil derived hydrocarbon feedstocks may be utilised for the production of clean, high quality liquid fuels (particularly middle distillate fuels such as diesel and jet fuel), aiding in alleviating the demand on crude oil reserves.

One technique whereby this may be achieved involves the conversion of the non-crude oil derived hydrocarbon feedstock (for example stranded gas, remote natural gas, coal or biomass) to syngas (a mixture of CO and H_2). This syngas is subsequently converted to paraffinic wax by Fischer-Tropsch Synthesis, and this wax selectively hydrocracked down to the desired distillate fuels fraction.

This hydrocracking may be conducted utilising either monofunctional or bifunctional catalysts. Monofunctional catalysts, such as the supported sulphided base metals or metal oxides utilised in many crude oil refineries, yield a product with minimal additional branching, as desired, though would contaminate the otherwise clean Fischer-Tropsch wax with sulphur. Bifunctional catalysts, utilising a metal on an acidic support, yield a product with significant branching, yet do not contaminate the product. Furthermore, the acid supports utilised in oil refinery applications are limited to either amorphous silica-alumina, or H-USY (a thermally treated large pore zeolite) due to the presence of large, bulky polycyclic and highly branched molecules in the feedstock.

Fischer-Tropsch wax exhibits only minimal branching, and it was hence the aim of this investigation to determine whether zeolites with pores smaller than those utilised in the hydrocracking of crude oil derived feedstocks, specifically medium pore zeolites such as H-MFI, may be utilised in the bifunctional hydrocracking of this wax to impart shape selectivity upon the reaction, thereby limiting the extent to which branching may occur.

In this regard, four different zeolites (H-MFI, H-BEA, H-USY and H-MOR) were tested under the same, industrially relevant conditions, and the results collated so as to quantify the effects of the each zeolite's unique properties, in particular their pore geometries (in terms of pore size, shape and channel inter-connectivity), the performance of each catalyst in terms of its activity (the overall conversion of the feedstock) and selectivity (with regards to both carbon number distribution and the degree of branching). Furthermore, it was desired to determine the extent to which the anticipated transition state shape selectivity of some of the zeolites affected the stability (on-stream lifetime) of the catalyst through a reduction in coke formation.

The results of this investigation indicated that medium pore zeolites show significant potential for use in the selective hydrocracking of a Fischer-Tropsch wax feedstock. It was found that those zeolites possessing medium sized pores (specifically H-MFI and H-BEA) exhibited a significantly higher activity than did those with only larger pores (H-USY and H-MOR), a phenomenon theorised to be due to the more orderly and efficient configuration of the adsorbed molecules within the medium pores promoting contact with active acid sites. Furthermore, it was found that H-MFI, with a porous network comprised entirely of medium pores, showed an improved selectivity towards the desired linear products, whilst zeolites with only wide pores (H-USY and H-MOR) and those with intersecting wide and medium pores (H-BEA) showed branched product selectivities roughly equivalent to one another, all greatly favouring the production of mono-methyl branched species. Unfortunately, due primarily to the large variations in the observed activity between the zeolites tested, the results of the deactivation analysis were inconclusive.

It is believed that the data obtained in this investigation will prove valuable as a stepping stone on the path toward the development of a highly selective bifunctional hydrocracking catalyst for the production of high quality middle distillate fuels from Fischer-Tropsch wax.

Table of Contents

List of Figures

List of Tables

Nomenclature

Associated Gas
Gaseous hydrocarbons liberated during the stabilisation (depressurisation) of crude oil from well.

BEA or Zeolite Beta
A zeolite utilised in its acid (H-BEA) form in this investigation.

BPR
Back-**P**ressure **R**egulator.

BTL
Biomass-**t**o-**L**iquids comprises technologies whereby various biomass-based feedstocks may be converted into liquid hydrocarbon fuels.

CTL
Coal-**t**o-**L**iquids technologies allow for a coal-based feedstock to be converted into liquid hydrocarbon fuels.

FAU or Faujasite or Zeolite-Y
See also USY. A zeolite utilised in thermally treated, acid form as H-USY in this investigation.

FID
Flame **I**onisation **D**etector.

FT
Fischer-**T**ropsch Synthesis is a process whereby a mixture of carbon monoxide and hydrogen (known as syngas) is reacted to produce a variety of hydrocarbon products.

GTL
Gas-**t**o-**L**iquids technologies allow for gaseous hydrocarbons, such as natural gas, to be converted into liquid hydrocarbon fuels.

GWP
Global **W**arming **P**otential.

Lagging
The term used to describe an insulation jacket designed to wrap around a cylindrical heated line, being secured to itself by small hooks.

LEL
The **L**ower **E**xplosive **L**imit of a substance is the minimum amount, in air, required to form an explosive mixture. Hydrogen, for instance, has a lower explosive limit of 4 vol%.

Metal : Acid Site Ratio
The molar ratio of active metal sites to active acid sites.

MFC
Mass **F**low **C**ontroller.

MFI
See also ZSM-5. The name, derived from its synonym Zeolite Socony **M**obil **FI**ve, of a zeolite utilised in its acid (H-MFI) form in this investigation.

Middle Distillate Fuels
Consisting predominantly of minimally branched saturated hydrocarbons with carbon numbers between approximately 10 and 22, the middle distillate fuels group includes such products as diesel and jet fuel.

MOR or Mordenite
A zeolite utilised in its acid (H-MOR) form in this investigation.

Pipeline Gas
Gaseous hydrocarbons which are piped, as a gas, to their destination.

PTFE
Poly**t**etra**f**luoro**e**thylene, commonly known by its brand name "Teflon", is a flexible plastic with high temperature and chemical resistance.

Remote Gas
(see Stranded Gas).

Rig
Self-supporting experimental apparatus.

SiC
Silicon Carbide.

Stranded Gas
Natural gas reserves located too far from the market to be economically exploited as gas.

Syncrude or Synthetic Crude
Synthetic equivalent to crude oil.

Syngas or Synthesis Gas
A gaseous mixture, comprised predominantly of hydrogen and carbon monoxide, produced from the reformation of natural gas or the gasification of coal or biomass.

TCD
Thermal **C**onductivity **D**etector.

TIC
Temperature **I**ndicating **C**ontroller.

USY
Ultra-**S**table Zeolite-**Y**. See also FAU. A thermally treated (to dealuminate and improve stability) zeolite utilised in its acid (H-USY) form in this investigation.

VCR
A fitting type, manufactured and marketed by Swagelok, which seals by compressing a metal gasket between two opposing ridges.

ZSM-5
See also MFI. **Z**eolite **S**ocony **M**obil **5**, utilised in its acid (H-ZSM-5) form in this investigation.

The beginning of knowledge is the discovery of something we do not understand.

Frank Herbert (1920 - 1986)

1

Introduction

Background

Satisfying the global demand for liquid fuels has led to the wide-spread exploitation of crude oil reserves, from which virtually all such fuels are currently derived. Despite speculation regarding the lifetime of these reserves, it cannot be doubted that they are finite, and as such there exists a drive to identify and implement alternative sources and techniques for the production of the desired liquid fuels.

Environmental concerns, embodied in ever more stringent government legislation, have resulted in the demand for fuels which may be utilised with minimal harmful emissions. This is in particular reference to sulphur, nitrogen, heavy metals and particulate matter, as such substances not only have direct negative environmental effects, but often interfere with catalytic converters (an example being the poisoning of catalytic converters designed to reduce nitrogen oxide emissions from diesel engines by various sulphurous combustion products (ORNL, 2000)).

The production of liquid fuels from renewable sources would be ideal, though this represents one of the ultimate goals of the field. For the present, it is desired to help alleviate the demand on crude oil reserves by seeking alternative feedstocks and devising techniques and procedures whereby clean liquid fuels may be produced.

In this regard, attention has been focussed on the production of distillate fuels (such as diesel and jet fuel) which, when compared with their petrol counterparts, not only possess greater energy densities per unit mass (due to higher hydrogen to carbon ratios) and reduced carbon dioxide emissions upon combustion, but current diesel engines also operate with efficiencies exceeding those of their petrol counterparts (ORNL, 2000).

Towards this end, processes have been developed whereby hydrocarbon feedstocks such as coal, natural gas or renewable biological sources may be converted to liquid fuels (with these processes being termed Coal-to-Liquids, Gas-to-Liquids and Biomass-to-Liquids respectively).

This is achieved, for instance, by the non-catalytic partial oxidation or steam gasification of the feedstock to produce "syngas" (a mixture of mainly CO and H_2) and the subsequent conversion of this syngas to a variety of clean hydrocarbon fuels by a process known as Fischer-Tropsch (FT) Synthesis. Unfortunately, the Fischer-Tropsch process is unselective, with the distillate fuel reaching a maximum per pass yield of approximately 35 wt% (Dry, 2001). A far more economical method is to utilise Fischer-Tropsch synthesis to produce wax from the syngas feed, with high selectivities towards this product being achieved with ease (Dry, 2003), and selectively hydrocrack this wax into clean, high quality distillate fuels (Dry, 2001).

The primary benefit of this technology is that the distillate fuels thus produced are clean (containing no aromatics, sulphur, nitrogen or heavy metal contaminants) and are of high quality with regards to cetane number (consisting of minimally branched paraffins and being free of aromatics and cyclic compounds) (Chevron, 2006).

Catalysts suitable for the selective hydrocracking of the Fischer-Tropsch Synthesis derived wax may, for instance, be bifunctional, comprising both metal and acid functions, with the solid acid often serving the dual purpose of supporting the active metal crystallites. It is this acid co-catalyst upon which this investigation focuses.

Whilst hydrocracking is common in oil refineries, the feedstock to such units is not only contaminated with a variety of sulphurous compounds but also contains large amounts of bulky (polycyclic and highly branched) hydrocarbons. The presence of sulphur in the feedstock necessitates the use of sulphided metals whilst the bulky molecules require that these metals be supported on amorphous supports, with any zeolites utilised being limited to those with large pore diameters (such as Zeolite-Y), and crystals often being steam treated to further break open and expose the pore structure (such as zeolite H-USY).

A feedstock of Fischer-Tropsch wax, however, comprises paraffinic hydrocarbons with minimal branching and is free from all sulphurous compounds (Dry, 2003). As such, not only may more active pure metals be utilised, but the possibility of implementing acidic zeolite supports with narrower, more restrictive pore structures is also possible and of great interest.

Hypothesis

It is thus hypothesised that, due to the linearity of the Fischer-Tropsch wax feed, zeolites with pores smaller than those utilised for the hydrocracking of crude oil based feedstocks, including medium pore zeolites such as ZSM-5, may now be sufficiently active to be considered viable.

Further, it is believed that increasing the severity of the physical constraints, through the reduction of pore diameter, will induce shape selectivity upon the reactions and products. This is likely to manifest as increased yields of the desired lesser branched products (i.e. products with a higher cetane number) and possibly in improved catalyst on-stream lifetime, through the reduction of the formation of bulky coke precursors.

Key Questions

The performance of the catalyst must be evaluated in terms of its activity (cracking conversion of the feed) and selectivity (preferential formation of the desired minimally branched paraffinic products).

It is thus important to determine the effects which each zeolite's characteristic properties have on said activity and selectivity, with interest focussing on the effects of:

- The density and strength of acid sites (fundamentally linked to the SiO_2/Al_2O_3 ratio)
- The pore geometry (pore dimensions, shape and interconnectivity)

Furthermore, it is desired to qualitatively examine whether the restrictive pore dimensions of zeolites with smaller pores will reduce the formation of coke precursors, thereby prolonging catalyst life, or whether the increased reaction severity required to attain similar levels of conversion in these zeolites will negate any benefit in this regard.

All men by nature desire knowledge.
Aristotle (384 BC - 322 BC)

2

Background

2.1 The Need and Potential for Alternative Liquid Fuels Production

2.1.1 Current Production Methodology and Direction of Change

At present the world relies almost exclusively on crude oil for liquid fuels production, and despite debate regarding the useful life of crude oil reserves, what is certain is that they are finite and will eventually become depleted, bringing an end to the supply of liquid fuels from this source.

Furthermore, to reduce environmental impact, ever more stringent government legislation is placing restrictions on the contaminants and additives allowed in such fuels (USA, 2007). This has included banning the use of heavy metal additives to increase the octane number of petrol and imposing vast restrictions on the presence of sulphur or aromatics in distillate fuels such as diesel and jet fuel.

Such distillate fuels have, however, begun to gain favour in consumer and industrial markets alike. This is mainly due to distillate fuels (specifically diesel) offering a greater energy density per unit mass (due to higher hydrogen to carbon ratios), greater engine efficiency, and a reduction in carbon dioxide emissions over their petrol counterparts (ORNL, 2000).

As such, interest is being focused on the production of clean, high quality distillate fuels, with such a fuel ideally being comprised of paraffinic hydrocarbons with carbon numbers of between 10 and 22 and exhibiting minimal branching together with a minimal amount of aromatics (Chevron, 2006). These characteristics would afford the fuel a high cetane number, with a value of 51.0 being the current minimum required in the European Union (CEN, 2004), whilst ensuring the fuel is still operable in colder climates (pure linear alkanes, whilst having higher cetane numbers than branched species, also exhibit a greater tendency than branched species to crystallise out of the fuel at lower temperatures, making such pure mixtures unfavourable in colder climates where they may solidify within the fuel system).

The eventual goal is thus to be able to produce such clean liquid fuels from alternative feedstocks, with the present step toward this being to identify and develop methods for the production of such fuels from the non-crude oil sources presently available.

2.1.2 Currently Available Alternative Sources

There exist at present numerous feedstocks which could be converted into the desired liquid fuels, including associated gas, stranded gas (also known as remote gas) and various biological alternatives.

Due to the elevated reservoir pressure of crude oil reserves, large amounts of light paraffinic hydrocarbons (predominantly methane) are dissolved within the liquid oil. In order to store and transport such crude oil, it must be "stabilised", a process involving the careful reduction of pressure to liberate these light hydrocarbons (which appear as "associated gas") from the liquid. This practice, which is extremely common, is also extremely wasteful, with virtually all of the gases liberated in this manner, amounting to an estimated 10^{12} m^3 per year (Djumena, 2004), being flared. Despite the plethora of combustion-based pollutants produced, with the composition of flare products consisting mainly of unburnt fuel, NOx, CO, CO_2, H_2O and particulate matter (Calinescu, 2005), this practice of burning the associated gas is greatly preferred over its direct venting to the atmosphere. This is due to the fact that, not only is the venting of large amounts of highly flammable gas extremely dangerous, but methane has a Global Warming Potential (GWP) approximately 20 times greater than that of carbon dioxide (Calinescu, 2005).

At present, the small quantity of associated gas not vented or flared is usually used for heating purposes on site or as pipeline gas, with the implementation of large scale process units for the capture, storage and transportation of the associated gas being economically infeasible *under current legislation* (Kaldany, 2001). However, as environmental legislation against the release of greenhouse gases becomes ever more stringent (PFC Energy, 2007; World Bank Group, 2003), the economic balance relating to the processing of the associated gas versus the flaring thereof is shifting in favour of the former (PFC Energy, 2007). At present, only a handful of countries have begun to implement measures for the large-scale utilisation of associated gas, among them: Norway, the UK, Alberta (Canada) and the USA, with strict government policy and legislation being the dominant factors in the move away from flaring (PFC Energy, 2007). In the majority of situations where this associated gas may be utilised, however, the oil wells are in close proximity to either the end-users for the gas or existing gas pipelines, with wells located any substantial distance from such markets or infrastructure requiring alternative methodologies for the transport, sale and/or utilisation of this gas.

As such, a technique whereby this gaseous "by-product" may be converted to liquid fuels on site, cheaply and easily, would be extremely desirable for implementation on more remote oil drilling installations as it would allow the primary obstacle, that of the transportation of a gaseous product, to be overcome as the liquid product thus produced could be either shipped separately or mixed with the crude oil and transported as such. This aspect of gas-to-liquids (GTL) production is of great importance in terms of the exploitation of natural gas deposits for, as is the case with the Qatar Petroleum / SASOL Oryx GTL plant in Qatar, some natural gas fields are simply too remote for transport of a gaseous product to a suitable market to be economically feasible. It is for this reason that conversion of the gas to a stable liquid fuel (i.e. that is liquid without the need for pressurisation or cooling) is required to make the utilisation of such reserves profitable.

Other technologies whereby liquid fuels may be produced from non-crude oil derived feedstocks include various GTL processes (with that utilised at the Oryx GTL plant, converting natural gas to liquid fuels via Fischer-Tropsch Synthesis and hydrocracking as discussed in Section 2.1.3, being but one example), coal-to-liquids (CTL), covered in Section 2.1.3, or biomass-to-liquids (BTL). These techniques all offer alternative routes for the production of liquid fuels or an intermediate, "syncrude", from non-crude oil derived feedstocks.

2.1.3 Coal or Gas to Liquids Production

At present, numerous technologies exist for the production of liquid fuels from solid or gaseous carbonaceous feedstocks. One of particular interest (illustrated in Figure 2.1) involves the conversion of these feedstocks into a mixture of mainly carbon monoxide and hydrogen (known as syngas). This syngas is subsequently converted into wax by a process known as Fischer-Tropsch Synthesis (FT). This wax, consisting entirely of paraffinic hydrocarbons with minimal branching, is then selectively hydrocracked into the desired distillate fuels range.

Not only does this technique make it possible to convert gaseous or solid feedstocks to liquids on site, but the product is completely free of sulphur, nitrogen, and metal contaminants. Any potential feedstock contaminants may be removed by various scrubbing or washing processes prior to or after conversion to syngas.

The Fischer-Tropsch process is, in itself, capable of producing a large variety of hydrocarbon fuels, as indicated in Figure 2.2. However, it is generally far from selective, with the maximum yield of the desired middle distillate fuels (jet fuel and diesel) reaching only approximately 35 wt%. Wax, on the other hand, may be produced with very high selectivities (under operating temperatures of 200 to 250°C (Dry, 2001)) and it is this eventuality that facilitates the need to convert the syngas to wax and then hydrocrack this wax down to the desired product range. Overall distillate fuel yields for this technique have been reported in the range of 80 wt% (Dry, 2001; Sie *et al.*, 1991).

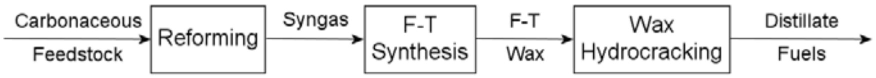

Figure 2.1: Block Flow Diagram Illustrating the Conversion of Natural Gas or Other Carbonaceous Feedstocks to Distillate Fuel
(Redrawn from Dry, 2001)

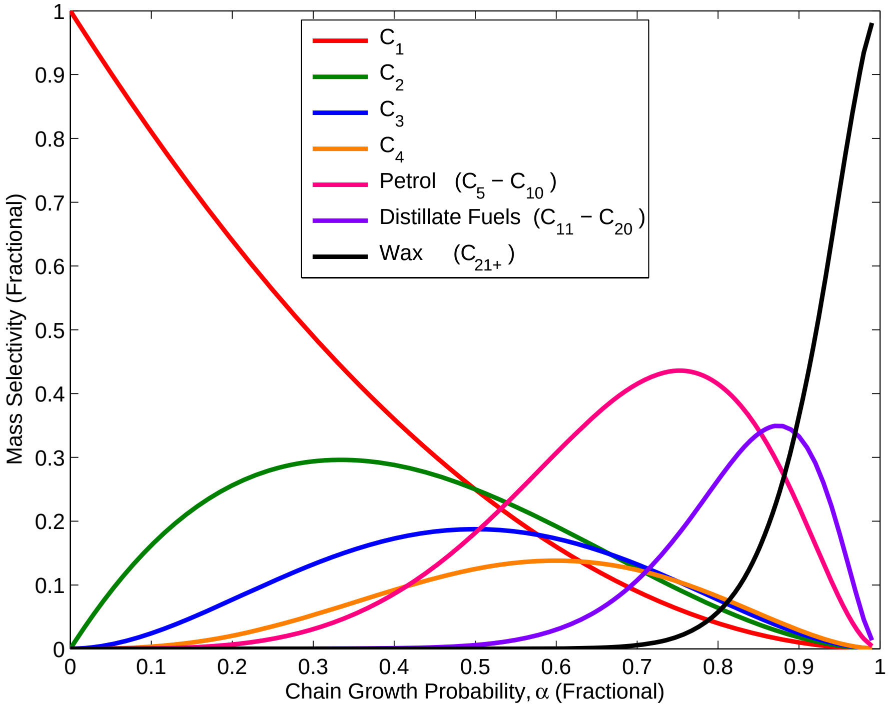

Figure 2.2: Fischer-Tropsch Synthesis Product Selectivity as Predicted by the Anderson-Schulz-Flory Distribution

As such, it is of extreme importance that the hydrocracking step be selective toward the desired fuel; if it is not, the wax may be cracked into fractions of little value, thereby not only completely circumventing the desire to produce distillate fuel, but resulting in poor economic incentive for the entire process.

This research focuses on this crucial hydrocracking step of the process.

2.2 Monofunctional and Bifunctional Hydrocracking Mechanisms

Simply put, hydrocracking is the splitting of a carbon-carbon bond (such as in a hydrocarbon chain) and the saturation of the resulting fragments through the addition of hydrogen. This can, for instance, be conducted over a bifunctional catalyst, comprising both a metal and acid function whereby, in accordance with the "classical" hydrocracking mechanism, proceeding via carbenium ion intermediates, the metal function serves to dehydrogenate the paraffinic feed and hydrogenate the olefinic products, whilst the acid exacts isomerisation and cracking and the hydrocarbon intermediates migrate between these sites by gaseous diffusion. These designations have recently been contested by the proponents of the "hydrogen spillover" mechanism, whereby it is claimed that the hydrogen is activated upon a metal site and migrates by surface diffusion (Roessner and Roland, 1996)) to an acid site where it reacts with the paraffinic feed molecules, thereby producing the various products observed.

Aside from these mechanisms, a third cracking mechanism (typical for metal, metal oxide and metal sulphide catalysts) known as “hydrogenolysis”, and a special variant thereof, “methanolysis”, have been observed and are included below.

2.2.1 “Classical” Acid Catalysed Hydrocracking Mechanism

Originally proposed by Mills *et al.* (1953) and Weisz and Swegler (1957), this hitherto widely accepted mechanism suggests that the hydrocracking reaction occurs via a series of intermediates on two separate, physically distinct active centres, namely metal and acid sites. As illustrated in Figure 2.3, the metal (e.g. Pt) serves to dehydrogenate the feed molecules, for example n-paraffins, to form n-olefins. These olefins migrate by gaseous diffusion (Weisz and Swegler, 1957) to an acid site whereupon they are protonated to form carbenium ions. The carbenium ions then undergo skeletal isomerisation and subsequent cracking on the acid site with the resultant olefinic compounds diffusing back to a metal site for rehydrogenation to paraffinic products (Park and Ihm, 2000).

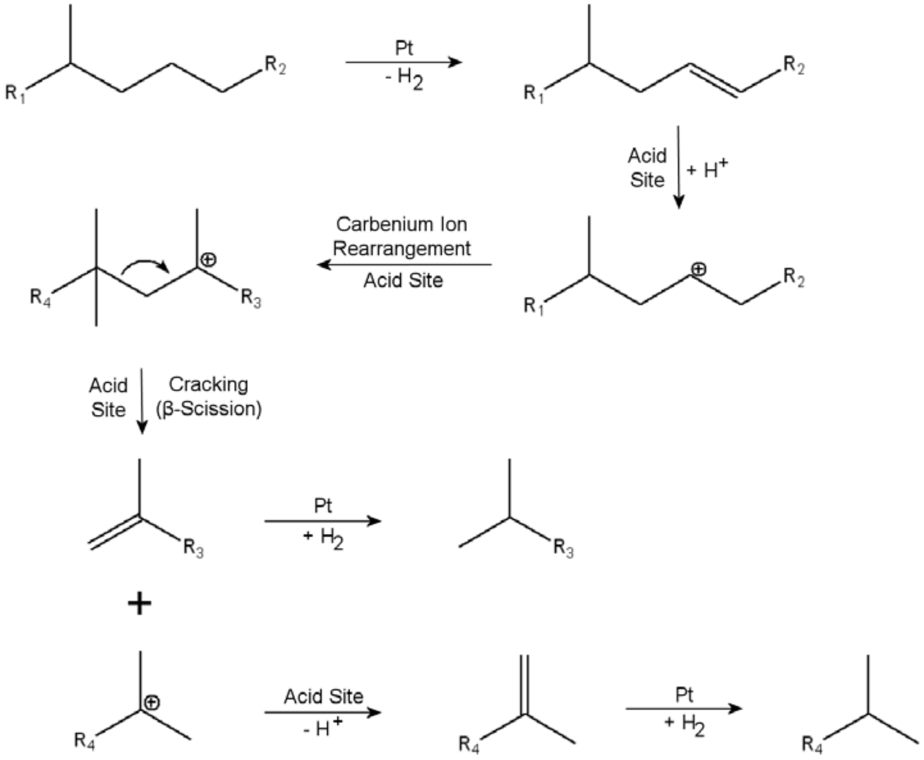

Figure 2.3: Representation of Classical Bifunctional Hydrocracking Mechanism over Pt/Acid Catalyst (Adapted from general mechanism by Weitkamp *et al.*, 1983)

As indicated in Figure 2.3, the cracking of the carbenium ion occurs by β-scission to form two smaller fragments, an olefin and a paraffinic carbenium ion. The rate at which this cracking occurs increases with increasing stability of the reactant and product carbenium ions in the cracking step, with carbenium ion stabilities generally ranked as:

$$tertiary > secondary \gg primary$$

Examples of cracking mechanisms involving secondary and tertiary carbenium ions are presented in Figure 2.4, with the far reduced stability of their primary counterparts resulting in mechanisms featuring such primary carbenium ions being considered negligible in so far as hydrocracking processes are concerned (Martens and Jacobs, 1990). Of the β-scission mechanisms presented, the relative rates of reaction may be ordered as $A \gg B_1, B_2 > C$.

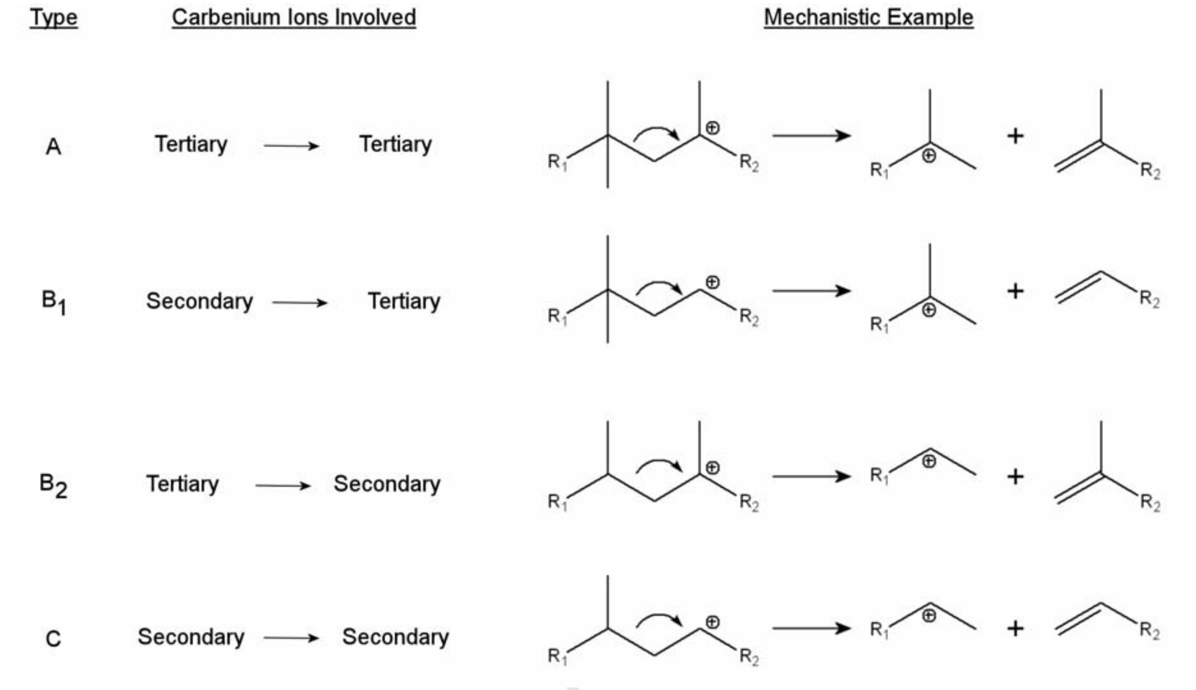

Figure 2.4: β-Scission Reactions Involving Secondary and Tertiary Carbenium Ions (Weitkamp *et al.*, 1983)

In this regard, it is believed that both the rearrangement of the originally linear alkyl carbenium ions (to form species with sufficient branching for Type A cracking to proceed) together with the β-scission cleavage itself are the rate limiting steps in the classical hydrocracking mechanism (Martens and Jacobs, 1990).

It is hence clear that tertiary-tertiary cracking will occur most rapidly, but will proceed only when a quaternary carbon is located in the β-position of a tertiary carbenium ion. Thus, such rapid cracking can occur only on central C-C bonds, though with equal probability, from the fourth carbon atom onwards (Dry, 2003), thereby resulting in a relatively even product distribution from C_4 onwards for “true” primary hydrocracking (Böhringer *et al.*, 2006), i.e. when no re-adsorption or secondary cracking occurs. It is also noted that, due to the superior stability of the tertiary carbenium ion, the smallest favourable fragment from such true hydrocracking will be C_4, with C_3 and particularly C_2 fragments forming to a much lower extent, with C_1 not forming at all. These trends are illustrated in Figure 2.5 (solid line) for an n-tetradecane (n-C_{14}) feedstock.

Under more severe conditions and higher conversions however, re-adsorption and secondary cracking begin to play a role, resulting in a decline of the longer chain products and a concomitant increase in the yield of short chain products (with C_4 remaining the smallest favourable fragment). These trends are presented in Figure 2.5 (dotted line).

At low conversions isomerisation of the feed to form carbenium ion intermediates will be dominant in terms of determining the product distribution. As the conversion increases, however, the increasing amounts of highly branched isomerisation products being formed will begin undergoing rapid cracking, with a resultant increase in the cracking selectivity (favouring shorter chain products). These trends are depicted in Figure 2.6.

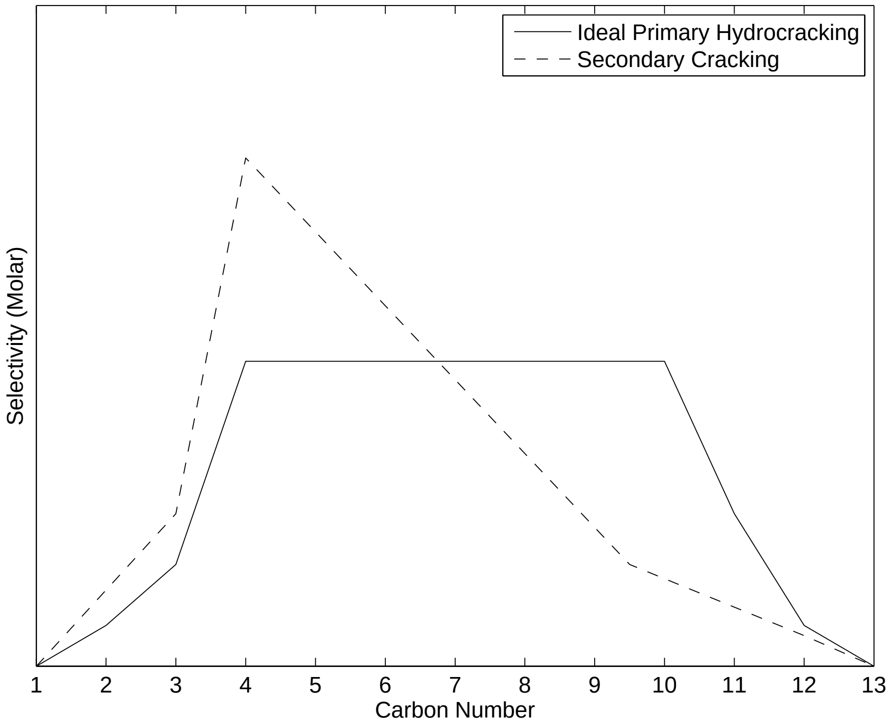

Figure 2.5: Theoretical Carbon Number Distribution of Products from the Bifunctional (Metal/Acid) Hydrocracking of n-C_{14}
(Redrawn from Böhringer *et al.*, 2006)

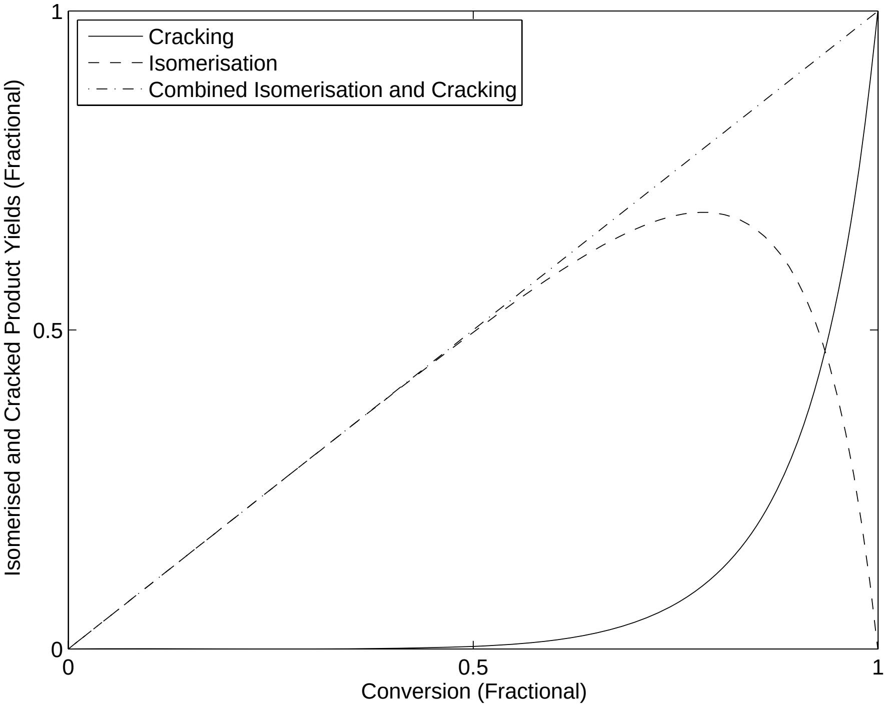

Figure 2.6: Yield of Isomerisation and Cracking Products for the Bifunctional (Metal/Acid) Hydrocracking of a Long n-Alkane
(Redrawn from Martens and Jacobs, 2001)

2.2.2 "Hydrogen Spillover" Mechanism

If only the classical hydrocracking mechanism is considered, however, there exist a variety of experimental results and phenomena which cannot be explained (Roessner and Roland, 1996), these being predominantly associated with the physical separation of the metal and acid functions.

By the classical hydrocracking mechanism, the paraffinic hydrocarbon reactant must be activated at a metal site (dehydrogenation), with the intermediary olefins migrating by gaseous diffusion to an acid site for isomerisation and cracking, and the olefinic product fragments then diffusing back to a metal site for rehydrogenation. This process is illustrated in Figure 2.7c. In accordance with this mechanism, the metal and acid functions of the catalyst are desired to be in close proximity to allow such diffusion to occur rapidly.

It is for this reason that bifunctional catalysts are usually prepared by the dispersion of the active metal component upon the acid support, with this technique allowing the sites to be sufficiently close for inter-diffusion to be plausible (Roessner and Roland, 1996).

To investigate the effect of the distance of separation between the metal and acid functions, researchers such as Steinberg *et al.* (1990) experimented with the physical separation of metal (Pt/Alumina) and acid (H-Erionite) co-catalysts in the bifunctional hydroisomerisation of n-paraffins, as depicted in Figure 2.8,(with the classical bifunctional hydroisomerisation reaction, depicted in Figure 2.9, being analogous to the classical bifunctional hydrocracking reaction, illustrated in Figure 2.3, of interest in this investigation). It was noted that in three of the four arrangements (beds (a), (b) and (d) in Figure 2.8), the typical bifunctional reaction products and product distributions were observed, though with reduced conversion for increased separation distance (bed arrangement (d) in Figure 2.8). Only if no physical contact was afforded between the co-catalysts (bed arrangement (c) in Figure 2.8), the products observed did not conform to those of typical bifunctional hydroisomerisation. Furthermore, the possibility that the metal co-catalyst's alumina support itself was contributing as an acid co-catalyst was eliminated as the supported metal alone exhibited negligible activity (bed arrangement (e) in Figure 2.8). These results were found to be reproducible given the outcome of similar experiments performed by Roessner and Roland (1996).

Were the classical mechanism alone assumed to be responsible for any hydroisomerisation, relying on the gas-phase diffusion of olefinic intermediates as discussed in Section 2.2.1, the product from bed arrangements (a), (c) and (d) in Figure 2.8 would be expected to contain only a small amount of isomerised olefinic products (due to the lack of any downstream metal function required to re-hydrogenate these species, as indicated in Figure 2.9), whilst bed arrangement (b) would be expected to yield only a small amount of non-isomerised dehydrogenated feed (as there exists no acid function downstream of the metal).

These observations were anticipated as bed arrangements (a), (c) and (d) in Figure 2.8 would require the gaseous diffusion of olefinic isomerisation products, and bed arrangement (b) would require the gaseous diffusion of dehydrogenated (olefinic) feed molecules, against the hydrodynamic flow in order for bifunctional hydroisomerisation to occur (as illustrated in Figure 2.7a for bed arrangements (a) and (d) (with the metal co-catalyst above the acid co-catalyst), and in Figure 2.7b for bed arrangement (b) (with the metal below the acid)). This back-diffusion was not believed to be possible given the reaction conditions (Roessner and Roland, 1996).

It was, however, observed by (Steinberg *et al.*, 1990) that bed arrangements (a), (b) and (d) in Figure 2.8 all exhibited a clearly bifunctional hydroisomerisation product (i.e. paraffinic isomers of the feed), a product which, by the classical hydroisomerisation mechanism, would be expected to require a well-mixed bed of metal and acid co-catalysts (as per Figure 2.7c) and hence allow for the gas-phase diffusion of olefinic intermediates between the metal and acid active sites as required.

Furthermore, were gaseous diffusion playing a key role, bed arrangements (c) and (d) in Figure 2.8 would be thought to exhibit similar conversions and selectivities given the identical distance of separation between, and physical arrangement of, the metal and acid co-catalysts (i.e. in both cases the metal co-catalyst is located above, but not in direct physical contact with, the acid co-catalyst). This was not the case however, with bed arrangement (c) instead being observed to be noticeably less active under the test conditions (Steinberg *et al.*, 1990).

These trends observed for the physical separation of co-catalyst beds in the hydroisomerisation reaction

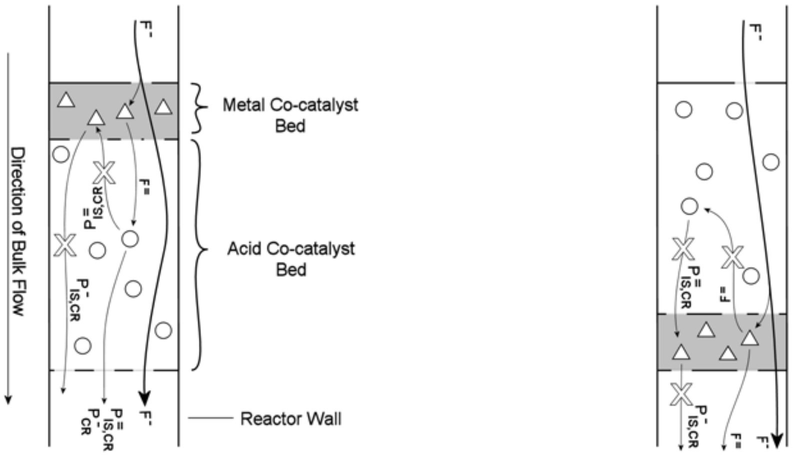

(a) Metal co-catalyst bed above, and in physical contact with, acid co-catalyst bed (arrows indicate gas-phase flows and pathways in accordance with the "classical" mechanism)

(b) Metal co-catalyst bed below, and in physical contact with, acid co-catalyst bed (arrows indicate gas-phase flows and pathways in accordance with the "classical" mechanism)

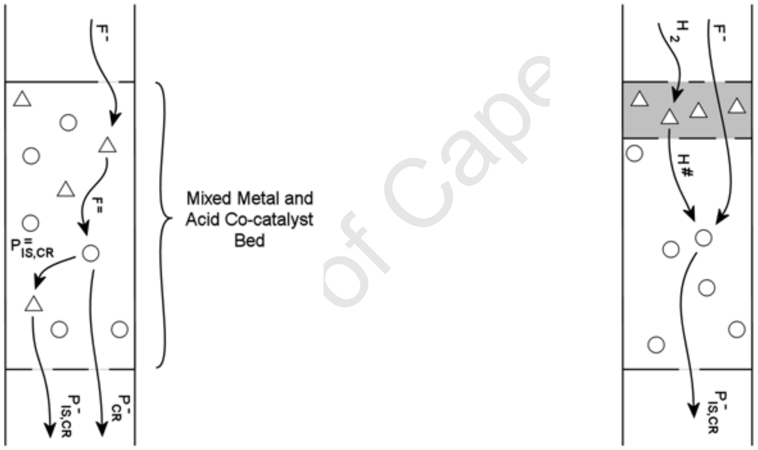

(c) Mixed metal and acid co-catalysts (arrows indicate gas-phase flows and pathways in accordance with the "classical" mechanism)

(d) Hydrogen spillover in system with metal co-catalyst bed above acid co-catalyst bed (arrows indicate surface diffusion flows and pathways according to the "spillover" mechanism)

Figure 2.7: Flows and Required Diffusion Pathways of Reagents, Intermediates and Products Through Various Co-catalyst Bed Arrangements and their Interaction with Active Sites in Hydrosiomerisation (IS) and Hydrocracking (CR)

△ - Active metal site
○ - Active acid site
F^- - Paraffinic feed molecule
$F^=$ - Dehydrogenated (olefinic) feed molecule
P^- - Paraffinic product
$P^=$ - Olefinic product
P_{IS} - Hydroisomerisation product
P_{CR} - Hydrocracking product
$H^\#$ - Activated hydrogen species migrating by surface diffusion

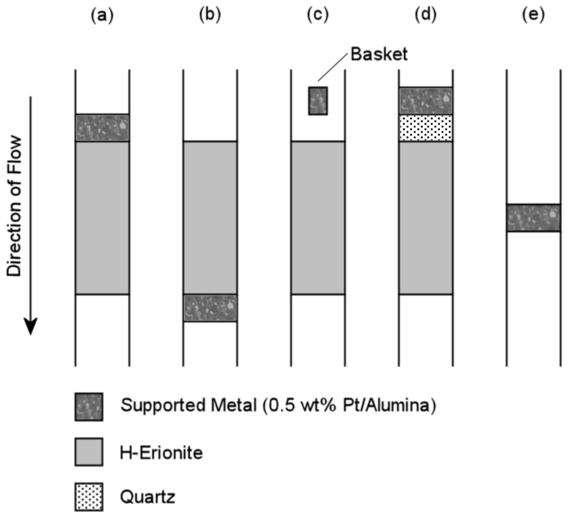

Figure 2.8: Different Physical Arrangements of Metal and Acid Co-Catalysts (Pt/Alumina [10mg] and H-Erionite [1g]) for n-Hexane Hydroisomerisation Experiments (T = 225°C)
(Redrawn from Steinberg *et al.*, 1990)

- (a) Metal co-catalyst layer directly above and in physical contact with acid co-catalyst layer
- (b) Metal co-catalyst layer directly below and in physical contact with acid co-catalyst layer
- (c) Metal and acid co-catalysts separated by gap of gaseous reaction mixture
- (d) Metal and acid co-catalysts separated by, and in physical contact with, layer of catalytically inert quartz
- (e) Metal co-catalyst with no acid co-catalyst

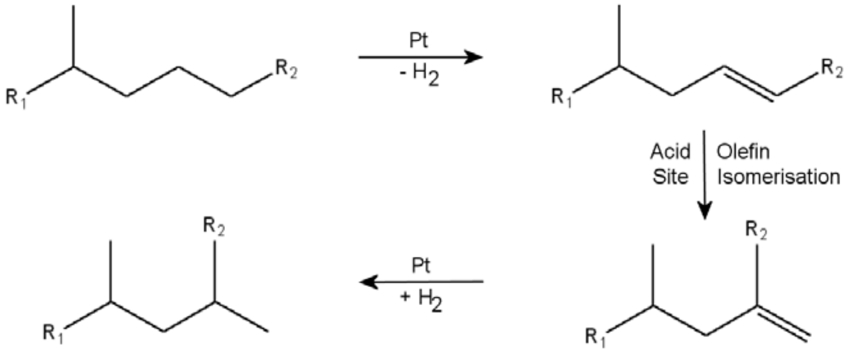

Figure 2.9: Representation of Classical Bifunctional Hydroisomerisation Mechanism
(Created based on general mechanism presented by Weisz and Swegler, 1957)

are analogous to what would be anticipated for a bifunctional hydrocracking reaction system. Herewith, the product from bed arrangements (a), (c) and (d) in Figure 2.8 would be expected to contain a small amount of partially olefinic cracking product (with the olefinic species remaining unsaturated given the absence of a downstream re-hydrogenation function), whilst the product from bed arrangement (b) in Figure 2.8 would be anticipated to comprise only a very small fraction of dehydrogenated (olefinic) feed (with no acid function downstream of the metal to exact isomerisation or cracking). Monofunctional acid cracking would not be expected in any of the bed arrangements given the relatively low temperature of the investigation (conducted at 225°C, with acid cracking only becoming significant above approximately 475°C (Kotrel *et al.*, 2000)).

Based on these results and observations, it was suggested that the classical mechanism was, in fact, not the sole mechanism by which bifunctional hydroisomerisation may occur (Steinberg *et al.*, 1990). Rather, it has since been proposed that the hydrogen itself is in some way activated on the metal site and migrates, presumably by surface diffusion, to the acid sites where it is able to interact with the hydrocarbon feed and product molecules (Conner and Falconer, 1995; Kusakari *et al.*, 2002; Roland *et al.*, 1997). This concept of hydrogen activation and migration of the activated hydrogen species is known as "hydrogen spillover" and is exemplified in Figure 2.7d for a bed arrangement such as (a) in Figure 2.8. This hydrogen spillover reaction is, however, also believed to be a carbenium ion based mechanism in that the product obtained for bifunctional hydroisomerisation and hydrocracking reactions thought to require hydrogen spillover to proceed exhibit a great degree of branching if not specifically limited (Roessner and Roland, 1996), such as by spatial restraints within zeolite pores.

Whilst the work by Steinberg *et al.* (1990) and Roessner and Roland (1996) present the most definitive evidence for the occurrence of hydrogen spillover, there has unfortunately, to date, been little progress made concerning the exact nature of the spill-over hydrogen species, with the various proposed possibilities including H_3 (Bianchi *et al.*, 1981), H^+ ions (protons) (Levy and Boudart, 1974), H^+/H^- ion pairs, H_3^+, and even paramagnetic H radicals (Roland *et al.*, 1997).

Thus, although the hydrogen spillover mechanism is neither fully understood nor widely accepted, it does explain experimental results which, heretofore, remained a mystery. Furthermore, the concept of hydrogen spillover may be exploited for practicality in terms of catalyst testing in that it suggests that the metal need not be loaded directly onto the acid support, but may indeed be introduced on an inert support, with pellets of this supported metal physically mixed with the acid co-catalyst (see Section 6.4.1). Such a technique is, however, only suitable for laboratory investigations in that it has been noted that the bifunctional synergy existing between the physically separated metal and acid co-catalyst beds declines with increasing distance of separation (Roessner and Roland, 1996), manifesting in a decline in the overall conversion exhibited by the system. As such, for industrial applications, minimising the metal-acid diffusion distance is still best achieved by loading the metal directly onto the acid support.

2.2.3 Hydrogenolysis and Methanolysis Mechanisms

The third hydrogenolytic mechanism believed to occur, as either the main or side reaction, in hydrocracking systems is that of hydrogenolysis and hydrogenolytic demethylation ("methanolysis") (Böhringer *et al.*, 2006), with an example of the latter depicted in Figure 2.10. These hydrogenolysis and methanolysis reactions proceed (on noble metals, base metals, base metal oxides and base metal sulphides, with the lattermost being the typical crude oil refinery hydrocracking catalyst) via a radical mechanism with either the unselective cleavage of any C-C bond of the adsorbed hydrocarbon molecules (hydrogenolysis), or the preferential cleavage of the terminal C-C bonds of the adsorbed hydrocarbons (methanolysis, a special case of hydrogenolysis). Which of these mechanisms is favoured is determined by the type of metal used, with those such as Ni, Co, Pd and Ir being known to catalyse methanolysis, whereas Pt and Rh favour non-bond-specific hydrogenolysis (Sinfelt, 1973).

Contrary to the product distributions of the classical and spillover mechanisms which require an acid co-catalyst, primary hydrogenolysis would result in an even product carbon number distribution from C_1 onwards (illustrated in Figure 2.11) and a mostly linear, i.e. minimally branched, cracking product (in particular when feeding, for example, n-paraffins) due to the small differences in stability between secondary and tertiary radicals being an insufficient driving force for isomerisation. Methanolysis, however, would result in the smallest favourable product being C_1, and hence more of the high carbon number products in the tail end, as illustrated in Figure 2.12. In both cases the carbon number of the largest product would consequently exceed that from the aforementioned two acid catalysed cracking mechanisms.

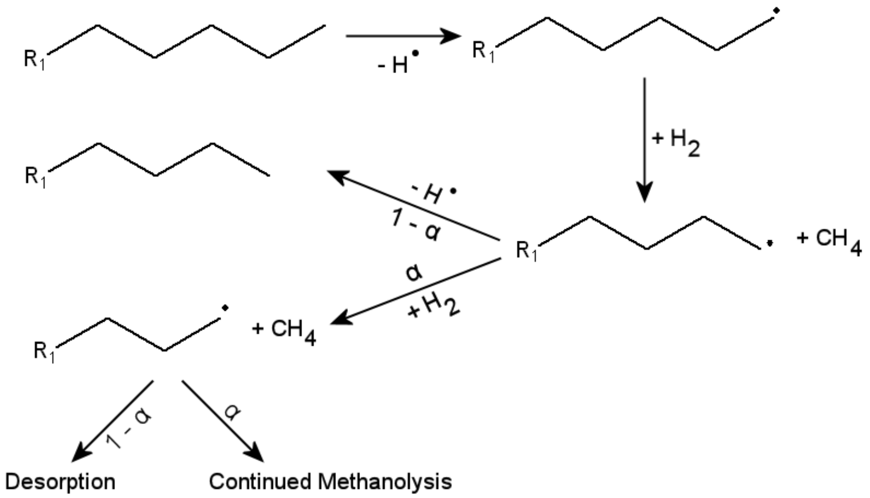

Figure 2.10: Mechanism of Hydrogenolytic Demethylation (Methanolysis)
α - Probability for Continued Demethylation
(Redrawn from Böhringer *et al.*, 2006)

2.3 Hydrocracking Catalysts

Catalytic hydrocracking has long been implemented in the refining of crude oil, although the catalysts developed in this regard are not necessarily optimal for the desired high selectivity hydrocracking of Fischer-Tropsch wax. This, as shall be discussed, is due to the use of sulphided base metal catalysts tailored to the processing of large, bulky molecules in a sulphur-containing environment.

2.3.1 Hydrocracking Catalysts for Crude Oil Derived Feed

Due to the presence of sulphur in all crude oil refinery cuts, particularly the heavier cuts such as those to be hydrocracked, hydrocracking catalysts implemented in such facilities possess a sulphided metal function. The metal sulphide is required so as to reduce the impact of sulphur poisoning on catalyst performance for, were a more active metal to be utilised (for example Pt instead of sulphided CoMo or NiW), even very small concentrations of sulphur (in the range of several ten ppm by mass) would poison the metal resulting in a significant loss in activity. This problem would be amplified by the fact that in the heavier crude oil fractions to be hydrocracked, the sulphur content is usually far higher, sometimes reaching as high as several percent (by mass). Thus, research into crude oil refinery hydrocracking has focused on optimising the metal function as a sulphide and relying on the hydrogenolytic properties of these metal sulphides for C-C bond cleavage reactions (Section 2.2.3). Thus the acidity of the carrier serves to enhance the bond cleavage activity of the sulphide rather than acting as a separate co-catalyst.

Crude oil based feedstocks also contain high concentrations of large, bulky hydrocarbons and heterocompounds (such as polycyclic and heavily substituted rings). In the case of highly desulphurised feedstocks where a metal/acid catalyst may be used for hydrocracking, the acidic support used must thus have acid sites which are exposed and easily accessible, with the use of amorphous silica-alumina (SiO_2-Al_2O_3) being common in this regard. An alternative would be the use of acid zeolites, crystalline alumino-silicates with well defined and consistent pore structures. However, even in the case of the larger pore zeolites, such as Zeolite Y, the pores are often too narrow and restrict the entry of larger molecules. As such, where zeolites are utilised in cracking processes in oil refineries, they have undergone hydrothermal pre-treatment, serving to dealuminate the structure, thereby breaking open the lattice and introducing a system of mesopores within the crystals, greatly improving mass transfer properties and simultaneously increasing access to the micropore

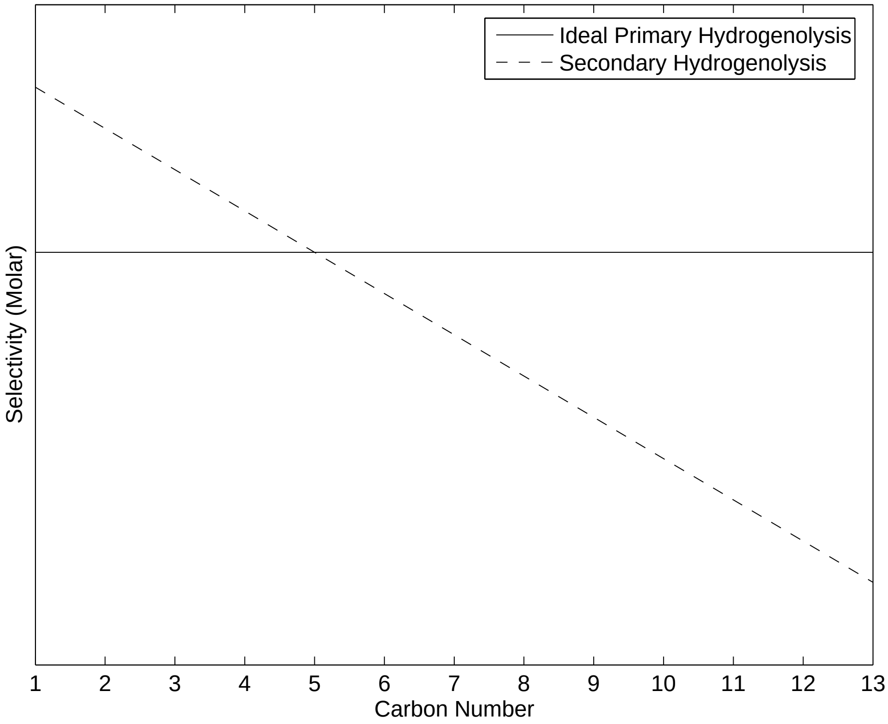

Figure 2.11: Theoretical Carbon Number Distribution of Products from Non-Specific C-C Bond Cleavage Hydrogenolysis of n-C_{14} (Redrawn from Böhringer *et al.*, 2007)

network for reaction (Scherzer and Gruia, 1996). The resulting material is termed "ultra-stable", for example ultra-stable Zeolite Y (H-USY).

2.3.2 Hydrocracking Catalysts for Fischer-Tropsch Wax Feed

Processing of Fischer-Tropsch wax thus offers two clear advantages over the processing of crude oil derived feedstocks: it is clean, containing no sulphur or other heteroatoms, and it is comprised entirely of long, minimally branched and almost entirely paraffinic hydrocarbons. As such, not only may more active non-sulphided metals be used in the catalyst (such as Pt or Pd which are known to be highly active hydrogenation/dehydrogenation metals), but as there are no bulky molecules, acid zeolites with narrower pores and crystals with fully intact pore structures may also be used.

It is this use of intact acid zeolite crystals which is of key interest in this research endeavour, for shape selective phenomena are known to be associated with reactions within these restrictive channels, and may be the key to producing distillate fuels, specifically diesel, with very high cetane numbers (i.e. paraffins exhibiting limited branching).

2.3.3 Bifunctional Hydrocracking Catalysts in the Experimental Environment

Thus, in essence, any catalyst to be utilised for the hydrocracking of hydrocarbons is required to possess C-C bond cleavage and saturation functions.

By the classical acid hydrocracking mechanism, these functions are provided separately by the acid and metal co-catalysts respectively (Section 2.2.1). The metal function is regarded as being responsible for dehydrogenation and hydrogenation, whilst the acid exacts isomerisation and cracking. Thus, so as to facilitate the diffusion of reactants between these two functions, the acid co-catalyst, in the form of small

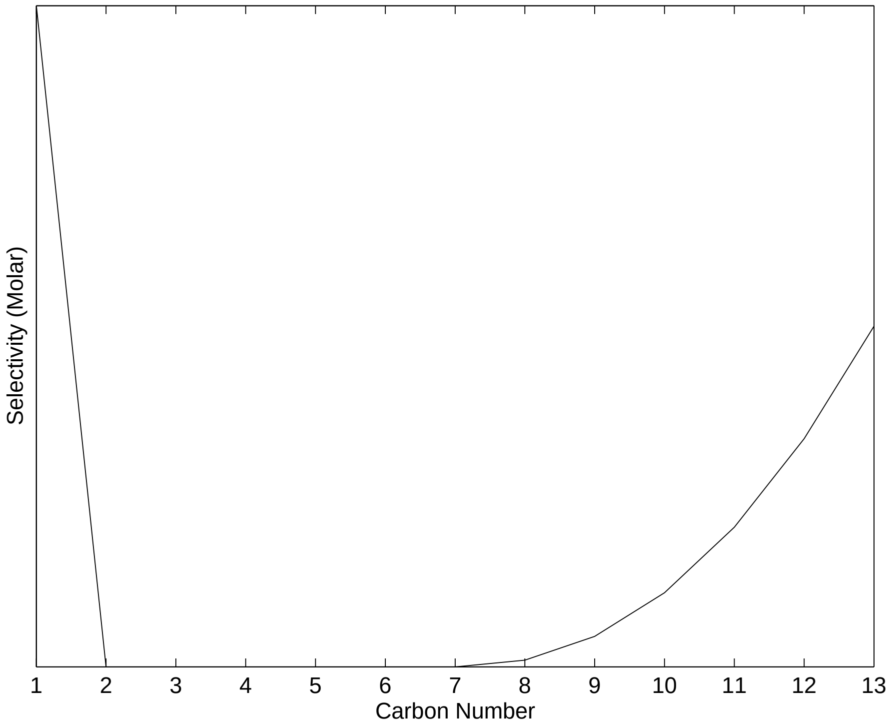

Figure 2.12: Theoretical Carbon Number Distribution of Products from Methanolysis of n-C$_{14}$ (Redrawn from Böhringer *et al.*, 2007)

crystallites, often doubles as a support upon which the metal is loaded during catalyst preparation. A common preparation technique involves the wet coating of the support surface with a metal salt solution, drying and reducing the metal to its metallic form under hydrogen flow (Pinna, 1998).

This, however, results in numerous complexities when experimental comparisons between different acid supports are to be drawn. These complications arise predominantly from the unique effect each support's surface chemistry will have on the dispersion of the metal (in terms of the crystallite size, number, distribution over the support surface, possible strong metal-support interactions, etc.) when following the same preparation procedures. Some simplified examples of this uncertainty are illustrated in Figure 2.13.

Furthermore, to maximise the area for reaction, a porous support material is often utilised (whether this is the zeolite itself or zeolite crystals in a macroporous binder), with this porosity adding yet another dimension, the pore structure, to the uncertainty surrounding the distribution of metal crystallites in the final catalyst as depicted in Figure 2.14.

Given the spillover mechanism (Section 2.2.2), however, many of these uncertainties may be circumvented for, unlike the classical mechanism which requires repeated diffusion of intermediates between metal and acid sites, bifunctional hydrocracking which proceeds by the spillover mechanism requires that the hydrogen be activated on a metal site before migrating to an acid site where all remaining reactions occur. As such, the metal co-catalyst need not be loaded directly onto the acidic support but may instead be loaded onto an inert support, with the reactor charged with a physically well-mixed bed consisting of pellets of supported metal together with acid co-catalyst particles. Furthermore, using samples of metal co-catalyst from a single, large batch of metal on inert support for all investigations allows for the comparison of different acid co-catalysts while always having the same metal co-catalyst, thereby mitigating to a great degree the effects of the aforementioned variations and uncertainties.

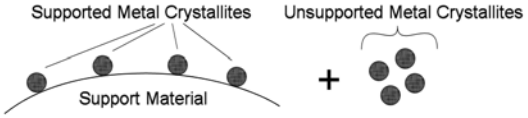

(a) Partial loading of support with metal

(b) Few large metal crystallites on support surface (poor dispersion)

(c) Even distribution of small metal crystallites (good dispersion)

(d) Unevenly sized metal crystallites on surface

Figure 2.13: Illustration of Some Possible Metal Crystallite Dispersions and Distributions on Support Material

(a) Metal crystallites solely on external surface of porous support particle

(b) Concentration of metal crystallites near pore mouth

(c) Metal crystallites distributed evenly throughout pores

(d) Accumulation of metal crystallites within pore recesses

Figure 2.14: Illustration of Some Possible Metal Crystallite Distributions on Porous Support Material

2.4 Zeolite-Based Hydrocracking Catalysts

Zeolites, crystalline alumino-silicates, possess not only a well-defined and consistent porous structure, but also surface acid sites, arising from the interaction of aluminium and silicon ions which are present within the crystal lattice with interconnecting oxygen ions. These oxygen ions may carry a proton as a charge balancing species, thereby producing a Brønsted acid site. These two features afford the zeolite not only the ability to serve as the acid function in a bifunctional (metal/acid) catalyst, but may also impose a degree of shape selectivity upon reactions occurring within the porous channels (specifically the acid-catalysed isomerisation reactions) (Csicsery, 1986).

2.4.1 Porous Structures of Selected Zeolites

Below (presented in alphabetical order of their International Zeolite Association (IZA) codes) are the structures (presented in Figures 2.15 through 2.18), dimensions (van Bekkum *et al.* (2001, Appendix) and IZA, 2002) and brief descriptions of the zeolites of interest in this investigation.

2.4.1.1 BEA - Zeolite Beta

Zeolite Beta exhibits a three-dimensional porous system, with a single set of straight 12-member-ring pore channels of 7.7 x 6.6 Å intersecting perpendicularly with two sets of alternating straight 12-member-ring channels measuring 7.7 x 6.6 Å and 5.6 x 5.6 Å. This structure of regular intersections results in the manifestation of a set of pseudo-sinusoidal pores as illustrated in Figures 2.15b and 2.15c.

2.4.1.2 FAU - Faujasite (Zeolite Y)

Zeolite Y, or Faujasite, has a three-dimensional system of spherical cavities (or "supercages") measuring 11.8 Å in diameter connected in a tetrahedral structure by 12-member-ring windows of 7.4 x 7.4 Å. Note that in Figure 2.16, these windows have been represented as elongated pores for clarity. Zeolite Y often undergoes hydrothermal pre-treatment prior to use, producing what is termed "ultra-stable" Zeolite Y, or USY. This treatment process serves to dealuminate the structure, thereby introducing a system of mesopores within the zeolite crystals, greatly improving mass transfer properties and simultaneously increasing access to the micropore network for reaction (Scherzer and Gruia, 1996). This is a very important step for the industrial implementation of Zeolite Y as it allows very bulky feed molecules (such as polyaromatic species in crude oil derived feedstocks) access to a far larger surface area for reaction.

2.4.1.3 MFI - ZSM-5

The three-dimensional structure of ZSM-5's pore system consists of a set of straight 10-member-ring pores measuring 5.1 x 5.5 Å intersecting perpendicularly with a set of sinusoidal 10-member-ring pores of 5.3 x 5.6 Å. The intersection cavities thus created are approximately 9 Å at their widest point.

2.4.1.4 MOR - Mordenite

Mordenite exhibits a two-dimensional pore structure consisting of alternating straight 12-member-ring (7.0 x 6.5 Å) and zig-zag 8-member-ring (approximately 3 Å) channels connected by short channels measuring approximately 5.4 x 5.4 Å that appear as "pockets" off the sides of the 12-member-ring channels.

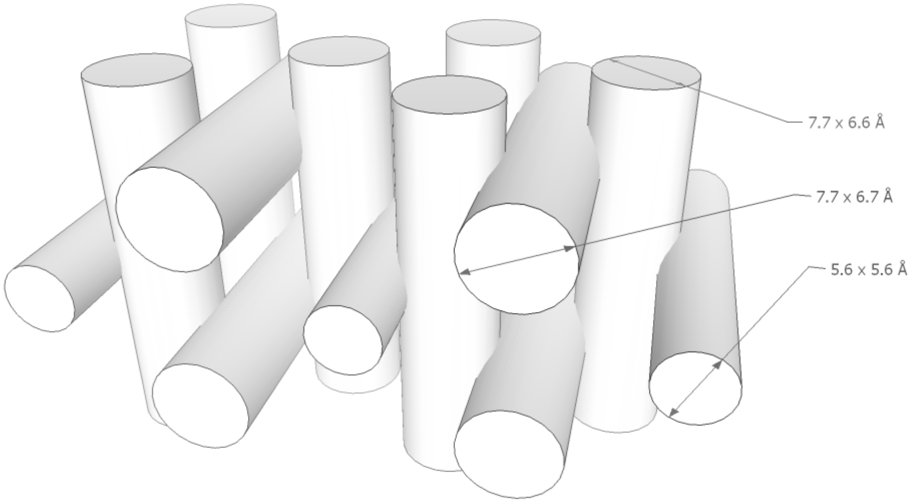

(a) Representation of the pore network with pore dimensions

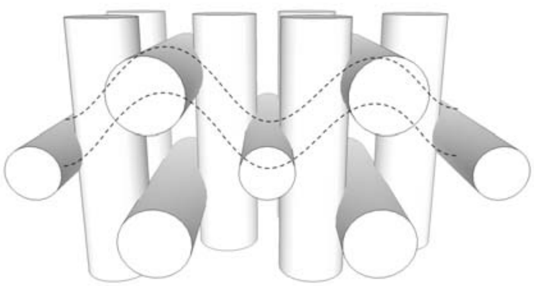

(b) View along y-axis with pseudo-sinusoidal channels illustrated by the dashed line

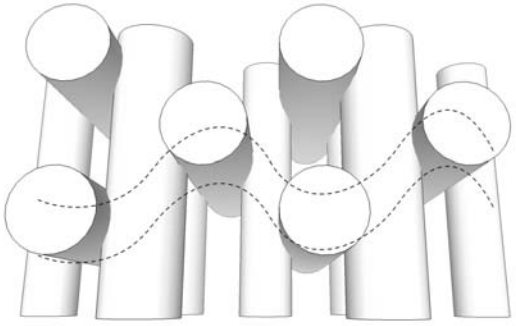

(c) View along z-axis with pseudo-sinusoidal channels illustrated by the dashed line

Figure 2.15: Three-Dimensional Representation of Zeolite-Beta Pore Structure with Pore Dimensions (Note that the pore lengths have been exaggerated for clarity)

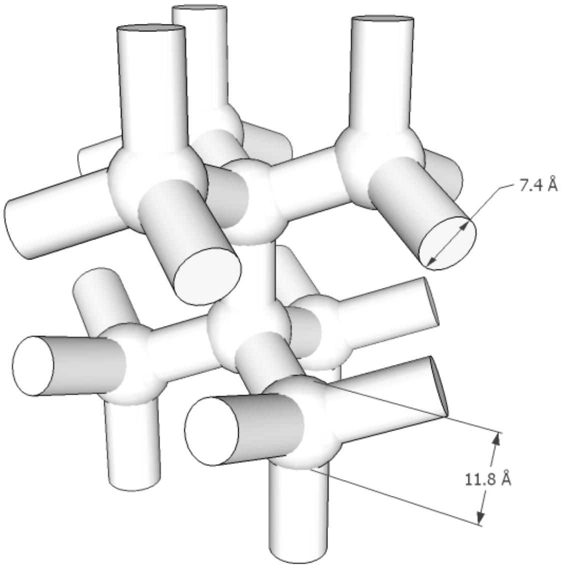

Figure 2.16: Three-Dimensional Representation of Faujasite (Zeolite-Y) Pore Structure with Pore Dimensions
(Note that the windows connecting the supercages are presented as elongated pores for clarity)

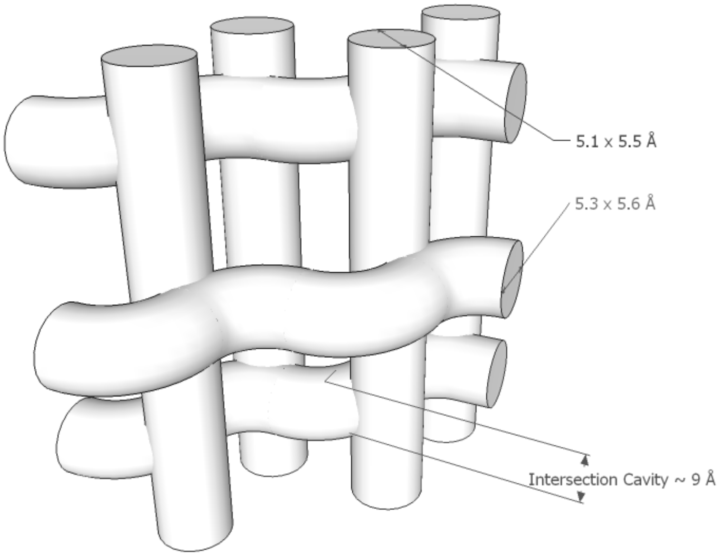

Figure 2.17: Three-Dimensional Representation of ZSM-5 Pore Structure with Pore Dimensions
(Note that the pore lengths have been exaggerated for clarity)

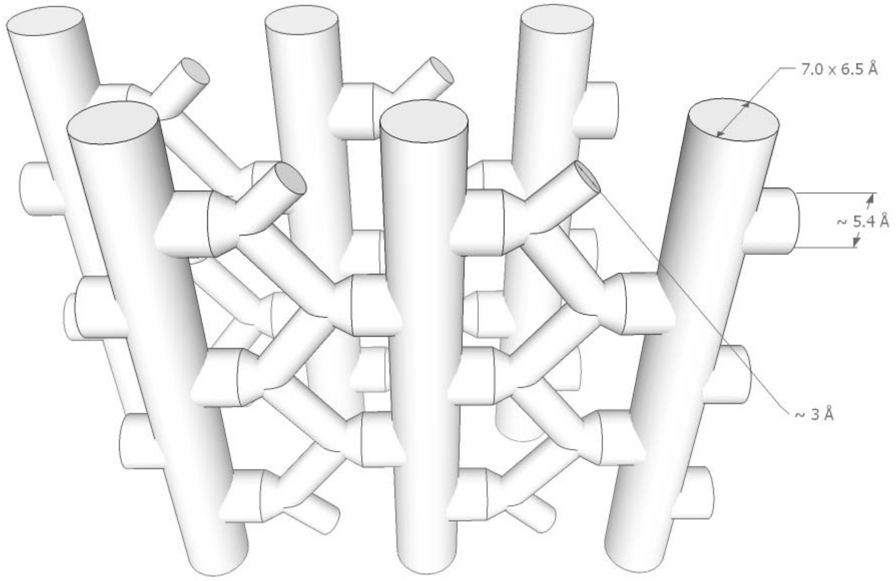

(a) Representation of the pore network with pore dimensions

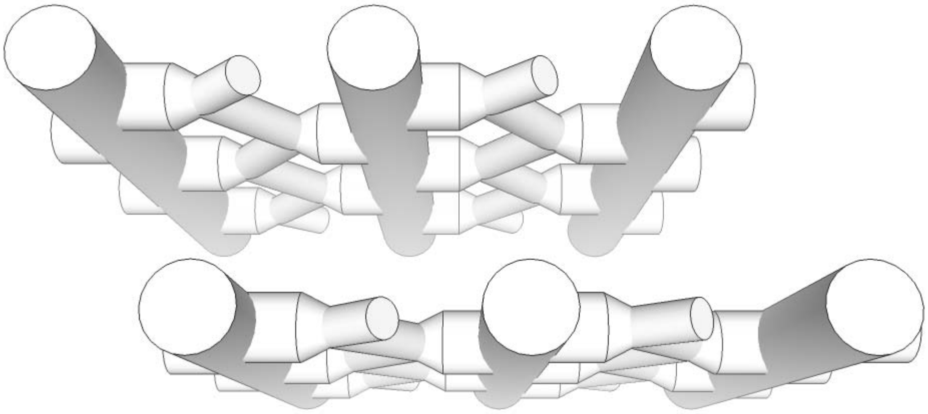

(b) Elevated view to illustrate two-dimensional nature of the pore network

Figure 2.18: Three-Dimensional Representation of Mordenite Pore Structure (Note that the pore lengths have been exaggerated for clarity)

2.4.2 Zeolite Acidity and its Effect on Bifunctional Hydrocracking Catalysts

The acidity of an H-zeolite is directly related to both the number and strength of acid sites present on the surface, with this in turn being directly related to the SiO_2/Al_2O_3 ratio of the framework (Martens and Jacobs, 1997).

From Figure 2.19, it may be seen that the zeolite acid sites arise from the charge imbalance between Si^{4+} and Al^{3+} atoms embedded in a tetrahedral framework of linking O^{2-} anions, and the subsequent interaction of the oxygen atom of the hydroxyl group, formed on the Si, with a neighbouring Al atom as indicated by the dashed line in Figure 2.19 (note that this dashed line indicates an interaction, not an actual bond). This interaction has two effects. The first of these is the weakening of the hydroxyl group's O-H bond, thereby increasing the Brønsted acidity of that hydrogen atom (bold in Figure 2.19a), and the second is the associated weakening of the Al-O bonds, thereby increasing the Lewis basicity of these oxygen atoms (bold in Figure 2.19b) (Martens and Jacobs, 1997).

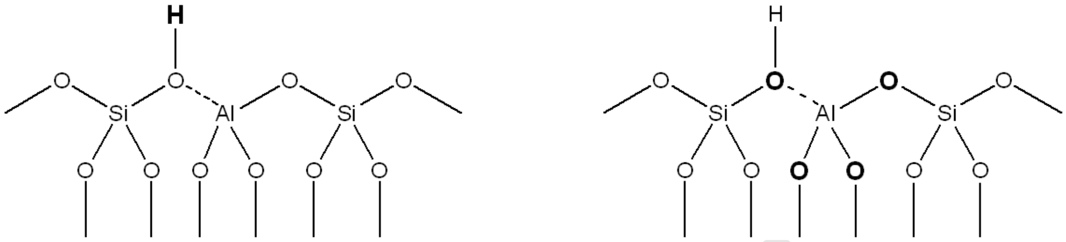

(a) Brønsted acidity due to weakening of the O-H bond

(b) Lewis basicity of the Al oxo-ligands due to weakening of the Al-O bonds

Figure 2.19: Surface of Zeolite Crystal Showing Brønsted Acid and Lewis Base Sites (Redrawn from Martens and Jacobs, 1997)

Thus, lower SiO_2/Al_2O_3 ratios result in an increase in the number of acid sites due to the greater occurrence of Al which is able to interact with the surface hydroxyl groups. These interactions do, however, decline in strength with decreasing SiO_2/Al_2O_3 ratio, with each individual acid site becoming marginally weaker. Similarly, zeolites with higher SiO_2/Al_2O_3 ratios possess fewer acid sites, but each of greater strength. This relationship was examined by Rastelli *et al.* (1982) who examined the observed activity of various zeolites for n-butane cracking as a function of their Si and Al composition as illustrated in Figure 2.20.

Rastelli *et al.* (1982) determined that, starting at a low SiO_2/Al_2O_3 (i.e. a high Al/(Al+Si) ratio in Figure 2.20), the zeolites investigated possess a very high concentration of weak acid sites, with the overall acidity (determined by both acid site number and individual strength) and associated activity hence being very low. As the SiO_2/Al_2O_3 ratio increases (i.e. a decrease in Al/(Al+Si) ratio), the concentration of acid sites on the zeolite becomes lower, but the individual strength of each site increases. This results in an increase in the overall acidity and hence the increase in the observed activity as noted by the researchers. At very high SiO_2/Al_2O_3 ratios (i.e. very low Al/(Al+Si) ratios), whilst the acid sites may possess a high individual acidity, the low concentration of these sites results in a decrease in overall zeolite acidity and a subsequent decline in the associated activity.

Investigations by Park and Ihm (2000) confirmed the observations of Rastelli *et al.* (1982) by relating the acidity of zeolites to the activity of a bifunctional (metal/zeolite) catalyst in hydrocracking and hydroisomerisation reactions. They noted that zeolites with strong acid sites, quantified in terms of ammonia temperature programmed desorption data, exhibited a greater overall conversion of the n-hexadecane (n-C_{16}) feed that was used and greater cracking conversion than did those with weaker acid sites.

Explained in terms of the classical bifunctional hydrocracking mechanism (Martens and Jacobs, 1997) (Section 2.2.1), the metal would serve to dehydrogenate the paraffinic feed, forming an olefin. This olefin would be protonated by the acid function, with the carbenium ion thus formed undergoing isomerisation

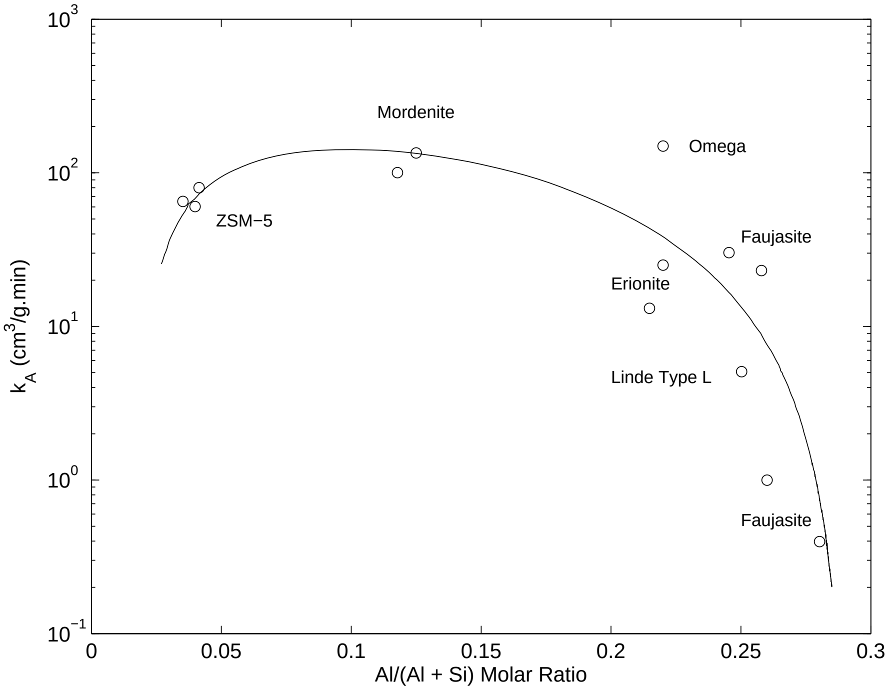

Figure 2.20: Observed Zeolite Activity (k_A) as a Function of Aluminium Content for n-Butane Cracking (Redrawn from van Bekkum *et al.*, 2001, Chapter 8)

and/or cracking by β-scission. The olefinic molecules thus formed would then be rehydrogenated by the metal, resulting in paraffinic products. In terms of the hydrogen spill-over mechanism (Section 2.2.2), all hydrocarbon reactions would occur on the acid site, initiated and controlled by the activated hydrogen which would be formed on the metal sites, and similarly to the classical mechanism, producing paraffinic products.

It is thus clear that, regardless of the type of paraffin activation mechanism, as the overall strength of the acid function increases (itself being a trade-off between the number of acid sites and their individual acidity), the primary cracking products will undergo secondary cracking at greater rates, resulting in the formation of shorter chain paraffinic products.

Alvarez *et al.* (1996) investigated this concept as it relates to the relative presence of the metal and acid functions on each catalyst. Based on the ratio of exposed metal atoms to active acid sites, the authors theorised, in terms of the classical mechanism, that if the number of acid sites is too high (compared to the number of metal sites), then the primary cracking products may reach another acid site prior to a metal site, thereby undergoing further cracking, with the observed effect being similar to that for stronger acid sites. They determined that for a molar ratio of exposed metal active sites to active acid sites (i.e. tetrahedrally oriented framework aluminium atoms) of below 0.03 (for the Pt/HY catalysts utilised in the study for the hydroconversion of n-decane at 200°C and a total pressure of of 1 bar), the metal function was limiting, with cracking products undergoing a great deal of consecutive cracking reactions prior to being rehydrogenated at a metal site (this being in terms of the classical mechanism, whereas in the spillover mechanism one may view this as there being insufficient activated hydrogen species present to "quench" the reaction before consecutive cracking may occur). Alvarez *et al.* (1996) further indicated that for such a "metal:acid site ratio" above 0.17 (for the Pt/HY catalysts utilised in the study for the hydroconversion of n-decane at 200°C and a total pressure of of 1 bar), the acid sites became limiting, resulting in a system that exhibits "true" hydrocracking (see Figure 2.5), i.e. one that undergoes only primary cracking, with there being ample metal sites to rapidly rehydrogenate the cracking products (or, in terms of the spillover mechanism, there being a vast excess of activated hydrogen to rapidly quench the cracking reaction).

2.4.3 Shape Selectivity Induced by Narrow Zeolite Pore Dimensions

Zeolites have well-defined and understood crystal structures and pore networks, with the various pore networks differing depending on the zeolite type and ranging, for example, from isolated parallel channels (such as ZSM-12) to interconnecting, two dimensional channels (as in ZSM-5) to those with interconnected "supercages" occurring regularly throughout the pore structure (an example being Zeolite Y). The dimensions of these channels (which are generally well known and documented for each zeolite) differ between zeolite types, ranging for instance from 5.6 Å (as in ZSM-5) to 7.4 Å (in Zeolite Y) (van Bekkum *et al.*, 2001, Appendix). The physical restrictions imposed by narrow and less interconnected channels are believed to be responsible for a great degree of shape selectivity in acid catalysed reactions utilising zeolites.

Such shape selectivity may be divided into three groups: reactant, product and transition-state shape selectivity (Csicsery, 1986).

Reactant shape selectivity occurs when the reactant molecules are too large to enter the zeolite pores, thereby limiting, to a great extent, the accessible acid sites on which they may react to those few located on the external surface of the zeolite crystallites (Csicsery, 1986). This phenomenon is illustrated in Figure 2.21a for the isomerisation of n-octane and 3-ethylhexane. The observed activity to reactants which are subject to exclusion by such shape selectivity (i.e. the 3-ethylhexane in Figure 2.21a) will hence be lower than that of reactants which are not excluded in this manner.

Product shape selectivity, illustrated in Figure 2.21b for the isomerisation of n-octane, occurs when products which are able to form within the wider sections of the zeolite's pore network (such as within the supercages of Zeolite Y or the intersections of channels in ZSM-5) are too bulky to leave through the narrower channels and experience a great deal of resistance to this diffusion (Csicsery, 1986). The consequence of this phenomenon is that, as the less bulky species diffuse out of this section of the pore network, so their local concentration declines and the associated shift in the reaction equilibrium causes the more bulky molecules (such as the 3-ethylhexane in Figure 2.21b) to isomerise into more compact species which are then able to quickly diffuse out of the restrictive channels. The selectivity of the reaction towards the bulkier products is thus observed to decline, even below equilibrium levels (although these products may still form with impunity on the external surfaces of the zeolite crystals), whilst the selectivity towards the less bulky isomers or smaller cracking products would be observed to rise (Zhang and Smirniotis, 1999). The observed product distribution of such a system is thus determined by mass transfer limitations (as discussed in Section 2.4.4).

Transition-state (or intermediate) shape selectivity is a phenomenon whereby the reaction paths which would lead to the formation of certain species are restricted by the pore dimensions, with the formation of bulky reaction intermediates being inhibited due to spacial constraints affected by the pore walls themselves. This phenomenon is illustrated in Figure 2.23 for two C_8 isomers, with the overall consequences of such shape selectivity depicted in Figure 2.22 for the isomerisation and cracking of C_8 over a medium pore acid zeolite (such as H-ZSM-5).

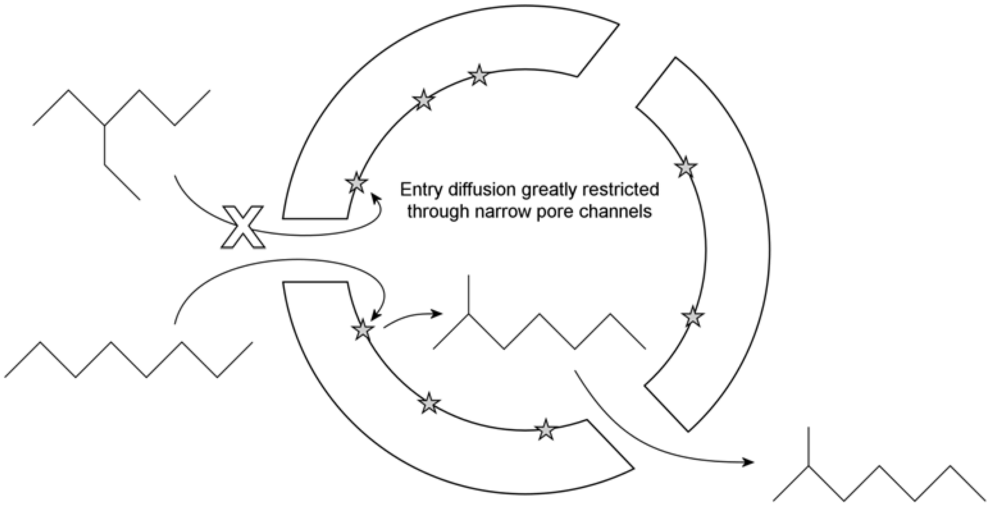

(a) Example of reactant shape selectivity illustrating the exclusion of the bulky 3-ethylhexane whilst the narrower n-octane may enter the pores and react

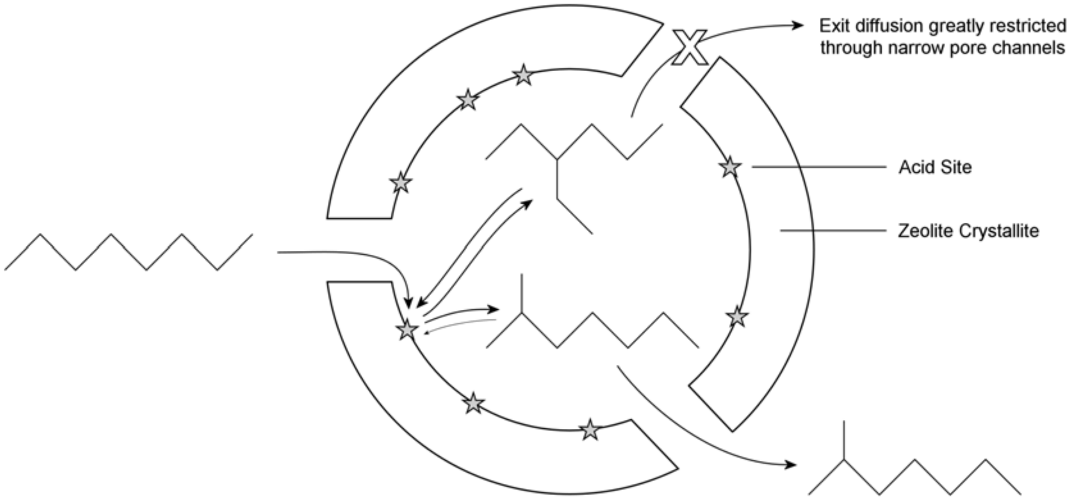

(b) Example of product shape selectivity whereby n-octane isomerises into 3-ethylhexane and 2-methylheptane with the former being restricted from leaving the pore system due to the narrow channels and hence isomerising to the latter (preferential) product which is able to diffuse easily out of the pore network

Figure 2.21: Reactant and Product Shape Selectivity Over a Medium Pore Zeolites (such as H-ZSM-5)

As may be seen in Figures 2.22 and 2.23, whilst the hydrocarbon chain itself is potentially able to undergo much isomerisation, easily achieving configurations which allow for either Type B or Type C β-scission (as per Figure 2.4), the restrictive pore dimensions in medium pore zeolites such as H-ZSM-5 impose great restrictions on the rate at which the quartery carbon intermediates (with the tertiary carbenium ion in the β position), required for what is believed to be the most rapid (Type A) β-scission, may form. Thus, as noted by Park and Ihm (2000), whilst this phenomenon restricts any significant branching of a n-alkane feed

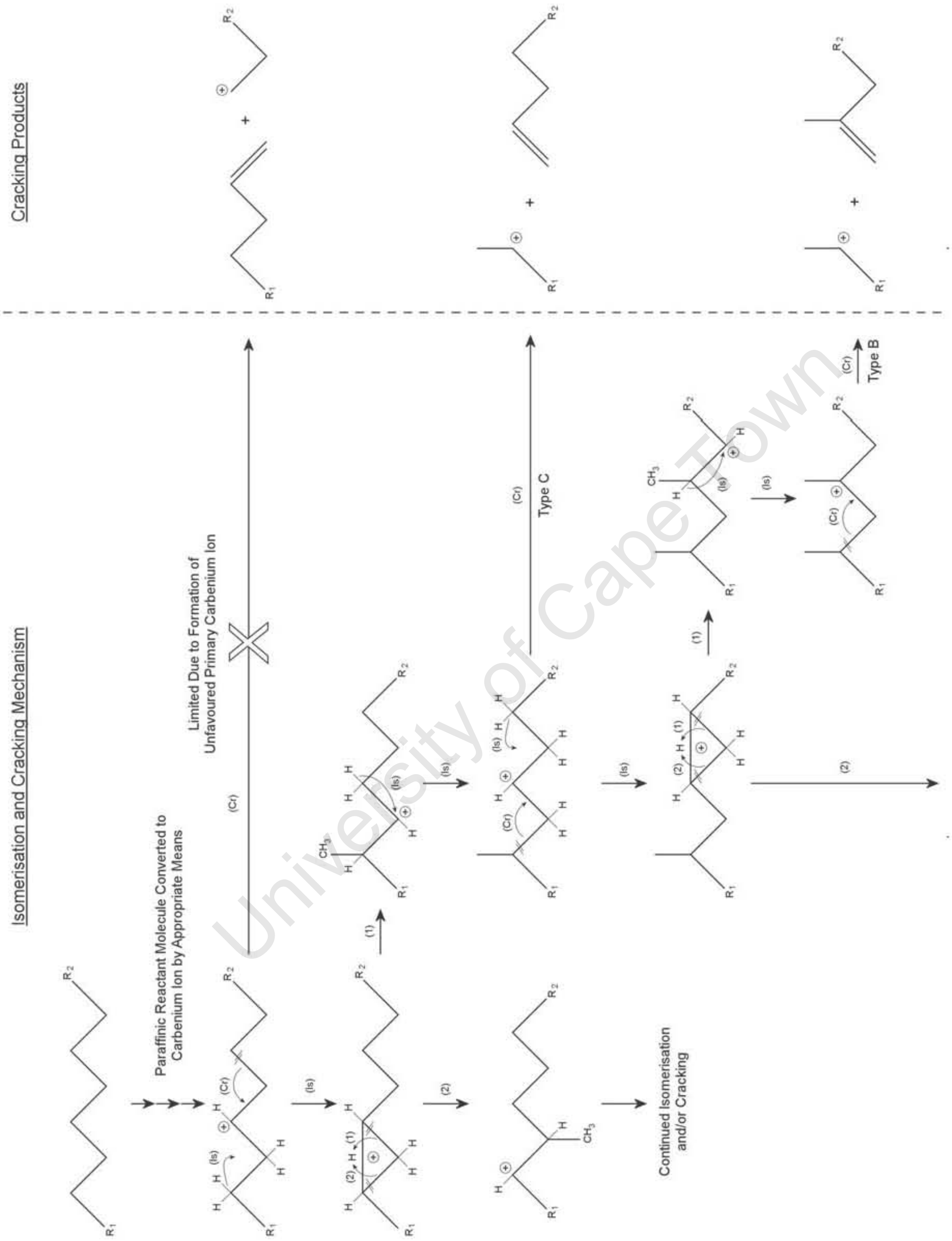
Isomerisation and Cracking Mechanism
Cracking Products
Paraffinic Reactant Molecule Converted to Carbenium Ion by Appropriate Means
Limited Due to Formation of Unfavoured Primary Carbenium Ion
(Cr)
(Is)
(1)
(2)
Type C
(Cr)
Type B
Continued Isomerisation and/or Cracking
R_1
R_2
CH_3
H
+

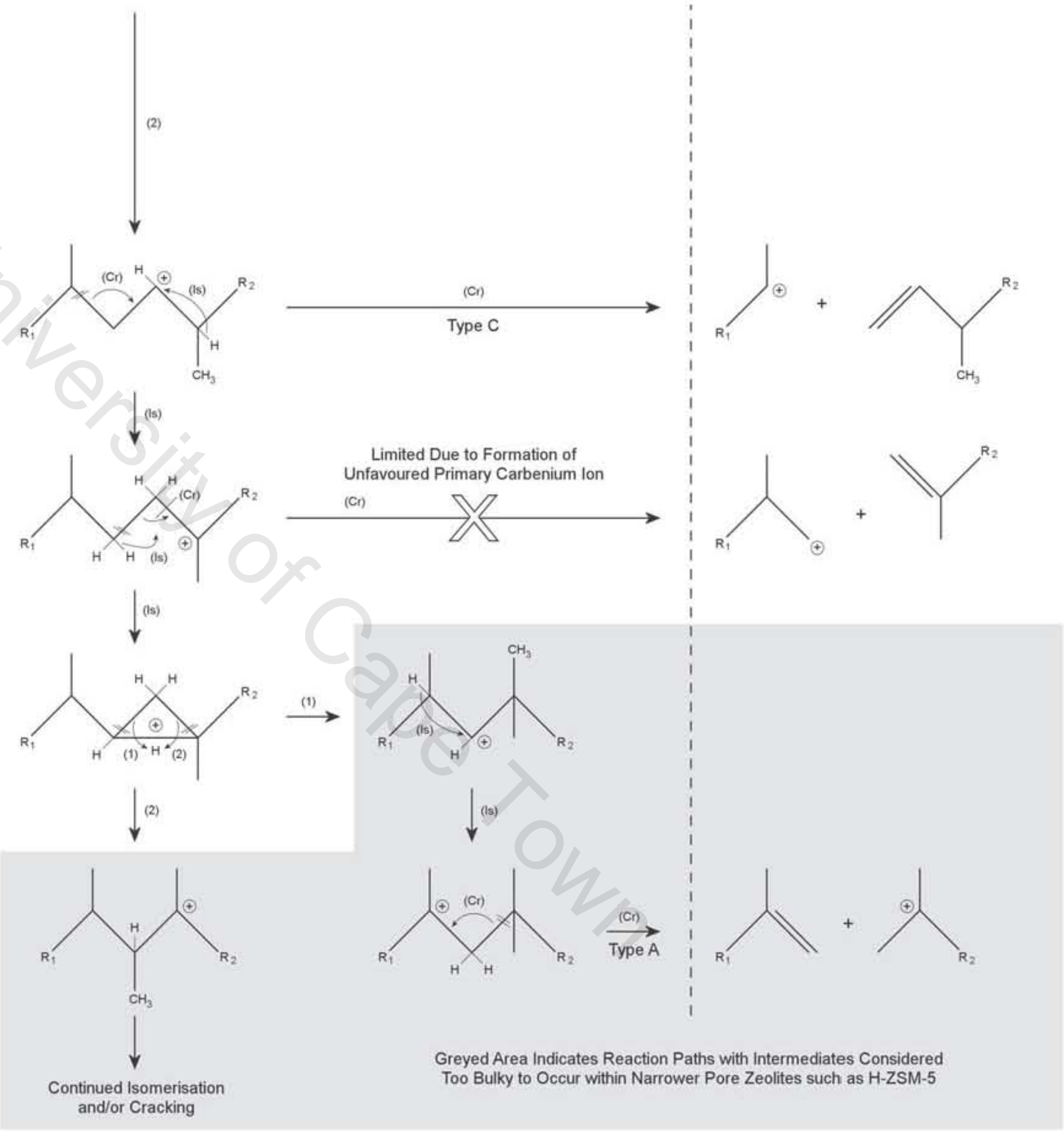

Figure 2.22: Carbenium Ion Mechanism of n-Alkane Isomerisation and Cracking over an Acid Catalyst

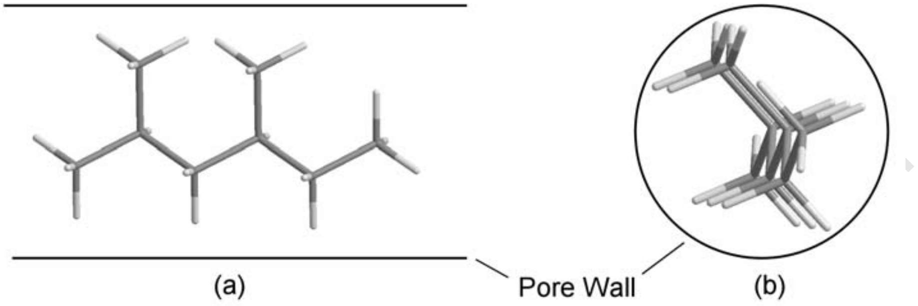

(a) Representation of 2,4-dimethyl hexane within medium pore, with a side "sliced through" view (a) and axially along the pore (b), showing minimal spatial restriction

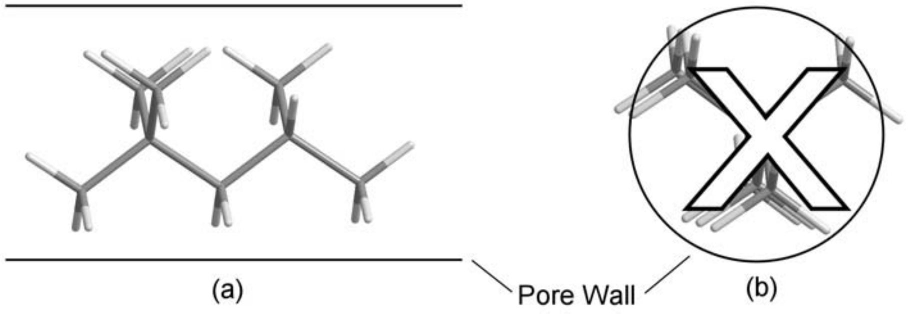

(b) Representation of 2,2,4-trimethyl hexane within medium pore, with a side "sliced through" view (a) and axially along the pore (b), showing severe inhibition due to spatial constraints

Figure 2.23: Transition State Selectivity Over a Medium Pore Zeolite (such as H-ZSM-5)

molecule, thereby increasing the selectivity of the system towards lesser branched products, it simultaneously reduces the rate at which cracking can proceed by forcing the system to proceed via the slower Type B and Type C β-scission mechanisms over Type A. An increase in the reaction temperature may serve to counteract this reduced activity, however, an increase in the severity of the reaction conditions will likely result in both the formation of additional amounts of coke within the zeolite pores and in a greater yield of light products (due to, for instance, additional monofunctional acid cracking and diffusion control).

Rollmann and Walsh (1979), however, studying the conversion of a five component feed (consisting of n-hexane, 3-methylpentane, 2,3-dimethylbutane, benzene, and toluene) at a temperature of 425°C over various acid zeolites (including H-ZSM-5, H-ERI, H-FER, H-MOR, H-L, H-Y and H-ZSM-4) noted a distinct relationship between each zeolite's reactant shape selectivity and the formation of coke. Specifically, the medium pore zeolites which exhibited high reactant, transition state and product shape selectivity (H-ZSM-5, H-ERI and H-FER) yielded a far reduced amount of coke, particularly H-ZSM-5, than did the less shape selective wide pore zeolites (H-MOR, H-L, H-Y and H-ZSM-4). This phenomenon was suggested to be due to the increased spatial constraints, imposed by the geometrically restrictive channels in the medium pore zeolites, which served to reduce the rate at which bulky coke precursors (polyaromatics for instance) could form within the zeolite channels, thereby reducing the overall coke formation and prolonging catalyst on-stream life.

The reduction in coke formation due to shape selectivity and the increase in coke formation due to the more severe reaction conditions (required to force the reaction to proceed by less favourable pathways), will hence be counteracting effects, and the question is now raised as to which will be more influential. In this regard it should be noted that whilst Rollmann and Walsh (1979) determined that the majority of coke formed on all of the zeolites tested did so within the channels themselves, the reduced amount present in the pore network of the medium pore zeolites was not sufficient to reduce the effective diameter of the pores (thereby negatively affecting the reaction due to diffusion limitations) or even block the pores entirely any sooner than did the greater amounts of coke in the larger pore zeolites.

It must, however, be noted that the pore dimensions of zeolites are calculated based on the van der Waals radii of the atoms constituting those pores (i.e. the spheres of weak inter-atomic force surrounding the atoms) and that these atoms, as with any atoms in a crystal lattice, vibrate in their positions. This weak sphere of force around each of the atoms, their vibration, and the vibration and bending of the molecular bonds of hydrocarbon molecules, allows molecules which theoretically could not enter the channels to do so, although to a smaller extent (Csicsery, 1986). This is particularly evident at elevated temperatures for as not only would the hydrocarbon molecule and the zeolite's atoms be vibrating to a greater extent, but the hydrocarbon molecules would also possess greater kinetic energy with which to overcome the repulsive forces associated with entering the pore mouth (Csicsery, 1986).

2.4.4 The Influence of Zeolite Characteristics through Mass Transfer Limitations

To facilitate a basic understanding of some of the factors influencing the catalytic system under investigation, and to aid in the interpretation of results, the effect which variations of the key zeolite characteristics have on the activity and selectivity of the system must be examined. These characteristics, in so far as this investigation is concerned, are limited to:

- The acidity of the zeolite through the number and strength of the acid sites (fundamentally linked to the SiO_2/Al_2O_3 ratio)
- The geometry of the pore network (in terms of the pore dimensions, shape and interconnectivity)
- The size of the individual zeolite crystallites

Each of these characteristics has a unique affect on the system through its individual influence on the mass transfer properties of the pore system of the zeolite crystallite. In order to relate variations in these properties to the observed phenomena of activity and selectivity, the Thiele modulus is employed.

The Thiele modulus (Φ) is a dimensionless group defined, assuming a spherical zeolite crystallite, by relating the radius of the crystallite, the intrinsic activity of the active sites and the diffusivity (itself a function of the pore geometry) as follows (Weisz and Prater, 1954):

$$\Phi = R_c \left(\frac{k}{D_{eff}}\right)^{\frac{1}{2}}$$

R_c - Radius of spherical zeolite crystallite
k - Intrinsic rate constant based on gas-phase concentrations
D_{eff} - Effective intra-crystalline species diffusivity

The Thiele modulus may then be used to determine the effectiveness factor (η), which indicates the observed reaction rate of a component (for instance the consumption of the feed or formation of a product) as a factor of its intrinsic rate (e.g. for a first order reaction whereby $A \xrightarrow{k} B$ and hence $r_A = k \times C_A$, $\eta = k_{observed}/k_{intrinsic}$). The exact relationship between the effectiveness factor and the Thiele modulus takes into account numerous details of the physical system, among them the order of the reaction and the geometry of the catalyst. As such, for clarity and simplification in this explanation, a first order reaction and spherical zeolite crystallites will be assumed throughout, with the effectiveness factor then being defined as (Weisz and Prater, 1954):

$$\eta_A = \frac{3}{\Phi_A}\left(\frac{1}{tanh\Phi_A} - \frac{1}{\Phi_A}\right)$$

η_A - Effectiveness factor with respect to component A
Φ_A - Thiele modulus with respect to component A

It is thus clear that acid site activity, pore dimensions (by virtue of the diffusivity) and crystallite size all have a definitive influence on the observed activity of the system. This, however, also indicates that the selectivity will be influenced by these factors for, as the diffusion of the primary cracking products away from the active sites is inhibited, so there exists the possibility that these product molecules themselves will encounter acid sites and undergo further cracking before leaving the zeolite crystallite. This phenomenon, if occurring to any great extent, can result in a pseudo-parallel reaction. For example, with the formation of secondary cracking product C from the consecutive reaction of primary product B as per Figure 2.24a, it would appear to the observer that products B and C are formed concurrently, as per Figure 2.24b, with only an understanding of the fundamental mechanism of the reaction allowing for an opinion to be drawn regarding the actual reaction sequence.

(a) Secondary cracking as consecutive reaction

(b) Secondary cracking depicted as pseudo-parallel reaction

Figure 2.24: Secondary Cracking Represented as Either Consecutive or Pseudo-Parallel Mechanism (Wheeler, 1951)

For the specific case of hydrocracking, as the severity of such internal mass transfer limitations increases, so does the possibility of product re-adsorption and further cracking, hence resulting in a progressive shift of the product carbon number distribution towards lighter products as depicted in Figure 2.25.

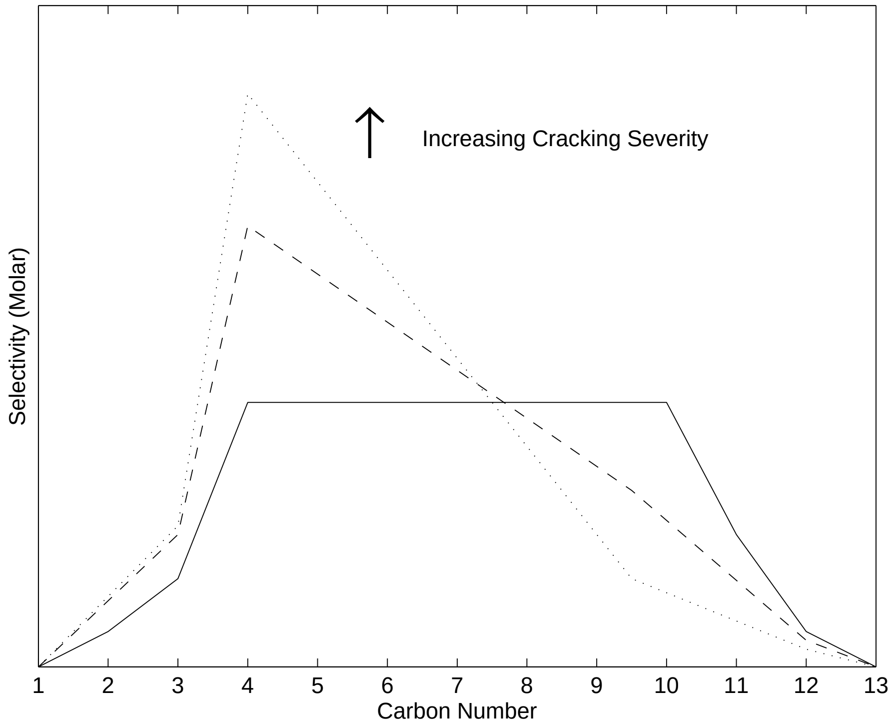

Figure 2.25: Representation of the Effect of Mass Transfer Limitations on Carbon Number Distribution (Adapted from Sie *et al.*, 1991)

This simplified explanation of the observed pseudo-parallel reactions, however, only holds when the reaction whereby the secondary product, C, is formed from the primary product, B, has a rate constant approximately equivalent to that for the reaction whereby B is formed from the feed, A, i.e. $k_1 \approx k_2$ in the following reaction sequence (with any reverse reactions omitted for both clarity and applicability to cracking products):

$$A \xrightarrow{k_1} B \xrightarrow{k_2} C$$

If, however, the rate constants differ significantly (i.e. $k_1 > k_2$ or $k_1 < k_2$), the two reaction steps will possess greatly different Thiele modulus values even though they may occur within the same zeolite crystallite (as predicted by the presence of k in the definition of the Thiele modulus), and hence exhibit different effectiveness factors for the formation of each product. These variations are illustrated in Figure 2.26 for the effectiveness factor as it relates to the formation of primary product B as a function of the Thiele modulus (for the generalised reaction presented in Figure 2.25). It should be noted that the rate constant as it relates to the observed formation of B is a function of both k_1 and k_2 (whereas the rate constant associated with the formation of C is solely k_2) and hence the Thiele modulus for the formation of B is defined as:

$$\Phi_B = R_c \left(\frac{k_2 - k_1}{D_{eff.B}} \right)$$

It is thus seen that whilst variations in the relationship between k_1 and k_2 have a distinct impact on the observed rate of formation of B, they do not alter the inherent relationship between kinetic and diffusion control. This is clear for, at low values of the Thiele modulus for the formation of primary product B (corresponding to an unrestricted system of large pores and/or the reaction occurring within very small zeolite crystallites) the effectiveness factor for the formation of B is determined to be close to unity, indicating that

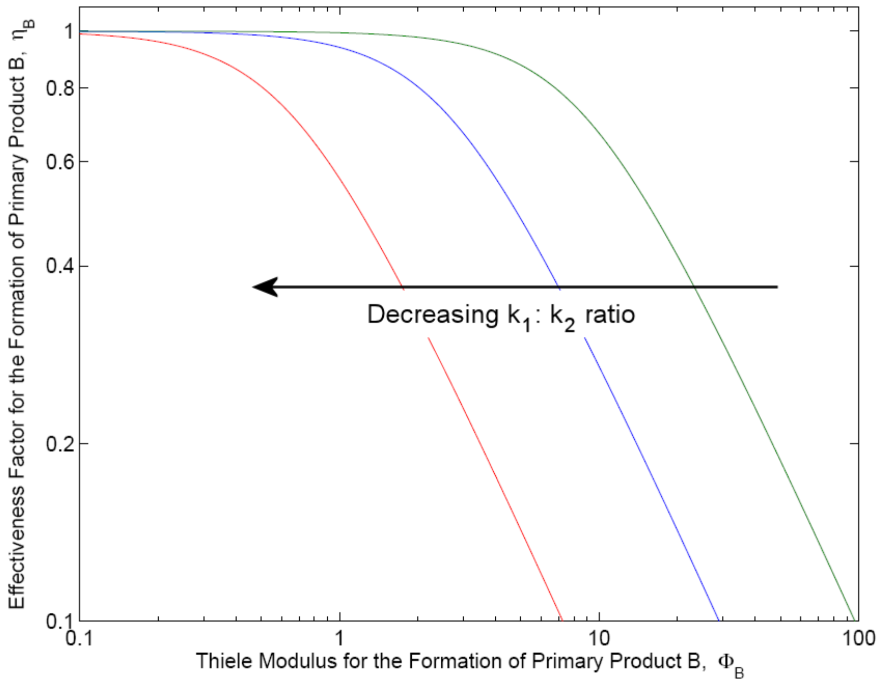

Figure 2.26: Effectiveness Factor of Primary Product, B, with Variations in Thiele Modulus for the Formation of B in the Reaction $A \xrightarrow{k_1} B \xrightarrow{k_2} C$
(Redrawn and modified from van Bekkum *et al.*, 2001, Chapter 12)

the system is kinetically controlled, with the observed rate of formation of B being approximately equivalent to its intrinsic rate of formation. This remains true for a small increase in the Thiele modulus (caused, for instance, by utilising a zeolite with a more restrictive pore system and/or present as larger crystallites) up to a critical point whereat any further increase in the Thiele modulus results in a rapid decline of the effectiveness factor away from unity. This decline corresponds to the system transitioning from a region of kinetic control into one of diffusion control wherein the observed rate of formation of B is lower than the intrinsic rate associated with the reaction on that specific zeolite, therewith indicating that the diffusion of the reactants and/or products to or from the active sites respectively becomes the limiting factor.

In order to examine how the selectivity towards a reactive intermediary product (i.e. primary product B in the generalised reaction being examined) was affected by the characteristics of the system, Wheeler (1951) devised the following relationship to predict the yield of B (S_B) in the reaction:

$$S_B = \frac{Q}{Q-1}(1-X_A)[(1-X_A)^{-(1-1/\sqrt{Q})}-1]$$

X_A	-	Fractional conversion of feed, A
S_B	-	Fractional yield of desired primary product, B (i.e. fraction of A converted to B)
Q	-	Ratio of primary and secondary reaction rate constants, i.e. k_1/k_2

The interpretation of this equation may be varied slightly by noting that:

$$Q = \frac{k_1}{k_2} = \left(\frac{\Phi_1}{\Phi_2}\right)^2 \times \left(\frac{D_1}{D_2}\right) \times \left(\frac{R_2}{R_1}\right)^2$$

From this rearrangement, it may be seen that the general trends associated with variations in k_1/k_2 (by virtue of Q) also hold for D_1/D_2 and $(R_2/R_1)^2$. It must be noted that the subscripted 1 and 2 in these ratios still refer to reactions whereby B is formed from A and C from B respectively and thus, whilst the ratio of diffusivities is generally of great importance (particularly for cracking reactions in pore networks where the secondary products may have diffusivities vastly different from that of the primary product) for a series reaction occurring within a single crystallite, the ratio of particle radii is generally less applicable as it suggests that the two stages of the reaction take place in entirely different crystallites, a less likely scenario.

A graphical examination of these relationships, as illustrated in Figure 2.27, allows for a clearer explanation of the trends noted in Figure 2.26 for variations in the k_1/k_2 ratio. At larger k_1/k_2 ratios, the yield towards the primary product is higher for all Thiele modulus values (much as the associated effectiveness factors were closer to unity), for even though the primary products may be re-adsorbed, the rate at which these re-adsorbed molecules react is far lower than that by which they are being formed. A decline in the $k_1 : k_2$ ratio, however, results in this yield dropping over the Thiele modulus range examined (as the associated effectiveness factors were observed to decline from unity), corresponding to the more rapid reaction of any primary product molecules which are re-adsorbed.

Furthermore, the transfer between kinetic and diffusion control evident from Figure 2.26 has a clear impact on the yield of the system as shown in Figure 2.27 for, whilst the primary products formed in a zeolite with a low Thiele modulus (i.e. higher D_1/D_2 and R_2^2/R_1^2 ratios) may diffuse rapidly away from the active sites and out of the zeolite crystallite, thereby minimising the extent to which their re-adsorption and continued reaction may occur, such primary products formed within a zeolite with a higher Thiele modulus (i.e. lower D_1/D_2 and $(R_2/R_1)^2$ ratios) will experience hindered diffusion out of the crystallite, greatly increasing the probability of re-adsorption and continued reaction.

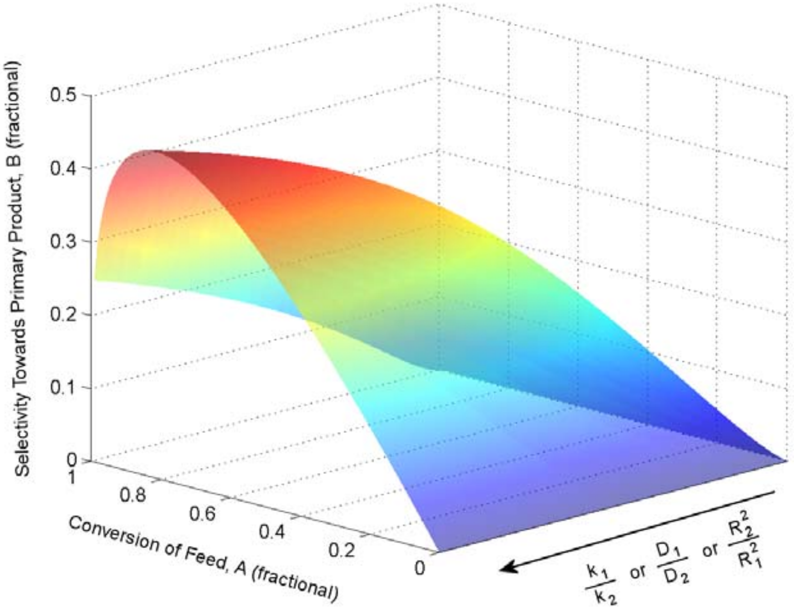

Figure 2.27: Observed Yield of Primary Product, B, as Influenced by Reaction Rate Constants, Diffusivities and Crystallite Dimensions

These phenomena are well known and have been observed by numerous researchers.

Zhang and Smirniotis (1999), studying the hydroisomerisation of n-octane over H-ZSM-12 and H-Beta at temperatures between 180 and 450°C and 100 psig (approximately 6.8 bar), found that an increase in acid strength resulted in a shift towards a more branched product. This result was anticipated for, with an increase in the acidity of the zeolite, the intrinsic rate constants of the sequential isomerisation reactions increase, thereby increasing the Thiele modulus associated with each of the intermediary products. This increase in the Thiele modulus, as per Figure 2.26, would result in a decline of the effectiveness factor associated with each product, manifesting as a shift in the observed product spectrum towards more branched isomers (i.e. products further down the sequential reaction chain).

This research by Zhang and Smirniotis (1999) together with that conducted by Chao *et al.* (1996) (investigating the hydroisomerisation of n-pentane, n-hexane and n-heptane over Pt/H-Beta and Pt/H-Mordenite at 190 to 300 °C and 1 to 27 bar) indicated that wide pore zeolites exhibited a greater selectivity towards more branched products, with both groups concluding that this was due to reduced spatial constraints on more branched isomerisation intermediates and products. A possible concurrent factor to this shift in the selectivity may be the variation in diffusivities associated with more restrictive pore systems (van Bekkum *et al.*, 2001, Chapter 12). This reduction in the diffusivity with decreasing pore dimensions (or indeed with pore structures that are more restrictive to the diffusion of the primary products, depending on the type of zeolite being utilised) would serve to increase the Thiele modulus of the various products, thereby reducing their effectiveness factor and resulting in the observed shift of the product spectrum towards more highly branched species. The spatial constraints imposed upon reaction intermediates and products in more restrictive zeolite channels thus manifest in a complex, interacting array of effects. This results due to the spatial constraints directly inhibiting the formation of more branched species through shape selective phenomena (see Section 2.4.3), whilst simultaneously amplifying the effects of diffusivity variations between species. By this latter point, reduction in the diffusivity of the lesser branched primary products will serve to shift the product spectrum towards the more branched consecutive reaction products. These more branched products, however, experience a greater degree of diffusional inhibition, driving the system back towards lesser branched isomers, with the observed product spectrum thus being a fine balance between these various competing effects.

Furthermore, investigations by Möller *et al.* (1999) into the effect of crystallite size of an H-ZSM-5 catalyst on the methanol-to-olefins reaction (whereby methanol is converted via dimethyl-ether to olefins) conducted in an ideally back-mixed reactor at 300 and 420°C and 1.9 bar indicated a clear and dramatic effect whereby an increase in the size of the H-ZSM-5 crystallites resulted in an increase in the selectivity towards the secondary product (i.e. the olefins). Möller *et al.* (1999) deduced that this was due to the increasing crystallite size manifesting as an increased diffusional resistance on all products, thereby increasing their residence time within the pore channels, and hence shifting the yield in favour of the secondary olefinic products as the reactive dimethyl-ether intermediate had a "greater opportunity" to undergo secondary reaction. This phenomenon of increased diffusional resistance shifting the selectivity towards the secondary products was likewise explained by Möller *et al.* (1999) in terms of the rise in the diffusivities resulting in higher Thiele modulus values for all products, reducing their effectiveness factors and hence shifting the selectivity of the system towards the secondary product. Chen *et al.* (1999) investigating the effect of crystallite size of a SAPO-34 catalyst on the methanol-to-olefins reaction at 425°C confirmed these observations and conclusions. It is thus clear that the widely accepted Thiele modulus, and by extension the effectiveness factor associations, is a tool of great importance in the explanation of phenomena observed in hydrocracking and hydroisomerisation reactions over porous media.

2.4.5 The Effect of Zeolite Pore Geometry through Variations in the Intraporous Concentrations and Orientations of n-Alkanes

2.4.5.1 The Effect of Pore Dimensions on n-Alkane Intraporous Concentrations

Assuming a first order reaction, the rate of consumption of a species A, r_A, may be expressed in terms of the rate constant of the reaction, k, and the partial pressure (or for a liquid system, the concentration) of the reacting species in the bulk fluid, P_A, by the following equation:

$$r_A = k \times P_A$$

For reactions occurring over porous catalysts, however, this rate equation must be presented in terms of the concentration of the active species at the active site (i.e. $C_{A.at.site}$) (Wei, 1996). The conversion from bulk to intraporous conditions is made by means of a modified rate constant, k_{eff} in the equation below, which represents the combined effects of the intrinsic rate constant and transport effects in the migration of the reacting species from the bulk to the active sites (i.e. $k_{eff} = k \times k_{ads}$).

$$r_A = k_{eff}.C_{A.at.site}$$

In a gaseous system wherein the conditions of sufficiently high temperature and/or low pressure are such that there exists a very low occupancy of hydrocarbons within the porous system of the zeolite (i.e. spaces exists between hydrocarbon chains within the channels whilst some channels may even be empty), an n-alkane reactant would transfer directly from the gas phase to the adsorbed phase on the internal surface of the zeolite. Researchers have observed that, in such low occupancy, unsaturated situations, the adsorption constant of an n-alkane increases with increasing carbon number (Denayer and Baron, 1997a). This phenomenon (which, in the rate equation, results in an increase in the effective rate constant, k_{eff} due to an increase in the adsorption constant k_{ads}) manifests in an observed preferential adsorption, and hence reaction, of the longest (i.e. the heaviest) n-alkane reactants (Denayer and Baron, 1997a).

This effect is, however, greatly dependent on the pore size and structure of the zeolite, with larger pores and less restrictive pore networks (such as those incorporating large intersections of pores or supercages) allowing for the distortion of n-alkane molecules within the pore channels, intersections and supercages. These distortions, discussed in detail in Section 2.4.5.2 and represented in Figures 2.28 and 2.29, reduce the extent of adsorbate-zeolite interaction, instead partially replacing it with adsorbate-adsorbate interaction with neighbouring molecules, thereby reducing the effective rate constant and with it, the observed reaction rate (Denayer *et al.*, 2003). It is thus clear that as the porous system becomes less restrictive, the extent to which longer n-alkanes are favoured, in terms of adsorption, and hence reaction, declines.

Whilst these trends have been studied extensively for n-alkanes, they have also been found to hold for a variety of iso-alkanes, although to a lesser extent, with the magnitude of the adsorption/carbon number dependency decreasing with an increase in the extent of branching as per the sequence (Denayer *et al.*, 1998b):

n-alkane > mono-methyl iso-alkane > di-methyl iso-alkane > tri-methyl iso-alkane

Research into these adsorption phenomena has indicated that, as the total occupancy of the zeolite pores increases (due to reduced temperature and/or increased pressure), the magnitude of the preferential longer n-alkane adsorption (for instance from a mixture of n-alkanes of different carbon numbers) declines. This was hypothesised to be due to the increase in adsorbate-adsorbate interactions mentioned above and competitive zeolite surface coverage caused by shorter hydrocarbon chains packing around the longer chains under elevated occupancy conditions, thereby hindering the adsorption of longer chains onto the zeolite surface (Denayer *et al.*, 2006).

At very high occupancies (i.e. when all, or nearly all, accessible channels of the pore network are occupied with hydrocarbon chains packed "head-to-tail"), for instance under gas-liquid hydroconversion conditions, the selectivity by which long n-alkanes are preferentially adsorbed onto the zeolite's internal surface from the liquid phase within the pores becomes negligible, with the apparent rates of reaction for alkanes of various carbon numbers (on any given zeolite) then corresponding well with their intrinsic rates of reaction (Denayer *et al.*, 2002). As such, under these conditions of zeolite pore saturation, only the rate increase associated with increasing hydrocarbon chain length (as the increased number of alkyl carbenium ion transformations possible with increased carbon number allows for a greater number of reaction pathways and hence an elevated rate of reaction) (Denayer and Baron, 1997b) is believed responsible for the preferential conversion of longer n-alkanes (Denayer *et al.*, 2002).

2.4.5.2 The Effect of the Pore Structure on n-Alkane Intra-pore Orientation

The orientation of molecules within the pore system of a zeolite affects the reaction not only through adsorption trends and affinities, as discussed in Section 2.4.5.1, but also more directly through the influence which the extent of zeolite-adsorbate interaction has on the kinetics of the system (De Meyer *et al.*, 2003; Denayer *et al.*, 2006; Wei, 1994).

This phenomenon is due to the ability of n-alkanes to bend, twist, coil and otherwise distort when afforded sufficient space within the pore network. This distortion may result in a portion of the adsorbed molecule straying away from the wall of the zeolite, reducing the adsorbate-zeolite interaction with it instead, should other adsorbate molecules be present, being partially replaced by adsorbate-adsorbate interactions. Such variations in pore-structure-directed molecular packing, illustrated in Figures 2.28 and 2.29 for narrower/more restrictive and wider/less restrictive pore systems respectively, have been theorised to have a distinct influence on the activity and selectivity exhibited by different zeolites by virtue of their pore structure (Denayer *et al.*, 1998a). It should be noted that this effect is completely independent of that which may be induced by transition-state shape selectivity as indicated in Section 2.4.3.

This phenomenon is theorised to manifest due to imperfections in the adsorption of longer alkane molecules as they distort within less restrictive pore systems, resulting in two simultaneous interlinked effects, namely the loss of contact between the adsorbate species and the zeolite surface and the subsequent blocking or masking of potentially active surface sites by the distorted molecule.

Examining the situation more closely, in zeolites with pores of a similar magnitude to the kinetic diameter of an n-alkane molecule (approximately 5.8 Å), such as ZSM-5 (with pore channels of approximately 5.5 Å), the molecule is unable to distort to any significant extent within the pore system due to spatial constraints (Wei, 1994). This forces the molecules to move in single file through the pores, hence maintaining an "ideal adsorption configuration" (i.e. maintaining the maximum contact with the zeolite surface and hence maximum adsorbate-zeolite interaction and maximum activity under the given conditions due to contact with as many potentially active surface sites as possible) (Denayer *et al.*, 2006). Such molecular configurations are illustrated in Figure 2.28 (a) through (c), wherein it may be seen that, even in the intersections of narrower pores, molecules are unable to distort to any significant extent, moving either directly across the intersection along the same pore (as proposed by Wei (1994) and illustrated in Figure 2.28 (b)) or bending in such a manner so as to continue being adsorbed along the intersecting pore, with it being proposed that more than one molecule may occupy the intersection at any given time (De Meyer *et al.*, 2003) as illustrated in Figure 2.28 (c).

In zeolites with less-restrictive pore systems, however, especially those with supercages, it has been theorised (Denayer *et al.*, 1998a) that only a portion of a longer alkane will be adsorbed with ease onto the surface of the zeolite (as illustrated in Figure 2.29 (a) and (b) for a straight pore and a large intersection or supercage respectively), and hence be exposed to potentially active sites and capable of undergoing reaction, with the remainder of the hydrocarbon being located in the "free-space" of the pores and supercages and hence surrounded by other alkane molecules and experiencing adsorbate-adsorbate interactions. This distortion has two effects which reduce the overall activity of the system for, not only is the portion of the molecule in contact with potentially active surface sites reduced when compared to the more ideal configurations in Figure 2.28, but the distortion of such long molecules is able to effectively screen portions of the zeolite surface (highlighted by dashed regions in Figure 2.29), thereby preventing other molecules from accessing potentially active sites. These effects result in a reduction in the overall activity of the system.

It is thus clear that the spatial constraints imposed on adsorbed species within more restrictive/narrower pore zeolites (such as the medium pore ZSM-5) will have a promotional effect on the adsorption of linear (or minimally branched) hydrocarbons by limiting the extent of molecular distortion, thereby maximising adsorbate-zeolite interactions and thus the overall rate of conversion of these molecules. This increase in the rate of reaction is subject to two limiting factors, specifically: as the length of the reactant molecule increases, so does the extent of the adsorption difference; and as the pore size increases, so this effect will gradually decline as the molecules are afforded ever more space to distort and move away from the zeolite walls.

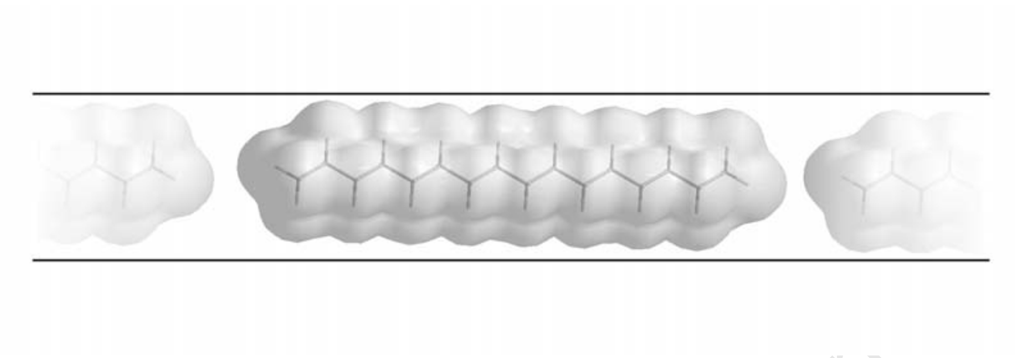

(a) "Ideal adsorption configuration" of n-hexadecane molecules moving single-file through narrow pores

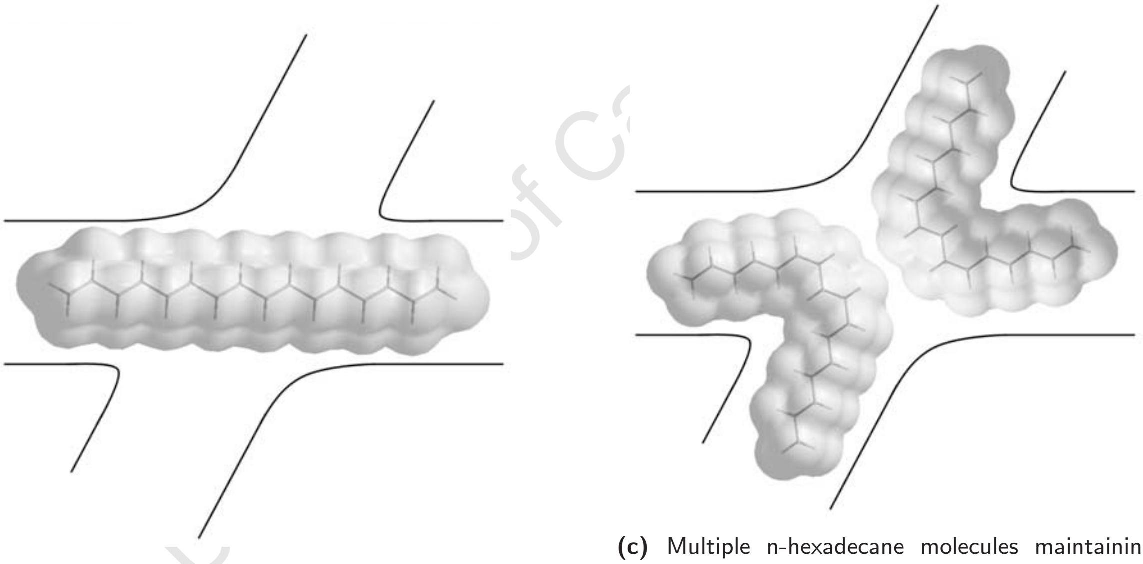

(b) n-Hexadecane molecule adsorbing straight through intersection of pores
(Created from description by Wei, 1994)

(c) Multiple n-hexadecane molecules maintaining optimum adsorption by bending through pore intersection
(Adapted from figures by De Meyer *et al.*, 2003)

Figure 2.28: Adsorption of n-Hexadecane Molecules in Narrower Pore Channels and Intersections

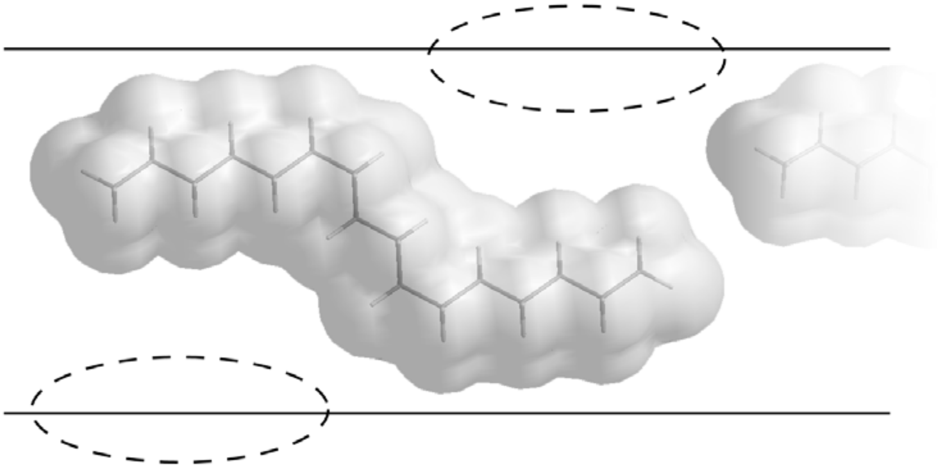

(a) n-Hexadecane molecule distorting within widepore channel

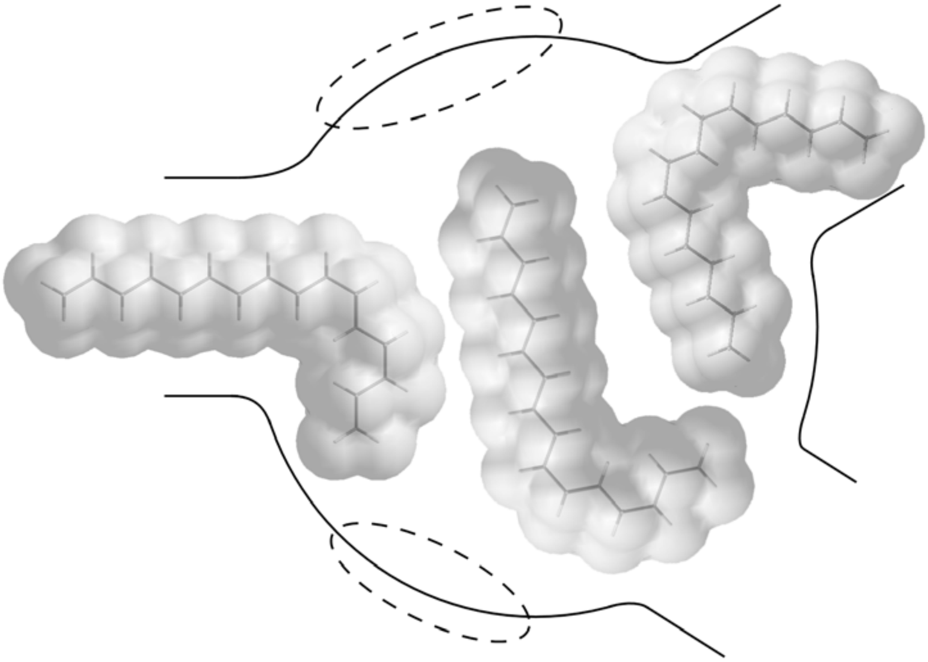

(b) Distortion of n-hexadecane molecules within supercages or large intersections wide pore systems (Adapted from figures by Denayer *et al.*, 2006)

Figure 2.29: Adsorption of n-Hexadecane Molecules in Wider Pore Channels, Intersections and Supercages (dashed lines indicate regions of inaccessible yet potentially active zeolite surface)

Much learning does not teach understanding.
Heraclitus (540 BC - 480 BC)

3

Summary of Findings from Literature

3.1 Summary and Critical Review of Literature

For the purposes of producing clean, high quality middle distillate fuels from the hydrocarbon feedstocks currently available as alternatives to conventional crude oil, the approach of producing wax from syngas by Fischer-Tropsch Synthesis and selectively hydrocracking this wax to the desired fuel fractions, seems to offer the most promise.

To be viable, such a production would require a bifunctional (metal/acid) hydrocracking catalyst which is able to achieve both a high conversion of the FT wax feed and, perhaps more importantly, a high selectivity towards the desired high quality middle distillate fuels product (i.e. minimally branched alkanes with a carbon number of between approximately 11 and 20).

Given that FT wax is free of both sulphurous and nitrogenous compounds, the sulphided metals utilised in crude oil refinery hydrocracking catalysts are not required (and indeed, are not suitable as they would contaminate the otherwise clean hydrocarbons) and may instead be substituted for more active, non-sulphided alternatives, such as metallic Pt on an acidic support. Further, considering that such a wax feed is comprised almost of entirely linear hydrocarbons, the implementation of acid-zeolites with pores narrower than those materials currently used in the hydrocracking of crude oil derived feedstocks may, due to their unique properties, be beneficial in this situation.

These properties include the zeolite acidity (a function of both acid site concentration and individual strength), the pore geometry (in terms of the pore dimensions, interconnectivity, etc.) and the zeolite crystallite size, with experimental observations into the effects of variations in these properties being supported by theoretical predictions and explanations from both mechanistic and mass transfer perspectives.

In terms of the effects of these properties, it has been noted in hydroisomerisation and hydrocracking investigations that an increase in the overall acidity of a zeolite results in an increase in both isomerisation and cracking yields, whilst the zeolite pores themselves have been found to impose a degree of transition state shape selectivity on the reaction intermediates, with this latter point being reported to limit the degree of branching of hydrocarbon products. It has also been suggested that such shape selectivity may even extend the on-stream life of the catalyst through a reduction in the formation of coke by imposing a degree of spatial hindrance upon the formation of bulky coke precursors. This intermediate or transition-state shape selectivity has, however, been found to result in reduced overall catalyst activity, thereby facilitating the need to operate under more severe conditions, thereby potentially producing more coke whilst also increasing the yield of light hydrocarbons in hydrocracking reactions.

Interestingly, it has been determined that there is a significant increase in the rate and strength of adsorption of various hydrocarbon chains into zeolites with pores of similar diameters to the kinetic diameter of the hydrocarbons (such as the adsorption of linear alkanes (with a kinetic diameter of approximately 5.8 Å) into the pores of H-MFI (with diameters of approximately 5.5 Å)) as opposed to those zeolites with much wider pores. This increase in the observed adsorption rate and strength has been theorised to be due to the adsorbate being forced to assume an “ideal adsorption configuration”, thereby maximising the adsorbate-zeolite interaction and thus promoting the overall adsorption process. When the pores are significantly wider than the kinetic diameter of the molecule, however, distortion of the adsorbate within the pores not only reduces the adsorbate-zeolite interaction, but molecules may also block one another from making contact with the zeolite surface. This suggests that the activity of zeolites with narrower pores may be promoted through adsorption to a far greater extent than in their wider pore counterparts.

The size of the zeolite crystallites themselves has also been shown to have a clear effect on the product distribution, with increasing crystallite size resulting in a progressive shift of the system away from primary products, in favour of secondary and later products. In a hydrocracking scenario, this would result in a reduction in the average carbon number of the product spectrum.

Unfortunately, to date, the majority of research conducted into the use of bifunctional catalysts (specifically pure noble metals on acidic zeolite supports) in hydrocracking and hydroisomerisation reactions has focused on using short-chain or cyclic hydrocarbon feedstocks (such as n-octane or cyclohexane respectively), neither of which are representative of FT wax products. Furthermore, the conditions (predominantly in terms of temperature and pressure) utilised in these investigations are often far removed from those of the FT process itself (being either too severe, as per crude oil derived feedstock hydrocracking, or too mild, usually to study the reaction mechanism), with a catalyst able to perform at conditions closer to that of the FT process being greatly desired (due to the reduced FT wax conditioning required prior to feeding into a separate hydrocracking reactor or even the eventual incorporation of both the FT and hydrocracking catalysts within a single reactor). Much of the previous research has also made use of batch reactors, as opposed to the more industrially applicable continuous flow systems. These factors all impart a degree of uncertainty to the applicability of the results obtained by many researchers in this field to the hydrocracking of Fischer-Tropsch wax for the production of high quality middle distillate fuels.

3.2 Conclusions and Implications from Literature

Regardless of the industrial applicability of the test conditions utilised in much of the previous research conducted in this field, the effects highlighted by researchers show great promise in terms of their implementation under more industrially applicable conditions for the development of a highly selective bifunctional (metal/acid zeolite) hydrocracking catalyst for the production of high quality middle distillate fuels from FT wax. These effects include those which the fundamental zeolite properties of acidity, pore geometry (in terms of both shape selectivity and adsorption phenomena) and crystallite size have on the overall activity and selectivity of the catalyst.

Furthermore, the proposed “hydrogen spillover” mechanism, indicating that bifunctional synergy between metal and acid co-catalysts may be achieved even upon physical separation of the metal and acid by several millimetres, has afforded research the opportunity to test different acid supports without the complication imposed by the effect of support surface chemistry on metal loading and dispersion.

A goal without a plan is just a wish.
Antoine de Saint-Exupery (1900 - 1944)

4

Research Aims and Objectives

4.1 The Optimisation Challenge

Optimisation of a bifunctional (metal/acid) catalyst for the selective hydrocracking of Fischer-Tropsch wax is dependent on three key factors, these being: the operating conditions, the metal function and the acid function. These factors may be tailored so as to obtain optimal activity, selectivity and on-stream life time of the catalyst. This research endeavour concerns itself with the acid support component, with exclusive interest into the feasibility of using zeolites with narrower pores than those currently implemented industrially in the hydrocracking of crude oil derived feedstocks, to not only provide the active acid sites required for bifunctional hydrocracking to occur, but to improve product selectivity towards high cetane number minimally branched paraffins through the physical restrictions imposed upon the reaction intermediates by the zeolite channel system (i.e. through transition-state and product shape selectivity).

4.2 Hypotheses

It is hypothesised that, due to the linearity of the Fischer-Tropsch wax feed, acid zeolites with pores smaller than those currently utilised in the processing of crude oil derived feedstocks, including medium pore zeolites such as H-MFI, may now be considered viable in terms of offering comparable, or perhaps even superior, activity to wide pore zeolites whilst affording improved selectivity towards the desired products.

Further, it is believed that variations in the severity of the physical constraints imposed upon the reaction intermediates, specifically by virtue of variations in the pore geometry (i.e. pore dimensions, interconnectivity, etc.) between different zeolites, will induce different degrees of transition-state and product shape selectivity, manifesting as increased yields of the desired lesser branched products (i.e. products with a high cetane number) as the pore geometry becomes more spatially restrictive.

It is also hypothesised that increasing severity of such transition-state shape selective constraints will result in improved catalyst on-stream life time, through a reduction in the formation of bulky coke precursors due to spatial inhibition. Whilst it is foreseen that this inhibition will result in a reduction in the activity of the more restrictive catalysts, given the limitations imposed on cracking mechanisms occurring within the confined pore spaces, the promotional effect due to more idealistic adsorption is hypothesised to counteract this reduced activity to some extent. The magnitude of this counteractive effect can only be guessed to be of a similar order of magnitude to that of the inhibition.

4.3 Key Questions

This investigation required that the performance of each zeolite be evaluated in terms of the:

- Activity per acid site (conversion of the hydrocarbon feed in terms of both isomerised and cracked products)

- Branching selectivity (preferential formation of the desired minimally branched products)
- Carbon number distribution of products (to determine the severity of cracking)
- On-stream life time of the catalyst

4.4 Scope and Constraints

It should be noted that, of the three main factors associated with the development of a selective bifunctional hydrocracking catalyst (i.e. the reaction conditions, the metal component and the acid component), only the acid function was to be investigated in this endeavour. The performance of the zeolites tested was thus collated so as to determine how their various unique properties (in terms of acidity and pore geometry) affected both activity and selectivity. Furthermore, with the primary focus on the affect of the acid function properties, numerous efforts were instituted to negate the effects of variations in factors other than those inherent to the acid components between samples.

Foremost among these, all samples were evaluated under the same conditions of temperature, total pressure and H_2/hydrocarbon feed ratio. These conditions were selected to closely represent the conditions which would be implemented industrially for the hydrocracking of a Fischer-Tropsch wax feedstock to middle distillate fuels. This was important as one of the goals of research in this field is to combine the Fischer-Tropsch Synthesis and hydrocracking catalysts within a single reactor, allowing for the efficient production of middle distillate fuels with a minimal number of process steps. The actual feed rates, and hence the space velocities, were varied so as to achieve a range of conversions, thereby allowing for a comparison of selectivities at the same total conversion.

Further, all zeolites were loaded on the basis of total acid site number rather than mass, with the active metal loaded so as to achieve a constant ratio between the number of active metal and the number of active acid sites for all tests. This ratio was such that the acid co-catalyst served as the limiting component in the bifunctional reaction, thereby facilitating the detection of variations in activity and selectivity resulting from the use of different zeolites.

Finally, to help reduce the effects of variations in hydrodynamic flow patterns through the catalyst beds, the various catalyst samples to be loaded were, as far as possible, diluted to the same bulk volume using pelletised silica. This ensured that the total catalyst bed volume was identical for all initial investigations.

For details on the conditions and loadings, see Sections 6.2 and 6.1.3 respectively.

Opportunity is missed by most people because it is dressed in overalls and looks like work.

Thomas A. Edison (1847 - 1931)

5

Design and Construction of the Experimental Apparatus

5.1 Experimental Objectives

In order to evaluate the performance of the different acid zeolites used in this work (in terms of overall activity and selectivity towards the desired minimally branched paraffinic products) in such a manner so as to compare the effects of the various physical properties of each (e.g. the total acidity, pore geometry, surface area and crystallite size), investigations were to be conducted under identical conditions with only the zeolite being varied.

To allow for the desired comparisons of activity and selectivity, it was necessary to be able to vary the space velocity (by changing the feed flow rate) so as to achieve a range of conversions of between approximately 20 and 80%. This would allow the activity of each zeolite to be quantified in terms of the relationship between conversion and space velocity, whilst simultaneously allowing the branching selectivity and carbon number distributions to be compared by projecting the data, as necessary, to simulate all zeolites exhibiting equivalent conversions.

To ensure the data gathered in this investigation was both accurate and reproducible, it was clear that the experimental apparatus to be utilised in this investigation would have numerous demands placed on it. As such, it was decided to construct an entirely new experimental unit from the ground up rather than modifying one previously designed for a different purpose. This design, construction and commissioning process is detailed below, being a substantial undertaking and forming a major portion of the work done during this investigation, with the operating procedures utilised for the investigations provided in Chapter 6.

5.2 Equipment Requirements

Fundamental to the efficient and meaningful comparative testing of the various zeolites, the equipment utilised in this investigation had to meet several key criteria. These requirements were defined as follows:

Safety - Foremost of the design requirements, the apparatus had to operate safely under all foreseeable circumstances, with suitable measures in place to prevent the system from becoming dangerous or uncontrollable during operation.

Type of Reaction System - To appropriately mimic industrial settings, a continuous flow system had to be utilised.

Feed Supply - A suitable model hydrocarbon feed, hydrogen and nitrogen had to be simultaneously supplied to the system in appropriate phases and accurately metered flows.

Reaction Conditions - To be representative of industrial conditions, the reaction system to be used had to be able to achieve and maintain the desired high temperature and pressure reaction conditions.

Catalyst Incorporation - The solid catalyst had to be immobile within the well-mixed hydrogen/hydrocarbon feed stream and maintained at the desired reaction conditions for the duration of the investigation.

Catalyst Replacement - Removal and replacement of the catalyst had to be possible with minimal disassembly of the apparatus.

Product Handling and Analysis - The reaction product had to be conveyed to a suitable analytical device for accurate and reproducible compound analysis. The nature of the analytical device selected for this purpose would define any post-reaction handling required of the product stream.

Stability and Reliability - All features and functions had to be implemented in such a manner so as to ensure that they functioned reliably and accurately for the duration of even the longest investigative run.

To satisfy all of the above requirements, a packed bed, "trickle-phase" dual reactor system was designed and constructed. The two stainless steel reactors were positioned within a single solid brass housing with multi-zone heating and temperature control allowing for the accurate establishment and maintenance of an isothermal region within the reactors (see Sections 5.5.1 and 5.7.1). The reactor pressures and post-reactor dilution rates were established and maintained through a system of pressure regulators and high-precision metering valves (see Section 5.7.2). The catalyst was immobilised within the isothermal region of each reactor utilising silicon carbide (SiC) as an inert spacer (see Section 5.5.2). A feed of liquid n-hexadecane and gaseous hydrogen, pre-mixed in the initial section of each reactor, was passed over the catalyst (see Section 5.4). The product from each reactor was diluted with gaseous nitrogen (with the flow dependent on the feed rate of liquid hydrocarbon and gaseous hydrogen) and passed through a heated SiC bed (to ensure the entire product stream was vaporised) before travelling, via a multi-port switching valve (allowing for the automated selection of either reactor), to an on-line gas chromatograph with a flame ionisation detector for analysis (see Section 5.6).

5.3 Overall Design Considerations and Limitations

From a practical perspective, the apparatus was required to be mobile and, due to the dynamic nature of experimental requirements, was also desired to be modular in its construction. This modular assembly would allow facets of the apparatus to be removed and replaced with minimal effort, thereby allowing for possible variations in the requirements of the investigation, as well as facilitating any repairs should they ever be required. As such, a stainless steel frame with movable shelf units was utilised (illustrated in Figures 5.30a and b respectively).

To facilitate mobility, the experimental apparatus (henceforth referred to as the "rig") was equipped with four wheels on its base together with two stabilisation feet which could be extended when the rig was in position to ensure the unit was both stable and level. Furthermore, the rig was fitted with a single switch box (housing four mains-power switches utilised for the simple on/off control of heating lines, pumps and balances) and three modular control boxes (housing the control units for mass flow and temperature controllers). The layout of these control boxes is illustrated in Figure 5.31.

The electrical connection for the unit was limited to a single three-phase power supply point. All gases were supplied by house-gas lines, with connections above the apparatus.

5.4 Feedstock Selection and Supply

For successful operation, this system required three feed components: an n-paraffin, hydrogen and nitrogen. The first two of these form the basis of the hydrocracking reaction itself (see Section 2.2), with the nitrogen being used for simultaneous pressurisation of the system and dilution of the product stream after leaving the reactor (see Sections 5.7.2 and 5.6.1 respectively).

(a) Stainless steel frame forming the basis of the apparatus

(b) Movable shelving unit attached to wall-bands on frame

Figure 5.30: Stainless Steel Frame and Removable Shelving Units

5.4.1 Model Hydrocarbon Selection

To be truly applicable to the use of hydrocracking for the industrial production of middle distillate fuels from FT wax, the hydrocarbon feed should ideally be said wax, such as that for which the carbon number distribution is portrayed in Figure 5.32.

There are, however, numerous logistical concerns associated with the use of such a heavy wax feed. Foremost among these is the supply of the wax from its feed container to the reactors themselves. Given that the melting point of such wax may be in excess of 100°C (de Klerk, 2008), a substantial amount of heating and insulation would have been required for the feed vessels, pumps and all tubing, valves and fittings to and from the reactors through which the wax must flow.

Furthermore, as FT wax samples do not comprise a single, pure compound but instead exist as a mixture of alkanes spanning carbon numbers from approximately 10 to above 100 (Leckel, 2007) as illustrated in Figure 5.32, even with an accurate analysis of the feed, determination of the performance of each catalyst would have been vastly complicated given the sheer number of possible cracking and isomerisation pathways and respective products which may result from such a diverse feedstock.

Even should these factors be considered acceptable, one would still have to acknowledge that the reactor effluent is certain to contain not only many heavy product fragments, but also unreacted heavy compounds present in the feed and, as such, a liquid product capturing system would be required. Such a product capture setup would comprise a "knock-out trap" wherein the higher boiling (liquid) fraction (i.e. the heavier compound) in the product is collected for off-line analysis, for instance by gas chromatography, with the lighter compounds being in the vapour phase and analysed on-line. This segregated product collection and analysis technique would, however, add additional complications to the situation.

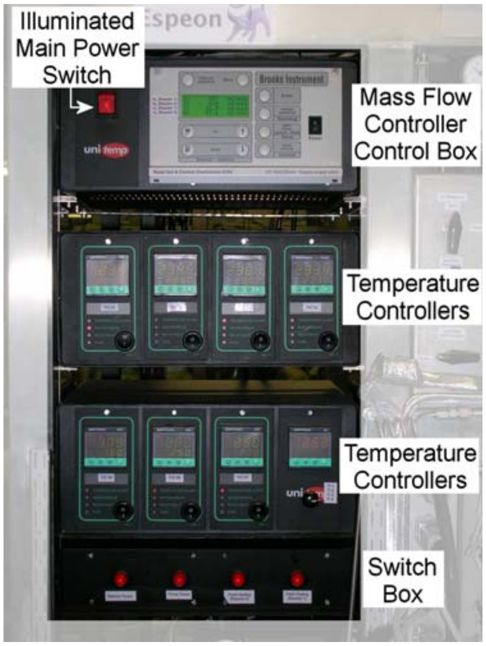

Figure 5.31: Control Boxes for Power, Mass Flow Controllers and Temperature Controllers

With these factors in mind, it was decided that a single, pure hydrocarbon compound would be fed to the system. This compound was required to be representative of the long-chain saturated hydrocarbons present in FT wax whilst avoiding, in so far as was possible, the expense and complication associated with feeding FT wax itself. Table 5.1 provides a truncated listing of the n-alkanes examined for this purpose together with information relating to their melting and boiling points.

For the selection process, it was vital to consider both the normal melting and boiling points of the candidate compounds for, whilst the melting point dictated the ease (or lack thereof) associated with conveying the feed from the feed pot to the reactors, so the boiling point was indicative of the difficulty to be encountered should an analysis technique be implemented which required a gaseous sample (see Section 5.6.1).

n-Hexadecane (99% purity, supplied by Sigma-Aldrich) was selected as the hydrocarbon feedstock for this process for, in the absence of any sudden and distinctive increases in the melting or boiling points between the compounds examined, the predominant motivation for the choice rested on how large a hydrocarbon could be easily sustained as a liquid at the laboratory's average conditions. As such, given an average laboratory temperature of 22°C, n-C_{16} was the safest, largest candidate. As an additional safety consideration in the event of a sudden drop in the laboratory temperature (for instance due to an air conditioner failure on a cold night), the n-C_{16} supply system was heated as discussed in Section 5.7.1.

5.4.2 Hydrocarbon Supply

To err on the side of safety, the entire hydrocarbon supply system was heated with 60°C self-regulating heating tape which, implemented with minimal additional insulation, was found to maintain a temperature of approximately 45°C. Given the influences of heat transfer between the heating tape and the feed lines, and the effect of the hydrocarbon flowing through these lines, this temperature was deemed to be acceptable for the purposes of ensuring the n-C_{16} remained liquid within the feed lines and apparatus.

Two 2 l metal tins with screw-caps (see Figure 5.33) were selected as feed pots for the rig due to improved safety as compared with glass bottles. The caps themselves were modified to accommodate a connection between a static line inside the tin and a flexible PTFE tube outside. The static line, a short section of 1/8"

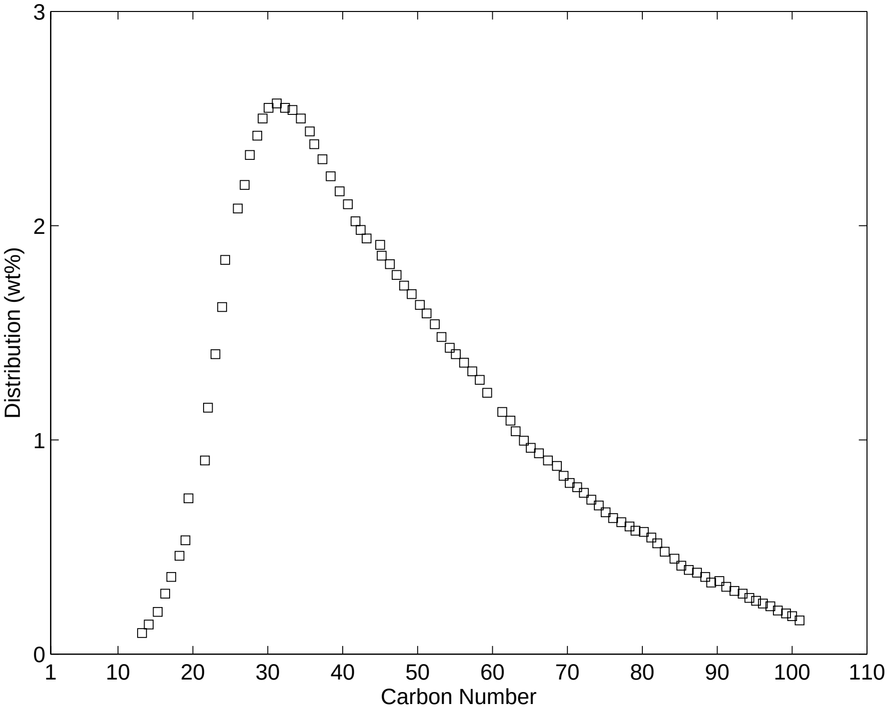

Figure 5.32: Typical Carbon Number Distribution for Wax Product from SASOL Iron-based Low Temperature Fischer-Tropsch Slurry Reactor
(Redrawn from data presented by Leckel, 2007)

Table 5.1: Normal Melting and Boiling Points of n-Alkanes Considered as Feedstocks (Daubert *et al.*, 1999)

Carbon Number	Formula	UIPAC Name	Normal Melting Point (°C)	Normal Boiling Point (°C)
14	$C_{14}H_{30}$	n-Tetradecane	6	254
15	$C_{15}H_{32}$	n-Pentadecane	10	271
16	$C_{16}H_{34}$	n-Hexadecane	18	287
17	$C_{17}H_{36}$	n-Heptadecane	22	302
18	$C_{18}H_{38}$	n-Octadecane	28	317

stainless steel tubing, served to ensure that the feed inlet, terminated with a 0.5 μm filter to prevent any possible particulate matter from entering the system, remained on the bottom of the feed pot at all times, whilst the PTFE tube connected the feed pots to their respective pumps. Each tin was placed on a separate A&D GX-4000 electronic balance with a readability of 0.01 g. These balances allowed the pumping rate to be confirmed by mass measurements.

The pumps selected for this investigation were Lab Alliance Series 1+ units, which deliver a maximum flow rate of 10.00 ml/min with the interface allowing for 0.01 ml/min graduations and readability. These pumps were also equipped with pulse dampeners which served to smooth the flow of their liquid outlet during operation (required as the pumps utilise a single piston mechanism to pump the liquid). An additional safety feature was afforded by the pressure sensor mounted in each pump's pulse dampener by virtue of which the maximum pressure against which the pump may forced liquid could be controlled.

As illustrated in Figure 5.35, the pulse dampener consisted of an oil reservoir separated from the flow

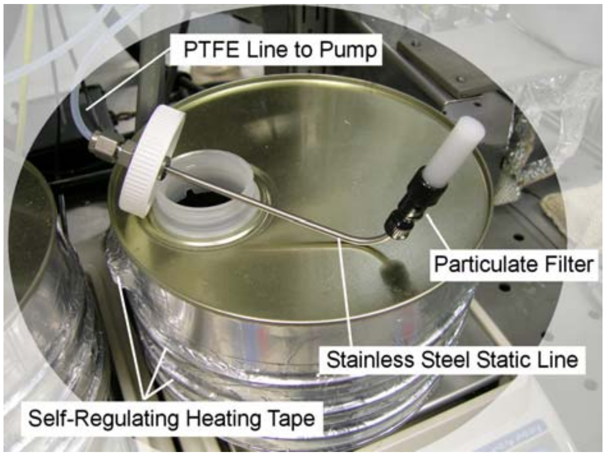

Figure 5.33: Feed Container with Withdrawal Line, Filter and Heating

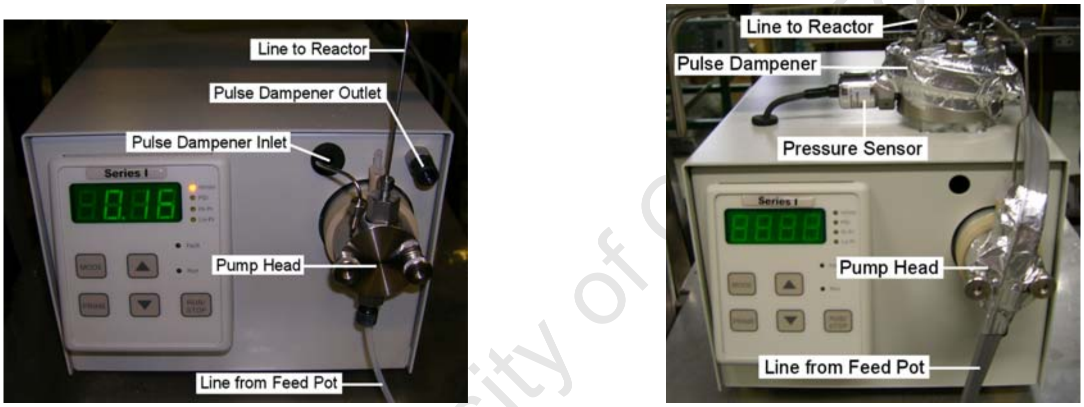

(a) Pump in standard form but with internal pulse dampener and pressure sensor bypassed

(b) Pump modified for external pump head, pulse dampener and pressure sensor heating

Figure 5.34: Series 1+ Piston Pump Utilised Showing Relocation and Heating of Pulse Dampener/Pressure Sensor Unit

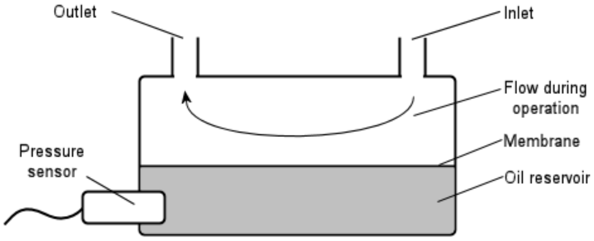

Figure 5.35: Illustration of Pulse Dampener Internal Construction and the Position of the Pressure Sensor Therein

stream by a flexible membrane. The purpose of this unit was to ensure that, should the pump be utilised for high pressure liquid chromatography (HPLC), that fluctuations in the liquid flow did not damage the packing of the column. For the implementation of these pumps in this investigation, however, the ability to limit the maximum outlet pressure by virtue of the pressure sensor located on the pulse dampener was of primary interest given that the large gas volume within the reactor system during operation would more than adequately dampen any liquid flow fluctuations. For interest, however, the pulse dampening functionality of the unit is achieved in that, during the piston delivery stroke, the increased pressure on the feed stream compresses the oil reservoir, slightly reducing the flow out of the dampener. During the piston chamber filling stroke, however, the oil reservoir expands again, slightly increasing the flow out of the dampener. This counter-acting effect ensures a consistent flow of liquid out of the pump.

The pressure sensor extended into the oil reservoir of the pulse dampener, effectively measuring the pressure against which the pump was forcing the liquid. By virtue of this sensor, the maximum outlet pressure of the pump may be regulated, an important safety feature when considering that the Series 1+ type pump is capable of a maximum outlet pressure of approximately 340 bar, uncomfortably close to the approximately 300 bar pressure rating of the 1/4" stainless steel tubing (316SS at the temperatures under which it is utilised) widely used in the rig.

In their shipped form, however, the pulse dampener/pressure sensor unit is located within the pump housing as seen in Figure 5.34a, which shows the inlet and outlet ports of the pulse dampener being visible on the front face of the pump housing. This internal placement of the pulse dampener prohibited the application of heating to these devices without placing the internal electronics of the pump at risk of damage from the elevated temperatures. As such, the pumps were modified and the pulse dampeners mounted externally on the top of each pump (see Figure 5.34b). This configuration allowed the pulse dampener, pressure sensor and pump head to be heated with the same self-regulated heating tape utilised on the remainder of the feed lines carrying the liquid hydrocarbon.

The alternative to external mounting and heating of the pulse dampener/pressure sensor unit was to bypass it entirely as shown in Figure 5.34a. This approach was, however, quickly dismissed as it would render their pressure limiting abilities obsolete.

Each pump was supplied with manufacturer calibration certificates which indicate flow errors of only approximately 1.5 vol% for the flows of interest in this investigation (0.01 ml/min to 0.10 ml/min).

The line exiting the pulse dampener/pressure sensor unit of each pump was fed to a heated three-way valve. One exit from this valve led to a small catch bottle and was used to prime the pump during start-up, whilst the other exit diverted the hydrocarbon flow to the reactor. This flow to the reactor proceeded through a heated line, via a heated pressure relief valve (set to 60 bar so as to act as a secondary safety system for the prevention of over-pressurisation), to the reactor inlet.

5.4.3 Hydrogen and Nitrogen Feeds

The gaseous hydrogen and nitrogen required for this investigation were provided by the 100 bar house lines accessible from within the walk-in fume-hood where the rig was located. The lines connecting the rig to the house line system were formed into "pig-tails" (see Figure 5.36a) to minimise any transference of motion from the rig itself to the house line system and to reduce strain on the connections. 0.5 μm filters were installed on these inlet lines to remove any particulate matter which, although unlikely, may have entered the supply lines. The filtered gases were stepped from 100 bar to 50 bar by Tescom pressure regulators (as seen in Figure 5.36b) before being supplied to the mass flow controllers.

Metering of the gas feeds was conducted utilising four Brooks thermal mass flow controllers (MFC), illustrated in Figure 5.37 linked to a Brooks MFC control box (depicted in Figure 5.31). In this configuration, each reactor had separate MFCs for its H_2 and N_2 supply, allowing for accurate and independent flow control. The two hydrogen mass flow controllers had flow ranges from 0 to 200 ml/min, whilst the nitrogen flow controllers allowed flows between 0 and 1000 ml/min. One-way (check) valves were installed on the outlet lines immediately proceeding each mass flow controller. These check valves, as discussed in Section 5.8.1.2, served as a final measure to prevent any hydrocarbons from entering the mass flow controllers or house-gas lines.

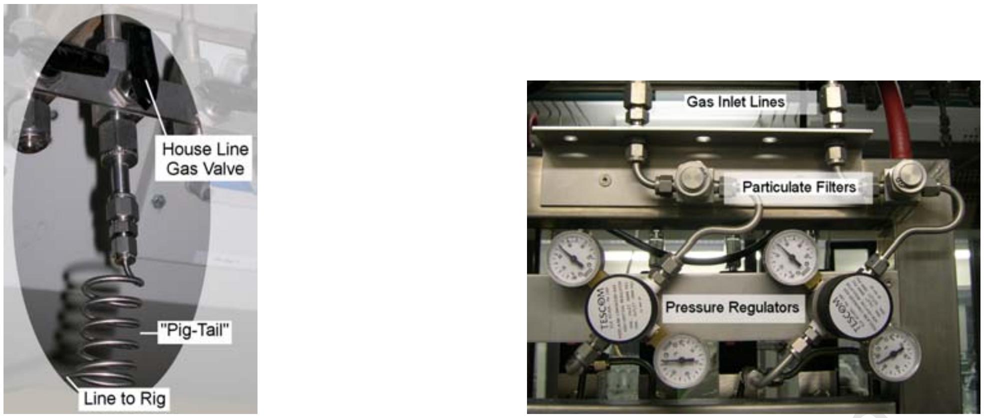

(a) Tubing formed into a "pig-tail" and attached to house line valve manifold

(b) Filters and pressure regulators on gas inlet lines

Figure 5.36: Gas Inlet Tubing and Equipment

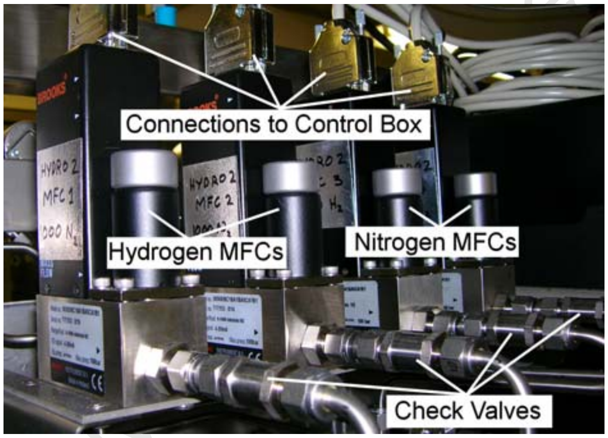

Figure 5.37: Mass Flow Controller Bank Consisting of Two 200 ml/min Hydrogen and Two 1000 ml/min Nitrogen Units

All mass flow controllers utilised in this investigation were provided with manufacturer calibration certificates which indicated flow errors below 5 vol% for all flows above 10% of the maximum flow (the region to be utilised during this investigation).

5.5 Catalyst Incorporation and Associated Reactor Requirements

To ensure the reproducibility and reliability of catalyst testing and to lend credence to their comparison, it was essential that physical parameters such as the reaction temperature and pressure, the feed conditions and pre-mixing, and the hydrodynamic flow within the catalyst bed be held as constant as possible between evaluations, with only the acid co-catalyst itself and the space velocity being varied as necessary. To facilitate this goal and allow for efficient testing of multiple catalysts, a dual reactor setup was selected for this investigation, with both reactors being the relatively simplistic tubular fixed bed type.

5.5.1 Reactor Form and Features

Each reactor, as depicted in Figure 5.38, comprised a stainless steel tubular body 500 mm in length and with an internal diameter of approximately 15.75 mm (specifically an external diameter of $\frac{3}{4}$", 19.05 mm, and wall thickness of 0.065", 1.651 mm). The head of each reactor was designed as a separate, removable unit, facilitating the ease with which the catalyst may be loaded and unloaded. During operation, the reactor head and body are sealed using Swagelok VCR connections and replaceable gaskets (see Figure 5.39). This sealing technique allowed for the frequent opening and resealing of the reactor for catalyst changing with negligible deterioration of the quality of the seal (presuming new gaskets were used each time).

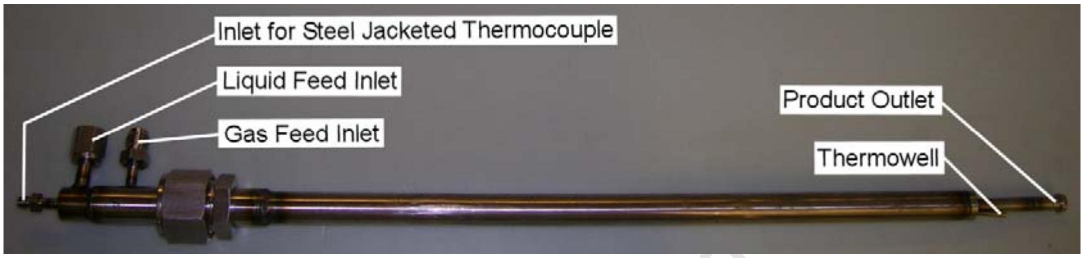

Figure 5.38: Reactor Body

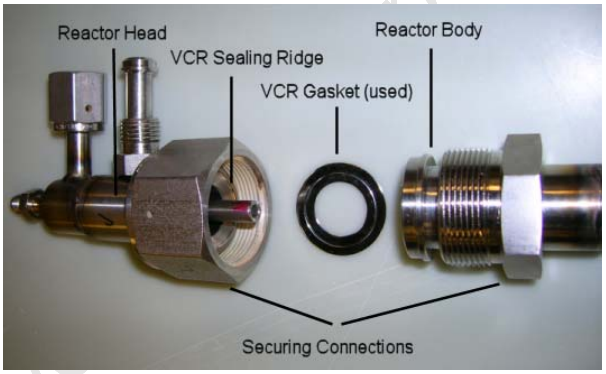

Figure 5.39: VCR Connections and Gasket for Connecting Reactor Head to Body

The inlet ports of the reactor head were designed in a staggered configuration (see Figure 5.40) so as to avoid the unsteady dripping of the liquid hydrocarbon feed into the reactor with insufficient mixing with the gaseous hydrogen feed. In the form implemented, the central liquid feed tube was designed to touch the top of the reactor packing, allowing the liquid to flow onto the upper surface of the particles of the packing, with the capillary action of the void spaces between the packing particles assisting to draw the liquid smoothly into, and to disperse it across, the packed bed. The gaseous hydrogen feed flowed simultaneously in an annulus around the sides of the liquid feed tube, thereby greatly facilitating the mixing of the two feed streams within the initial section of the packed bed and moving the liquid hydrocarbon smoothly down the reactor. These two inlet ports, together with the single outlet line, were also sealed with VCR connections when connected to their respective lines on the rig during operation. Furthermore, the sections of feed line immediately preceding the reactor head inlets were formed into pig-tails (in the same manner as the house gas connections illustrated in Figure 5.36a) to allow some degree of movement and hence easier positioning of these lines during reactor removal and when reconnecting them after replacing the catalyst.

Each reactor was designed to incorporate two thermocouples: a stationary steel-jacketed thermocouple

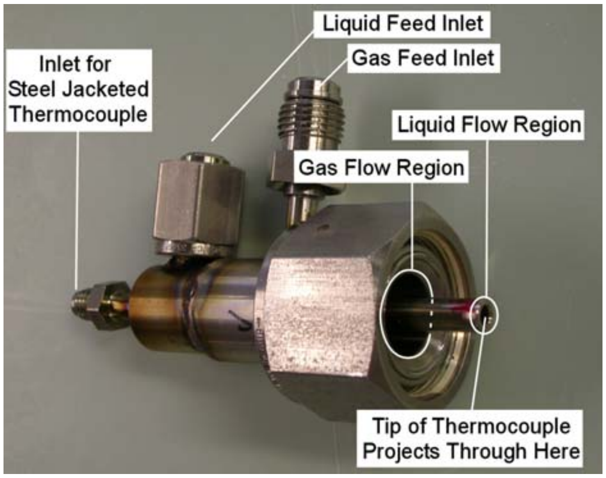

Figure 5.40: Reactor Head Showing Staggered Gas and Liquid Inlet Ports and Annular Flow Regions

entering through the reactor head and protruding approximately 1 mm beyond the end of the central liquid feed tube and a non-fixed steel-jacketed thermocouple entering beside the product outlet and travelling up the length of the reactor through the thermowell. The former was utilised to measure the hydrocarbon inlet temperature, whilst the latter, by virtue of its mobility within the thermowell, was used to determine the temperature at any point along the length of the reactor, thereby allowing an accurate temperature profile to be ascertained.

Both reactors were positioned in parallel within a single, solid, multi-zone temperature controlled brass housing (see Figure 5.41a) during operation. This brass block, measuring 115 x 55 x 360 mm, had two parallel cylindrical slots machined longitudinally through it, allowing the reactors the fit snugly during operation, and yet from whence they could be easily removed for emptying and reloading of the catalyst as required. This brass block rested on a ceramic insulation pad so as to minimise heat transfer to the frame during operation.

Brass was selected as the material of choice in this application for it affords the desired combination of cost effectiveness, high thermal conductivity and durability. Copper, whilst exhibiting a higher thermal conductivity, is more expensive and less durable. Stainless and mild steels are less thermally conductive but exhibit higher durabilities, although this makes them more expensive to machine. Aluminium is lightweight, cost effective, has a good thermal conductivity, is easy to machine and is prone to warping and distortion with repeated heating.

The primary practical disadvantage associated with the use of a solid brass housing with the aforementioned dimensions was the weight of the unit, weighing approximately 20 kg, and it was clear during the design stages that repeated lifting and replacing of the brass block (for loading and unloading of the reactors) would not be feasible, not the least from a safety perspective. As such, a mechanism was devised whereby the brass housing was mounted to the frame using a heavy duty hinge on the housing base. The top of the housing was then secured in an upright position using two steel hooks. A short chain on either side allowed the entire housing, with the reactors suitably disconnected, to be unhooked and leaned forward away from the frame of the rig. This mechanism, depicted in Figure 5.42, allowed the reactors themselves to be quickly and easily removed and replaced.

Reaction temperature control is discussed in Section 5.7.1.2, with pressure control in Section 5.7.2.

5.5.2 Catalyst Positioning

As discussed in Section 4.4 and elaborated upon through calculation in Section 6.1.3, the total volume of the catalyst bed was, as far as possible, to be kept constant for all investigations. This afforded a degree of consistency in reaction conditions by allowing the different catalyst beds to be located in same position within

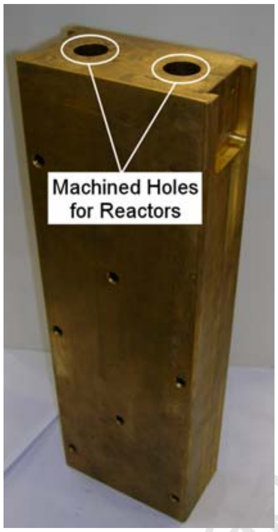

(a) Machined brass reactor housing

(b) One of the heating elements surrounding the reactor and vaporiser housings

(c) Custom insulation jacket for reactor housing

Figure 5.41: Reactor Housing, Heating Element and Insulation Jacket

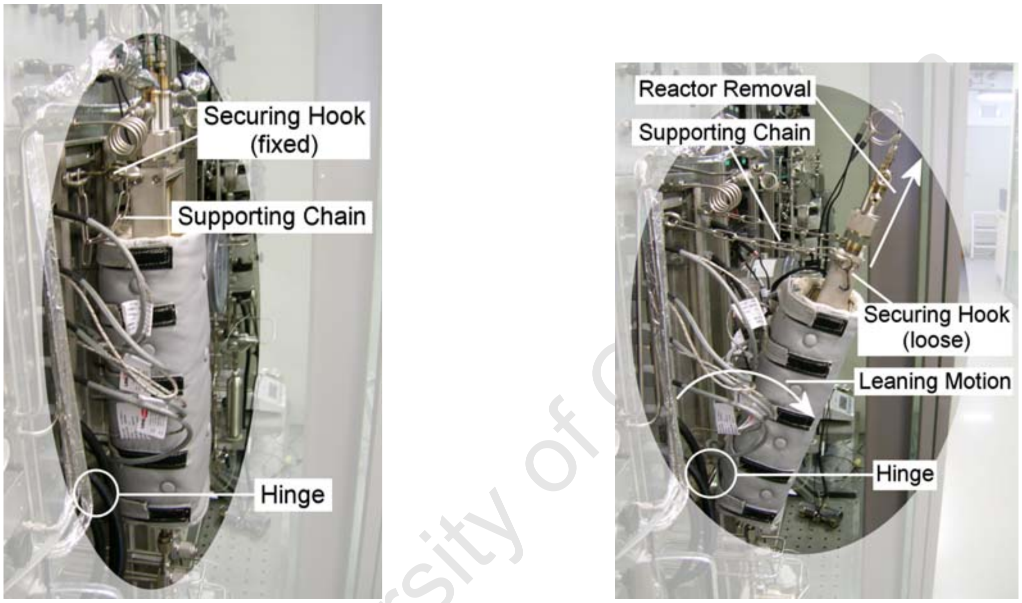

(a) Reactor assembly in vertical, secured position

(b) Reactor assembly leaning out with reactors disconnected and ready for removal

Figure 5.42: Reactor Assembly Lean-out Mechanism Facilitating Reactor Removal and Maintenance

the fixed bed reactor. However, as the catalyst particles were essentially randomly dispersed within this bed volume, it was vital that the catalyst bed as a whole be maintained at the same conditions (specifically with regards to ensuring that the the entire bed was isothermal), with the specifics of the overall condition control being provided in Section 5.7.

From a practical perspective, it was clear that the catalyst bed (consisting of the solid catalyst pellets and silica pellets [as the bed diluent material], with catalyst selection and preparation being discussed in Section 6.1.2) had to be immobilised within the reactor in such a manner so as to ensure that the feed streams had sufficient space prior to the catalyst for mixing and heating and that isothermal and isobaric conditions were maintained for the full length of the catalyst bed. These requirements were achieved through the use of SiC granules (with a particle size of 400 - 600 μm). A bed of SiC granules below the catalyst allowed the position of the catalyst bed to be adjusted when loading, whilst another SiC bed above the catalyst bed afforded the zone for feed pre-heating and mixing. The former point is of particular interest for, whilst the majority of the unit may be maintained at a constant pressure with relative ease (see Section 5.7.2), a temperature profile exists within the reactor and it is within a specific isothermal region that the entire catalyst bed must be positioned as illustrated in Figure 5.43.

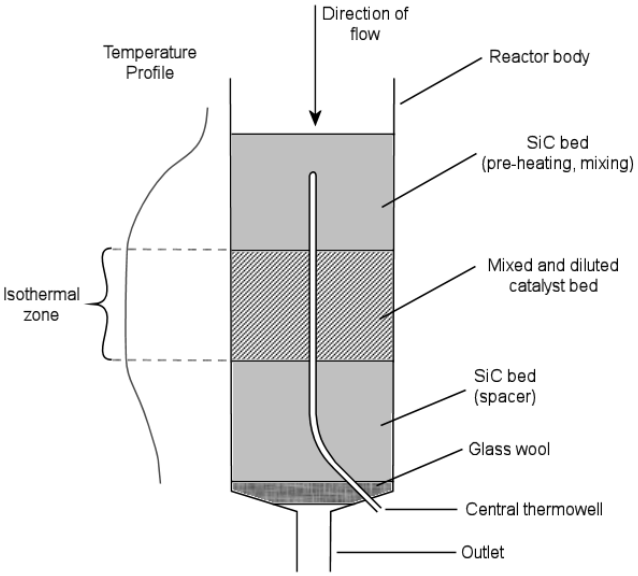

Figure 5.43: Illustration of the Use of SiC Granules as a Spacer to Position the Catalyst Bed Within the Isothermal Zone of the Reactor and Provide a Pre-Heating and Mixing Zone

The isothermal zones were determined by measuring the temperatures of the central thermowells at different points along the length of each reactor during operation through the use of the non-fixed thermocouples described above (with specifics of the temperature control system itself being discussed in Section 5.7). Information regarding the location of the isothermal zones of the two reactors was determined through two separate temperature profile investigations (with and without a catalyst charge) as outlined in Table 5.2, being conducted simultaneously in both reactors. Confirmation that both thermocouple readings were comparable was obtained by swapping them over during the initial SiC only investigation.

As may be seen, these temperature profiles were evaluated under the conditions and with the flows anticipated to be utilised during catalyst testing (see Section 6.3) so as to ensure their accuracy and applicability to the system. For the set of temperature profiles wherein a catalyst charge was present, the start-up procedure in Section 6.4.1 was followed. Specifically, the aims of these separate analyses were to:

Table 5.2: Conditions and Loadings for the Two Simultaneous Temperature Profile Investigations (for a desired isothermal zone temperature of 250°C)

Reactor	Reactor Conditions		Flow Rates		Reactor Charges
	Desired Temperature (°C)	Pressure (bar)	n-C_{16} (ml/min @ 40°C)	H_2 (SCCM)	
1	250	40	0.10	76.2	SiC only
2	250	40	0.10	76.2	SiC only
1	250	40	0.10	76.2	0.800g H-MFI-90, 0.119g 5wt% Pt/SiO_2, 0.667g SiO_2, SIC (as spacer)
2	250	40	0.10	76.2	0.800g H-MFI-90, 0.119g 5wt% Pt/SiO_2, 0.667g SiO_2, SIC (as spacer)

- Ensure that both reactors exhibited the same temperature profile (a vital point if catalysts tested in the separate reactors are to be compared)
- Determine the location of the isothermal zone from the SiC only loading (to know where the catalyst bed must be positioned during investigations)
- Determine the extent to which the heat of reaction influenced the isothermal zone (in terms of its total length and location within the reactor)

The temperature profiles for the two reactors are provided in Figure 5.44. The initial SiC only loadings afforded basic information regarding the location of the isothermal zone within each reactor (without the influence of a reaction) and hence the positions in which the first catalyst charges were to be loaded. These profiles also indicated that, barring minor variations believed to be due to systematic errors associated with the two different thermocouples used, both reactors exhibited virtually identical temperature profiles.

Furthermore, it may be seen from the temperature profiles wherein catalyst charges were loaded within the isothermal zones predicted by the SiC only profiles, that the heat of reaction, calculated to be endothermic by less than approximately 0.27 $\frac{kJ}{(ml_{C16}@40°C)}$ only (assuming complete conversion of the n-C_{16} to n-C_4, see Appendix A.2 for calculations), did not affect the temperature profile to any significant extent and hence did not vary the location of the isothermal zone. (To place this value in perspective, the adiabatic reaction of 1 mol n-C_{16} (i.e. 298 ml @ 40°C) with 10 mol H_2 at 250°C and a constant 40 bar, yielding 4 mols n-C_4 with 7 mols H_2 remaining, would have a final temperature of approximately 210°C).

It was thus determined that an isothermal zone for both reactors exists in the region between approximately 44 cm and 26 cm from the top of the reactor body, as illustrated in Figure 5.44, with the desired reaction temperature of 250 $\pm$ 2°C being achieved in this zone (see Appendix B.1 for the full isothermal zone data).

5.6 Reactor Effluent Handling and Analysis

5.6.1 Control of Conditions and Phase in the Reactor Effluent Line

The effluent stream of each reactor, immediately proceeding the reactor itself, was passed through a 230 μm in-line filter (to remove any particulate matter breaking free from the reactor packing) before a flow of gaseous nitrogen was added to the stream. The purpose of this nitrogen flow was twofold: to maintain the pressure of the reactors during operation (as set by a pressure regulator on the nitrogen supply line, see Section 5.7.2) and to reduce the temperature required for complete vaporisation of the effluent stream, by reducing the partial pressures of the various hydrocarbons, and thereby allowing for analysis to be conducted

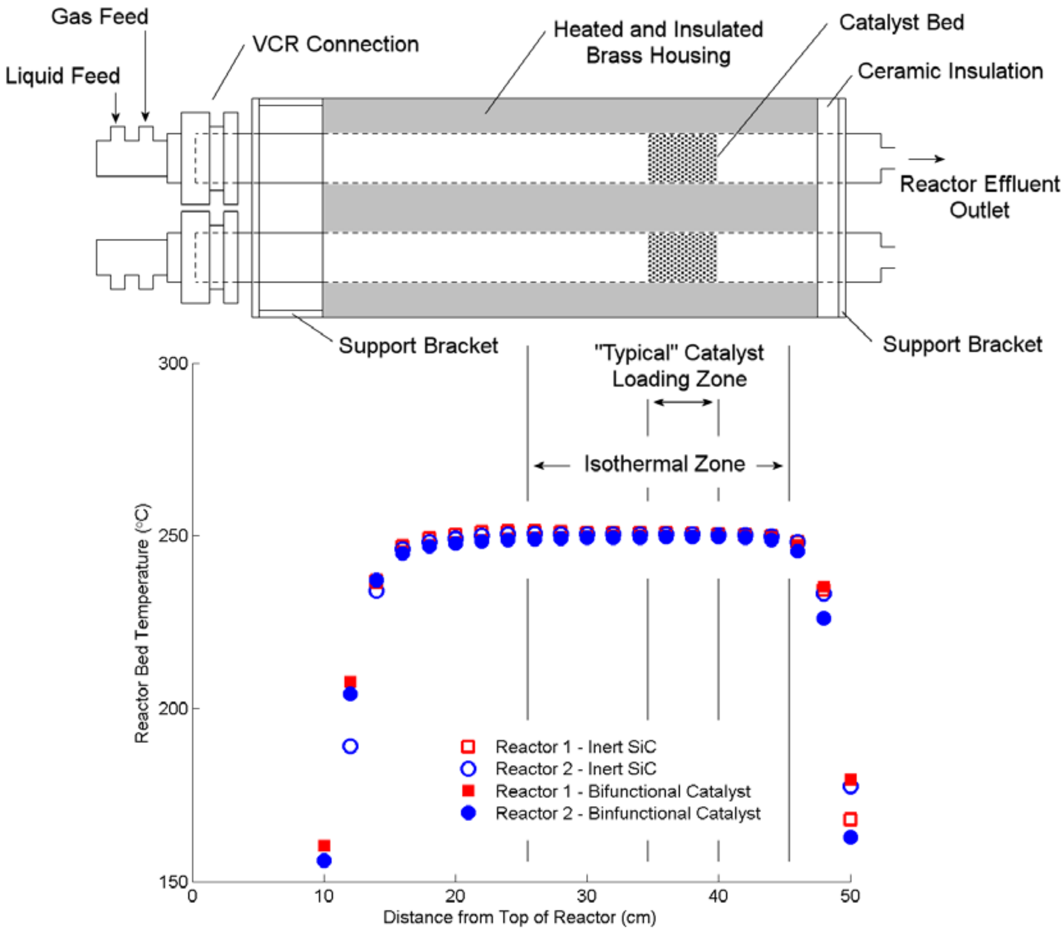

Figure 5.44: Temperature Profiles of Reactors Comparing Inert SiC and Bifunctional (0.800g H-MFI-90, 0.119g 5wt% Pt/SiO_2, 0.667g SiO_2 Diluent) Catalyst Loadings at 40 bar total pressure with 0.10 ml/min n-C_{16} and 76.2 SCCM N_2 flows

by on-line gas chromatography (GC), introducing a vaporous sample to the column via a sample loop (see Section 5.6.2). As indicated in Figure 5.45 however, which illustrates the minimum flow rate of nitrogen required to vaporise a 0.10 ml/min flow of n-C_{16} (the worst case scenario as it represents the highest flow rate utilised in this investigation with no conversion) at various temperatures and pressures (see Appendix A.1 for the method of calculation), dilution alone was not feasible from a practical perspective and heating of the effluent lines to a temperature significantly above ambient temperature was deemed necessary.

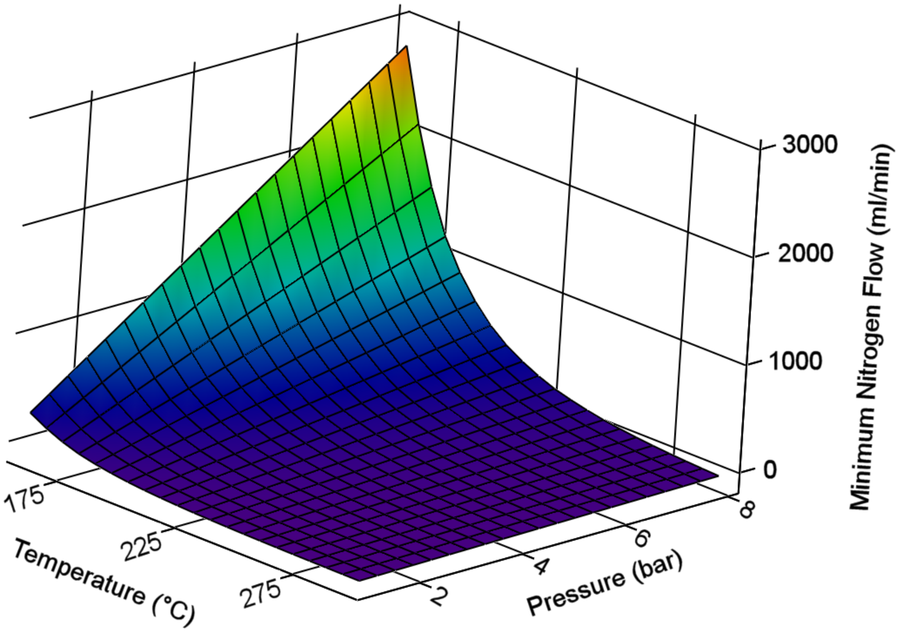

Figure 5.45: Minimum Nitrogen Dilution Required to Vaporise a Stream of 0.10 ml/min n-Hexadecane as it Relates to Both the Pressure and Temperature of the Product Line

To ensure that condensation of the product would never occur during normal operation, the product line temperature was determined to be required at approximately 250°C (see Section 5.7.1) with the associated flow rates of diluent nitrogen calculated for each hydrocarbon feed rate such that, even should no reaction occur and the only hydrocarbon in the reactor effluent be n-C_{16} (the highest boiling compound in the system), total vaporisation of the stream would still be achieved (calculations are provided in Appendix A.1). In practise, it was found that a nitrogen dilution flow rate of above 500 ml/min, per reactor, yielded the most consistent results for all n-C_{16} feed rates investigated (i.e. up to an n-C_{16} feed flow rate of 0.10 ml/min @ 40°C).

Following the addition of the nitrogen diluent, each reactor's product stream was passed through a separate high-precision needle (metering) valve followed by a gate valve. The purpose of the needle valve was twofold, serving to reduce the pressure of the reactor effluent down to the desired pressure for the GC sample loop (approximately 2 barg) (see Section 5.7.2) before it proceeded through the vaporiser and multi-port switching valve, whilst also allowing the nitrogen diluent flow rates to each reactor to be controlled. As such, by adjusting each needle valve, the flow rate of nitrogen diluent into its respective product line, as measured by an MFC (installed upstream of the pressure regulator used to set the reaction pressure due to the inherent flow resistance and pressure drop over the MFC itself) configured to operate as a mass flow indicator for the nitrogen stream into that system (i.e. by setting the flow to 100%). The gate valve allowed the reactor outlet to be shut off, being required as needle valves such as those implemented cannot be closed completely. The decision to implement this specific technique for dilution control was made due to the very low dead volume and high reliability of these needle valves under the conditions they would be exposed to and is detailed in Section 5.7.2.

To ensure that the entire reactor effluent stream was vaporous prior to entering the line to the on-line GC for analysis, the outlet flow from each of the gate valves was passed through a vaporiser unit. These devices were designed to provide a large, heated surface area from whence any liquid still present in the product stream after passing through the needle and gate valves could vaporise rapidly and smoothly. As indicated in Figure 5.46a, the implementation of this concept took the form of two stainless steel tubes, 240 mm in length and with an internal diameter of 10.2 mm (specifically an external diameter of $\frac{1}{2}$", 12.7 mm, and wall thickness of 0.049", 1.245 mm, the same as for the reactor tubes), packed with inert SiC granules and with a stainless steel mesh insert on the outlet to prevent any packing from being carried downstream (see Figure 5.46b). These tubes were positioned within a machined brass housing, measuring 115 x 55 x 240 mm, with the desired temperature being established and maintained through the use of two independently controlled heating elements (see Figure 5.46a and Section 5.7.1), a very similar approach to that utilised for the heating of the reactors and, as with the reactor block, the vaporiser block rested on a ceramic insulation pad to minimise heat transfer to the frame. Unlike the reactors, however, the vaporisers were not envisioned to require frequent removal and, as such, these units were not equipped with the same VCR fittings or leaning-out mechanism described for the reactors, instead being installed as in-line units. Upon exiting the vaporisers, the now completely gaseous effluent from each reactor was conveyed through heated $\frac{1}{8}$" stainless steel lines (see Section 5.7.1.4) to the multi-port switching valve (see Section 5.6.2), with the selected reactor's effluent then being sent, again through a heated $\frac{1}{8}$" line, to the on-line GC for analysis, whilst the unselected reactor's effluent was diverted to vent.

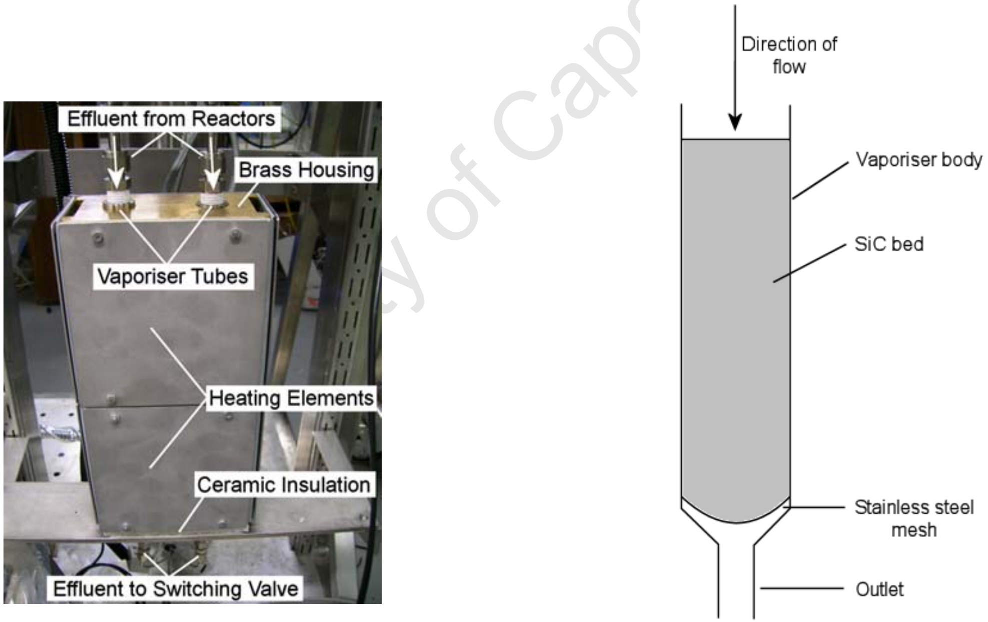

(a) Vaporiser unit (shown without insulation for clarity)

(b) Diagram of vaporiser tube

Figure 5.46: Vaporiser Implemented on Product Line

5.6.2 Analysis Equipment Selection and Configuration

Given its ability to analyse hydrocarbon samples on both a qualitative (able to differentiate both on carbon number, degree of saturation and extent of branching) and quantitative (relative molar concentrations of each compound) basis, gas chromatography was selected as the most applicable technique for use in this regard.

The GC selected for the task was a Varian 3900 with heated internal injection valve and cryogenic cooling (using liquid CO_2 from a dip-tube cylinder located close to the apparatus). The 6-port injection valve, pneumatically operated and controlled by the supporting PC, was utilised in two positions as illustrated in Figure 5.48. The first position (Figure 5.48a) loaded the sample loop with reactor effluent whilst flushing the GC injection port with hydrogen carrier gas. The second position (Figure 5.48b) flushed the effluent sample out of the sample loop and into the GC injector port for analysis using the hydrogen carrier gas, temporarily diverting all reactor effluent entering the valve back along a separate heated $\frac{1}{8}$" line to the multi-port switching valve for disposal. After a short time interval (approximately 60 seconds), the valve was switched back to its initial position, allowing hydrogen carrier gas to continue entering the GC injector port whilst flushing the sample loop with fresh reactor effluent in preparation for the next analysis.

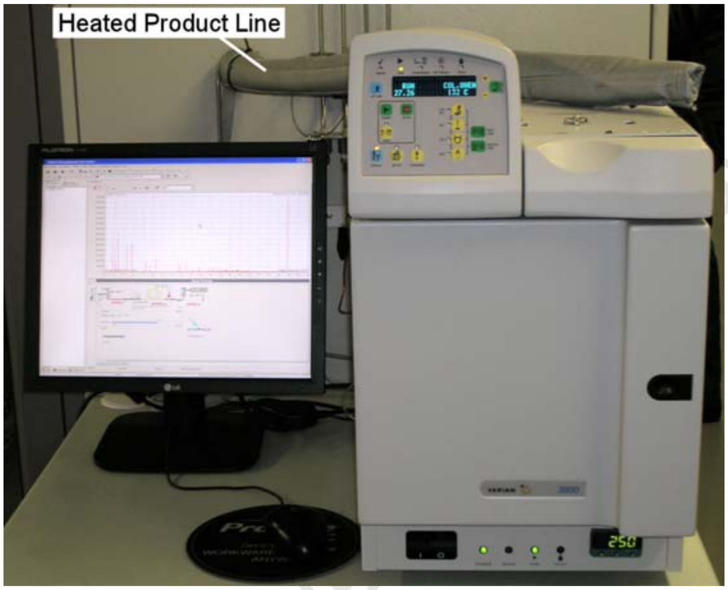

Figure 5.47: Varian 3900 GC and Monitor of Supporting Computer

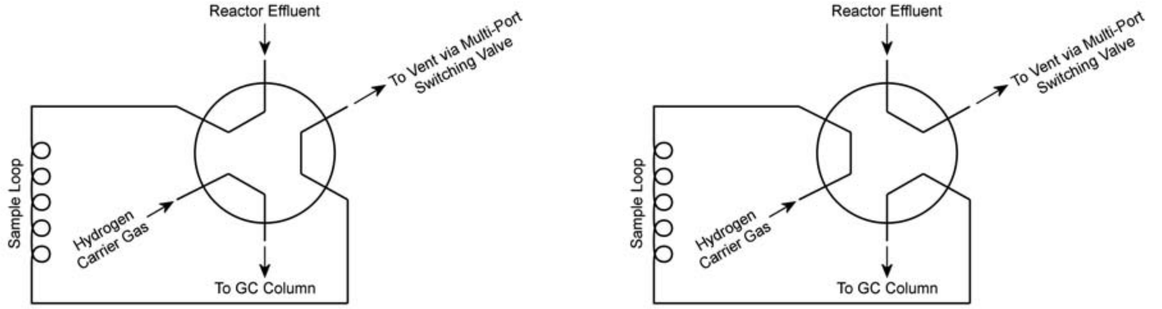

(a) Loading of sample loop with reactor effluent whilst carrier gas flows onto GC column

(b) Injection of sample onto GC column using carrier gas whilst reactor effluent is diverted for disposal

Figure 5.48: Diagram of Port Layout for GC Internal Injection Valve

The feed stream to the chosen GC configuration was intended to be completely vaporous, and it was for this reason that the dilution and vaporisation steps mentioned above were implemented. Furthermore, although the injection valve of the GC was heated (operated at 290°C with a maximum operating temperature of 325°C), the lines from the rear connectors of the GC (in its shipped form) to this valve were not, and as such additional heating and insulation was installed to ensure product condensation within these tubes was averted (with these lines maintained at an operating temperature of approximately 250°C).

In an effort to maximise automation of the product analyses, and given that the GC was only able to analyse a single sample at a time, a heated electrically actuated VICI (Valco Instruments Co. Inc.) 6-port multi-port switching valve was utilised to allow for the switching of the GC feed line between one of four inlet streams (two from the rig utilised in this investigation and two from an adjacent unit) whilst all remaining lines are collected to a common vent (see Figure 5.49). Where a subsequent analysis was to be conducted on a different reactor, the switching of the multi-port valve was done immediately after injection of the previous sample on the GC so as to allow ample time between any two sample analyses to flush the line between the multi-port switching valve and the GC injection valve as well as the sample loop . The multi-port switching valve, as indicated in Figure 5.50, operates on a simple principle whereby the primary outlet port and vent port are staggered vertically off-centre (above and below) whilst all of the inlet ports are located midway between these. In this manner, rotation of the inner head and its grooved Teflon seal serves to align the inlet ports in such a manner that, in any given position, only a single inlet stream is conveyed to the outlet port connected to the GC (note the different port selections achieved by rotating the head illustrated in Figures 5.50a and b) whilst all other inlet streams flow out through the common vent port.

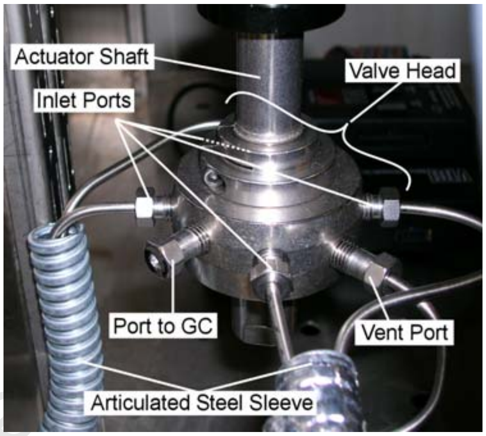

Figure 5.49: Multi-Port Switching Valve Arrangement of Inlet and Outlet Ports

Furthermore, to ensure help reduce condensation of the reactor effluent which may occur within the multi-port switching valve itself when at the operating pressure of approximately 2 barg, the head of the unit was heated to 190°C (maintaining a 5% safety margin over the device's maximum operating temperature of 200°C due to its Teflon internals) (see Section 5.7.1). It was essential that only this head section (the portion onto which the various inlet and outlet lines are connected) be heated, with the elongated shaft (indicated in Figure 5.49) serving to allow heat to disspiate and thereby preventing damage to the electronic actuation controls.

The GC itself was equipped with a non-polar PONA column (50m (length) x 0.2mm (internal diameter) x 0.5μm (film thickness)) and flame ionisation detector (FID) to allow for the separation and detection of the various hydrocarbons anticipated in the product. For this investigation, hydrogen was used as both the carrier gas and to fuel the FID flame (with the hydrogen passing through a combined activated carbon and molecular sieve 13X filter prior to entry to the GC so as to remove any hydrocarbon or water contamination), with nitrogen being fed as a make-up gas and pressurised synthetic air provided for the FID flame and pneumatic injection valve operation. Cryogenic cooling of the GC, required for the detection of the lighter

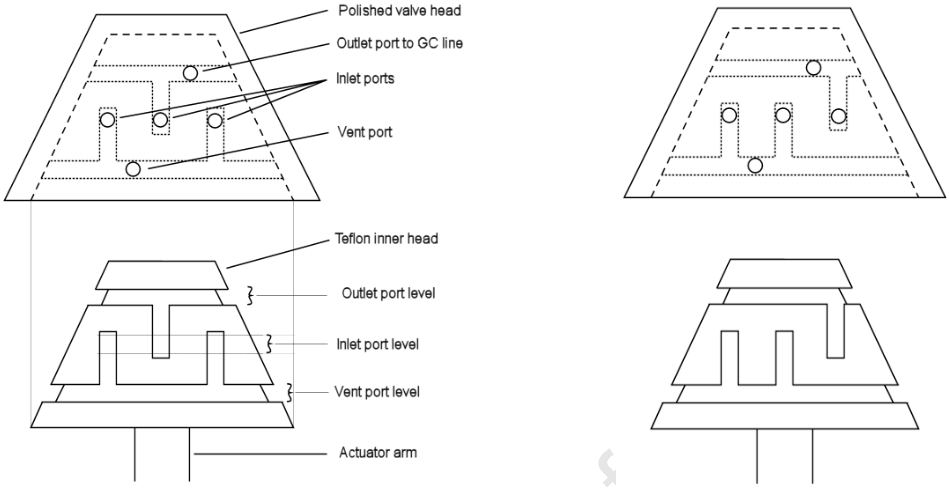

(a) Diagram illustrating multi-port valve selection of an arbitrary inlet stream

(b) Diagram illustrating multi-port valve selection of next inlet stream for comparison

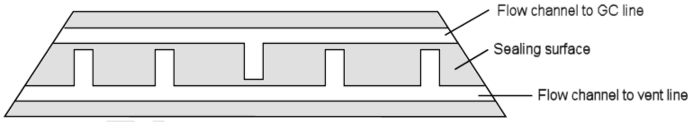

(c) Diagram of Teflon seal on inner, rotating head (flattened for clarity)

Figure 5.50: Diagrams of Multi-Port Switching Valve Internal Mechanism and Layout

hydrocarbons (such as methane), was achieved through the use of liquid CO_2 (supplied from a cylinder, with a dip-tube, located close to the rig). The GC was connected to a desktop computer for the purposes of control and data capture utilising the Varian Galaxie software package supplied with the GC. Full details of the GC settings together with the three step temperature ramping analysis programme are provided in Table 5.3. Furthermore, the external event signals of the GC were set up in such a manner that one, as supplied, controlled the internal pneumatic sample injection valve whilst the second was set up, through the use of a solid state relay, to allow control of the multi-port switching valve by the computer. This arrangement allowed for multiple runs to be conducted autonomously.

Table 5.3: Gas Chromatograph Settings and Outline of Temperature Ramping Programme

Injector	Temperature	(°C)	290		
	Split Ratio		100		
Column	Flow Control		Isobaric at 2.5 barg		
	Carrier Gas		Hydrogen		
	Ramping Programme		Step 1	Step 2	Step 3
	Initial Temperature	(°C)	-20	-20	10
	Ramp Rate	(°C/min)	0	5	8
	Final Temperature	(°C)	-20	10	250
	Hold Time	(min)	1	5	0
Detector	Temperature	(°C)	300		
	Nitrogen Make-Up	(ml/min)	50		
	Hydrogen	(ml/min)	30		
	Air	(ml/min)	300		

5.7 Reaction and Reactor Effluent Condition Control

5.7.1 Heating and Temperature Control

Heating of the system was divided into four distinct regions based on the temperature required and means by which this temperature was achieved and maintained:

The feed pots, pumps and liquid feed lines were maintained at approximately 45°C using self-regulating heating tape secured with adhesive aluminium tape.

The reactors were enclosed within a solid brass housing with four independent heating elements and insulated with a custom-made insulation jacket. The controller of the uppermost heating element was setpoint only, in that only a single setpoint could be entered and had to be changed manually if desired, whilst the bottom three were programmable, allowing for various time dependent temperature ramping programmes to be executed (such as that utilised during catalyst reduction).

The vaporisers were enclosed within a solid brass housing with two independent, setpoint only heating units and insulated with a second custom-made insulation jacket.

The reactor effluent lines and multi-port switching valve were heated through the use of high-temperature heating lines linked to a setpoint only controller. The reactor effluent lines were insulated with custom-made lagging whilst the multi-port switching valve head was insulated with glass wool

5.7.1.1 Feed Supply

The liquid feed storage and delivery system, including the feed pot, pump head, pulse dampener and feed lines were maintained at approximately 45°C (above the 18°C melting point of the n-C_{16} feedstock) through the use of self-regulating heating tape. These heating lines were connected separately for each reactor's feed system, allowing them to be turned on and off independently should the need arise. Due to the relatively low temperatures, insulation on these sections was minimal, limited to the use of adhesive aluminium tape to hold the heating line in position whilst simultaneously, being conductive in itself, improving heat transfer between the heating line and the object being heated by increasing the contact area.

5.7.1.2 Reactors

The temperature of the reactors, housed within a solid brass block which rested on a ceramic insulation pad to minimise heat transfer to the frame (see Figure 5.54a), was controlled through the use of four independent heating elements as illustrated in Figure 5.51. These elements served to heat the entire brass block within which the reactors were housed during operation, thereby ensuring that both reactors maintained near-identical temperature profiles for all investigations. Of these four controllers, the first (maintaining the temperature of the initial feed heating zone) was a Gefran 600 controller (with all Gefran controllers used in this investigation being supplied by Unitemp), accepting only a temperature setpoint and being unable to execute temperature ramping programmes (a functionality which was considered unnecessary for this region). The remaining three, Gefran 800p controllers, were fully programmable, accepting both temperature setpoints and customisable temperature ramping programmes (with the ramping programmes being essential in the lower portions of the reactor, where the catalyst bed was to be located, as they were required during the reduction of supported metal catalyst as indicated in Section 6.4.4.2). Insulation of the reactor block was achieved through the use of a custom-made heavy insulation jacket (Figure 5.41c).

During the initial heating procedures, it was noted that the internal reactor temperature (measured by the thermocouple located within the central thermowell) deviated from the temperature at which the brass block was being maintained as indicated by the heating element controller thermocouples (as illustrated in Table 5.4). This was speculated to be due to the location of the controller thermocouples for these heating elements, which were held by a spring mechanism against the external surface of the brass housing as illustrated in Figure 5.52. Thus, a potential cold spot due to the small gap in the insulation close to the thermocouples, combined perhaps with imperfect contact between the thermocouples and the surface of the brass housing, resulted in the controller thermocouples always detecting a temperature below the true temperature of the brass housing, and hence below that within the centre of the reactor, in their respective regions. Awareness of how the temperature indicated by the controllers deviated from the actual reactor temperature was essential in order to ensure the correct controller setpoints were utilised during reaction and reduction to ensure the desired temperatures within the reactor were achieved (see Sections 6.4.1 and 6.4.4.2 respectively) and was thus studied in detail to compile the required relationships as presented in Table 5.4. This deviation was also observed to influence the heating rates attainable using the apparatus for, whilst the heating element controller thermocouples indicated the maximum heating rate of the brass housing to be approximately 7°C/min, a slight time lag between the heating of the housing and the heating of the reactor bed meant that the associated maximum heating rate of the isothermal zone, as measured by the internal thermocouple, was only approximately 6°C/min. This point had an influence on the catalyst reduction programme as described in Section 6.4.4.2.

5.7.1.3 Vaporisers

The vaporiser temperature was controlled in much the same way as that of the reactors, with the vaporiser tubes housed within a solid brass housing surrounded by heating elements and insulation (Figure 5.46). For the vaporisers, however, the brass block was smaller than that housing the reactors, requiring only two 120 mm long heating elements, both controlled by setpoint only Gefran 600 controllers. These controllers were selected as the vaporisers were to be operated at a fixed temperature, not requiring the temperature ramping functionality of the Gefran 800p units. As mentioned in Section 5.6.1, the vaporiser brass housing rested upon a ceramic insulation block, minimising heat transfer to the frame, with the remainder of the unit being insulated with a jacket similar to that surrounding the reactor block. To ensure complete vaporisation of the hydrocarbons in the reactor effluent, the vaporiser unit was operated with a temperature profile across it,

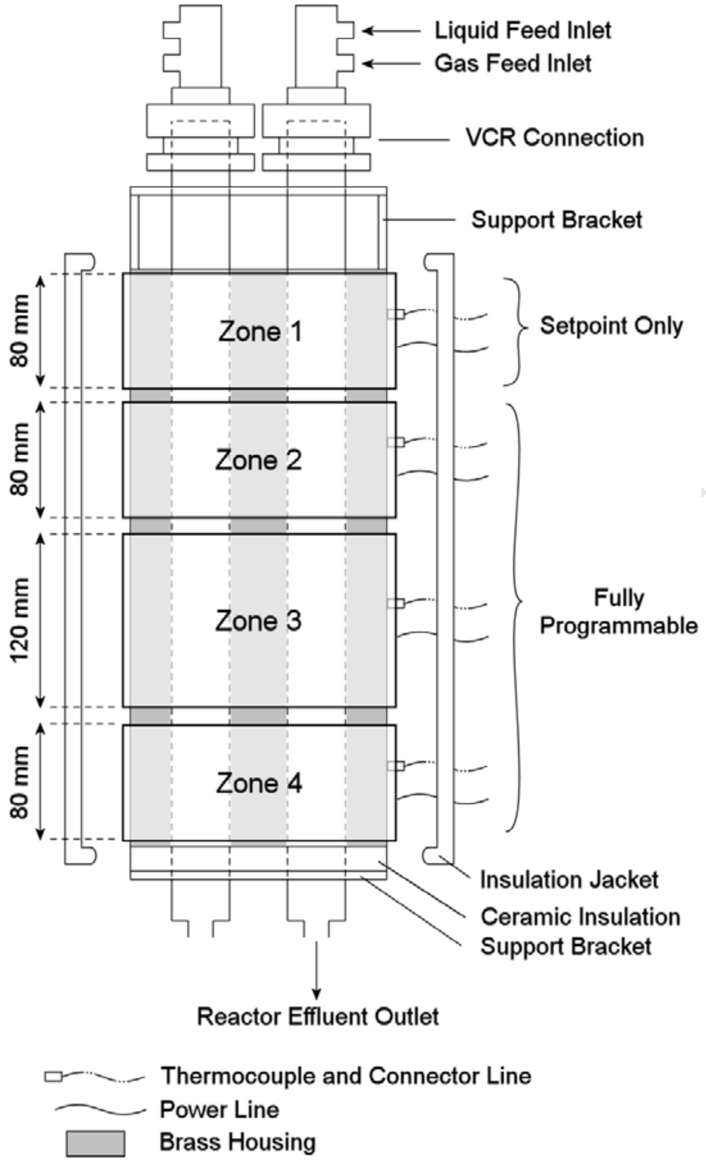

Figure 5.51: Diagram of Reactor Housing Illustrating Heating Element Layout

the top zone being maintained at approximately 260°C and the bottom zone at 290°C. In this manner, any liquid flowing onto the top of the SiC granule bed in the vaporiser would spread across the large surface area of the granules before vaporising smoothly further down the bed rather than flash vaporising on contact, an eventuality which may have resulted in pulsing of the heavier hydrocarbons in stream leaving the vaporiser, resulting in large fluctuations in the results from the GC analyses.

5.7.1.4 Reactor Effluent Lines

The effluent lines from both reactors were enclosed within a single articulated steel sleeve between the vaporiser exit and the multi-port switching valve and between the switching valve and the GC injection valve. This sleeve was heated through the use of high-temperature glass fibre heating cord spiralled around the

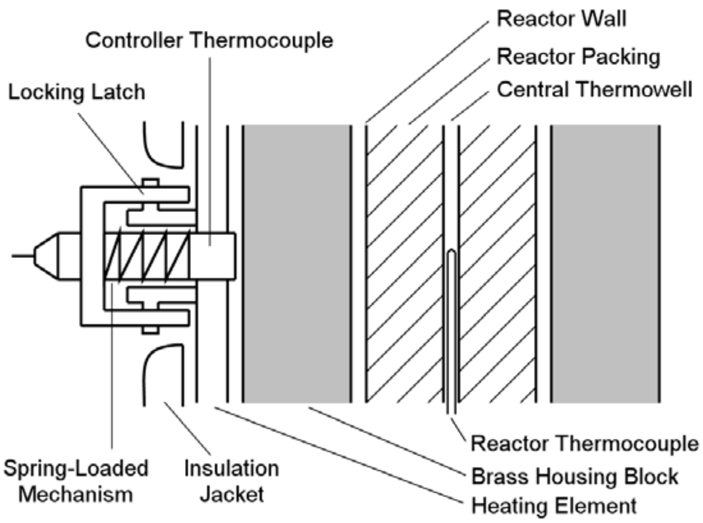

Figure 5.52: Slice Through Reactor Showing Location of Heating Element Control Thermocouple as Compared to Internal Thermocouple

Table 5.4: The Relationship Between the Controller Setpoint Temperatures[1] and the Temperature of the Isothermal Zone within the Reactor[2]

Controller Setpoint Temperatures (°C)				Isothermal Zone Temperature (°C)
Zone 1	Zone 2	Zone 3	Zone 4	
47	47	46	47	50
94	94	93	94	100
102	102	100	101	108
142	142	139	140	150
153	153	150	152	162
189	189	185	187	200
236	236	231	234	250
283	283	278	281	300
330	330	324	328	350

1 - Indicated by the controller thermocouples to be the stabilised temperature of the brass housing in their respective regions

2 - Compiled by manually changing the heating element setpoints over the range of temperatures indicated

outside of the sleeve and insulated using a combination of custom-made insulation lagging, glass wool and adhesive aluminium tape (see Figure 5.53). The controller thermocouple, linked to a setpoint only Gefran 600 controller, was positioned on the inside of the sleeve and in direct contact with the $\frac{1}{8}$" effluent lines (with this positioning being essential to reduce the lag in temperature control associated with heat transfer through an air gap were the thermocouple not in contact with a solid surface).

As indicated in Section 5.6.1, heating of the effluent lines was necessary to prevent the condensation of any of the heavier hydrocarbon in the line prior to analysis, with the technique described above being selected as the heated internal volume of the sleeve aided in the distribution of heat along the length of the lines, helping to reduce the chance of cold-spots being present.

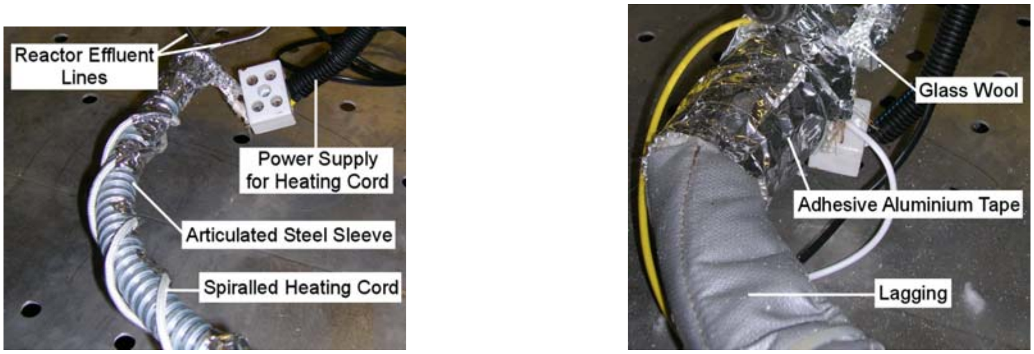

(a) Uninsulated product line immediately proceeding vaporisers

(b) Fully insulated product line immediately proceeding vaporisers

Figure 5.53: Product Line Heating and Insulation

Unfortunately, whilst these lines could be, and were, heated to approximately 250°C, the maximum operating temperature of the multi-port switching valve was only 200°C (due to the Teflon seal on the inner head). It was hence desired to heat the valve head to only approximately 180°C during operation. This was achieved using high-temperature glass fibre heating cord linked to a separate Gefran 600 controller, with the control thermocouple in direct contact with the valve head itself, and insulating the awkwardly shaped valve with glass wool and adhesive aluminium tape.

5.7.2 Pressure Control

As indicated in Section 5.6.1, during normal operation, gaseous nitrogen was required to be utilised for both the dilution of the hydrocarbon product and for the control of the reaction pressure. Two techniques whereby this could be achieved were investigated, the first being to utilise back-pressure regulators whilst the second was to use high-precision needle (metering) valves in conjunction with a pressure regulator downstream of each nitrogen stream's MFC.

The use of back-pressure regulators (BPRs) was the first technique tested, with two such units being installed (one located on the effluent stream of either reactor as shown in Figure 5.54a). As indicated in Figure 5.54b, these devices function by applying a pre-set pressure to one side of a diaphragm. This pressure serves to hold a Teflon seal in place, blocking the outlet port and preventing flow through the BPR whilst the inlet pressure is below the pre-set pressure. When the inlet pressure rises above the pre-set pressure, the diaphragm is forced back, opening the outlet port and allowing flow through the device. This effectively maintains the pressure on the inlet side at the pre-set level.

With this pressure control technique, the nitrogen diluent, metered through a Brooks mass flow controller, was added to the reactor effluent stream prior to its entry into the BPRs. This was done so as to assist in the smooth operation of the BPR diaphragms by providing a higher flow through them during operation, continuously holding the outlet port open rather than having it periodically open and close.

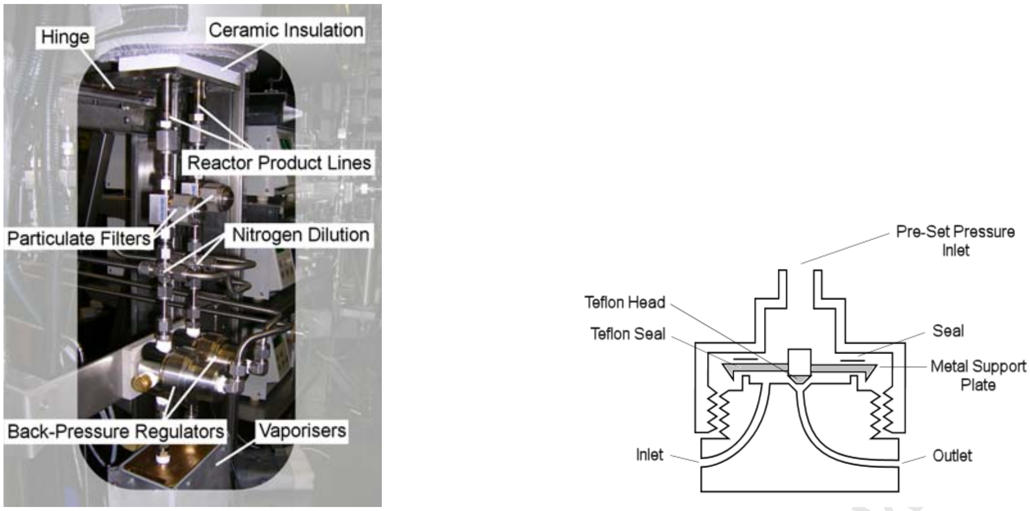

(a) Back-pressure regulators as installed on reactor outlets

(b) Side view of back-pressure regulator to illustrate internals

Figure 5.54: Diagram of Back-Pressure Regulator and Implementation

Unfortunately, the BPRs were found to cause fluctuations in the hydrocarbon content of the stream to the vaporiser, and hence to the GC, determined to be due to agitation of a pool of liquid hydrocarbons which collected within the large internal cavity of the BPR during operation. This eventuality, illustrated in Figure 5.55, resulted in the periodic splashing of liquid hydrocarbons into the line exiting each BPR, resulting in an occasional, dramatic spike in the content of heavier hydrocarbons. This splashing effect, as illustrated in Figure 5.55b, was particularly pronounced given the addition of the nitrogen diluent prior to the product entry to the BPR. Thus, short of vaporising the entire product stream at reaction pressure prior to its entering the BPR, a feat which, assuming the maximum operating temperature of 200°C of the BPRs, would require more than 3000 ml/min of nitrogen dilution or, assuming a dilution flow rate of 500 ml/min as applied, would require heating the BPRs to approximately 260°C (impossible due to the Teflon internals), little could be done about these fluctuations. (Both values were obtained utilising the calculation method in Appendix A.1 assuming 0.01 ml/min of liquid n-C_{16} fed).

As such, the BPR system was replaced by the implementation of a precision metering valve on the reactor effluent stream of each reactor. Herewith, the two aforementioned nitrogen mass flow controllers were set to function as mass flow indicators (by setting the flow to 100%, i.e. keeping the regulating valve completely open), with a pressure regulator, installed on the outlet of each, used to set the nitrogen diluent stream to the desired reaction pressure. These nitrogen diluent streams joined their respective reactor effluent streams upstream of the metering valves, as illustrated in Figure 5.56a. With the precision metering valves being unable to seal entirely without damaging them, a gate valve was installed downstream of each, with these gate valves being utilised during reactor startup (see Section 6.4.1).

This simultaneous dilution and pressure control technique functioned in that, during operation, the metering valves were adjusted until the desired nitrogen dilution flow rate was achieved (as displayed by the mass flow indicators). This not only provided the nitrogen required to sufficiently dilute the hydrocarbon stream (so as to achieve total vaporisation after throttling and heating) but, as the nitrogen was supplied at the desired reaction pressure (by the regulators following either of the nitrogen mass flow indicators), the system was maintained at this pressure during operation. Furthermore, as indicated in Figure 5.56b, the metering valves offered minimal liquid hold-up, with their implementation being observed to result in a

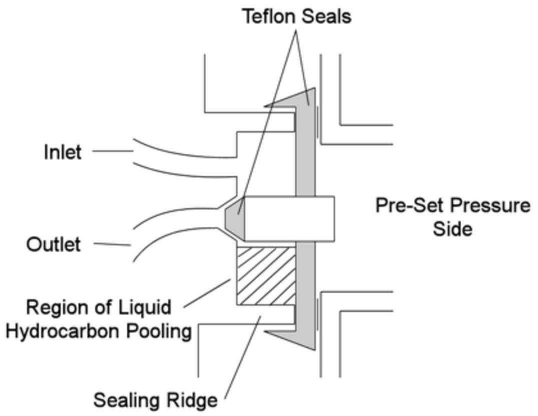

(a) Enlarged side view of back-pressure regulator to show liquid hydrocarbons pooling in large internal cavity

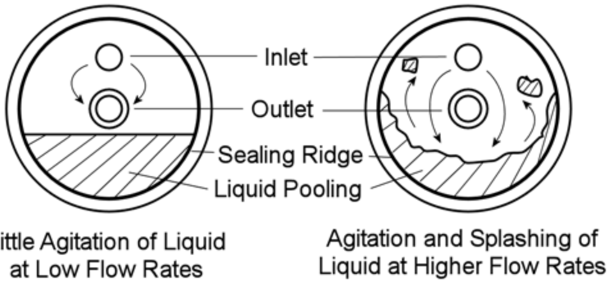

(b) Front view of back-pressure regulator with comparison of the effects of greatly varied flow rates

Figure 5.55: Collection and Agitation of Condensed Hydrocarbons within the Back-Pressure Regulator

dramatic reduction in the pulsing of hydrocarbons in the product. Contrary to the BPRs where the increased flow through the unit due to the nitrogen dilution resulted in worsened performance due to agitation of the liquid hydrocarbons in the "pool", increased flow through the metering valves was observed to improve performance by rapidly flushing the small internal volume of the valves.

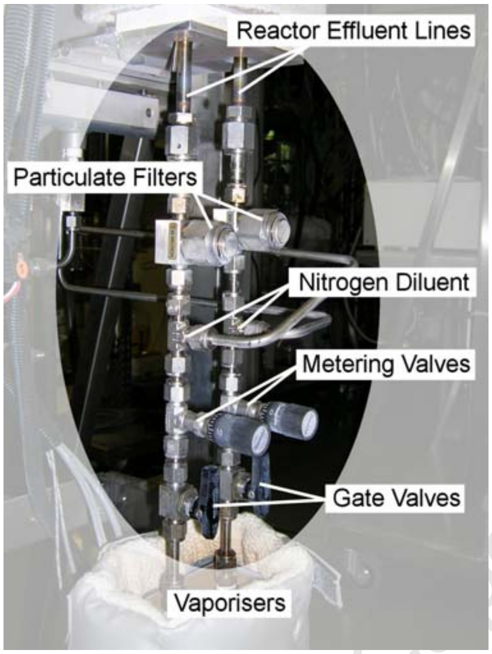

(a) Photograph of metering (needle) valves and diluent stream addition lines on reactor outlet

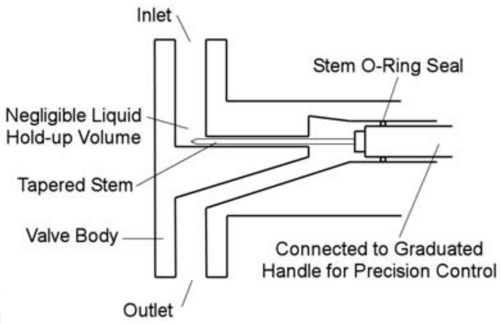

(b) Diagram illustrating minimal liquid hold-up through metering valves

Figure 5.56: Metering Valve Implementation to Replace Back-Pressure Regulators

5.8 Safety Considerations and Precautions

The safety and preventative measures incorporated in the design centred around five considerations:

- Leaks in the gas supply lines
- Blockages in the system which could result in flow of hydrocarbons into the gas supply lines
- General pressure related issues, specifically over-pressurisation
- Temperature and temperature control related issues, such as over-heating and fire hazards
- General emergency shutdown procedures

Each of these scenarios is discussed in detail below together with the measures implemented to minimise the likelihood of their occurrence and facilitate their control.

5.8.1 Leak and Undesired Flow Path Related Safety Issues

During the design and construction of this apparatus, two key facets were foreseen in terms of leaks and undesirable flow paths, with appropriate measures implemented to help minimise the occurrence of any such malfunctions and to ensure the detection and response should any occur. These facets were:

- The fire and explosion hazard posed by the leakage of gaseous hydrogen or flammable hydrocarbons (as vapour or liquid) out of the rig
- The contamination of the mass flow controllers, pressure regulators and house gas supply system by the undesired flow of hydrocarbons into the gas feed lines.

5.8.1.1 External Leaks and Waste Effluent Disposal

The possible leakage of flammable and potentially explosive material from the rig was, of course, of the greatest concern, posing a clear threat to both people and property, with the primary method of controlling such leaks being, of course, prevention. In this regard only Swagelok high pressure approved and guaranteed fittings were used together with comprehensive leak testing prior to the operation of the rig. This leak testing was conducted in two phases, first by pressurising the system to 50 bar (25% above the operating pressure of 40 bar) with nitrogen and testing all fittings with Swagelok Snoop Liquid Leak Detector, and then by pressurising with hydrogen, also to 50 bar, (with the smaller molecule being able to penetrate narrower leak paths) and ensuring that all of the fittings were leak-free by utilising a Varian TCD Leak Detector. During this process, any leaking fittings were tightened as appropriate and re-tested. If the leaking were to have persisted, the fitting would have been replaced, although such a scenario was not encountered on this rig.

Regarding the detection of and reaction to such leaks during rig operation, environment monitoring, ventilation and gaseous waste disposal were all of importance. To ensure the rapid detection of leaks and the control of any leaked material, the rig was positioned within a walk-in fume hood during operation. This fume hood was not only equipped with both hydrogen and smoke detectors, but afforded a ventilation system whereby gaseous waste was disposed of in a safe and controlled manner.

The hydrogen alarms in the fume hood were configured for three hydrogen detection levels (based on the lower explosive limit, or LEL, of hydrogen in air of 4 vol%) with escalating automated responses. At 10% LEL, highly visible strobe lights would be triggered throughout the laboratory, with this visual alert being accompanied and reinforced by a siren audible throughout the building should the hydrogen level rise to 25% LEL. Should the hydrogen concentration increase to 50% LEL, the system would automatically shut off all electrical power to the fume hood, preventing any heating or other electrical ignition sources. This shut off would also halt all pumping of liquid feed and close all mass flow controllers, terminating the supply of any flammable compounds to the rig.

The fire alarms within the fume hood, triggered by smoke produced, for instance, by liquid hydrocarbon contacting a heated surface on the rig, not only sounded a building-wide alarm but simultaneously and automatically alerted the appropriate emergency services to the situation.

To allow for the safe disposal of flammable and potentially explosive waste gases and gaseous mixtures, the fume hood afforded an extraction line to which the gaseous products could be safely vented. As such, all streams bypassing the GC (specifically the entire vaporised effluent stream of the reactor not being analysed), together with the gaseous reactor effluent stream flushing the GC sample loop and the split from the GC injector were sent, via an unheated vent guard catch pot, to the vent system for safe disposal. This guard catch pot, constructed from a 2250 ml stainless steel pressure vessel with a gate valve installed at the bottom to allow liquid to be drained, was maintained at ambient pressure by virtue of the outlet line (chemical and fire resistant rubber hosing), connecting it to the vent system, being $\frac{1}{2}$" external diameter as opposed to the $\frac{1}{4}$" stainless steel inlet line (carrying waste gas at only approximately 2 barg). The purpose of this low pressure unheated catch pot was to ensure that any heavier hydrocarbons would condense out from the lighter species and hydrogen in a manner whereby they may be easily collected and disposed of as opposed to condensing in the extraction line itself. The liquid collected in this guard catch pot was periodically drained and disposed of appropriately.

5.8.1.2 Blockages Resulting in Undesired Hydrocarbon Flow Paths

The flow of hydrocarbons into the mass flow controllers, pressure regulators and supply lines (house lines) of either the hydrogen or nitrogen gas feeds was also of great concern as it could result in permanent damage to the mass flow controllers and regulators as well as contaminate the gas being fed to other units using that gas supply system (i.e. any rigs being fed from the same section of the house gas manifold).

To prevent hydrocarbons, particularly the heavier species which would exist in the lines as a liquid at ambient temperature (approximately 25°C), from flowing into the gas feed system, guard catch pots and one-way valves were installed in various locations on the gas lines.

These 500 ml feed line guard catch-pots, unheated as per the vent line catch pot described in Section 5.8.1.1, were incorporated on all gas feed lines prior to entry to the reactors so as to ensure that any liquid flowing up these lines (for instance due to a blockage in the reactor) would be trapped before reaching the mass flow controllers or the house gas manifold. These guard catch pots, illustrated in Figures 5.57a and b, were installed with a dip-tube attached to the outlet line. These dip-tubes, extending internally to the bottom of each catch pot, ensured that any liquid reaching the guard catch pots during rig operation would always preferentially flow back into the system (should, for instance, the blockage causing the back-flow be cleared or one of the pressure relief valves [see Section 5.8.2] open due to over-pressurisation), with flow into the preceding gas lines occurring only if the catch pot was completely filled.

As a final line of protection against gaseous hydrocarbons or in the event of the complete filling of the guard catch pots, one-way valves (also known as "check valves") were installed immediately proceeding every mass flow controller as illustrated in Figure 5.37. These valves were installed as a redundant system to block the lines and prevent the flow of any material back into the mass flow controllers or house gas manifold.

5.8.2 Pressure Related Safety Issues

Of primary concern with regards to the pressure related safety of this rig was the fact that the liquid feed pump implemented could deliver pressures in excess of the maximum pressure ratings of the stainless steel tubing utilised, as indicated in Table 5.5. It was thus essential that preventative measures be put in place to prevent the over-pressurisation and associated rupture of any high pressure lines.

These preventative and safety measures comprised:

- Using only Swagelok high pressure approved and guaranteed fittings throughout the rig
- Setting each pump's maximum outlet pressure (by virtue of the pressure sensor in the pulse dampeners described in Section 5.4.2) to 60 bar (20 bar above the operating pressure of the system)

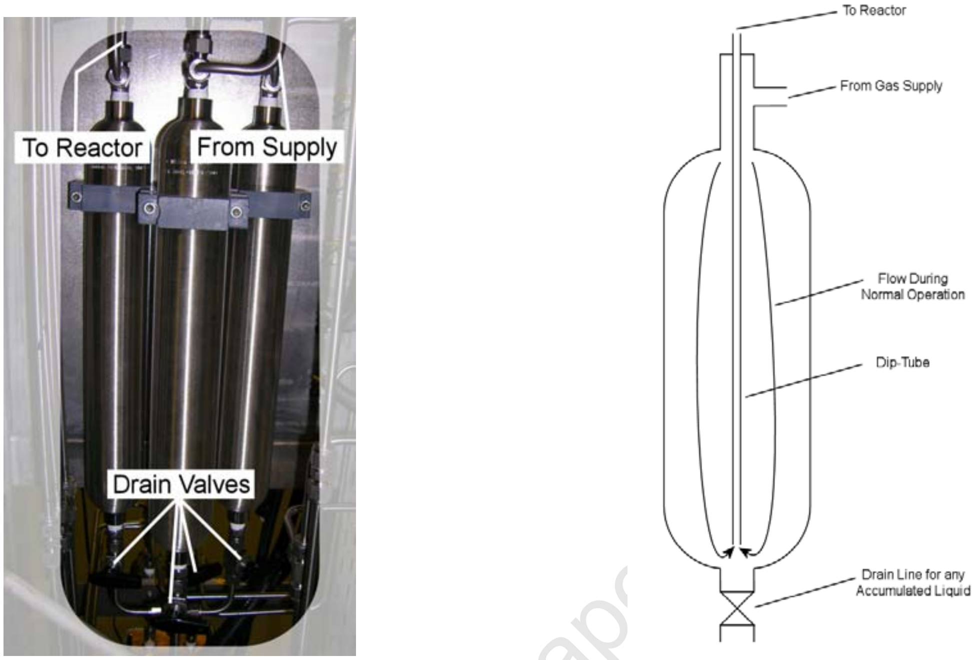

(a) Photograph of guard catch pots on gas feed lines

(b) Diagram of guard catch pots illustrating dip-tube design

Figure 5.57: Design and Implementation of Guard Catch Pots

Table 5.5: Maximum Pump Pressure as Compared to Pressure Ratings of Stainless Steel (316SS) Tubing at Different Temperatures
(Data from Callahan, 1998)

Pump Maximum Delivery Pressure	(bar)	340	
Tube Pressure Ratings			
Tube Dimensions (OD x Wall Thickness)		Operating Temperature	
		~ 25°C	~ 300°C
1/16" x 0.010"	(bar)	386	328
1/8" x 0.028"	(bar)	586	498
1/4" x 0.035"	(bar)	352	299
1/2" x 0.049"	(bar)	255	217

- Installing pressure relief valves on the gas feed lines to each reactor, calibrated to 60 bar
- Installing pressure relief valves on the liquid feed lines from each pump, just after exiting the pulse dampener, again calibrated to 60 bar

It should be noted that all of the pressure relief valves were installed in such a manner that, should they be triggered, any material released would be directed safely into the vent line via the main vent guard catch pot described in Section 5.8.1.1.

These measures were deemed to be sufficient to ensure that, even should the pulse dampener malfunction, or a blockage restrict or stop flow through the reactor, neither the tubing nor the fittings would fail due to over-pressurisation of the system and hydrocarbons would be prevented from entering the mass flow controllers or gas supply lines.

5.8.3 Temperature and Fire Related Safety Issues

Two safety related concerns were associated with the heating of the rig, these being the reduction in the pressure rating of the tubing utilised with increasing temperature and the potential formation of ignition sources due to excessive heating.

The former point, illustrated in Table 5.5 for the tubing sizes utilised in this rig, was of concern for the breach of a pressurised heated line would result in the rapid expulsion of a large volume of highly flammable, potentially explosive hydrogen gas and/or mixtures of vaporous or liquid hydrocarbons in close proximity to an active heating element. This danger was, however, deemed to be suitably controlled by the installation of the pressure relief valves discussed in Section 5.8.2, together with the fire detection and response measures indicated in Section 5.8.1.1.

Given the relatively low maximum temperature of 350°C (during catalyst reduction as indicated in Section 6.4.4.2) utilised in this investigation, it was foreseen that the formation of a heat source sufficient to present as an ignition source could only occur through uncontrolled heating. This eventuality could arise either through faulty temperature control algorithms, whereby the controller settings caused the temperature to greatly overshoot the desired setpoint value, or if the control thermocouple was dislodged, damaged or suffered a short circuit in the line to the controller and thus reading a temperature far below that of the region being heated by its associated controller, thereby resulting in the controller continuing to heat the region well beyond the desired level.

To prevent significant overshooting of the desired temperature, all temperature controllers had alarms which were set to allow a maximum temperature 10% above their setpoint at any given point during operation. Should the temperature rise, for any reason, above this alarm level, a visual indication would be presented together with all power being cut to the associated heating element until such time as the temperature returned to within acceptable bounds.

Furthermore, all temperature controllers had a fail-safe design in that, should the control thermocouple fail entirely (i.e. register as a broken sensor on the controller), the unit would immediately cut power to its associated heating element. The possibility that the control thermocouple could be accidentally dislodged from its respective heating zone, resulting in run-away heating given that the controller would read a temperature not corresponding to that of the actual heated zone, was minimised with all thermocouples being well secured prior to operation. This was accomplished by either locking the thermocouples in position within specially designed fixtures (as was the case for the reactor and vaporiser heaters), or by securing the thermocouples with adhesive aluminium tape and subsequent layers of insulation. To ensure that all thermocouples were functioning as desired and neither damaged nor short circuiting, two separate thermocouples, included specifically for this purpose, were used to verify the temperatures of all heated zones on a regular basis to determine if any of the control thermocouples were malfunctioning.

If any thermocouple were to have been found to be loose or damaged in any way, it would have been immediately re-secured in position or replaced as necessary.

The possibility of ignition sources being formed by electrical short-circuiting was minimised by isolating the rig on its own circuit breaker, configured to "trip" should an earth-leakage of 30 mA or greater or an overcurrent of 20 A or greater occur.

Finally, despite all of the above precautions, the fume hood within which the rig was located was equipped with both hydrogen and smoke detectors to both sense and, where appropriate, automatically respond to any hazardous situations (as detailed in Section 5.8.1.1).

5.8.4 Features Facilitating Emergency Shutdown

To ensure that, should an emergency shutdown be required for any reason, all electricity and feed supplies to the rig could be cut with minimal effort, two measures were instituted. Firstly, electricity supplied to the rig was controlled by two switches, one within the fume hood beside the socket where the rig connected to the mains line and a second large, illuminated switch on the front face of the rig (illustrated in Figure 5.31). Turning off either of these switches, whichever being the most convenient in an emergency, would cut all power to the rig, stopping heating, gas flows beyond the mass flow controllers and pumping of liquid feed. Secondly, all nitrogen and hydrogen being fed to the rig was supplied by the house lines, with these flows being easily terminated by closing their respective gate valves where the rig connected to the house line manifold (such as that depicted in Figure 5.36a).

As such, turning off one switch and shutting off the two gate valves would immediately halt all heating, pressurisation and gas and liquid flows on the rig.

5.9 Final Flow Diagram

The final flow diagram of the experimental apparatus utilised for this investigation is presented in Figure 5.58.

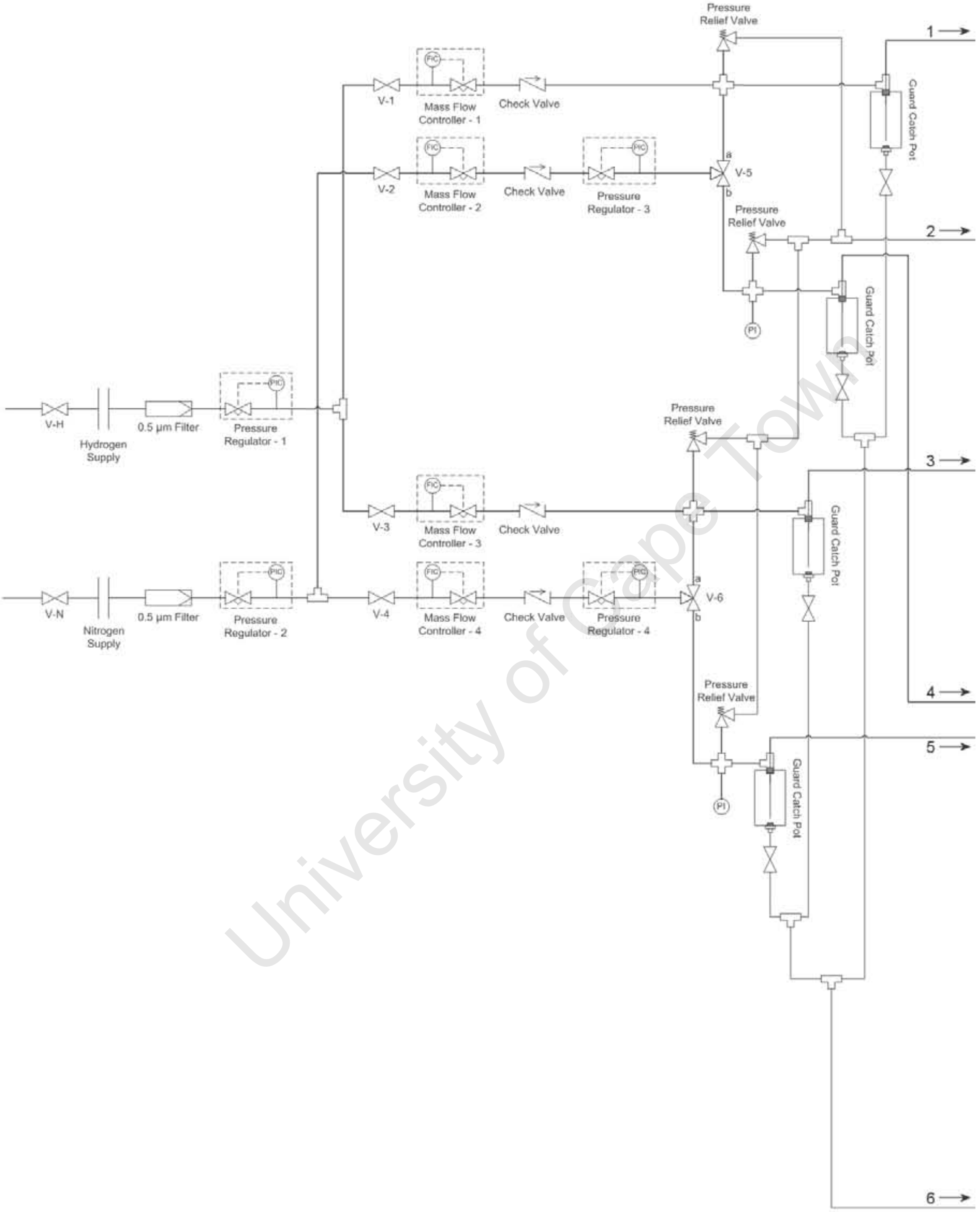
Pressure
Relief Valve
1 →
FIC
V-1
Mass Flow
Controller - 1
Check Valve
Guard Catch Pot
FIC
PIC
a
V-5
b
V-2
Mass Flow
Controller - 2
Check Valve
Pressure
Regulator - 3
Pressure
Relief Valve
2 →
Guard Catch Pot
PI
PIC
V-H
Hydrogen
Supply
0.5 µm Filter
Pressure
Regulator - 1
Pressure
Relief Valve
3 →
FIC
V-3
Mass Flow
Controller - 3
Check Valve
Guard Catch Pot
PIC
FIC
PIC
a
V-6
b
V-N
Nitrogen
Supply
0.5 µm Filter
Pressure
Regulator - 2
V-4
Mass Flow
Controller - 4
Check Valve
Pressure
Regulator - 4
Pressure
Relief Valve
4 →
5 →
PI
Guard Catch Pot
6 →

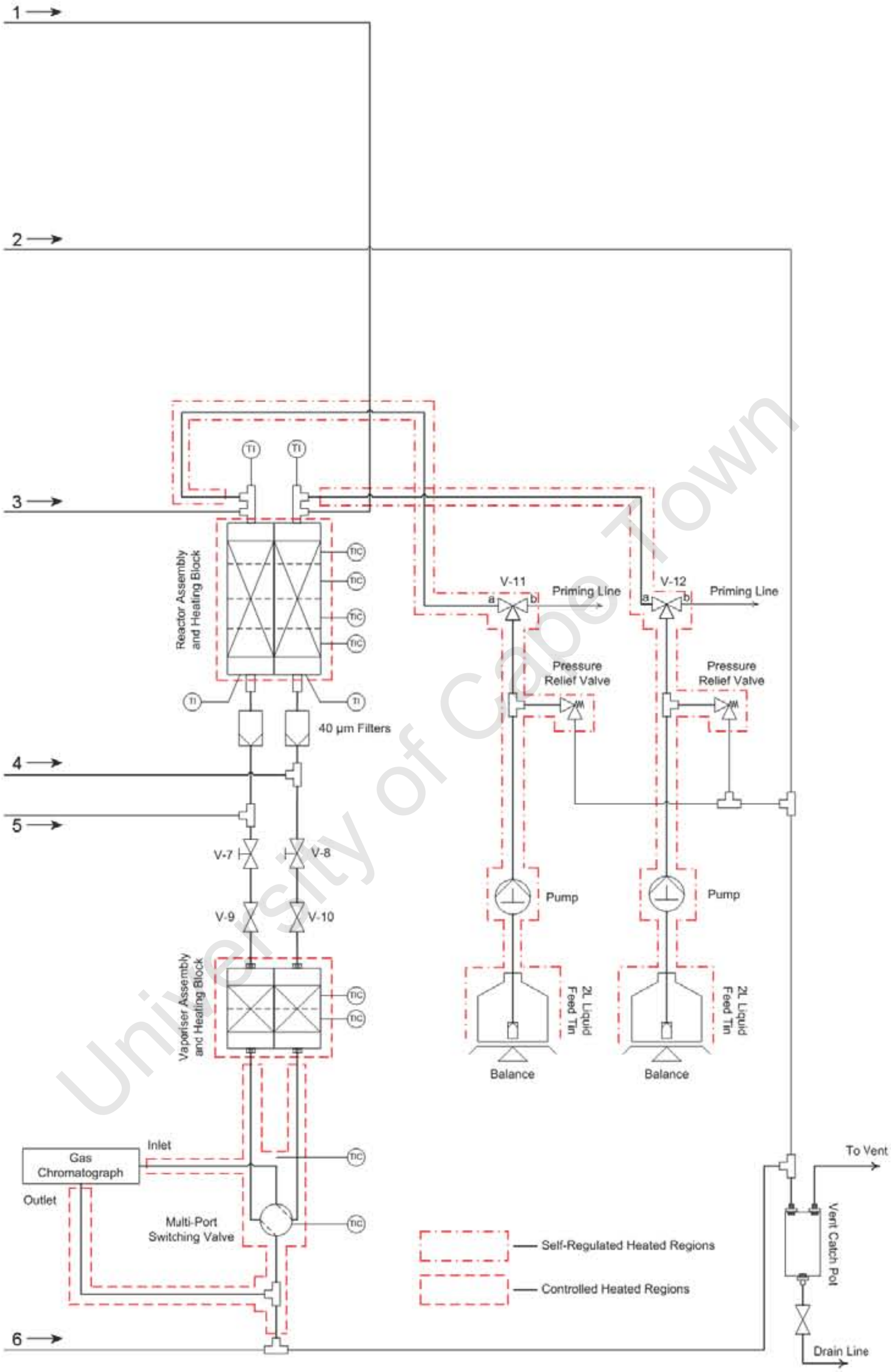

Figure 5.58: Flow Diagram of Experimental Apparatus

We learn by example and by direct experience
because there are real limits to the adequacy of verbal instruction.
Malcolm Gladwell

6

Experimental Programme and Operational Procedures

6.1 Catalysts to be Evaluated

The selection of acid zeolites to be utilised in this investigation was made based predominantly on the pore geometry of each in such a way so as to allow for overlap in both pore size and interconnectivity between samples, thereby facilitating a comparison regarding the effect of each of these properties. Furthermore, to mitigate the effect of variations in binder content and properties between the zeolites, all zeolites were obtained as binder-free powders which were pelletised as described in Section 6.1.1. To ensure that the unique pore structures and surface properties of each zeolite did not affect the dispersion or loading of the metal component, the platinum used in this investigation was obtained as a single batch supported on silica, with this ensuring that all catalyst charges would have identical metal loadings and dispersion.

6.1.1 Selection, Acquisition and Preparation of Catalysts

The four different acid zeolites chosen for this investigation, together with their suppliers and properties, are presented in Table 6.6, with the pore structures of each being discussed in Section 2.4.1.

The properties of the supported metal (5 wt% Pt/SiO_2) used are presented in Table 6.7.

Working with powdered catalysts was, however, seen to be impractical in the fixed bed reactor and as such, the zeolites, supported metal and diluent material (see Section 6.1.2) were pelletised separately to obtain particles with a size range of 500 - 800 μm. This particle size was selected as it:

- Minimised hydrodynamic wall effects by being $< 1/10$ the internal diameter of the reactor (15.75 mm) (Sinnot, 2005, Chapter 11)
- Reduced pressure drop over the reactor
- Made the catalyst easier to handle during loading and immobilise within the isothermal zone of the reactor.

This pelletisation was achieved by placing approximately 8g at a time of the co-catalyst or diluent to be pelletised in a stainless steel press-die and compressing the sample to 25 tons in a hydraulic press for 5 minutes, thereby forming a small "briquette". These briquettes were then carefully crushed and sieved into the desired size fraction and the pelletised catalysts stored within a desiccator to minimise moisture content.

6.1.2 Catalyst Properties and Characterisation

6.1.2.1 Zeolites

To accurately determine the effects of variations in the pore structure of the zeolite component in the system, detailed information regarding the acid site density of each zeolite was desired. This information, presented in Table 6.6, was of particular importance for, as may be seen, the zeolites obtained for this investigation differed not only in their pore structures, but in their SiO_2/Al_2O_3 ratios too. As discussed in Section 2.4.2, differences in SiO_2/Al_2O_3 ratios result in differences in overall acidity and hence activity. As accurate analytical data regarding the acidity of the zeolite samples to be utilised in this investigation was not initially available, catalyst charges were calculated based on the reported SiO_2/Al_2O_3 ratios, these being indicated in Table 6.6 together with the subsequently calculated "active acid site" densities. Each zeolite was later analysed for total aluminium content (using XRF) and for the ratio between tetrahedral and octahedral aluminium present (using solid state NMR). This data allowed for the determination of the number of Brønsted acid sites present for, whilst all aluminium is detected by XRF, NMR is able to distinguish between framework (tetrahedral) aluminium which contribute towards acid sites and extra-framework (octahedral) aluminium which generally exists as bulk Al_2O_3 on the surface, not contributing to zeolite acidity.

Thus, by relatively simple calculation, as indicated below, not only was the actual SiO_2/Al_2O_3 ratio determined from the molar densities of the silicon and aluminium (from XRF), but the density of "active acid sites" for each zeolite (i.e. the Brønsted acid sites which would participate in the reaction) was determined as the product of the total molar aluminium density (from XRF) and the molar ratio of tetrahedral to octahedral aluminium (from solid state NMR). This information was vital for determining the loading ratio of metal and acid co-catalysts as indicated in Section 6.1.3.

$$\begin{aligned}\mathrm{SiO_2/Al_2O_3\ Molar\ Ratio} &= 2 \times \left(\frac{mol_{Si}}{g_{Zeolite}} \bigg/ \frac{mol_{Al}}{g_{Zeolite}} \right) \\ \mathrm{Molar\ Acidity} &= \frac{mol_{Al}}{g_{Zeolite}} \times \frac{A_{Tetra}}{(A_{Tetra} + A_{Octa})}\end{aligned}$$

where

$\frac{mol_{Si}}{g_{Zeolite}}$ and $\frac{mol_{Al}}{g_{Zeolite}}$ = Molar density of silicon and aluminium per gram of zeolite respectively, as determined by XRF

A_{Tetra} and A_{Octa} = Relative areas of tetra- and octa-hedral oriented aluminium respectively within the zeolite sample as determined by solid state NMR

All data analysis was performed based on the acid site densities determined analytically and not on the initially assumed values. It should be noted that the large variations between the assumed SiO_2/Al_2O_3 ratios and the analytical was due to the initial assumptions being based on the product designations (e.g. H-MFI-90 having a SiO_2/Al_2O_3 ratio of 90), with these designations being only rough indications and hence NOT indicative of actual product analyses.

6.1.2.2 Supported Metal

It was decided to utilise platinum as the metal co-catalyst in this investigation for three reasons. Firstly, platinum is well known to exhibit a great degree of de-hydrogenation and re-hydrogenation activity (required in the reaction as discussed in Section 2.2) (Sinfelt, 1973), thus ensuring that it would be active at the relatively mild conditions utilised in this investigation (see Section 6.2). Secondly, whilst all noble metals exhibit some degree of monofunctional hydrocracking (see Section 2.2.3), Pt is known to be less active in this regard than other noble metals such as Ir or Rh (Sinfelt, 1973) and furthermore is known to produce a non-bond specific cracking product (i.e. yielding a wide distribution of primary cracking products with relatively equivalent molar selectivities to each) (Sinfelt, 1973). Thus, should all catalyst charges utilise the same amount of supported Pt, the yield of products formed by the metal's inherent hydrogenolysis reaction should be minimal (given the equal carbon number distribution of products, as illustrated in Section 2.2.3, and the relatively mild operating conditions) and identical for all investigations, with any variations being due to the zeolite itself. It was thus decided to use Pt in this investigation. Finally, on the topic of catalyst loading, it was decided (as discussed in Section 6.1.3) to make use of the results obtained by Alvarez *et al.* (1996) (see Section 2.4.2) utilising various weight loadings of Pt on H-Y as a guide (despite the conditions implemented by Alvarez *et al.* (1996) differing from those in this investigation, with Alvarez *et al.* (1996) feeding n-decane to a system operating at 200°C and a total pressure of 1 bar, with a H_2:hydrocarbon molar feed ratio of 9), choosing an active metal to active acid site ratio of 0.187, this being approximately 10% higher than the upper end of the transition region reported by Alvarez *et al.* (1996), so as to ensure that the metal function was in excess and only the acid function was controlling in the reaction.

Pending accurate analytical data regarding the properties of the supported platinum utilised in this investigation, a metal dispersion of 90% was assumed (as indicated in Table 6.7 together with the subsequently calculated metal crystallite size and active metal site density) for the purposes of calculating catalyst charges, with this being a value typical for highly dispersed industrial supported Pt catalysts. Later analysis of the supported Pt, however, indicated that this laboratory specimen was far more robust than anticipated, with larger Pt crystallites and hence a lower dispersion. These properties of the supported Pt utilised in this investigation, presented in Table 6.7, were obtained by CO chemisorption, yielding information regarding metal dispersion, crystallite size and "active metal site" density (these being those metal atoms present on the surface of the crystallites), with the MATLAB script utilised for this analysis being provided in Appendix A.3. In essence, these calculations were conducted by assuming spherical metal crystallites and mono-functional adsorption of the CO onto the metal surface, i.e. that every molecule of CO adsorbed corresponded to a single active metal site. This information, together with the actual acid site density of each zeolite, was required to determine the actual catalyst loadings (see Section 6.1.3).

6.1.2.3 Catalyst Bed Diluent

As indicated in Section 2.2.2, the hydrogen spillover phenomenon is believed to require the surface diffusion of the activated hydrogen species. The experimental technique in this investigation, i.e. the loading of a catalyst bed consisting of separately pelletised supported metal and acid zeolite co-catalysts, relies on this phenomenon, and it was thus decided to use a catalyst bed diluent material (required as discussed in Section 6.1.3) known to have a high surface area so as to promote the aforementioned surface diffusion. As such, SiO_2, from the same batch used in the preparation of the Pt/SiO_2, was employed in this regard as it not only afforded the desired high surface area for the surface diffusion of activated hydrogen species, but would maintain consistency in the properties of the surface across which such species must migrate.

6.1.3 Determination of Catalyst Loadings

The catalyst loading calculations were subject to three criteria:

- The proportions of metal and acid co-catalysts must be such so as to ensure that neither of these functions were limiting in the bifunctional reaction
- The entire catalyst bed must fit within the isothermal zone of the reactor
- The volume of the catalyst beds must, in so far as possible, be kept constant so as to minimise the variations caused by changes in the intra-bed hydrodynamic flow.

Work by Alvarez *et al.* (1996) quantified the relationship between the ratio of active metal and active acid sites within the bifunctional hydroconversion of n-decane over Pt/H-Y at 200°C and 1 bar. Therein it was indicated that a metal:acid site ratio (i.e. the molar ratio of active metal to active acid sites) of at least 0.17 was required so as to ensure that the acid co-catalyst was limiting in the reaction. Since, in this investigation, a significantly higher hydrogen pressure and high hydrogen excess were applied (see Table 6.11), a metal:acid site ratio of 0.187 was considered to be more than sufficient and was utilised in the loading calculations, with this value being selected so as not to allow for any significant degree of consecutive reaction. Furthermore, for all loadings (calculated based on the assumed active acid and active metal site densities), the number of each of the active metal and active acid sites within the reactor was intended to be constant, corresponding to the same mass of supported metal, but varying masses of zeolite (given the unique acid site density of each, see Table 6.6).

Table 6.6: Properties of the Zeolites Utilised in this Investigation

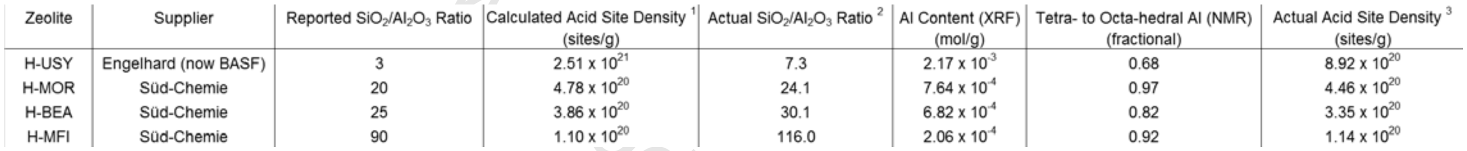

Zeolite	Supplier	Reported SiO_2/Al_2O_3 Ratio	Calculated Acid Site Density [1] (sites/g)	Actual SiO_2/Al_2O_3 Ratio [2]	Al Content (XRF) (mol/g)	Tetra- to Octa-hedral Al (NMR) (fractional)	Actual Acid Site Density [3] (sites/g)
H-USY	Engelhard (now BASF)	3	2.51×10^{21}	7.3	2.17×10^{-3}	0.68	8.92×10^{20}
H-MOR	Süd-Chemie	20	4.78×10^{20}	24.1	7.64×10^{-4}	0.97	4.46×10^{20}
H-BEA	Süd-Chemie	25	3.86×10^{20}	30.1	6.82×10^{-4}	0.82	3.35×10^{20}
H-MFI	Süd-Chemie	90	1.10×10^{20}	116.0	2.06×10^{-4}	0.92	1.14×10^{20}

1 - Determined based on the “reported” SiO_2/Al_2O_3 ratios
2 - Actual SiO_2/Al_2O_3 ratio calculated based on aluminium and silicon content determined by XRF
3 - The number of active acid sites (see Section 6.1.2.1) per gram of zeolite

Table 6.7: Properties of the Supported Metal Utilised in this Investigation

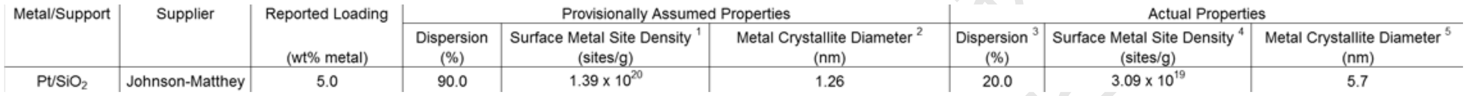

Metal/Support	Supplier	Reported Loading	Provisionally Assumed Properties			Actual Properties		
		(wt% metal)	Dispersion (%)	Surface Metal Site Density [1] (sites/g)	Metal Crystallite Diameter [2] (nm)	Dispersion [3] (%)	Surface Metal Site Density [4] (sites/g)	Metal Crystallite Diameter [5] (nm)
Pt/SiO_2	Johnson-Matthey	5.0	90.0	1.39×10^{20}	1.26	20.0	3.09×10^{19}	5.7

1 - The actual number of active surface sites calculated based on assumed dispersion
2 - Calculated based on the provisionally assumed dispersion
3 - Dispersion as determined by CO chemisorption
4 - The actual number of active surface sites (see Section 6.1.2.2) per gram of supported metal
5 - Metal crystallite diameter as calculated based on actual dispersion (see Section 6.1.2.2)

It should, however, be noted that the metal:acid site ratio range determined by Alvarez *et al.* (1996) holds specifically for the activity of the individual acid sites of the H-Y utilised in that work, corresponding to the balance between the rate at which dehydrogenated feed (in terms of the classical mechanism) or activated hydrogen species (in terms of the spillover mechanism) formed on active sites of the metal are supplied to, and consumed by, the acid sites of the zeolite. With equal ratios being utilised for all of the zeolites employed in this investigation, should the activity of the individual acid sites of the H-MFI-90, H-BEA-25, H-USY or H-MOR-20 be significantly higher than those of the H-Y used by Alvarez *et al.* (1996), so the implemented metal:acid site ratio of 0.187, despite being in 10% excess, may be insufficient, resulting in the metal co-catalyst being limiting, resulting in a greater extent of consecutive cracking (manifesting, for example, as a product spectrum shift toward lighter fragments).

In terms of the catalyst quantities to be loaded, the sheer size of the isothermal zone within the reactors, being approximately 18 cm long with a volume of 35 cm^3 (being the volume of the reactor over the given length less the volume of the central thermowell), ensured that a large range of catalyst bed volumes could be accommodated with ease. As such, an initial catalyst loading volume of 3.5 cm^3 was selected for the simple reason that it implied supported metal and zeolite masses which could be weighed with a relatively low uncertainty (with the loading masses being presented in Table 6.8) whilst not consuming significant amounts of either catalyst or feedstock.

Finally, so as to minimise the effect of hydrodynamic flow variations (resulting from differences in catalyst bed volumes) on the reaction, initial catalyst loadings were calculated to ensure the same bulk volume, with variations arising from different zeolite loadings (due to different acid site densities) being accounted for using pelletised SiO_2 as a catalyst bed diluent.

From Table 6.8, it may be noted that H-MOR and H-USY were analysed twice, initially highly diluted with the same small bed volumes and total active site loadings as the H-MFI and H-BEA and then with a far larger catalyst charge (although with these second, larger charges of H-MOR and H-USY having the same bed volumes and total active site loadings as one another and the same metal:acid site ratios as all of the other catalyst loadings investigated). This double analysis was required for the sole reason that the initial loading could not be exposed to a space velocity sufficiently low so as to achieve the desired levels of conversion (due to the lower limitation of the feed pump flow rate).

Thus, utilising the calculation methods presented in Appendix A.3, the loading masses presented in Table 6.8 were determined.

6.2 Reaction Condition Selection

With this research focussed ultimately on the conversion of an FT wax feed, it stands to reason that reaction conditions as close as possible to a wax selective FT synthesis reactor would be desirable as this would not only correspond to reduced costs in an industrial setting (as the processing of the effluent from the FT reactor to conditions suitable for feeding into the hydrocracking reactor would be minimal), but would support the possibility of incorporating both the FT and hydrocracking catalysts within a single reactor.

As such, given the range of temperatures indicated to be utilised in all-wax FT operation, i.e. 200 - 250°C (Dry, 2001), the upper bound of 250°C was selected for this investigation, predominantly so as to promote the overall rate of reaction.

A wide range of operating pressures and hydrogen:hydrocarbon feed ratios were found to have been utilised by researchers in this field, with a selection of these being summarised in Table 6.9. With these ranges in mind, an operating pressure of 40 bar and a hydrogen:hydrocarbon ratio of 10:1 were selected, with the full set of operating conditions utilised in this investigation being presented in Table 6.10.

Table 6.8: Catalyst Loading Masses

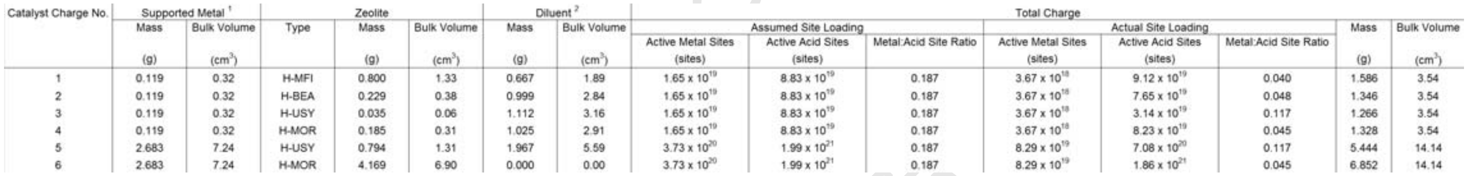

Catalyst Charge No.	Supported Metal [1]		Zeolite			Diluent [2]		Total Charge							
	Mass	Bulk Volume	Type	Mass	Bulk Volume	Mass	Bulk Volume	Assumed Site Loading			Actual Site Loading			Mass	Bulk Volume
								Active Metal Sites	Active Acid Sites	Metal:Acid Site Ratio	Active Metal Sites	Active Acid Sites	Metal:Acid Site Ratio		
	(g)	(cm^3)		(g)	(cm^3)	(g)	(cm^3)	(sites)	(sites)		(sites)	(sites)		(g)	(cm^3)
1	0.119	0.32	H-MFI	0.800	1.33	0.667	1.89	1.65×10^{19}	8.83×10^{19}	0.187	3.67×10^{18}	9.12×10^{19}	0.040	1.586	3.54
2	0.119	0.32	H-BEA	0.229	0.38	0.999	2.84	1.65×10^{19}	8.83×10^{19}	0.187	3.67×10^{18}	7.65×10^{19}	0.048	1.346	3.54
3	0.119	0.32	H-USY	0.035	0.06	1.112	3.16	1.65×10^{19}	8.83×10^{19}	0.187	3.67×10^{18}	3.14×10^{19}	0.117	1.266	3.54
4	0.119	0.32	H-MOR	0.185	0.31	1.025	2.91	1.65×10^{19}	8.83×10^{19}	0.187	3.67×10^{18}	8.23×10^{19}	0.045	1.328	3.54
5	2.683	7.24	H-USY	0.794	1.31	1.967	5.59	3.73×10^{20}	1.99×10^{21}	0.187	8.29×10^{19}	7.08×10^{20}	0.117	5.444	14.14
6	2.683	7.24	H-MOR	4.169	6.90	0.000	0.00	3.73×10^{20}	1.99×10^{21}	0.187	8.29×10^{19}	1.86×10^{21}	0.045	6.852	14.14

1 - Samples from a single batch of 5 wt% Pt/SiO_2 (see Table 6.7) were used for all investigations

2 - Samples of SiO_2 from the same batch used for the supported metal preparation were used for all investigations

Table 6.9: Hydrocracking Operating Conditions as Utilised by Previous Researchers

Researchers	Feedstock	Catalyst	Operating Conditions		
			Temperature (°C)	Pressure (bar)	Hydrogen:Hydrocarbon (molar feed ratio)
Steijns *et al.*, 1981	n-C_{10} and n-C_{11}	Pt/H-USY	130 to 250	5 to 100	~ 10 to 65 (10 to 60 : 2 to 80 dm^3/cm^3)
Martens *et al.*, 2000	n-C_8 to n-C_{12}	Pt/H-USY	220 to 260	5 to 50	30 to 300
Chavarria *et al.*, 2004	n-C_{16}	Mo/H-β-Alumina	260 to 325	48	5
Thybaut *et al.*, 2006	Mixed n-C_9 to n-C_{14}	Pt/H-USY	230 to 260	10 to 77	3 to 300
Leckel, 2007	n-C16 and LTFT wax	Pt-W/SiO_2-Al_2O_3	340 to 380	50	~ 13 for n-C_{16} (1000:1 m^3/m^3)

Table 6.10: Experimental Conditions Utilised in this Investigation

Temperature	(°C)	250
Total Pressure	(bar)	40
H_2:C_{16} Feed Ratio	(molar)	10 : 1

6.3 Experimental Programme

As it was desired to compare not only the overall activity of each zeolite, but the associated branching selectivities and carbon number distributions (as indicated in Section 4.3), it was necessary to evaluate each catalyst charge under a range of space velocities with this range yielding combined conversion and selectivity data. Utilising this information, the data was to be projected as necessary to allow for the selectivities of all of the zeolites to be compared at the same total conversion.

Table 6.11 provides a list of the feed and dilution flow rates, together with the associated space velocities, utilised in this investigation. Note that the data in this table was compiled retrospectively with the initial n-C_{16} flow rate of 0.06 ml/min (for all investigations) and the associated hydrogen flow rate being altered only after the preliminary induction period of 48 hrs (see Section 6.4.1) by either reducing the flow to reduce the space velocity (should the conversion be observed to be too low) or increasing the flow to increase the space velocity (should the conversion be observed to be too high). Furthermore, analogously to the catalyst being loaded on an active site basis, so the space velocities are presented in terms of the molar flow of hydrocarbon feed to the total moles of acid sites within the catalyst charge, an "acid site hourly space velocity" (SHSV), i.e. $\frac{\text{moles }_{\text{n-C}_{16}}}{\text{moles }_{\text{Acid Sites}} \times \text{hr}}$ (with the number of acid sites for each catalyst charge indicated in Table 6.8).

Table 6.11: Experimental Programme (for catalyst charges, refer to Table 6.8)

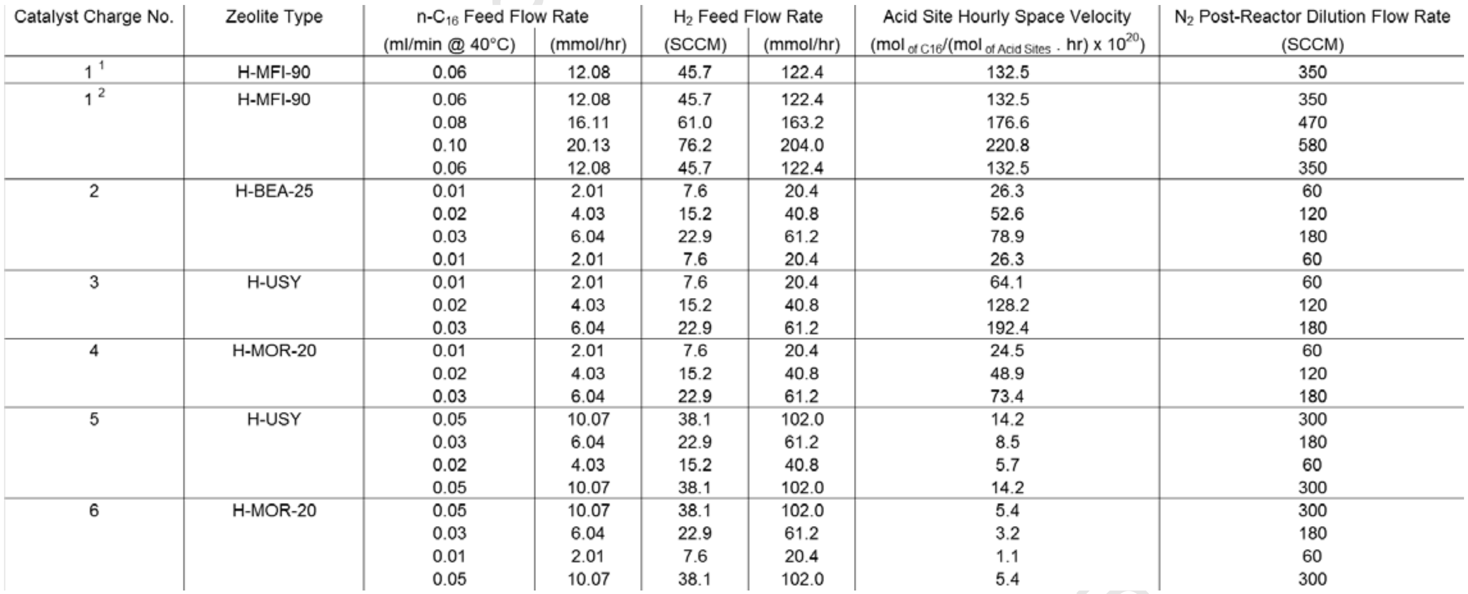

Catalyst Charge No.	Zeolite Type	n-C_{16} Feed Flow Rate		H_2 Feed Flow Rate		Acid Site Hourly Space Velocity	N_2 Post-Reactor Dilution Flow Rate
		(ml/min @ 40°C)	(mmol/hr)	(SCCM)	(mmol/hr)	(mol $_{\text{of C16}}$/(mol $_{\text{of Acid Sites}}$. hr) x 10^{20})	(SCCM)
1 [1]	H-MFI-90	0.06	12.08	45.7	122.4	132.5	350
1 [2]	H-MFI-90	0.06	12.08	45.7	122.4	132.5	350
		0.08	16.11	61.0	163.2	176.6	470
		0.10	20.13	76.2	204.0	220.8	580
		0.06	12.08	45.7	122.4	132.5	350
2	H-BEA-25	0.01	2.01	7.6	20.4	26.3	60
		0.02	4.03	15.2	40.8	52.6	120
		0.03	6.04	22.9	61.2	78.9	180
		0.01	2.01	7.6	20.4	26.3	60
3	H-USY	0.01	2.01	7.6	20.4	64.1	60
		0.02	4.03	15.2	40.8	128.2	120
		0.03	6.04	22.9	61.2	192.4	180
4	H-MOR-20	0.01	2.01	7.6	20.4	24.5	60
		0.02	4.03	15.2	40.8	48.9	120
		0.03	6.04	22.9	61.2	73.4	180
5	H-USY	0.05	10.07	38.1	102.0	14.2	300
		0.03	6.04	22.9	61.2	8.5	180
		0.02	4.03	15.2	40.8	5.7	60
		0.05	10.07	38.1	102.0	14.2	300
6	H-MOR-20	0.05	10.07	38.1	102.0	5.4	300
		0.03	6.04	22.9	61.2	3.2	180
		0.01	2.01	7.6	20.4	1.1	60
		0.05	10.07	38.1	102.0	5.4	300

1 - Identical charges loaded into both reactors for initial inter-reactor comparison and induction time determination
2 - Reloaded charge for comparison with other zeolites

6.4 Operating Procedures

The step-by-step start-up and normal operating procedures for the rig are presented in Section 6.4.1, with shutdown and emergency shutdown procedures covered in Sections 6.4.2 and 6.4.3 respectively. Detailed procedures relating to the catalyst loading, reduction and removal are presented in Section 6.4.4. All procedures refer to the flow sheet presented in Figure 5.58.

6.4.1 Start-up, Sampling and Space Velocity Change

1. Begin with the reactors empty and clean (details of reactor removal, emptying and cleaning are provided in Sections 6.4.2 and 6.4.4.3)
2. Load both reactors with the desired catalyst charges using the method detailed in Section 6.4.4.1
3. Place both reactors into their respective slots in the brass housing
4. Raise the brass housing into its vertical position and secure
5. Insert the appropriate thermocouple into the central thermowell of each reactor, adjusting to ensure that the tip of each thermocouple is located roughly in the centre of the catalyst bed (i.e. approximately 12 cm from the base of the reactor)
6. Loosely connect the gas and liquid inlet ports and the outlet ports, ensuring that the VCR gaskets are present in the fittings and are new or in good condition
7. Adjust the reactors slightly to ensure all lines connect without bending or stressing adjacent connections
8. Tighten the inlet and outlet fittings
9. Ensure that all guard catch pots are empty by opening the drain valves to each
10. Close all guard catch pot drain valves
11. Open nitrogen and hydrogen house gas lines (valves V-N and V-H respectively) and check supply pressure
12. Check the outlet pressure of pressure regulators 1 and 2 to ensure MFCs 1 through 4 are supplied with 50 bar
13. Open valves V-2 and V-4 and set V-5 and V-6 to position a, thereby allowing nitrogen to enter the top of the reactor when MFCs 2 and 4 are set to allow flow (this is necessary to ensure that the initial gas flow settles the packed bed rather than blowing it up the reactor and into the feed lines)
14. Close valves V-9 and V-10 on the reactor effluent lines
15. Set nitrogen flow on MFCs 2 and 4 to 100 ml/min to begin pressurising reactor
16. Ensure the pressure of both reactors is stable at the desired 40 bar (note that if the MFCs indicate a non-zero flow, there is a leak, see Step 16(a)ii)
    (a) If the pressure is too low, increase using pressure regulator 3 or 4 for the left or right reactor respectively
        i. If the pressure remains too low, verify that the inlet pressure on regulator 2 is approximately 100 bar (the normal house gas line pressure) and that the outlet to the MFCs is approximately 50 bar

ii. Use Swagelok Snoop to check all fittings on the rig, particularly the VCR fittings for the reactor inlets and outlets. If a fitting is found to be leaking:
    A. Attempt to tighten the fitting to stop the leak
    B. If the leak persists, depressurise the system as discussed in Section 6.4.2, clean the fitting and, in the case of a VCR fitting, replace the gasket
    C. If the leak is still not solved, depressurise the system and replace the fitting entirely

(b) If the pressure is too high, reduce the pressure using pressure regulators 3 or 4 for the left or right reactor respectively and briefly open valves V-9 or V-10 to drop the pressure in that reactor to below 40 bar

17. Set MFCs 2 and 4 to 100% flow such that they function as mass flow indicators instead of controllers

18. Set the temperature of all four reactor zones to 50°C

19. Set the temperature of the top vaporiser zone to 260°C and the bottom to 290°C (as discussed in Section 5.7.1.3) if the vaporiser is not already at temperature from a previous run

20. Set the effluent line temperature to 250°C if it is not already at temperature from a previous run

21. Set the multi-port switching valve temperature to 180°C if it is not already at temperature from a previous run

22. Turn on the power to the balances, pumps and hydrocarbon feed heating lines

23. Check the level of feed in the feed tins and record the masses

24. Set valves V-11 and V-12 to position b and prime the pumps for 60 seconds

25. Set valves V-11 and V-12 to position a to allow to the reactors

26. Carefully close the metering valves (V-7 and V-8) on the reactor effluent lines (**note that tightening these valves too much will damage them**)

27. Open valves V-9 and V-10 on the reactor effluent lines

28. Carefully adjust valves V-7 and V-8 to achieve a nitrogen flow rate of approximately 300 ml/min

29. Allow the system to stabilise for approximately 1 hr (to ensure nitrogen flow is stable and to allow heating elements to reach their desired temperatures)

30. Open valves V-1 and V-3 to allow hydrogen to enter the top of the reactor

31. Set the hydrogen flow rate on MFCs 1 and 3 to 30 ml/min (i.e. to allow for a gas flow 10% H_2 in N_2 to flow over the catalyst)

32. Allow flows to stabilise (the nitrogen flow will adjust itself to approximately 270 ml/min, if not, adjust valves V-7 and V-8 as appropriate)

33. Begin the catalyst reduction procedure detailed in Section 6.4.4.2

34. Set the hydrogen flow rate on MFCs 1 and 3 to that desired for the first space velocity for the left and right reactors respectively (as per Section 6.3)

35. Adjust valves V-7 and V-8 to obtain the desired nitrogen dilution flow rate

36. Allow the gas flows to stabilise

37. Set the pumps to the desired C_{16} flow rates (as per Section 6.3) and begin pumping
38. Record the start time of the run
39. Allow the system to run for approximately 48 hrs before sampling. This induction period was found to be necessary for the catalyst to "settle in" and reach a steady state
40. Sampling utilising this system is a relatively automated process
    (a) Ensure that the multi-port switching valve is set to the desired reactor output
    (b) Ensure that the CO_2 cylinder and supply valve are open
    (c) Instruct the GC to execute the sampling as per the method described in Table 5.3
    (d) If desired, create an analysis sequence for greater autonomy
41. Once the desired number of data-points for the current space velocity has been obtained:
    (a) Set the C_{16} and nitrogen flows to that of the next desired space velocity (as per Section 6.3)
    (b) Adjust valves V-7 and V-8 to achieve the desired nitrogen dilution flow rate
    (c) Allow the system to stabilise for at least 24 hrs before sampling
    (d) Return to Step 40
42. When all space velocities have been run, begin rig shutdown as per Section 6.4.2

6.4.2 Normal Shutdown

Should the reactors need to be removed (Start-up step 1), a persistent leak be encountered (Start-up step 16(a)iiB) or when all analyses for the current catalyst charge are completed (Start-up step 42), begin the standard shutdown procedure.

1. Shut off C_{16} flow on the pumps
2. Shut off hydrogen flows on MFCs 1 and 3
3. Close valves V-H, V-1 and V-3 to halt hydrogen supply
4. Set nitrogen flow rates to 100 ml/min on MFCs 2 and 4
5. Set valves V-5 and V-6 to position a so as to flow nitrogen into the top of the reactor (this will purge any hydrogen, gaseous hydrocarbons and most of the liquid hydrocarbons from the reactor)
6. Open valves V-7 and V-8 by two or three complete turns (this will help speed depressurisation of the system)
7. Shut off the appropriate heating and power:
    (a) If the reactor is to be reloaded immediately, shut off only the reactor heating
    (b) If the system will be off-line for a long period of time, shut off heating to the reactor, vaporiser, effluent line and multi-port switching valve (if necessary and if not in use by adjacent unit). Also shut off power to the balances, pumps and feed heating lines
8. Allow the system to cool and depressurise
9. Shut off the nitrogen flows on MFCs 2 and 4
10. Close valves V-N, V-2 and V-4 to halt nitrogen supply

11. Empty the liquid in the vent catch pot into a suitable container for disposal
12. Open the drain valves of the feed line guard catch pots one at a time
    (a) If liquid drains from a feed line guard catch pot, evaluate the situation and check suspect lines and valves for blockages
    (b) Clear blockages and clean or replace any faulty valves
13. Close the vent catch pot drain valve but leave the feed line guard catch pot drain valves open (to completely clear any liquid)
14. Disconnect the input and outlet VCR connections to the reactors
15. Lift the reactors slightly inside the brass housing to clear the outlet connections
16. Supporting the brass block, unhook the fastening hooks and gently lean the unit outwards
17. Gently but firmly, pull the reactors out of the brass housing
18. Empty and clean the reactors as described in Section 6.4.4.3

6.4.3 Emergency Shutdown

Should it be required at any time, this two-step procedure will halt all gas flows and electrical power to the rig.

1. Turn off the main illuminated power switch on the front panel (Figure 5.31). This will shut off all power to the rig including shutting off flow through the MFCs
2. Turn off the hydrogen and nitrogen house line supply valves (V-H and V-N) to the rig

6.4.4 Details of Catalyst Handling Procedures

6.4.4.1 Reactor Loading

When the loading of the reactors is required, as per Start-up step 2, the following procedure is followed.

1. Secure the reactor in a vice using an appropriate adapter so as to prevent damage to the unit
2. A small plug of silane treated glass wool is placed around the central thermowell and pushed to the bottom to cover the outlet port
3. SiC is added, with gentle tapping to help settle the bed, to a height of 40 cm below the upper lip of the reactor (i.e. the beginning of the isothermal zone)
4. Weigh the appropriate amounts of pelletised catalyst components (supported metal, zeolite and silica diluent) as indicated in Table 6.8 and physically mix them in a small container
5. Pour the mixed catalyst into the reactor and gently tapped to help the bed settle evenly
6. Fill the reactor to within approximately 1 cm of the top with SiC, again tapping gently to facilitate settling
7. Fill the remaining 1 cm gap with pelletised silica as this affords a small bed of high surface area material into which the liquid feed tube will protrude, further facilitating the dispersal of the liquid hydrocarbon across the reactor cross-section and its mixing with the hydrogen

8. Ensure that the VCR fittings are clean
9. Loosely fit the reactor head, ensuring the gasket is present and in good condition or new
10. If the head does not screw on easily and smoothly, particularly if it feels as though there is grit on the thread, remove the head immediately and clean the thread, applying high-temperature copper lubricating paste as necessary. Note that forcing the head on when SiC is trapped in the thread will permanently damage the fitting!
11. Tighten the VCR fitting to secure the reactor head
12. Release the reactor from the vice and repeat for the second reactor if necessary

6.4.4.2 Catalyst Reduction

Continuing from start-up step 6.4.4.2, catalyst reduction is conducted as described below.

1. Ensure that the gas flow of 10% hydrogen in nitrogen (30 ml/min H_2 and 270 ml/min N_2) is stable
2. Set the controller setpoint temperature of the topmost heating element to 236°C (note that this zone is sufficiently small and distanced so as to have only a minimal effect on heating up the catalyst bed at this stage)
3. Execute the following temperature ramping programme on the remaining three heating elements using the appropriate temperature controller settings as indicated in Table 5.4:
    (a) Hold the temperature at 50°C for 15 mins
    (b) Ramp to 100°C in 10 mins (5°C/min) and hold for 15 mins
    (c) Ramp to 150°C in 10 mins (5°C/min) and hold for 15 mins
    (d) Ramp to 200°C in 10 mins (5°C/min) and hold for 15 mins
    (e) Ramp to 250°C in 10 mins (5°C/min) and hold for 15 mins
    (f) Ramp to 300°C in 10 mins (5°C/min) and hold for 15 mins
    (g) Ramp to 350°C in 10 mins (5°C/min) and hold for 16 hrs
4. Set valves V-5 and V-6 to position b, such that the nitrogen flow is diverted to post-reactor dilution, resulting in pure hydrogen flowing over the catalyst bed
5. Increase the hydrogen flow rate to 100 ml/min on MFCs 1 and 3
6. Hold these conditions (350°C and 100 ml/min pure hydrogen) for 1 hr. This will ensure that the reduction is complete
7. Drop the temperature to the desired reaction temperature of 250°C
8. Allow the temperature to stabilise for approximately 1.5 hrs

Note that the 15 minute holding times during the ramping programme are to ensure that the catalyst bed heats up at approximately the desired rate for there exists a slight time delay in the heating between that measured by the controller thermocouple and that of the isothermal zone within the reactor (as discussed in Section 5.7.1.2).

6.4.4.3 Reactor Charge Removal

The removal of the spent catalyst and reactor packing together with the cleaning of the reactor, as required during Shutdown step 18, are discussed below.

1. Position the reactor in a vice using an appropriate adapter to prevent damaging the unit
2. Loosen and remove the reactor head
3. Remove the reactor body from the vice and, with gentle tapping, empty the spent catalyst and SiC into a container for disposal
4. Holding the reactor upside down, use compressed air fed into the outlet to force out the silane treated glass wool plug
5. Rinse the reactor head and body with acetone, taking special care to clean the thread and VCR sealing ridges, to remove residual hydrocarbons and particulate matter
6. Allow the reactor to dry

6.5 Chromatographic Analysis

6.5.1 Peak Identification

A sample chromatogram obtained from the system (see Section 5.6.2 for details of the GC analysis) is provided in Figure 6.59, with magnified views of select retention time ranges in Figures 6.60 and 6.61. As may be seen, the task of isolating and identifying individual component peaks becomes, as expected, progressively more difficult as the carbon number increases, being almost impossible above a carbon number of about 8. This is due primarily to the sheer number of isomers (reaching in excess of 10,000 for C_{16}, not including stereoisomers (AT&T, 2005)) and the inherent similarities in the retention indices of many of these species within each carbon number through the column and under the conditions utilised in product analysis in this investigation.

As such, to facilitate identification of these species, a GC Mass Spectrometry (GC-MS) analysis of the product was conducted. However, as the system was designed for on-line sampling, this analysis was performed on two separate samples, one being a liquid sample obtained from the liquid collected in the vent catch pot and one being a gas sample obtained from the vent line exiting the vent guard catch pot. As these analyses were solely to identify the elution order and approximate retention times of the various product components, that the samples were obtained from the mixed waste product stream of both reactors was considered to be inconsequential. These samples were analysed on a GC-MS equipped with a column identical to that utilised in the on-line sampling GC, operating under identical conditions (with the sole difference being the use of He as the carrier gas instead of H_2 as per the on-line GC) and with the same temperature ramping programme (see Section 5.6.2). The data obtained, by virtue of the overlap by which some species were present in both the liquid and gas samples, was collated to obtain a single, continuous, digital spectrum comprising all of the product species.

From this spectrum, it was determined that the various products elute in a particular sequence within each carbon number fraction, identifiable by the larger-than-average linear hydrocarbon peaks (see Figure 6.59), and may thus be grouped according to their degree of branching as indicated by the annotation to the chromatogram in Figure 6.61. Herewith it may be seen that the paraffinic species of any particular hydrocarbon number elute in three groups, with multi-methyl and higher (e.g. ethyl) branched isomers first (denoted by "Higher-i-C_x"), followed by mono-methyl isomers (denoted by "Mono-i-C_x") and finally the linear paraffin.

Such a pattern would, however, be influenced by the presence of any olefinic products which are known to elute in close proximity, both before and after, their respective saturated counterparts. An examination of

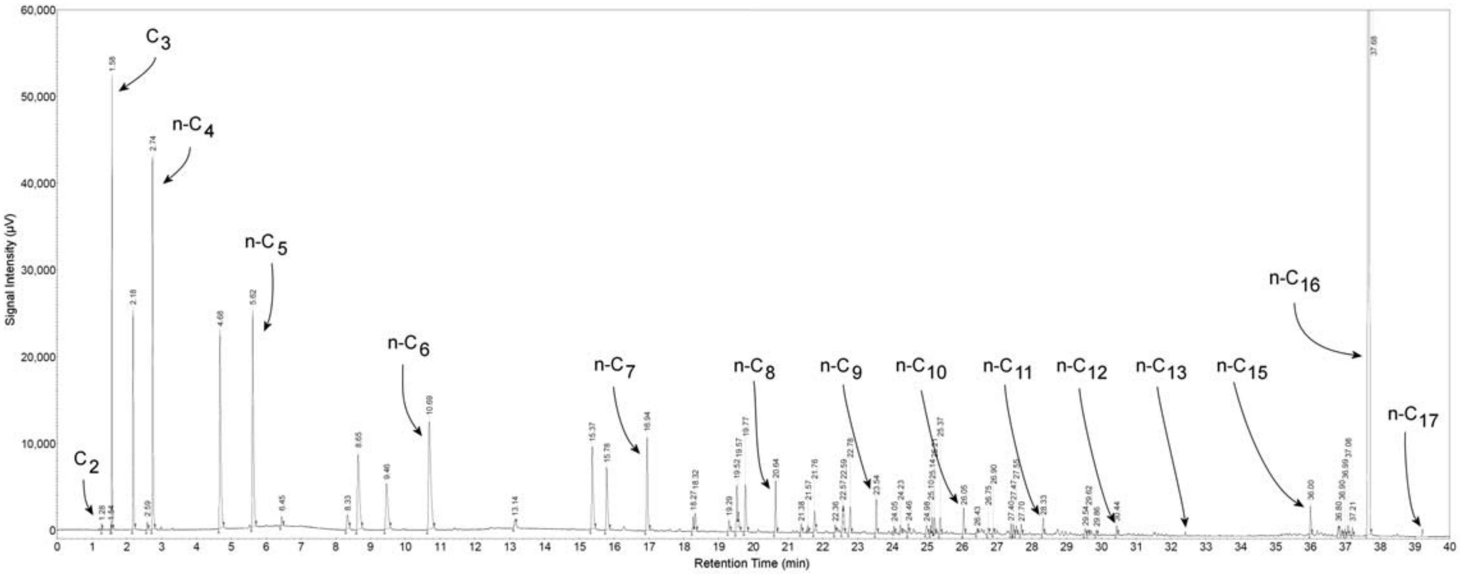

Figure 6.59: Sample Chromatogram Obtained for the System with a Loading of 0.800g H-MFI-90, 0.119g 5wt% Pt/SiO_2 and 0.667g SiO_2 Diluent at a temperature of 250°C, a total pressure of 40 bar, a H_2:n-C_{16} Molar Feed Ratio of 10:1 and a Site Hourly Space Velocity of 126.8 $mol_{n\text{-}C16}/(mol_{Total\_Sites} \times hr)$, Resulting in a Cracking Conversion of n-C_{16} of 27.3% (where n-C_x refers to the n-paraffin with carbon number x)

It should be noted that the small amount of n-C_{15} and trace amount of n-C_{17} are feed impurities (see Section 7.1).

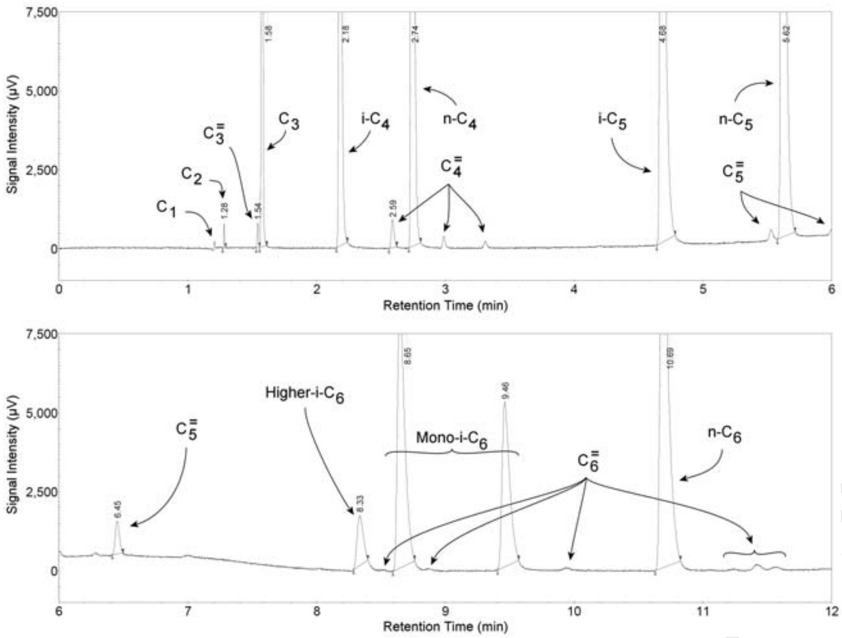

Figure 6.60: Magnification of Sample Chromatogram Presented in Figure 6.59, Focussing on Retention Times from 0.0 to 12.0 min (where C_x and $C_x^{=}$ refer to paraffinic and olefinic species with carbon number x respectively, whilst mono-i-C_x and Higher-i-C_x refer to multi-methyl branched species and multi-methyl and higher (e.g. ethyl) branched species with carbon number x respectively)

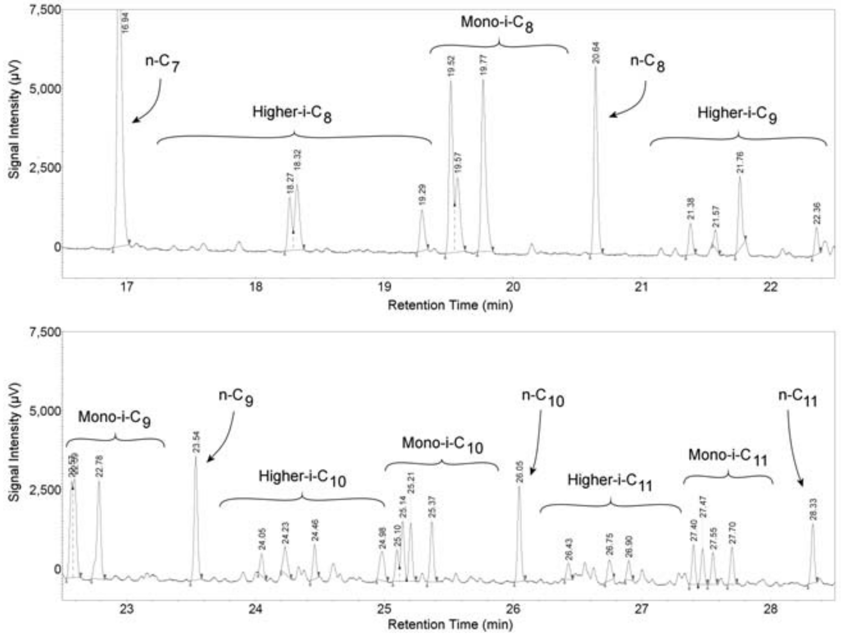

Figure 6.61: Magnification of Sample Chromatogram Presented in Figure 6.59, Focussing on Retention Times from 16.5 to 18.5 min (where C_x and $C_x^{=}$ refer to paraffinic and olefinic species with carbon number x respectively, whilst mono-i-C_x and Higher-i-C_x refer to multi-methyl branched species and multi-methyl and higher (e.g. ethyl) branched species with carbon number x respectively)

the GC chromatogram obtained from each zeolite did, however, show that all exhibited a product which, for all intents and purposes, consisted entirely of paraffinic species. Any olefinic species in the product spectra (such the small peaks in Figure 6.60 indicated by the $C_x^=$ notations) were found to constitute less than 1 mol% of the species in each carbon number (and hence in the total product).

It should be noted, with reference to the criticism regarding the use of the 0.187 metal:acid site molar loading ratio in Section 6.1.3, that the sample chromatogram presented in Figures 6.59 through 6.61 is that of H-MFI-90, observed to be the most active catalyst under the conditions of this investigation. Considering that this catalyst loading exhibited such a small proportion of olefinic products, it was deemed an acceptable assumption that this zeolite, together with the H-BEA-25, H-MOR-20 and H-USY, were all loaded with sufficient supported metal so as not to result in a bifunctional system which was metal site limited.

6.5.2 Data Analysis

Thus, with the integrated peak areas, as supplied by the Galaxie software, and the identification of the various isomer groups, it was possible to calculate both the conversion of the n-C_{16} feed and the various selectivities (both branching and carbon number distribution) with relative ease.

6.5.2.1 Conversion

By the classical hydrocracking mechanism (see Section 2.2), the reaction of the n-C_{16} feed would require its initial isomerisation followed by cracking to smaller fragments. As such, it was desired to examine the activity of each zeolite in terms of both its cracking conversion (i.e. the conversion of the n-C_{16} feed into fragments with carbon numbers less than 16) and total conversion (i.e. the conversion of the n-C_{16} feed into both isomerised C_{16} and fragments with carbon numbers less than 16). As indicated in Section 7.1, however, the feed also contained a small amount of n-C_{15}, with the ratio of this n-C_{15} contaminant to n-C_{16} being observed to be approximately equivalent in the feed and product (suggesting roughly equal rates of reaction of the n-C_{15} and n-C_{16}, with minimal formation of n-C_{15} via methanolysis on the metal). As such, C_{15} and C_{16} species were grouped for the purposes of conversion calculation. The calculations for these conversions are thus as follows:

$$\begin{aligned}\text{Cracking Conversion of } \mathrm{C}_{15} \text{ and } \mathrm{C}_{16} \text{ (fraction)} &= 1 - \frac{\sum_{n=15}^{16}\left(A_{lin,n} + A_{ism,n}\right)}{\sum_{n=1}^{16}\left(A_{lin,n} + A_{ism,n}\right)} \\ \text{Total Conversion of } \mathrm{C}_{15} \text{ and } \mathrm{C}_{16} \text{ (fraction)} &= 1 - \frac{A_{lin,16} + A_{lin,15}}{\sum_{n=1}^{16}\left(A_{lin,n} + A_{ism,n}\right)}\end{aligned}$$

where

$A_{lin,n}$ = Integrated area of linear product species with carbon number n
$A_{ism,n}$ = Integrated area of all isomerised product species with carbon number n

6.5.2.2 Extent of Branching

In order to determine the extent to which the various unique properties of each zeolite influenced the degree of branching of the product, it was necessary to not only differentiate between linear versus isomerised product fragments, but to further distinguish between the different extents of branching among the isomerised species. The evaluation was thus conducted by examining the amounts of linear, mono-methyl-branched (i.e. hydrocarbon chains with only a single methyl branch) and multi-methyl and higher branched species (i.e. hydrocarbon chains with multiple methyl branches and/or longer branches such as ethyl side-chains), as indicated in Figure 6.61, for each carbon number and for the full product spectrum.

This evaluation, however, limited the carbon number range which may be examined as C_4 is the smallest fragment length which may present any form of isomerisation, and C_6 is the smallest fragment length which may exhibit the aforementioned higher degrees of branching (specifically 2,3-dimethyl butane). Furthermore, as this examination of branching was specifically focussed on the products of the hydrocracking reaction, the contributions of the C_{15} and C_{16} species were not included in the calculation of the overall selectivity values.

As such, for any carbon number n, the contributions of the different groups of branched species to the product were calculated as follows:

$$\begin{aligned}\text{Fraction Linear} &= \frac{A_{lin,n}}{(A_{lin,n} + A_{m,ism,n} + A_{h,ism,n})}\\ \text{Fraction Mono-methyl Branched} &= \frac{A_{m,ism,n}}{(A_{lin,n} + A_{m,ism,n} + A_{h,ism,n})}\\ \text{Fraction Multi-methyl and Higher Branched} &= \frac{A_{h,ism,n}}{(A_{lin,n} + A_{m,ism,n} + A_{h,ism,n})}\end{aligned}$$

Similarly, the contributions in the C_6 to C_{14} combined product spectrum were calculated as follows:

$$\begin{aligned}\text{Fraction Linear} &= \frac{\sum_{n=6}^{14} A_{lin,n}}{\sum_{n=6}^{14} (A_{lin,n} + A_{m,ism,n} + A_{h,ism,n})}\\ \text{Fraction Mono-methyl Branching} &= \frac{\sum_{n=6}^{14} A_{m,ism,n}}{\sum_{n=6}^{14} (A_{lin,n} + A_{m,ism,n} + A_{h,ism,n})}\\ \text{Fraction Multi-methyl and Higher Branching} &= \frac{\sum_{n=6}^{14} A_{h,ism,n}}{\sum_{n=6}^{14} (A_{lin,n} + A_{m,ism,n} + A_{h,ism,n})}\end{aligned}$$

where

$A_{lin,n}$ = Integrated area of linear product species with carbon number n
$A_{m,ism,n}$ = Integrated area of mono-methyl branched product species with carbon number n
$A_{h,ism,n}$ = Integrated area of multi-methyl and higher branched product species with carbon number n

6.5.2.3 Carbon Number Distributions

To determine the carbon number distributions of the product spectra, it was necessary to convert the raw peak area data into equivalent molar compositions, as the signal intensity registered by the FID is proportional to the number of carbon atoms being detected, not the number of moles of hydrocarbon species. This calculation thus involved two steps, the first being the determination of the molar fraction of each individual species in the product, and the second being normalisation of these species, grouped in terms of their carbon numbers. It should be noted that, as C_1 was produced primarily through methanolysis occurring on the metal, it was omitted from the normalised carbon number distribution, being compared separately instead.

The molar composition of each species in the product was calculated as:

$$Y_i = \frac{\left(\frac{A_i}{C_i}\right)}{\sum_{n=1}^{k} \left(\frac{A_n}{C_n}\right)}$$

where

Y_i = Molar fraction of species i in product
A_i, A_n = Integrated peak area of species i and n
C_i, C_n = Carbon number of species i and n
k = Number of integrated peaks
(i.e. representative of the number of product species)

The calculation of the normalised carbon number distribution (for C_2 to C_{14}) was thus achieved as follows:

$$Q_i = \frac{(Y_{lin,i} + Y_{ism,i})}{\sum_{n=2}^{14} (Y_{lin,n} + Y_{ism,n})}$$

where

Q_i = Normalised molar fraction of all product species with carbon number i
$Y_{lin,i}, Y_{lin,n}$ = Molar fraction of linear product species with carbon number i or n
$Y_{ism,i}, Y_{ism,n}$ = Molar fraction of all isomerised product species with carbon number i or n

6.5.2.4 Data Projection for Comparison

To allow for the accurate and meaningful comparison of the data obtained between the four zeolites tested, it was necessary to conduct any comparisons at the same conversion. Given the ranges of conversions attained (see Section 7.3), this implied projecting the data (by inter- or extra-polation as appropriate) to 20% conversion. Whether this was conducted in terms of cracking conversion or total conversion was dependent on the comparison, with carbon number distributions being compared at 20% cracking conversion whilst branching selectivities were compared at 20% total conversion.

For carbon number distributions, the molar composition of the linear, mono-methyl branched and multi-methyl and higher branched species groups were evaluated against the cracking conversions for each carbon number. Equations fitted to these datasets were then used to project the molar compositions to the desired 20% cracking conversion comparison point.

To compare the extents of branching, the branching selectivities themselves were evaluated against total conversion, with equations fitted to this data being utilised to determine the selectivity values at the desired 20% total conversion comparison point.

As may be seen from the data presented in Sections 7.4.1 and 7.5.1, for the relationships between the carbon number distribution and cracking conversion and the branching selectivities and total conversion respectively, all catalysts, with the exception of H-MOR-20, exhibited roughly linear variations in terms of carbon number distributions and the extents of branching with changes in the cracking and total conversions respectively. As such, for H-MFI-90, H-BEA-25 and H-USY, linear inter- or extra-polation was conducted utilising the the two datapoints closest to the desired 20% conversion comparison value. For H-MOR-20, the data was observed to follow a non-linear trend and, as such, MATLAB was used to fit power functions (of the form $y = a \times x^b + c$) to the various datasets for both carbon number distributions and branching selectivities, thereby allowing for the projection of the trend to the desired comparison conversions (i.e. 20% cracking conversion and 20% total conversion respectively). This non-linear relationship for H-MOR-20 was believed to be due to the very low activities achieved over that zeolite, with the equation fitted to the data indicating a levelling off at conversions in the range obtained over the other three zeolites.

Power fits were also conducted for the H-MFI-90, H-BEA-25 and H-USY, but the initial results of these yielded points in good agreement with the linear projections and well within the experimental uncertainties associated with these values. As such, the higher computational load and time expenditure for the power trend predictions was deemed unnecessary for these three zeolites.

7

Results, Analyses and Trends

7.1 Feed Composition

To ensure the accuracy of the results obtained from the GC analyses of the product stream, it was necessary to determine the exact composition of the hydrocarbon feed stream. The n-hexadecane feed was thus analysed, with the results presented in Table 7.12. As may be seen, the only significant impurity detected was n-C_{15}, with n-C_{17} and C_{15} and C_{16} isomers present in only trace amounts ($<$ 0.01 mol%). The presence of a detectable amount of n-C_{15} in the feed necessitated its removal from the various conversion and selectivity calculations as indicated in Section 6.5.2.

Table 7.12: GC Analysis of n-Hexadecane Feedstock

	Peak Area (μV.s)						Average Molar Distribution (%)	Deviation (%)
	1	2	3	4	5	6		
n-C_{15}	592	862	697	548	333	9134	0.53	0.08
i-C_{15}	(Trace amounts below integration threshold)						< 0.01	
n-C_{16}	101950	178405	132593	94828	69927	2488737	99.47	0.08
i-C_{16}	(Trace amounts below integration threshold)						< 0.01	
n-C_{17}	(Trace amounts below integration threshold)						< 0.01	
							100.00	

7.2 Initial Induction and Reactor Comparison

So as to determine not only the "typical" initial induction period for the catalysts utilised (see Section 6.3), but to verify that the results produced by both reactors were comparable, a preliminary test was conducted whereby each reactor was loaded with identical catalyst charges (0.800 g H-MFI-90, 0.119 g 5 wt% Pt/SiO_2, 0.667 g SiO_2 diluent) and operated under identical conditions. The results of this analysis, presented in Figure 7.62, indicate an initial induction period of approximately 48 hrs on-stream (at a site hourly space velocity of approximately 76 $mol_{n\text{-}C16}/(mol_{Total\_Sites} \times hr)$) and confirm that, with the same catalyst loadings and under the same conditions, both reactors produce comparable results after this induction period.

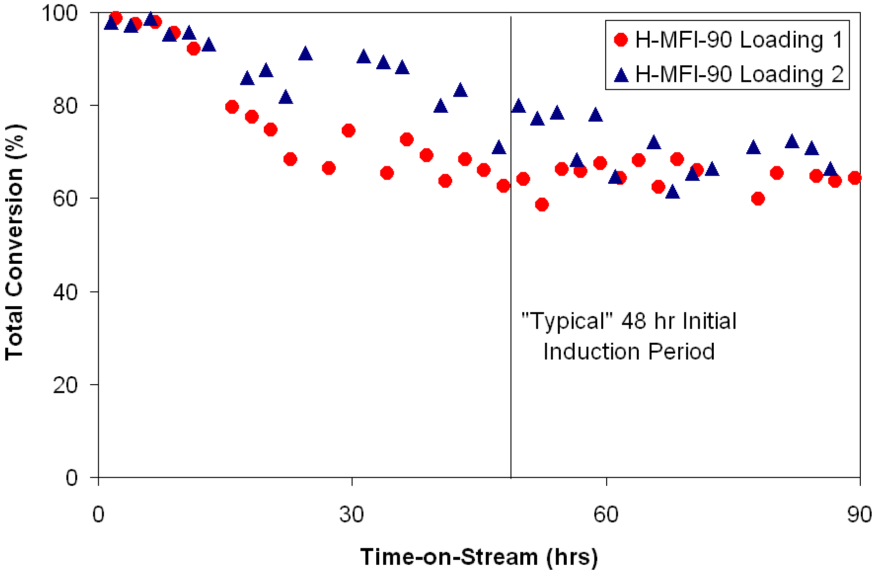

Figure 7.62: Inter-reactor Comparison and Initial Induction Period Determination (0.800 g H-MFI-90, 0.119 g 5 wt% Pt/SiO_2, 0.667 g SiO_2 diluent at a temperature of 250°C, total pressure of 40 bar, H_2:n-C_{16} molar feed ratio of 10:1 and a space velocity of 76.1 $mol_{n\text{-}C16}/(mol_{Total\_Sites} \times hr)$)

7.3 Activity Comparisons

The graphical representations of the total conversion versus time-on-stream data obtained for all four zeolites tested are presented in Figures 7.63 through 7.66, with overall comparisons of these activities in Figures 7.68 through 7.67 (the tabulated data may be found in Appendix B). As may be seen, each of the time-on-stream graphs is composed of four sections corresponding to the three space velocities examined (to obtain a range of conversions) together with the repeated initial space velocity to determine the extent of deactivation. As indicated in Section 6.1.3 and Table 6.8, the catalyst loadings were calculated so as to maintain a constant number of total active sites (i.e. combined metal and acid sites) for all catalyst charges (although an increase was required for H-MOR-20 and H-USY due to lower activities), with the space velocity (i.e. the "site hourly space velocities" (SHSV), provided in $mol_{n\text{-}C16}/(mol_{Total\_Sites} \times hr))$ being varied as necessary to obtain a range of conversions (see Table 6.11 for a full listing of flow rates utilised). Finally, Figure 7.70 presents a graphical indication of the contribution which feed isomerisation makes toward the total conversion of the n-C_{16} feed.

7.3.1 Zeolite Specific Total Conversion with Time-On-Stream Data

Note that the data for H-MFI-90 presented in Figure 7.63 is for the analysis conducted specifically for comparison with the other zeolites and is not the same data as that presented in Figure 7.62 for the inter-reactor comparison (see Table 6.11). Furthermore, for both H-USY and H-MOR-20, only the results of the second, larger catalyst loadings are presented below, but with the data for the initial, smaller loadings being included in Figures 7.68 through 7.67 for completeness.

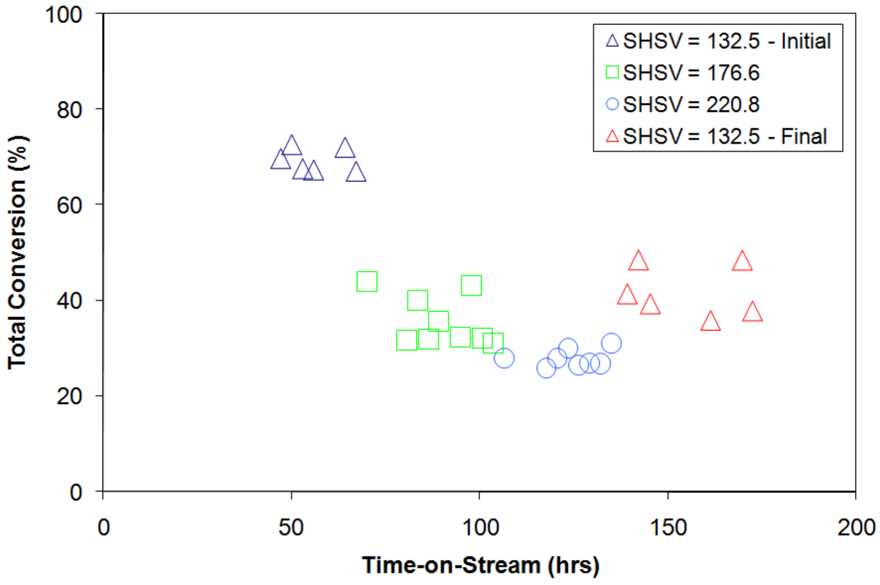

Figure 7.63: Conversion with Time-On-Stream for a Loading of 0.800 g H-MFI-90, 0.119 g 5 wt% Pt/SiO_2, 0.667 g SiO_2 Diluent (at a temperature of 250°C, total pressure of 40 bar and a H_2 : n-C_{16} molar feed ratio of 10 : 1) for Various Site Hourly Space Velocities (SHSV in $mol_{n\text{-}C16}/(mol_{Total\_Sites} \times hr)$)

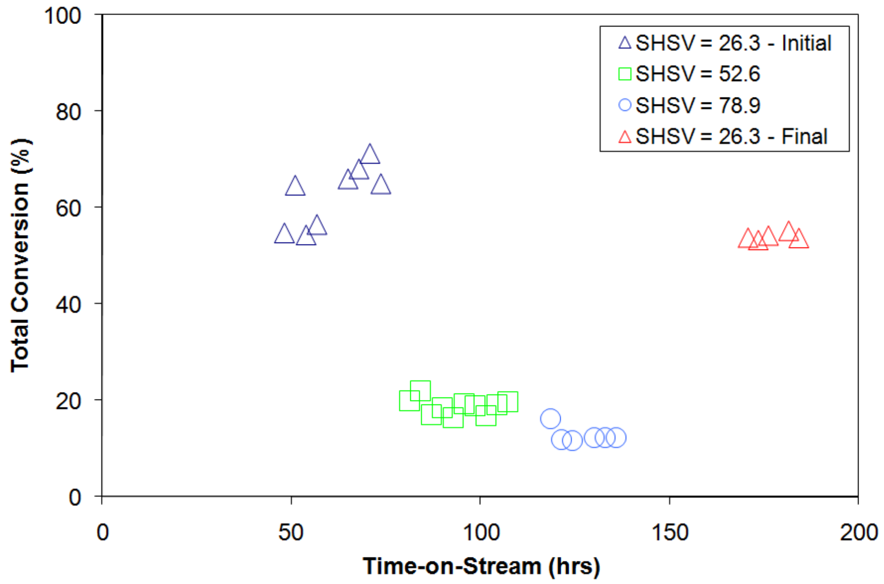

Figure 7.64: Conversion with Time-On-Stream for a Loading of 0.229 g H-BEA-25, 0.119 g 5 wt% Pt/SiO_2, 0.999 g SiO_2 Diluent (at a temperature of 250°C, total pressure of 40 bar and a H_2 : n-C_{16} molar feed ratio of 10 : 1) for Various Site Hourly Space Velocities (SHSV in $mol_{n\text{-}C16}/(mol_{Total\_Sites} \times hr)$

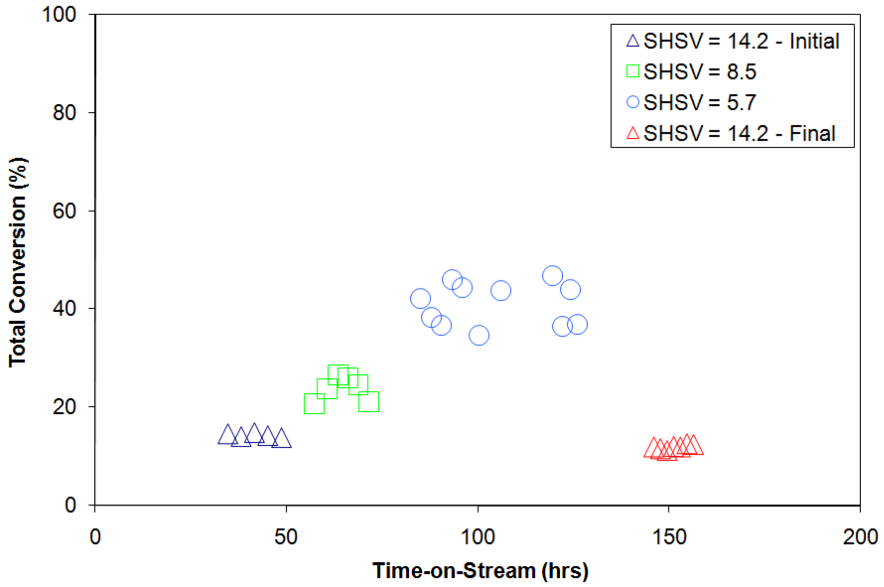

Figure 7.65: Conversion with Time-On-Stream for a Loading of 0.794 g H-USY, 2.683 g 5 wt% Pt/SiO_2, 1.967 g SiO_2 Diluent (at a temperature of 250°C, total pressure of 40 bar and a H_2 : n-C_{16} molar feed ratio of 10 : 1) for Various Site Hourly Space Velocities (SHSV in $mol_{n\text{-}C16}/(mol_{Total\_Sites} \times hr)$

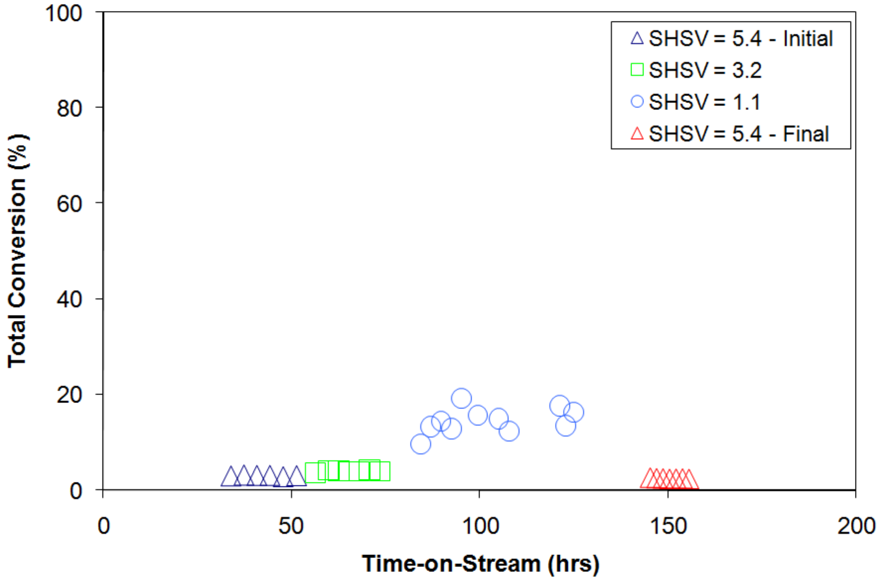

Figure 7.66: Conversion with Time-On-Stream for a Loading of 4.169 g H-MOR-20, 2.683 g 5 wt% Pt/SiO_2, no Diluent (at a temperature of 250°C, total pressure of 40 bar and a H_2 : n-C_{16} molar feed ratio of 10 : 1) for Various Site Hourly Space Velocities (SHSV in $mol_{n\text{-}C16}/(mol_{Total\_Sites} \times hr)$

7.3.2 Comparison of Total Conversion with Space Velocity

The data from Figures 7.63 through 7.66 was collated for comparison against both the more "traditional" weight hourly space velocity and the site hourly space velocity, where:

$$\text{Weight Hourly Space Velocity} = \frac{g_{n\text{-}C16}}{(g_{Combined\ Supported\ Metal\ And\ Zeolite} \times hr)}$$

$$\text{Site Hourly Space Velocity} = \frac{mol_{n\text{-}C16}}{(mol_{Total\ Active\ Sites} \times hr)}$$

As may be seen, all of the zeolites tested exhibit the trivial trend of declining conversion with increasing space velocity, with the relative activities of the zeolites being ranked as H-MFI-90 $>$ H-BEA-25 $\gg$ H-USY $>$ H-MOR-20. As indicated in Section 6.5.2.4, comparisons regarding the extent of product branching for each zeolite were conducted by projecting the data to 20% total conversion as indicated by the open symbols in Figures 7.67 through 7.69, whilst carbon number distribution comparisons were similarly conducted by projecting the data to 20% cracking conversion (with the tabulated data for these projections provided in Appendix B).

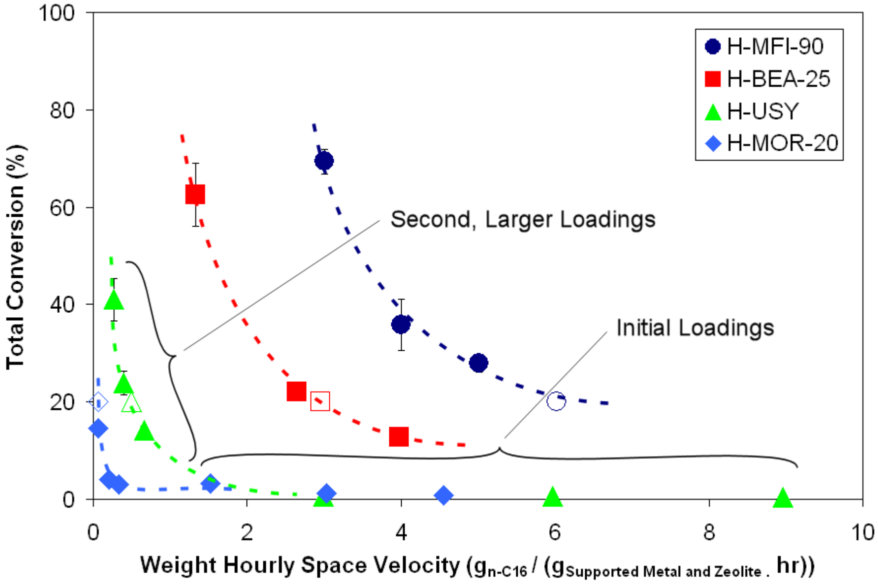

Figure 7.67: Comparison of Total Conversions over the Zeolites Investigated with Weight Hourly Space Velocity (open symbols indicate data points inter- or extra-polated to 20% total conversion for branching selectivity comparisons)

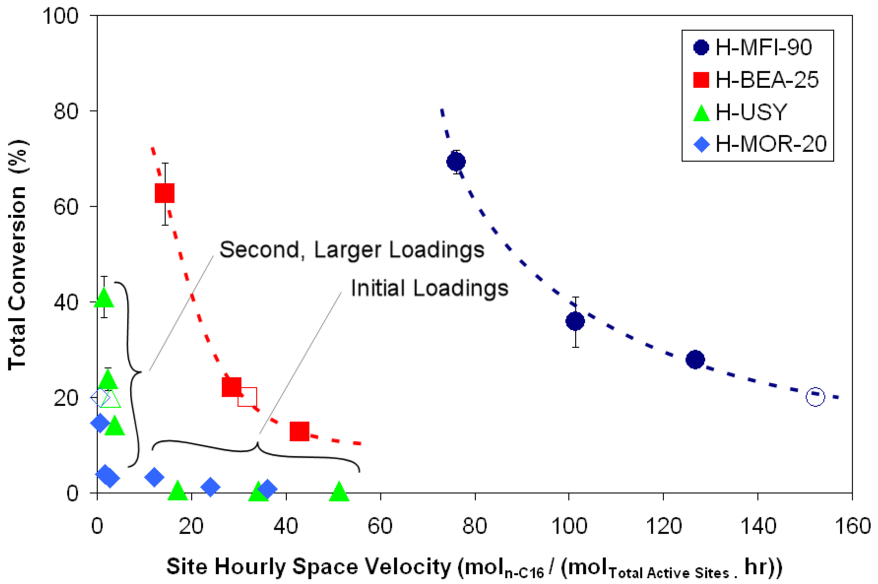

Figure 7.68: Comparison of Total Conversions over the Zeolites Investigated with Site Hourly Space Velocity (open symbols indicate data points inter- or extra-polated to 20% total conversion for branching selectivity comparisons)

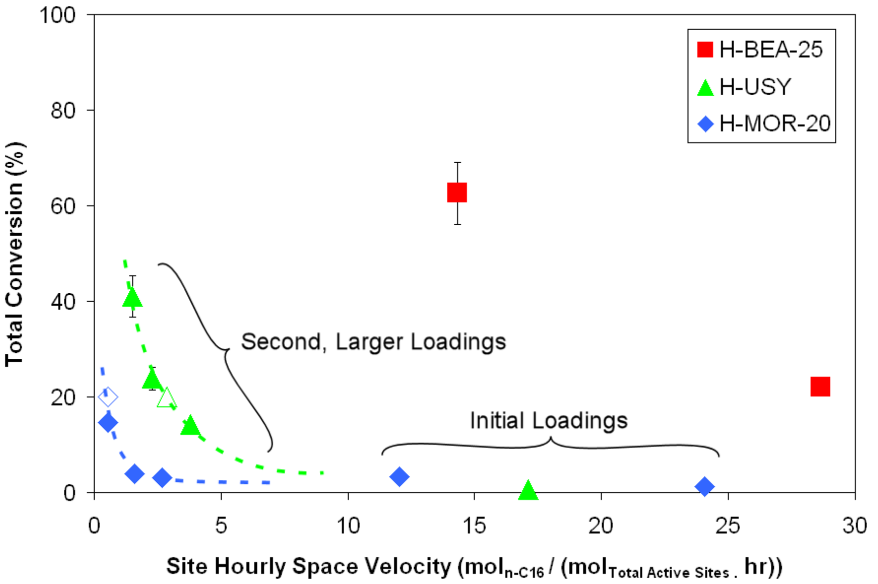

Figure 7.69: Magnified View of the Comparison of the Total Conversions over the Zeolites Investigated Presented in Figure 7.68 for Clearer Determination of H-USY and H-MOR-20 Trends (open symbols indicate data points inter- or extra-polated to 20% total conversion for branching selectivity comparisons)

7.3.3 Relationship Between Isomerisation and Cracking

From Figure 7.70 it is apparent that the extent of isomerisation of the linear feedstock is related to the total conversion, anticipated as the bifunctional hydrocracking reaction is theorised to proceed via isomerisation of the feed molecules to cracking (as discussed in Section 2.2.1). The contribution of isomerisation products over H-MFI-90 is noted to remain very low over the range of conversions investigated.

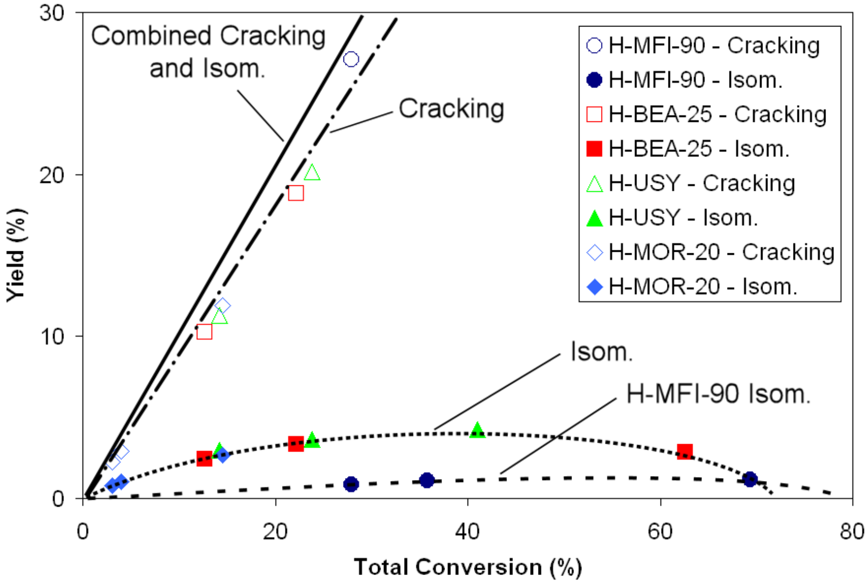

Figure 7.70: Relationship Between the Yields of Feed Isomerisation and Cracking Products with Total Conversion Utilising Data for H-MFI-90, H-BEA-25, H-USY and H-MOR-20 (for the loadings as presented in Table 6.8) All Evaluated at a Temperature of 250°C, Total Pressure of 40 bar and a H_2 : n-C_{16} Molar Feed Ratio of 10 : 1 ("Isom." refers to the yield of isomerised C_{16} species in the product whilst "Cracking" refers to the yield of those product species with carbon numbers below 15, with C_{15} species excluded given their presence as an impurity in the feed

7.4 Cracking Product Carbon Number Distributions

7.4.1 Variations with Cracking Conversion

Below are presented the carbon number distributions for the H-MFI-90, H-BEA-25, H-USY and H-MOR-20 tested in this investigation for the various cracking conversions achieved by varying the site hourly space velocities. It must be noted that these distributions, together with the comparative analysis in Section 7.4.2, are normalised for species from C_2 to C_{14}, with C_{15} and C_{16} being removed given their presence in the feed and C_1 being presented separately in Section 7.4.3. As may be seen from Figures 7.71 through 7.74, the H-MFI-90 and H-BEA-25 both exhibit an increase in the yield of lighter species (and a simultaneous reduction in the yield of heavier species) with an increase in the cracking conversion. The results obtained for the H-USY and H-MOR-20, however, show very similar carbon number distributions for the range of cracking conversions achieved.

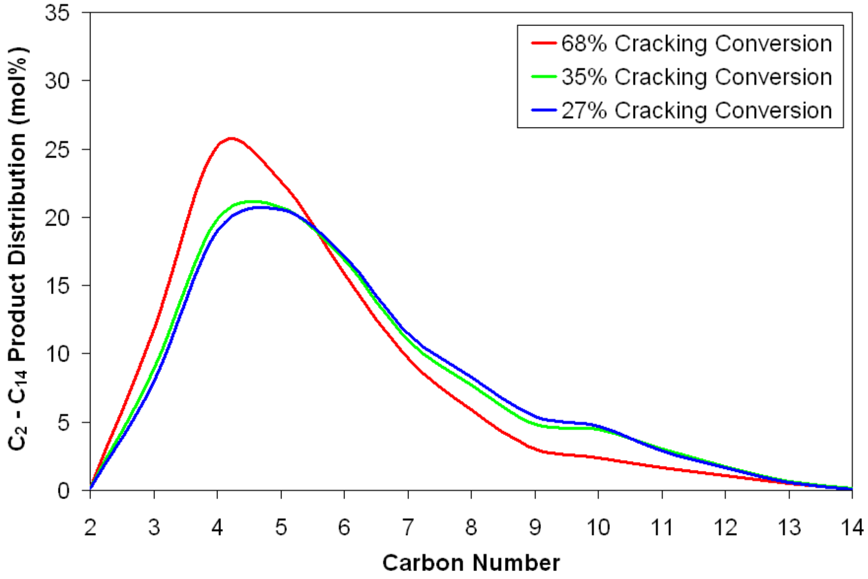

Figure 7.71: Relationship Between Cracking Product Carbon Number Distribution (from C_2 to C_{14}) and Cracking Conversion for a Loading of 0.800 g H-MFI-90, 0.119 g 5 wt% Pt/SiO_2, 0.667 g SiO_2 Diluent (at a temperature of 250°C, total pressure of 40 bar, a H_2 : n-C_{16} molar feed ratio of 10 : 1, and various space velocities)

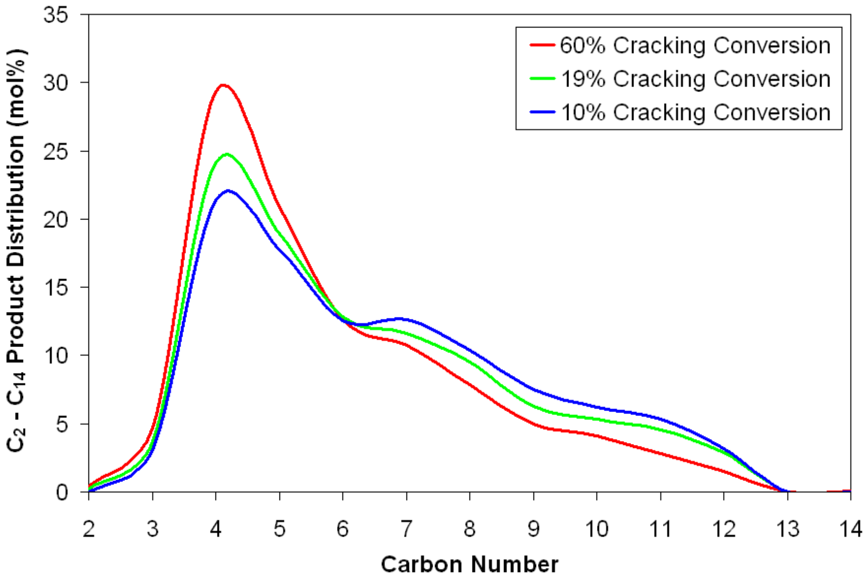

Figure 7.72: Cracking Product Carbon Number Distribution from C_2 to C_{14} for a Loading of 0.229 g H-BEA-25, 0.119 g 5 wt% Pt/SiO_2, 0.999 g SiO_2 Diluent (at a temperature of 250°C, total pressure of 40 bar, a H_2 : n-C_{16} molar feed ratio of 10 : 1, and various space velocities)

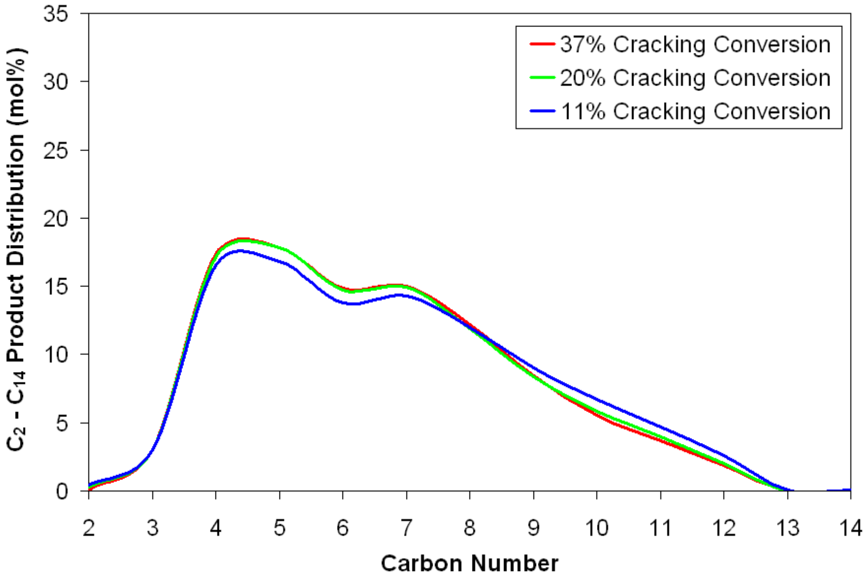

Figure 7.73: Cracking Product Carbon Number Distribution from C_2 to C_{14} for a Loading of 0.794 g H-USY, 2.683 g 5 wt% Pt/SiO_2, 1.967 g SiO_2 Diluent (at a temperature of 250°C, total pressure of 40 bar, a H_2 : n-C_{16} molar feed ratio of 10 : 1, and various space velocities)

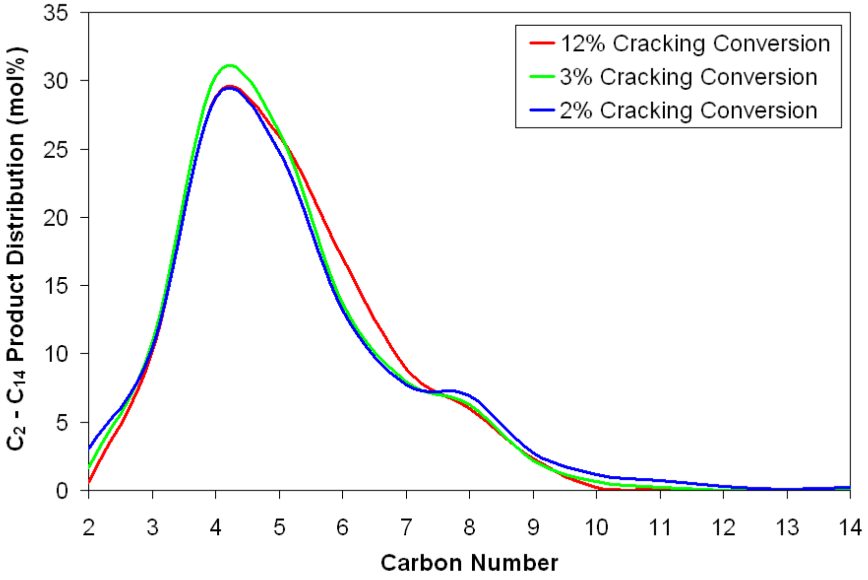

Figure 7.74: Cracking Product Carbon Number Distribution from C_2 to C_{14} for a Loading of 4.169 g H-MOR-20, 2.683 g 5 wt% Pt/SiO$_2$, no Diluent (at a temperature of 250°C, total pressure of 40 bar, a H_2 : n-C_{16} molar feed ratio of 10 : 1, and various space velocities)

7.4.2 Overall Comparison

Figure 7.75 illustrates an overlaid comparison of the carbon number distributions for the H-MFI-90, H-BEA-25, H-USY and H-MOR-20 utilised in this investigation, with this comparison being made possible by inter- and extra-polation of the data obtained (as presented in Section 7.4.1) to 20% cracking conversion for each zeolite (as described in Section 6.5.2.4). It may thus be seen that whilst, at 20% cracking conversion, none of the catalysts tested exhibited the flat ideal primary cracking product distribution presented and discussed in Section 2.2.1, H-USY was noted to exhibit a marginally higher yield of heavier species than the other three zeolites. The ranking of the catalysts in terms of their favouring the production of heavier species may thus be presented as H-USY > H-MFI-90 > H-BEA-25 > H-MOR-20.

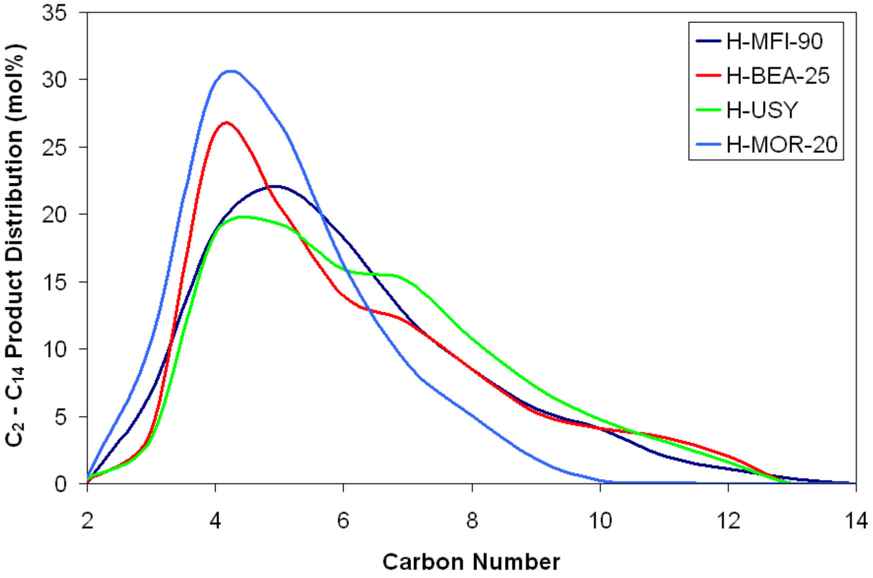

Figure 7.75: Comparison of Cracking Product Carbon Number Distributions (Normalised for C_2 to C_{14}) for H-MFI-90, H-BEA-25, H-USY and H-MOR-20 as Compared at 20% Cracking Conversion (for the loadings as presented in Table 6.8) with All Evaluated at a Temperature of 250°C, Total Pressure of 40 bar, a H_2 : n-C_{16} Molar Feed Ratio of 10 : 1 and Various Space Velocities

7.4.3 Methane Yields

Below is presented the comparison of the methane yields (with their associated site hourly space velocities) for the H-MFI-90, H-BEA-25, H-USY and H-MOR-20 utilised in this investigation, normalised for a product distribution from C_1 to C_{14} at 20% cracking conversion. It may thus be seen that, whilst the H-USY and H-MOR-20 both exhibit methane yields exceeding those of the H-MFI-90 and H-BEA-25, even the highest methane yield was still less than 4 mol%. When compared in light of the space velocity data, the general trend of increasing methane yield with decreasing space velocity may be discerned.

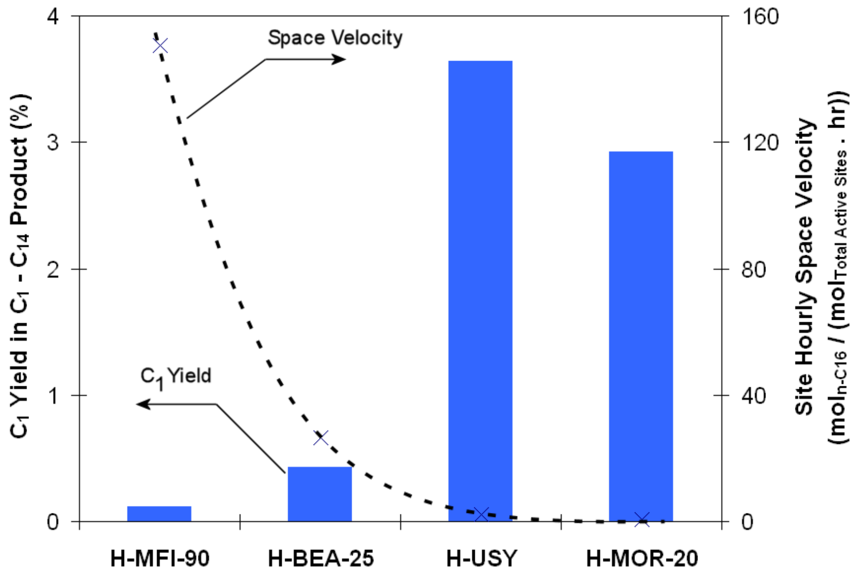

Figure 7.76: Comparison of Methane Yields (Normalised for C_1 to C_{14} Cracking Products) for H-MFI-90, H-BEA-25, H-USY and H-MOR-20 as Compared at 20% Cracking Conversion (for the loadings as presented in Table 6.8) with All Evaluated at a Temperature of 250°C, Total Pressure of 40 bar, a H_2 : n-C_{16} Molar Feed Ratio of 10 : 1 and Various Space Velocities

7.5 Cracking Product Branching Selectivities

In terms of the specifics of the branching selectivity data presented below, it must be kept in mind that for species with a carbon number less than 3, no branching is possible, whilst for C_4 and C_5 species, only mono-methyl branching can occur. Furthermore, as it was primarily sought to examine the branching of the cracked products, and as both n-C_{15} (in trace amounts) and n-C_{16} species were present in the feed, all C_{15} and C_{16} species were omitted from these selectivity comparisons.

As such, whilst Figures 7.84 through 7.90 provide comparisons of the branching selectivities for carbon numbers from 2 to 14, the comparisons provided in Figures 7.77 through 7.83 pertain only to species with carbon numbers between 6 and 14, with the trends in this data being used to inter- or extra-polate the selectivities to 20% total conversion for the comparisons presented in Figure 7.91. As the branching selectivities for this range of carbon numbers would be affected by the carbon number distributions themselves (presented in Section 7.4), a comparison over the more confined carbon number range of C_4 to C_5 was conducted (presented in Figure 7.92, again inter- or extra-polated to 20% total conversion), although limited to the linear and mono-methyl branched species.

From the data it is clear that, at 20% total conversion, whilst H-BEA-25, H-USY and H-MOR-20 all exhibit roughly the same selectivities towards the various linear and branched species, clearly favouring the formation of mono-methyl branched compounds, H-MFI-90 resulted in a product with a clear increase in the selectivity towards linear species, with a linear to mono-methyl branched molar ratio of almost 1:2 for the combined C_6 to C_{14} range, and 1:0.75 for the combined C_4 and C_5 species.

7.5.1 Variations with Total Conversion

The relationship between the selectivities toward the various groups of branched and un-branched species (i.e. linear, mono-methyl branched, and multi-methyl and higher, such as ethyl, branched) in the product and the total conversion over the H-MFI-90, H-BEA-25, H-USY and H-MOR-20 utilised in this investigation are presented in Figures 7.77 through 7.80. To ease comparison, the data for each of the selectivities was compared directly and is presented in Figures 7.81 through 7.83.

It may be seen that whilst the trends for the H-MFI-90, H-BEA-25 and H-USY are almost linear, the H-MOR-20 exhibited a power law type trend (i.e. of the form $y = a \times x^b + c$). These trends were utilised to predict the selectivities for each zeolite at 20% total conversion (indicated by the open diamonds in the figures) for comparison.

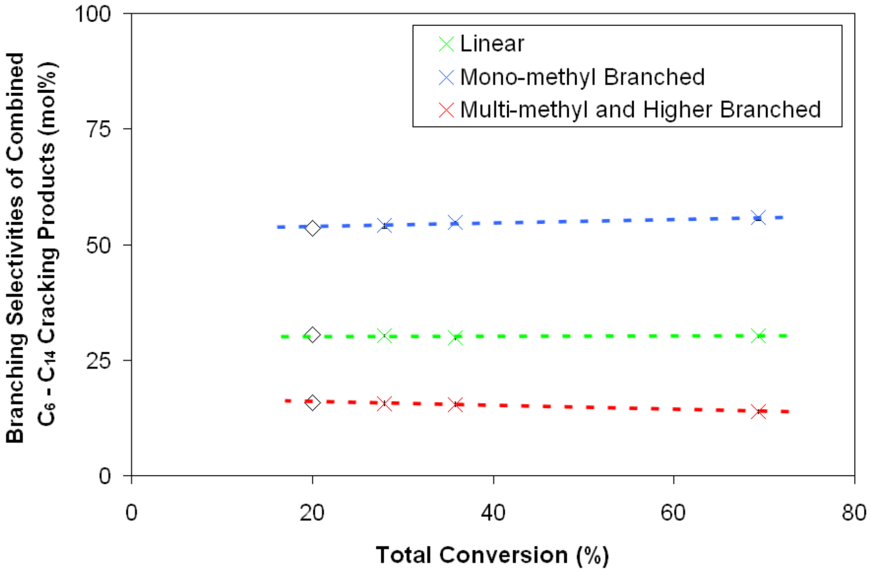

Figure 7.77: Relationship Between Branching Selectivities and Total Conversion for Combined C_6 to C_{14} Cracking Products for a Loading of 0.800 g H-MFI-90, 0.119 g 5 wt% Pt/SiO_2, 0.667 g SiO_2 Diluent (at a temperature of 250°C, total pressure of 40 bar, a H_2 : n-C_{16} molar feed ratio of 10 : 1 and various space velocities). (Open diamonds indicate points extrapolated to 20% total conversion)

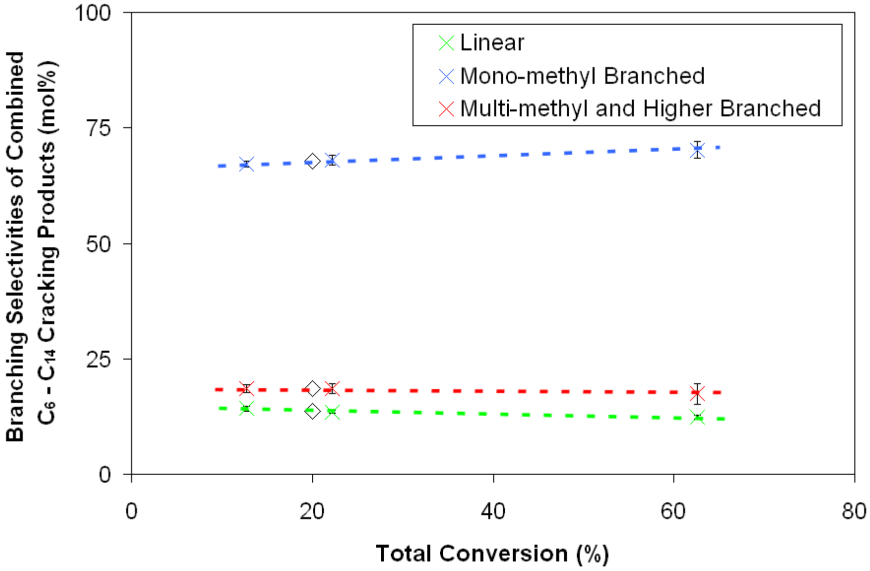

Figure 7.78: Relationship Between Branching Selectivities and Total Conversion for Combined C_6 to C_{14} Cracking Products for a Loading of 0.229 g H-BEA-25, 0.119 g 5 wt% Pt/SiO_2, 0.999 g SiO_2 Diluent (at a temperature of 250°C, total pressure of 40 bar, a H_2 : n-C_{16} molar feed ratio of 10 : 1 and various space velocities). (Open diamonds indicate points interpolated to 20% total conversion)

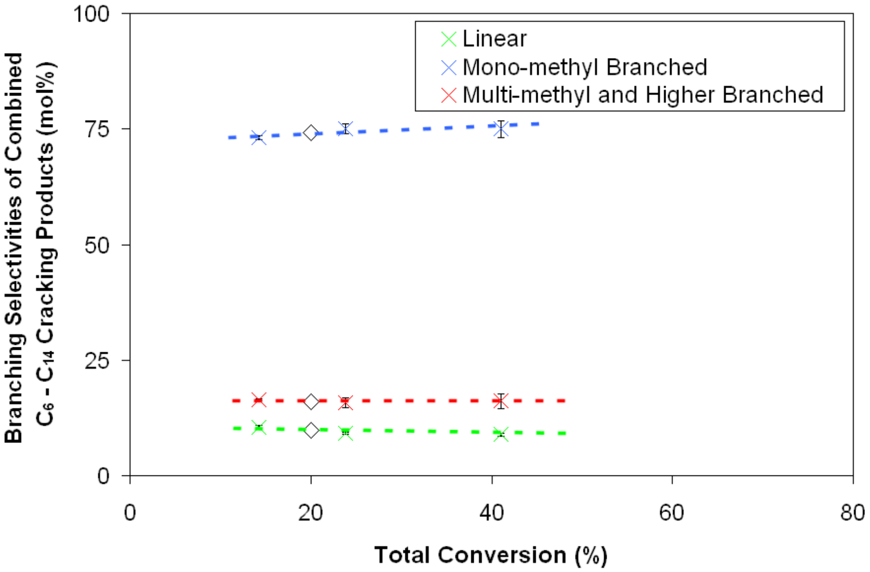

Figure 7.79: Relationship Between Branching Selectivities and Total Conversion for Combined C_6 to C_{14} Cracking Products for a Loading of 0.794 g H-USY, 2.683 g 5 wt% Pt/SiO_2, 1.967 g SiO_2 Diluent (at a temperature of 250°C, total pressure of 40 bar, a H_2 : n-C_{16} molar feed ratio of 10 : 1 and various space velocities). (Open diamonds indicate points interpolated to 20% total conversion)

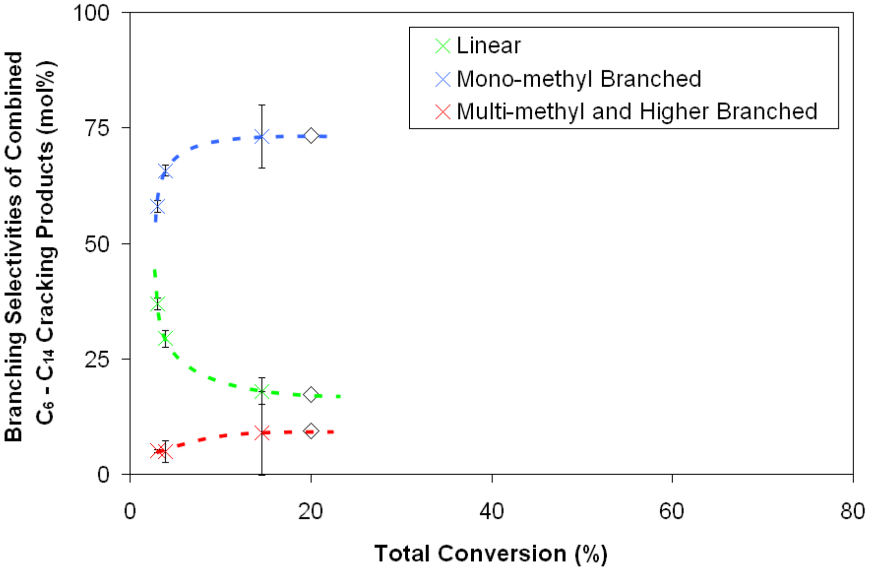

Figure 7.80: Relationship Between Branching Selectivities and Total Conversion for Combined C_6 to C_{14} Cracking Products for a Loading of 4.169 g H-MOR-20, 2.683 g 5 wt% Pt/SiO_2, no Diluent (at a temperature of 250°C, total pressure of 40 bar, a H_2 : n-C_{16} molar feed ratio of 10 : 1 and various space velocities). (Open diamonds indicate points extrapolated to 20% total conversion)

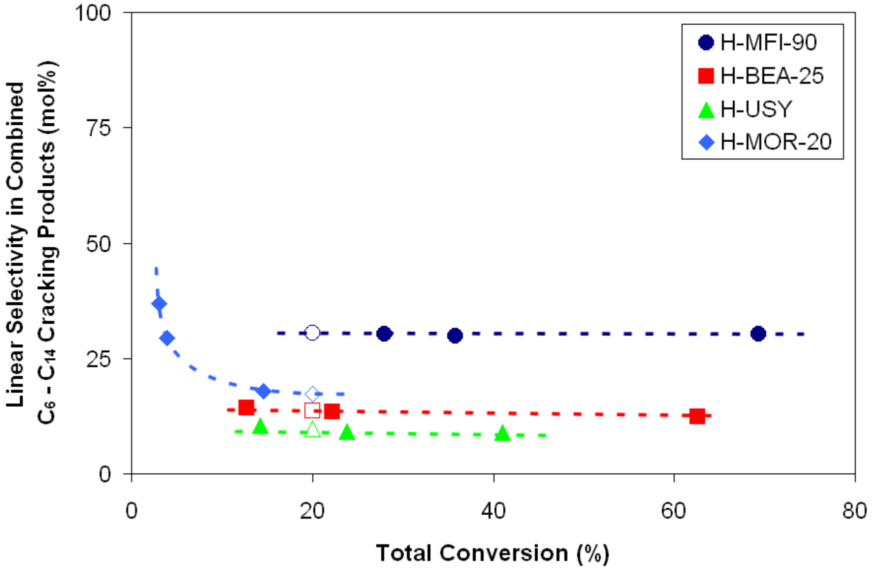

Figure 7.81: Comparison of Relationship Between Linear Selectivity and Total Conversion for the H-MFI-90, H-BEA-25, H-USY and H-MOR-20 Investigated (at a temperature of 250°C, total pressure of 40 bar, a H_2 : n-C_{16} molar feed ratio of 10 : 1 and various space velocities). (Open diamonds indicate points inter- or extra-polated to 20% total conversion)

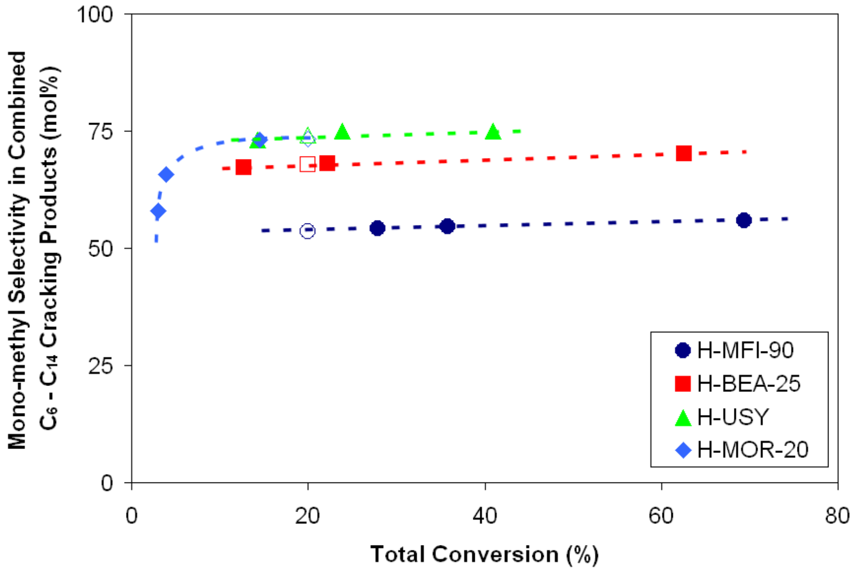

Figure 7.82: Comparison of Relationship Between Mono-methyl Branching Selectivity and Total Conversion for the H-MFI-90, H-BEA-25, H-USY and H-MOR-20 Investigated (at a temperature of 250°C, total pressure of 40 bar, a H_2 : n-C_{16} molar feed ratio of 10 : 1 and various space velocities) (Open diamonds indicate points inter- or extra-polated to 20% total conversion)

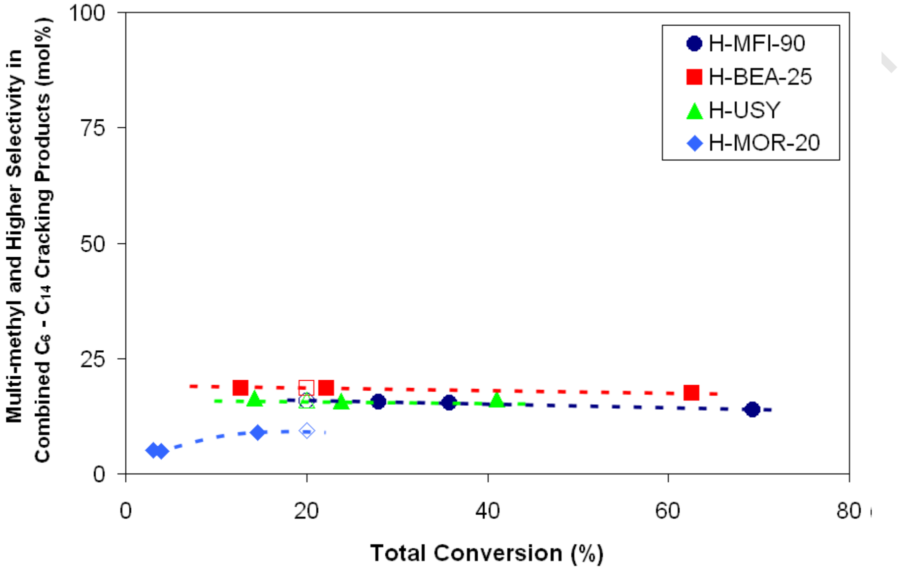

Figure 7.83: Comparison of Relationship Between Multi-methyl and Higher Branching Selectivity and Total Conversion for the H-MFI-90, H-BEA-25, H-USY and H-MOR-20 Investigated (at a temperature of 250°C, total pressure of 40 bar, a H_2 : n-C_{16} molar feed ratio of 10 : 1 and various space velocities) (Open diamonds indicate points inter- or extra-polated to 20% total conversion)

7.5.2 Comparison Over Carbon Number Range

Figures 7.84 through 7.87 present the branching selectivities of the species within each carbon number at a total conversion of 20% for each of the zeolites tested, with a direct comparison of these selectivities provided in Figures 7.88 through 7.90. It must be noted that these selectivity/distribution trends are, however, subject to the influence of the carbon number distributions themselves.

This data serves to reiterate the point indicated in Section 7.5.1 of H-MFI-90 exhibiting a product with a higher linear selectivity than the other three zeolites, with the apparent increased linear selectivity observed for H-MOR-20 in Figure 7.88 being due the combination of its higher yield of C_3 species and the fact that C_3 is present only as linear fragments rather than this zeolite selectively forming linear as opposed to branched isomers.

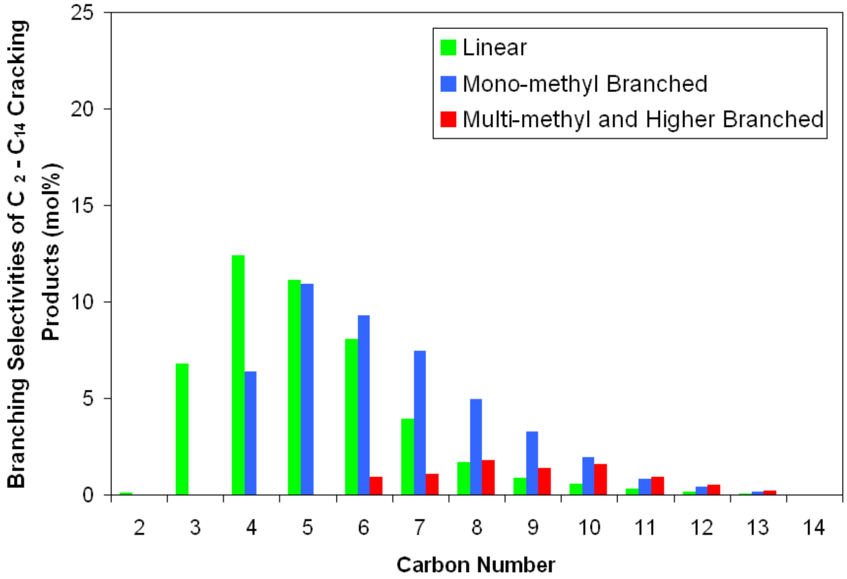

Figure 7.84: Cracking Product Branching Selectivities with Carbon Number for a Loading of 0.800 g H-MFI-90, 0.119 g 5 wt% Pt/SiO_2, 0.667 g SiO_2 Diluent (at a temperature of 250°C, total pressure of 40 bar and a H_2 : n-C_{16} molar feed ratio of 10 : 1) at an Extrapolated Total Conversion of 20%

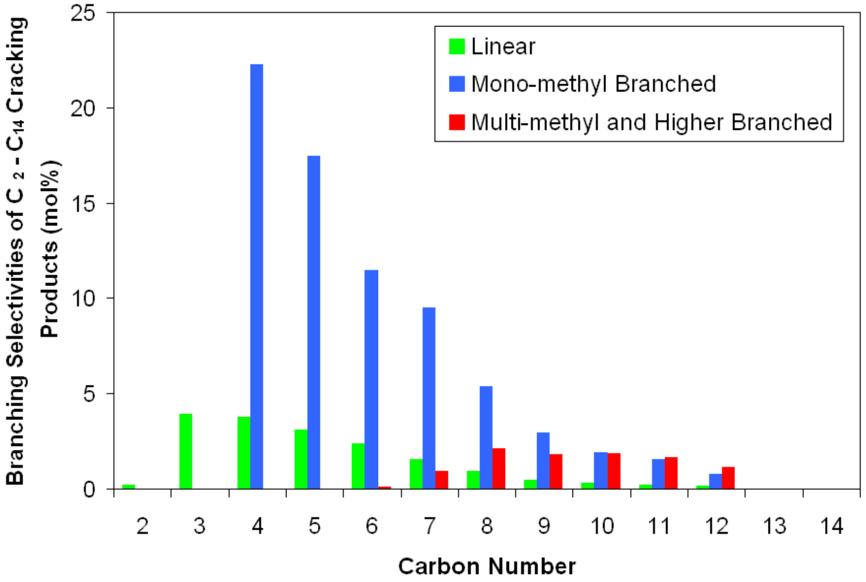

Figure 7.85: Cracking Product Branching Selectivities with Carbon Number for a Loading of 0.229 g H-BEA-25, 0.119 g 5 wt% Pt/SiO_2, 0.999 g SiO_2 Diluent (at a temperature of 250°C, total pressure of 40 bar and a H_2 : n-C_{16} molar feed ratio of 10 : 1) at an Interpolated Total Conversion of 20%

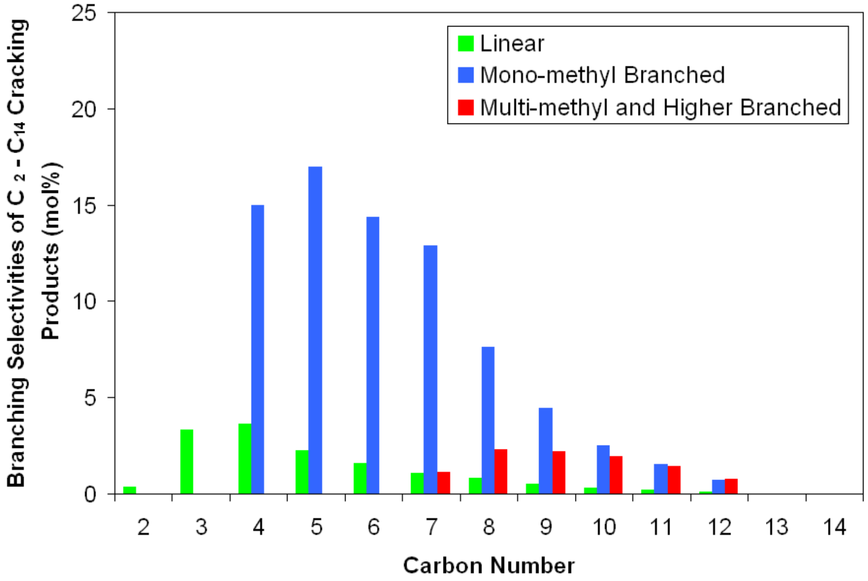

Figure 7.86: Cracking Product Branching Selectivities with Carbon Number for a Loading of 0.794 g H-USY, 2.683 g 5 wt% Pt/SiO_2, 1.967 g SiO_2 Diluent (at a temperature of 250°C, total pressure of 40 bar and a H_2 : n-C_{16} molar feed ratio of 10 : 1) at an Interpolated Total Conversion of 20%

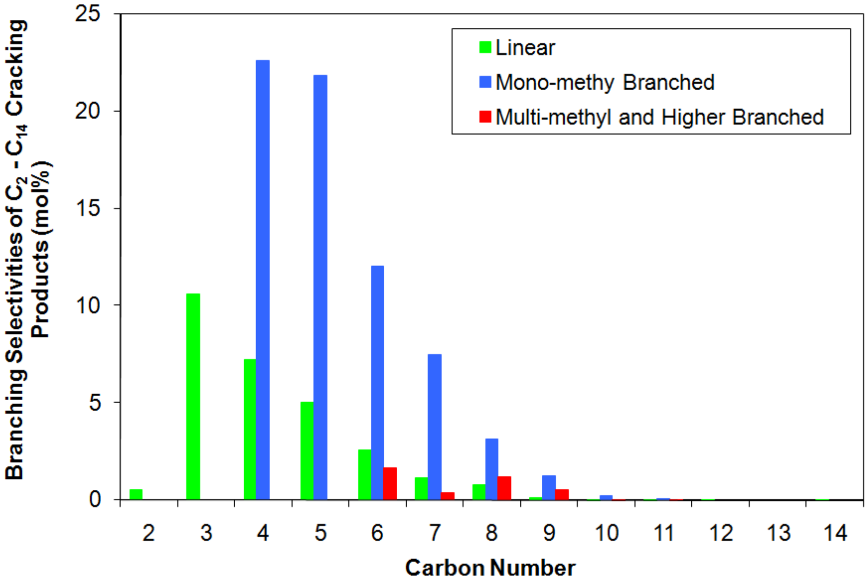

Figure 7.87: Cracking Product Branching Selectivities with Carbon Number for a Loading of 4.169 g H-MOR-20, 2.683 g 5 wt% Pt/SiO_2, no Diluent (at a temperature of 250°C, total pressure of 40 bar and a H_2 : n-C_{16} molar feed ratio of 10 : 1) at an Extrapolated Total Conversion of 20%

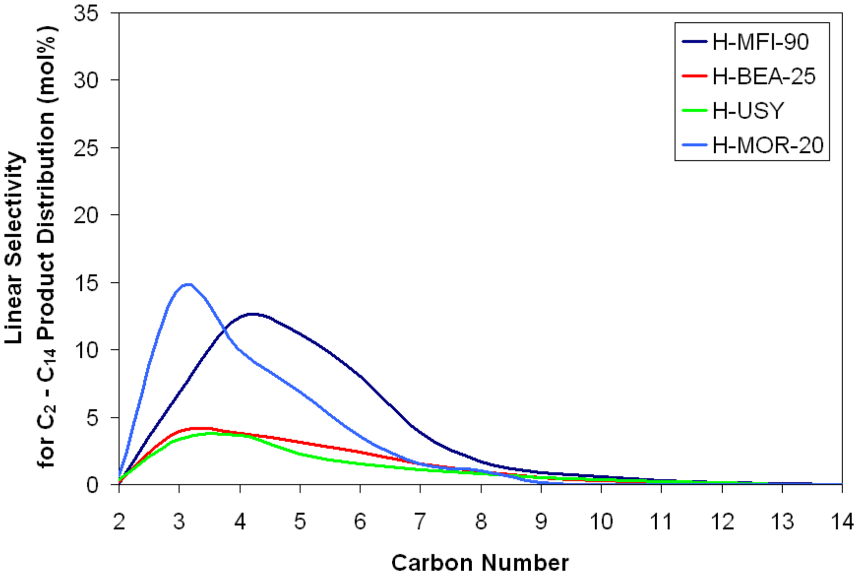

Figure 7.88: Comparison of Linear Cracking Product Selectivity with Carbon Number for C_2 to C_{14} over the H-MFI-90, H-BEA-25, H-USY and H-MOR-20 Investigated (at a temperature of 250°C, total pressure of 40 bar, a H_2 : n-C_{16} molar feed ratio of 10 : 1 and various space velocities) at a Total Conversion of 20%

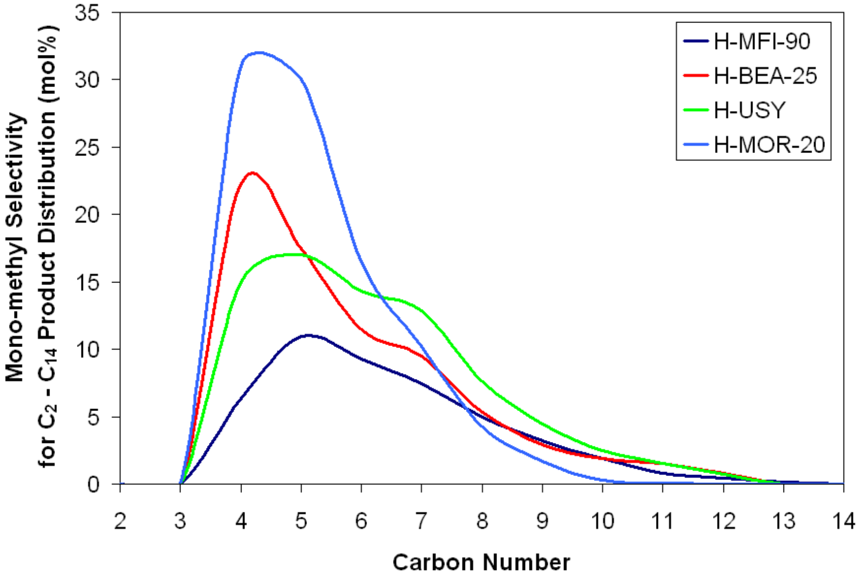

Figure 7.89: Comparison of Mono-methyl Branched Cracking Product Selectivity with Carbon Number for C_2 to C_{14} over the H-MFI-90, H-BEA-25, H-USY and H-MOR-20 Investigated (at a temperature of 250°C, total pressure of 40 bar, a H_2 : n-C_{16} molar feed ratio of 10 : 1 and various space velocities) at a Total Conversion of 20%

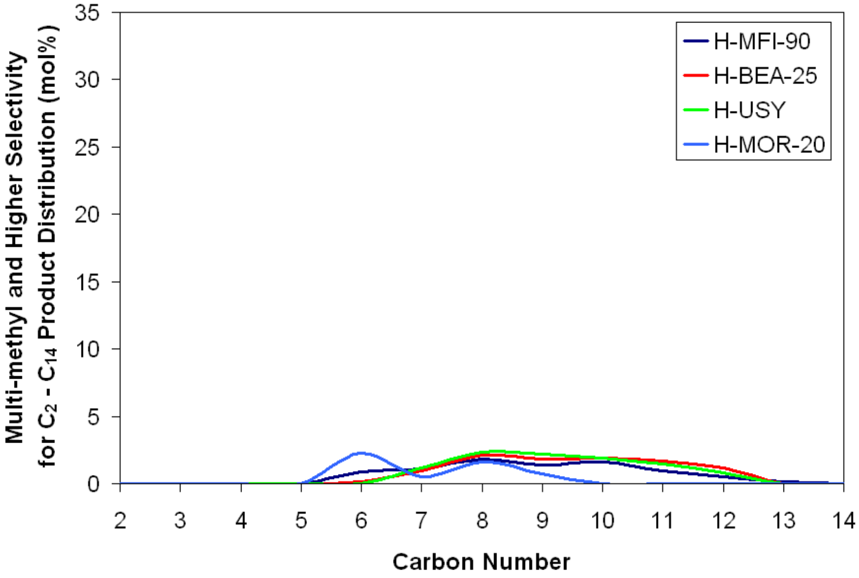

Figure 7.90: Comparison of Multi-methyl and Higher Branched Cracking Product Selectivity with Carbon Number for C_2 to C_{14} over the H-MFI-90, H-BEA-25, H-USY and H-MOR-20 Investigated (at a temperature of 250°C, total pressure of 40 bar, a H_2 : n-C_{16} molar feed ratio of 10 : 1 and various space velocities) at a Total Conversion of 20%

7.5.3 Overall Comparisons

The overall comparisons of the selectivities toward linear, mono-methyl branched and multi-methyl and higher branched species exhibited by the zeolites investigated are presented in Figure 7.91 for the combined C_6 to C_{14} cracking product and in Figure 7.92 for the combined C_4 and C_5 cracking products.

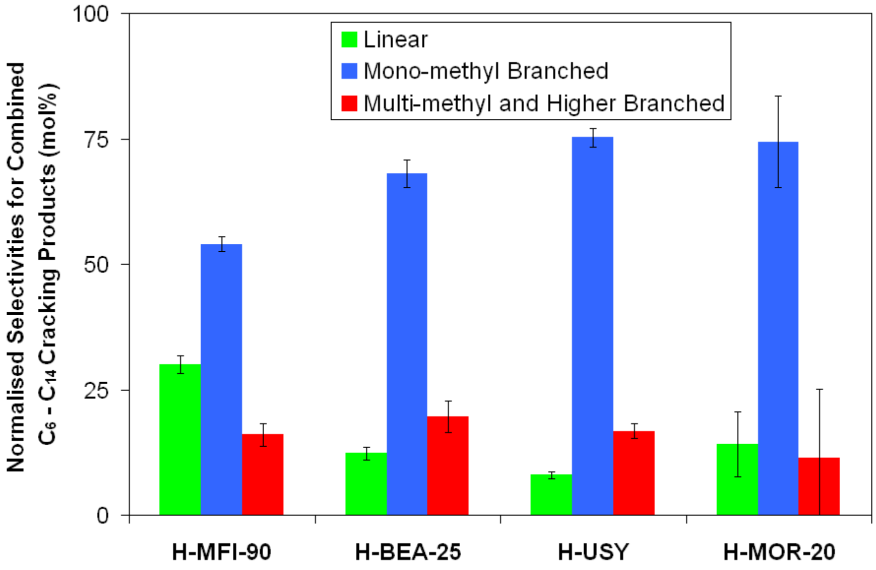

Figure 7.91: Comparison of Combined C_6 to C_{14} Cracking Product Branching Selectivities (normalised to 100%) for the H-MFI-90, H-BEA-25, H-USY and H-MOR-20 Investigated (at a temperature of 250°C, total pressure of 40 bar, a H_2 : n-C_{16} molar feed ratio of 10 : 1 and various space velocities) at a Total Conversion of 20%

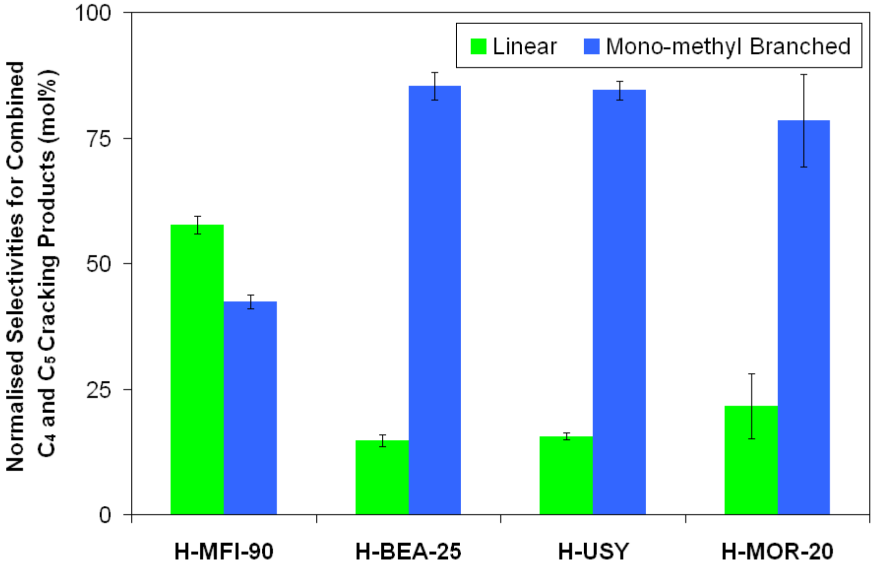

Figure 7.92: Comparison of Combined C_4 to C_5 Cracking Product Branching Selectivities for the H-MFI-90, H-BEA-25, H-USY and H-MOR-20 Investigated (at a temperature of 250°C, total pressure of 40 bar, a H_2 : n-C_{16} molar feed ratio of 10 : 1 and various space velocities) at a Total Conversion of 20%

7.6 Deactivation

Although somewhat inconclusive given the large variations in activity seen in Section 7.3.2, a comparison of the deactivation observed for each of the catalysts tested, and the effects thereof on the branching selectivities of the products, are presented in Figure 7.93 and Figures 7.98 through 7.101 respectively.

7.6.1 Activity Loss

To allow for a meaningful comparison of the extents of deactivation exhibited by each of the four zeolites tested, the loss of initial activity (in terms of the total conversion) of each zeolite is normalised with respect to the space-time yield (i.e. the product of site hourly space velocity [mmol/site.hr] and conversion [fractional] integrated over the time-on-stream [hr] to determine, in essence, the total mols of feed converted) of each, as indicated below, and presented in Figure 7.93.

$$\begin{aligned}\text{Space-Time Yield} &= \int_{ToS_{Initial}}^{ToS_{Final}} (X_{Total} \times SHSV)\, dToS \\ \text{Normalised Deactivation} &= \frac{X_{Total\ Final} - X_{Total\ Initial}}{\text{Space-Time Yield}}\end{aligned}$$

where

$\mathrm{X_{Total}}$ = Total conversion of feed
ToS = Time-on-Stream
SHSV = Site Hourly Space Velocity (see Section 7.3.2)

In this manner, the deactivation may be viewed as the "percentage activity lost per mol of feed converted". It may thus be seen that H-MFI-90, which was found to exhibit the highest activity under the test conditions, showed the least deactivation per mol of feed converted. The H-BEA-25 and H-USY showed similar extents of deactivation whilst the H-MOR-20, the least active of the zeolites tested, showed the greatest deactivation (approximately ten times that of the H-MFI-90).

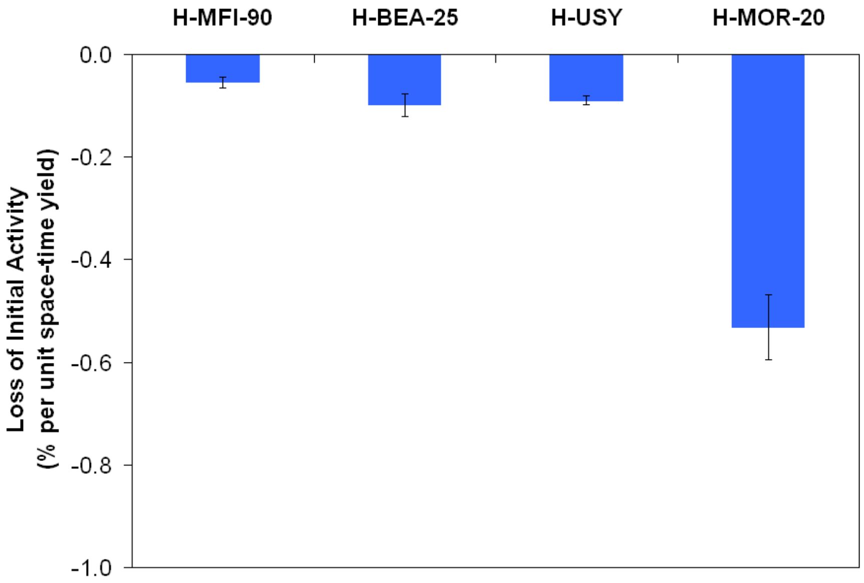

Figure 7.93: Comparison of Relative Deactivation, in terms of the Loss in Total Conversion per Unit Space-Time Yield, for the Zeolites Tested at a Temperature of 250°C, Total Pressure of 40 bar, a H_2 : n-C_{16} Molar Feed Ratio of 10 : 1 and Various Space Velocities, with Final Time-on-Stream for H-MFI-90 = 172 hrs, H-BEA-25 = 184 hrs, H-USY = 156 hrs and H-MOR-20 = 156 hrs

7.6.2 Changes in Cracking Product Carbon Number Distribution

Figures 7.94 through 7.96 present the variations in carbon number distribution with deactivation for the four zeolites tested. The carbon number distributions for the other cracking conversions investigated (as presented in Figures 7.71 through 7.73 are provided for comparison. As may be seen, the changes in carbon number distribution for all of the zeolites tested are inconclusive. For the H-USY and H-MOR-20, which exhibited only minor variation in the distribution with changes in cracking conversion, a comparison between the initial and final distributions indicates them to be almost identical. For the H-MFI-90 and H-BEA-25, the variation is slightly more pronounced, although not entirely uncharacteristic when compared to the distributions obtained for the other cracking conversions achieved.

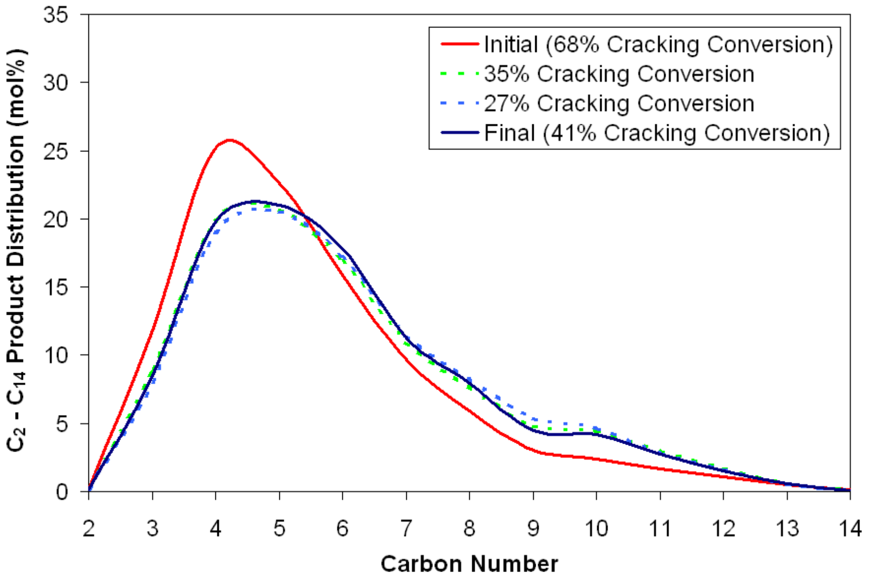

Figure 7.94: Changes in Cracking Product Carbon Number Distribution with Deactivation for a Loading of 0.800 g H-MFI-90, 0.119 g 5 wt% Pt/SiO_2, 0.667 g SiO_2 Diluent (at a temperature of 250°C, total pressure of 40 bar and a H_2 : n-C_{16} molar feed ratio of 10 : 1) after the Investigations Illustrated in Figure 7.63

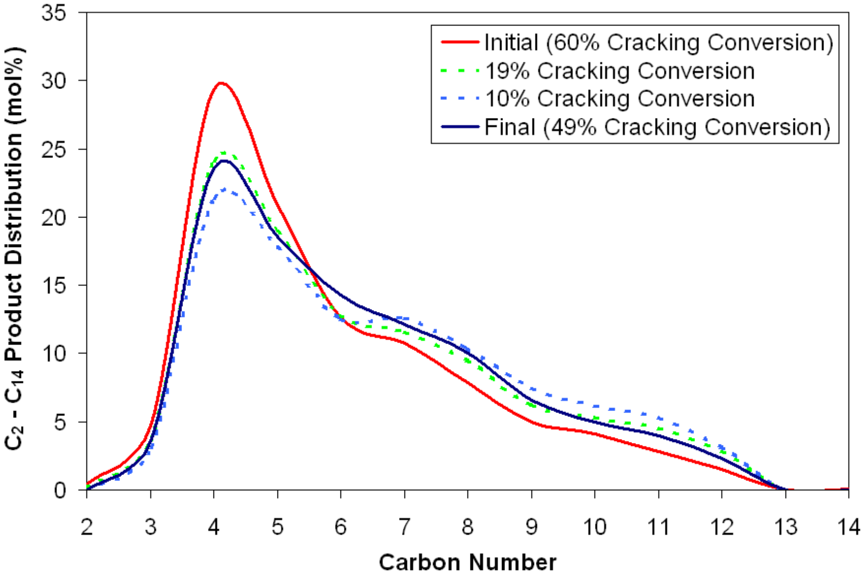

Figure 7.95: Changes in Cracking Product Carbon Number Distribution with Deactivation for a Loading of 0.229 g H-BEA-25, 0.119 g 5 wt% Pt/SiO_2, 0.999 g SiO_2 Diluent (at a temperature of 250°C, total pressure of 40 bar and a H_2 : n-C_{16} molar feed ratio of 10 : 1) after the Investigations Illustrated in Figure 7.64

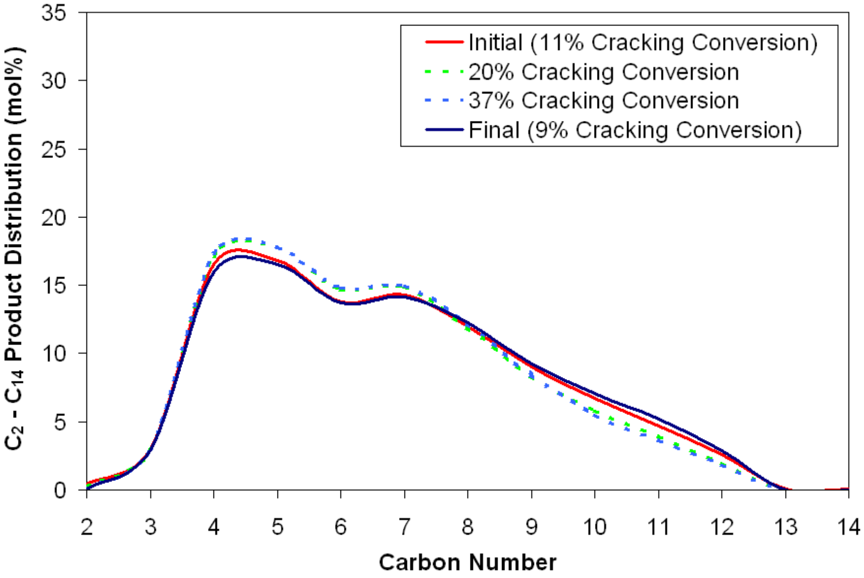

Figure 7.96: Changes in Cracking Product Carbon Number Distribution with Deactivation for a Loading of 0.794 g H-USY, 2.683 g 5 wt% Pt/SiO_2, 1.967 g SiO_2 Diluent (at a temperature of 250°C, total pressure of 40 bar and a H_2 : n-C_{16} molar feed ratio of 10 : 1) after the Investigations Illustrated in Figure 7.65

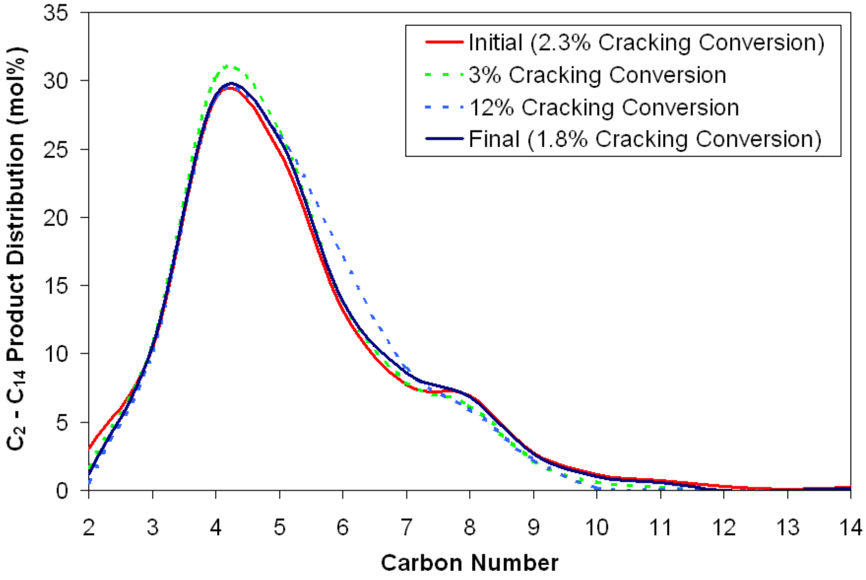

Figure 7.97: Changes in Cracking Product Carbon Number Distribution with Deactivation for a Loading of 4.169 g H-MOR-20, 2.683 g 5 wt% Pt/SiO_2, no Diluent (at a temperature of 250°C, total pressure of 40 bar and a H_2 : n-C_{16} molar feed ratio of 10 : 1) after the Investigations Illustrated in Figure 7.66

7.6.3 Changes in Cracking Product Branching Selectivity

In so far as the branching selectivities are concerned, Figures 7.98 through 7.101 indicate that none of the zeolites tested in this investigation showed any significant changes with deactivation.

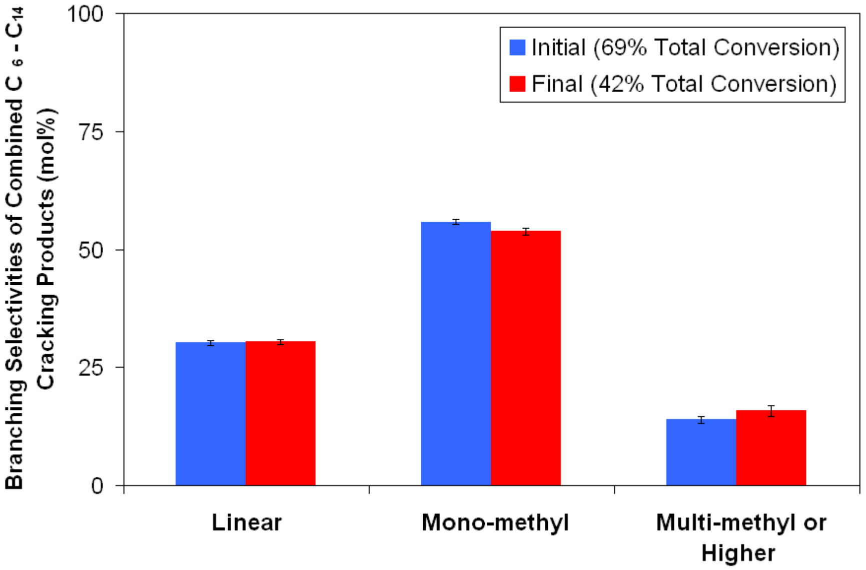

Figure 7.98: Changes in Cracking Product Branching Selectivities with Deactivation for a Loading of 0.800 g H-MFI-90, 0.119 g 5 wt% Pt/SiO_2, 0.667 g SiO_2 Diluent (at a temperature of 250°C, total pressure of 40 bar and a H_2 : n-C_{16} molar feed ratio of 10 : 1) after the Investigations Illustrated in Figure 7.63

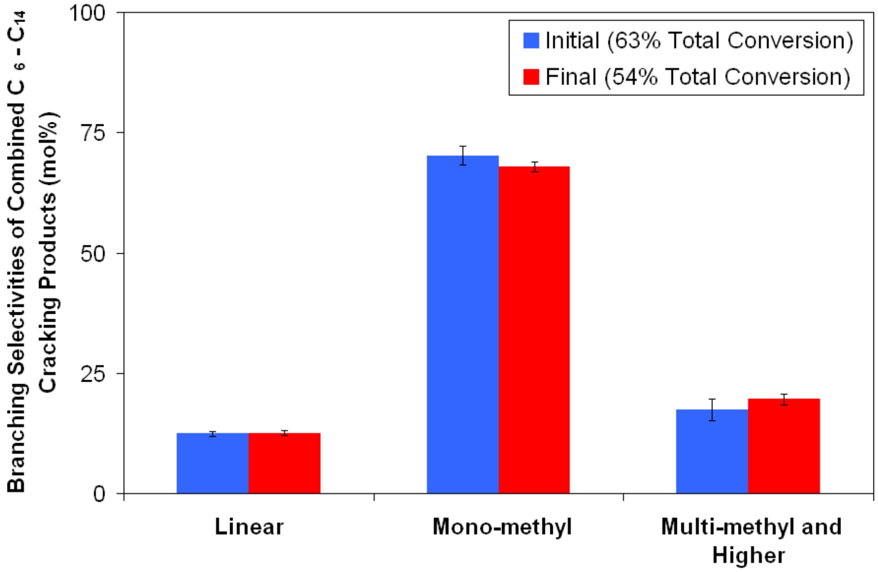

Figure 7.99: Changes in Cracking Product Branching Selectivities with Deactivation for a Loading of 0.229 g H-BEA-25, 0.119 g 5 wt% Pt/SiO_2, 0.999 g SiO_2 Diluent (at a temperature of 250°C, total pressure of 40 bar and a H_2 : n-C_{16} molar feed ratio of 10 : 1) after the Investigations Illustrated in Figure 7.64

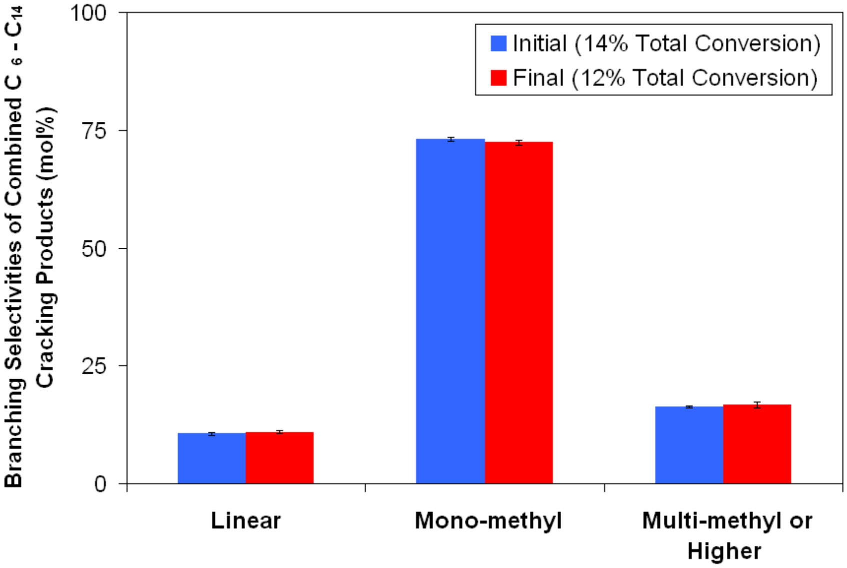

Figure 7.100: Changes in Cracking Product Branching Selectivities with Deactivation for a Loading of 0.794 g H-USY, 2.683 g 5 wt% Pt/SiO_2, 1.967 g SiO_2 Diluent (at a temperature of 250°C, total pressure of 40 bar and a H_2 : n-C_{16} molar feed ratio of 10 : 1) after the Investigations Illustrated in Figure 7.65

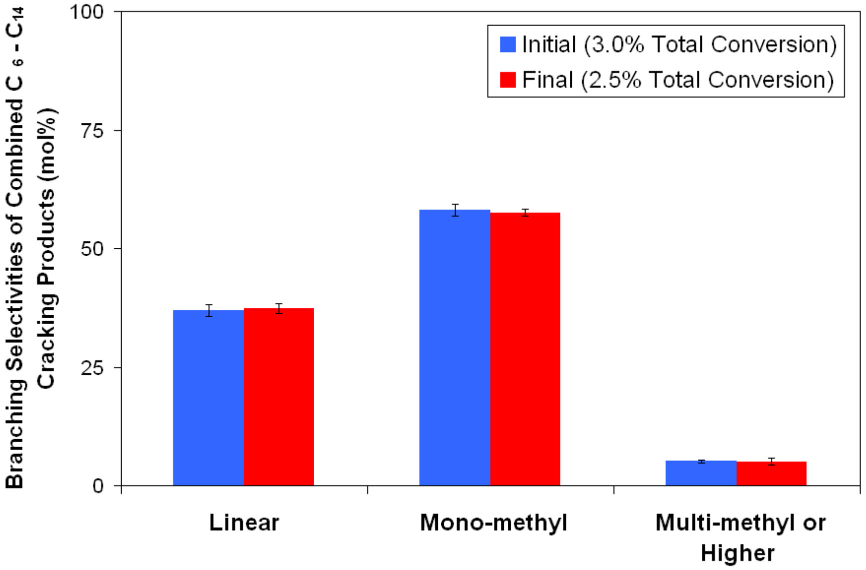

Figure 7.101: Changes in Cracking Product Branching Selectivities with Deactivation for a Loading of 4.169 g H-MOR-20, 2.683 g 5 wt% Pt/SiO_2, no Diluent (at a temperature of 250°C, total pressure of 40 bar and a H_2 : n-C_{16} molar feed ratio of 10 : 1) after the Investigations Illustrated in Figure 7.66

Learning without thought
Is labour lost;
Thought without learning
Is perilous.
Confucius (551 BC - 479 BC),
The Confucian Analects

8

Discussion

8.1 Suitability, Applicability and Reliability of Experimental Apparatus and Programme

From the results obtained (presented in Chapter 7) it was clear that the experimental apparatus (designed, constructed and commissioned for this investigation as indicated in Chapter 5) was well suited for this investigation into the effects of zeolite type on the hydrocracking of the Fischer-Tropsch wax model compound, n-hexadecane. This was due to the apparatus affording the ability to accurately control the reaction conditions, thereby allowing for the establishment of a stable, reproducible operating environment wherein the effects of the differences in the four zeolites (H-MFI-90, H-BEA-25, H-USY and H-MOR) being evaluated on the reaction system could be ascertained, with the on-line analysis of the reactor effluent allowing for the collection of the data required for comparisons in terms of activity, carbon number distribution and branching selectivity to be drawn. These comparisons were only possible given that all of the zeolite/supported-metal catalyst loadings achieved stable operational states during this investigation, exhibiting relatively constant activity with time, as indicated by the results in Section 7.2, (assuming no deliberate variations to operating conditions were made).

These catalyst loadings were not ideal however, being calculated based on provisional assumptions regarding the dispersion of the supported Pt and the SiO_2/Al_2O_3 ratio of each of the zeolites. This was a necessary step as detailed analytical data regarding the metal and acid co-catalysts was not available from the outset. Unfortunately, these initial assumptions were slightly flawed (as indicated in Tables 6.6, 6.7 and 6.8), resulting in the desired methodology of maintaining constant metal:acid site ratios and constant numbers of active acid sites in all catalyst charges not being achieved. As may be seen from the results presented in Section 7.3, and discussed in Section 8.2, however, the variations in activity observed between the different zeolite co-catalysts is far greater than may be accounted for by differences in acid site numbers. Likewise, the selectivities in terms of product carbon number distributions and product branching , being presented in Sections 7.4 and 7.5 respectively and discussed in Section 8.3, are compared at constant conversion, reducing the direct influence of these loading variations. Nevertheless, the implications of these differences in the metal:acid site ratio are discussed in Section 8.5.

8.2 Catalytic Activity

The results presented in Figures 7.67 through 7.69 clearly illustrate that the catalytic activity of the zeolites tested, in terms of the total conversion exhibited at any given space velocity, may be ranked as H-MFI-90 $>$ H-BEA-25 $\gg$ H-USY $>$ H-MOR-20. These differences in activity may be due to the various factors influencing the system, with the foremost among these being the acidity and unique pore geometry of each zeolite sample.

8.2.0.1 The Influence of Zeolite Acidity

The acidity of each of the four zeolites evaluated in this investigation, by virtue of the number and strength of acid sites as dictated by the lattice aluminium content of each, may have played a role in the activity trends observed. This is due to the relationship (discussed in Section 2.4.2 and depicted in Figure 2.20) whereby a high lattice aluminium content in the zeolite (i.e. a low lattice SiO_2/Al_2O_3 ratio) manifests as a high number of acid sites but of low individual strength, thereby resulting in a low overall acidity, and hence low activity, of the zeolite. On the other hand, a low lattice aluminium content (i.e. high lattice SiO_2/Al_2O_3 ratio) manifests as a small number of acid sites with high individual strength, which again results in a low overall acidity and hence a zeolite with a low activity. The change in activity with a unidirectional change (over a sufficiently large range) in the lattice SiO_2/Al_2O_3 ratio would thus be anticipated to pass through a maximum (analogous to that presented by van Bekkum *et al.* (2001) as illustrated in Figure 2.20).

The number of acid sites for each of the four zeolites evaluated in this investigation is represented by their respective acid site densities as presented in Table 6.6. As such, in terms of the number of acid sites per gram, the zeolites may be ranked as H-USY > H-MOR-20 > H-BEA-25 > H-MFI-90. Given the relatively large range of these acid site densities (with that of H-USY being approximately 8 fold higher than that of H-MFI-90), one would anticipate the activities of the zeolites to either pass through a maximum, decline steadily, or increase steadily for the zeolites in this order.

The activities of the zeolites (presented in Section 7.3) do not, however, follow any of these three trends, being ranked instead as H-MFI-90 > H-BEA-25 $\gg$ H-USY > H-MOR-20. Thus, whilst the effect of zeolite acidity may explain the increased activity of H-MFI-90 over H-BEA-25, and H-MFI-90 and H-BEA-25 over H-USY, it does not explain the reduced activity of H-MOR-20, which breaks the anticipated trend by presenting the minimum activity of the four zeolites.

However, as may be seen from Figure 2.20, there exists a great deal of variation and uncertainty around the relationship between the lattice aluminium content and observed activity for various zeolite types and thus, in the case of the zeolites utilised in this investigation, whilst the different acidities almost certainly have an influence on the activities, it is unlikely that this factor alone is responsible for the activity trends observed.

8.2.0.2 The Influence of Zeolite Pore Geometry

Another explanation for the observed activity trends stems from the unique pore geometry (in terms of pore size, shape and channel interconnectivity) of each of the various zeolites investigated. These geometries (described in Section 2.4.1 and presented in Figures 2.15 through 2.18) influence the activity of the catalysts through variations, not only in the overall adsorption constants of the hydrocarbon species into the pore channels, but in the orientation of these adsorbed species within the pores.

These phenomena (as discussed in Section 2.4.5 and illustrated in Figures 2.28 and 2.29) manifest by virtue of the more spatially restrictive medium pores of the H-MFI and H-BEA inhibiting the degree to which the adsorbed hydrocarbon chains are able to distort within the pores, forcing them to instead maintain an "ideal adsorption configuration". This ideal configuration represents that orientation of the molecules within the pores which affords maximum adsorbate-surface contact, thereby maximising the rate of reaction by promoting contact between the adsorbed hydrocarbon and active surface sites. In the wide pore H-USY and H-MOR, however, these molecules are able to bend, twist and otherwise distort within the less spatially restrictive pores, intersections and, in the case of H-USY, supercages. This distortion not only reduces the adsorbate-surface contact (resulting in a decline in activity by reducing the probability of the adsorbed molecule encountering an active surface site), but also block regions of potentially active surface from other adsorbed molecules.

Furthermore, spatial restrictions imposed on the reaction intermediates in narrower pore systems are also believed to affect both the rates of reaction and the product distribution, a phenomenon known as transition state shape selectivity (as discussed in Section 2.4.3 and illustrated in Figure 2.23).

With these points in mind, the activity trends obtained in this investigation indicate some form of counterinteraction between the various pore geometry related factors influencing the overall activity of each zeolite. Thus, whilst the H-MFI has the most restrictive pores of the four zeolites evaluated (with an average pore size of only 5.5 Å, as indicated in Section 2.4.1.3 and Figure 2.17), and is hence subject to some degree of activity inhibition due to transition state shape selectivity (i.e. with the more restrictive pores inhibiting the degree to which hydrocracking may proceed via the most rapid mechanism of tertiary-tertiary carbenium ion β-scission due to the restricted extent to which isomerisation of individual molecules may occur within the pores, as discussed in Section 2.2.1 and illustrated in Figure 2.4), it nonetheless was observed to have the highest total conversion under the conditions investigated. This eventuality is believed to be due to reaction promotion resulting from the stronger adsorption of the linear feed molecules in the narrower pores of the H-MFI (as compared to the H-USY and H-MOR-20), with these pores forcing adsorbed molecules to assume the aforementioned "ideal adsorption configuration", thereby maximising their contact with the internal zeolite surface and hence the probability of contacting an active acid site.

This phenomenon of promotion by adsorption may also be responsible for the H-BEA exhibiting an elevated activity over both the H-USY and H-MOR for, whilst the majority of pores in H-BEA are approximately 7.7 x 6.6 Å across, around one third are of 5.6 Å dimensions very similar to H-MFI (as indicated in Section 2.4.1.1 and Figure 2.15), with stronger adsorption and more ideal configuration of hydrocarbon species within these narrower pores possibly promoting the overall activity of the H-BEA in a manner similar to that of the H-MFI.

H-USY and H-MOR, however, possess no such smaller pores, and it ay be argued that the difference in activity between these two zeolites is due solely to the degree of mass transfer control occurring within their respective pore networks (with this topic discussed in Section 2.4.4). Thus, whilst the structure of H-USY exhibits large 11.8 Å supercages with interconnecting 7.4 Å "windows", H-MOR is limited to an almost one-dimensional structure, with 7.0 x 6.5 Å channels and small 5.4 Å side-pockets being connected by 3 Å channels which are, for all intents and purposes, completely inaccessible to hydrocarbons. From this perspective, it is thus clear that whilst the structure of H-USY allows for rapid, unrestricted diffusion of hydrocarbons, that of H-MOR imposes some degree of inhibition on this diffusion, and hence on the reaction itself, thereby reducing the observed activity of this zeolite.

8.2.0.3 The Relationship between Feed Isomerisation and Cracking

Although not one of the key points of focus in this investigation, the examination of the extent to which skeletal isomerisation of the linear feedstock contributed to the total conversion, as presented in Figure 7.70 (with the ideal relationship in Figure 2.6), was found to be of interest. This observation seems to indicate that, as anticipated for a carbenium ion hydrocracking mechanism (see Sections 2.2.1 and 2.2.2), the reaction proceeds via isomerised intermediates and, as the degree of isomerisation of the feed increases with increasing conversion, so does the consumption of these more isomerised species. It is further postulated that the observed lower extent of feed isomerisation exhibited by MFI is due to the inhibition of significant isomerisation by the more spatially restrictive pore system, implying that these species cannot isomerise to any greater extent at higher conversions and hence their intrinsic rates of consumption remain relatively constant for all observed conversions.

8.3 Cracking Product Selectivity

Of primary concern regarding the products from the various zeolites in this investigation were the carbon number distributions and the branching selectivities, for both have a significant influence on the overall viability and economic feasibility of any process desiring to convert FT wax into high quality distillate fuels by selective hydrocracking.

8.3.0.4 Carbon Number Distribution

The carbon number distribution of the products obtained from each catalyst is important for, in a process where a feedstock of FT wax is to be hydrocracked, it is highly undesirable to crack that wax to such an extent that only low value short-chain products are produced, with a flat distribution (such as that presented in Figure 2.5) being the most desirable outcome.

Of the product spectra obtained from the zeolites evaluated in this investigation (compared at a constant cracking conversion of 20%, obtained by inter- or extra-polation of the data as discussed in Section 6.5.2.4, with the results presented in Section 7.4 and a direct comparison in Figure 7.75), that of H-USY was the closest to this ideal distribution, with H-MFI and H-BEA exhibiting a progressively higher yields of lighter species, and H-MOR exhibiting the greatest tendency to produce lighter fragments. These distributions are believed to be due predominantly to the effect which the unique pore geometry of each zeolite had on the reaction.

Along this line of reasoning, the large, unrestrictive supercages and inter-connecting windows of H-USY, combined with the system of mesopores introduced during the ultra-stabilisation process (see Section 2.4.1.2), allowed any product fragments forming within the pore structure to diffuse rapidly out of the crystals, minimising the extent of consecutive cracking reactions.

H-MFI and H-BEA, whilst possessing far more restrictive pore systems in terms of dimensions, maintain a high degree of inter-connectivity within these pores. Thus, any fragments formed within the pore networks of these two zeolites encounter greater, but not yet excessive, diffusional resistance (with respect to fragments travelling through the H-USY pore system) and hence undergo some degree of consecutive cracking reaction as they encounter active sites during their diffusion out of the crystals, thereby cracking some of the potentially longer primary fragments into smaller species. This phenomenon is well understood and discussed in Section 2.4.4, being exemplified in Figure 2.27 wherein the longer primary fragments are analogous to the reactive intermediate, B. As such, the increase in the diffusional resistance of H-MFI and H-BEA over H-USY corresponds to a reduction in the D_1/D_2 ratio, resulting in a reduced yield of B (the longer primary cracking products) and a simultaneous increase in the yield of shorter consecutive cracking fragments.

H-MOR, however, whilst possessing pores of a similar size to the larger pores of H-BEA, has a very poorly interconnected pore structure in so far as hydrocracking is concerned for, whilst the 7 Å pores are connected, although not directly, to one another, the inter-connecting channels are only 3 x 3 Å, making them essentially inaccessible in this reaction, and rendering the entire pore structure virtually one-dimensional. This limitation results in cracking products experiencing far greater diffusional resistances along their path out of the pore network, allowing consecutive cracking reactions to occur to a greater extent than in any of the previous three zeolites, and hence rendering an observed carbon number distribution shifted heavily in favour of the lighter fragments.

The methane yields exhibited by each catalyst (presented in Figure 7.76 as a correlation between yield and site hourly space velocity). As may be seen, a rather trivial general trend exists indicating an increase in methane formation with decreasing space velocity. The trend in the relative amounts of methane formed over each zeolite, however, does not correspond to the trend relating their overall bifunctional activities. As such, it is believed that the formation of methane within this system was due almost exclusively to methanolysis occurring on the active sites of the platinum for, as the Pt/SiO_2 was identical for all zeolite comparisons, the production of methane would be relatively unhindered by which zeolite was present, establishing the rather simple trend observed (increasing methane yield with decreasing space velocity) with little correlation to the overall catalyst activity trend (with the small amounts of methane having little effect on the overall system). It should, however, be noted that regardless of the source of the methane, the small amounts observed make any definitive conclusions difficult to substantiate without further investigation.

8.3.0.5 Branching Selectivity

The branching selectivity of the product is of concern in the production of middle distillate fuels as it dictates the quality of the fuel for, whilst linear species exhibit higher cetane numbers, they are also characterised by precipitating out of the fuel (and subsequently blocking fuel lines, fuel filters, etc.) at temperatures higher than more branched hydrocarbons of the same carbon number (as discussed in Section 2.1.1). These branched species, however, have comparably poor cetane numbers. As such, a product comprising a mixture of both linear and moderately branched hydrocarbons is usually desired, possibly tending towards more of the linear components as such a fuel may serve as a blending medium to be mixed with, and thereby improve the cetane number (and hence the quality and value) of, less valuable hydrocarbons.

Of the zeolites examined in this investigation (compared at a constant total conversion of 20%, obtained by inter- or extra-polation as discussed in Section 6.5.2.4, with the results presented in Section 7.5 and direct comparisons in Figures 7.91 and 7.92), the H-BEA-25, H-USY and H-MOR-20, all exhibited roughly the same branching selectivities, whilst the H-MFI-90 was observed to exhibit a product with a significantly higher proportion of linear species. These trends held for both the combined C_4 and C_5 products and the combined C_6 to C_{14} products as seen in Figures 7.91 and 7.92 respectively (with the reasons for this segregation of the product being discussed in Section 7.5), wherein the H-MFI-90 exhibited linear to mono-methyl branched molar ratios of 1:0.75 and 1:2 respectively. Furthermore, all four of the zeolites were found to exhibit roughly the same low selectivity towards the higher branched species (illustrated in Figure 7.91). These observations are postulated to be due to the influence of the pore geometries of each zeolite.

In the cases of H-USY and H-MOR-20, the large, less restrictive pores allow for the formation of highly branched reaction intermediates, with these highly branched species cracking rapidly (as discussed in Section 2.4.3) and thus not observed to any greater extent in the product spectrum. Furthermore, the lack of spatial restriction within the pore systems of these two zeolites affords little imposition on the cracking reaction to favour the formation of linear fragments.

H-MFI-90, on the other hand, has a pore structure comprised entirely of spatially restrictive medium pores wherein the very formation of the more isomerised species is inhibited by transition state shape selectivity (as discussed in Section 2.4.3). Furthermore, although greater extents of isomerisation may occur within the 9 Å pore intersections, the only way highly isomerised fragments formed in these regions may diffuse out of the pore system is through the narrower pores. Thus, in a phenomenon known as product shape selectivity (discussed in Section 2.4.3 and illustrated in Figure 2.21b), the vast majority of such fragments would either react into smaller species, or isomerise into more compact species before being able to leaving the zeolite crystallites.

It is believed that, in the case of H-BEA-25, the relatively high overall activity of the zeolite in this investigation is due to promotion by adsorption within the medium pores of its pore system (as discussed in Section 8.2.0.2), whilst the selectivity manifests due to the presence of the larger pores within the pore network. These larger pores not only afford a less spatially restrictive environment wherein branched species may form but, in intersecting with the medium pores in the structure, allow the lesser branched fragments initially formed within these more spatially restrictive medium pores the opportunity to isomerise further before diffusing out of the crystal structure. These effects results in H-BEA-25 exhibiting a branching selectivity almost identical to that of the "large-pore-only" H-USY and H-MOR-20.

8.4 Catalyst Deactivation

As indicated in Section 7.6, the data regarding the deactivation of the four zeolites evaluated in this investigation is somewhat inconclusive. This uncertainty stems predominantly from the observation that whilst the most active zeolite, H-MFI-90, was observed to deactivate to the least extent in terms of its loss in initial activity (as seen in Figure 7.93) and the least active zeolite, H-MOR-20, deactivated to the greatest extent, the H-BEA-25 and H-USY were observed to deactivate to approximately the same extent despite their variations in observed activity.

Furthermore, despite the variations observed in terms of activity loss, it was noted that both the carbon number distributions (Figures 7.94 through 7.96) and the branching selectivities (Figures 7.98 through 7.100) of the four zeolites appear to remain relatively unchanged during the deactivation process.

For the cracking product carbon number distributions, the product exhibited by each of the "deactivated" catalysts did not show significant variation from the initial distributions obtained at similar cracking conversions.

This information may be useful in determining the mechanism by which deactivation occurs as it suggests, for instance, that activity is lost through the loss of active sites or their obstruction through occlusion by coke or the blockage of pores by coking rather than by gradual pore channel, cage and intersection narrowing. This postulation may be supported by the observation that the H-MFI-90 deactivates to the least extent, with its spatially restrictive medium pores inhibiting the formation of bulky coke precursors whilst the three-dimensional, highly interconnected structure allows for the flow of reacting species around pore blockages with relative ease. The opposite interpretation may be applied to the H-MOR-20, which deactivates to the greatest extent, by noting that the larger, less spatially restrictive pores of this zeolite offer little inhibition to the formation of bulky coke precursors, whilst the essentially uni-dimensional pore structure implies that pore blockages either prevent access to large portions of the potentially active internal surface or necessitate the flow of reacting species by longer paths to circumvent the obstruction. The H-BEA-25 and H-USY, however, are both possessed of pores larger and less spatially restrictive than those of the H-MFI-90, yet also exhibit three-dimensional, highly interconnected structures. It may be postulated that, for these reasons, the H-BEA-25 and H-USY were observed to deactivate to a greater extent than the H-MFI-90, yet to a lesser extent than the H-MOR-20.

These postulations are, however, very speculative, and detailed studies together with spent catalyst characterisation would be required to determine the most plausible deactivation mechanism.

8.5 The Influence of the Metal to Acid Site Balance

In this investigation, it was desired to maintain a constant ratio between the number of metal and the number of acid sites for all catalyst loadings. As discussed in Sections 6.1.3 and 8.1, however, the loadings were calculated based on provisional assumptions regarding the dispersion of the Pt on the supported metal catalyst and the SiO_2/Al_2O_3 ratios of the zeolites. Detailed analytical data of the metal and acid co-catalysts revealed, as indicated in Tables 6.6 and 6.7, that the actual metal:acid site ratio was far lower than the intended value of 0.187 (see Section 6.1.3).

This unforeseen variation in the ratio of the hydrogenating/dehydrogenating metal function and the isomerising/cracking acid function are numerous, with the affects on the activity, carbon number distribution and deactivation being perhaps the most conspicuous and transparent.

In terms of the activity, the insufficient metal function in the reaction would result in the rate of formation of dehydrogenated feed (per the classical mechanism) or activated hydrogen species (per the spillover mechanism) being too low to sustain the reaction at an optimum level.

The influence on the carbon number distribution is by virtue of the saturation of the olefinic cracking products. Herewith, the excess acid function would have resulted in the more rapid formation of unsaturated cracking products, with there being insufficient metal function present to rehydrogenate (per the classical mechanism) or provide sufficient activated hydrogen to saturate (per the spillover mechanism) the primary cracking fragments. This is evidenced by the product carbon number distributions being observed to be approximately equivalent, from C_4 onwards, regardless of conversion and zeolite type (as seen in Figures 7.71 through 7.75), indicating that there was insufficient "quenching" of the cracking reaction, with only the multi-cleaved equilibrium species being rapidly quenched and not the primary cracking fragments.

The deactivation is influenced in a similar manner to the carbon number distribution in that, with the over-abundance of the acid function, olefinic cracking products are forming at a rate whereby they are not immediately rehydrogenated by the metal function (per the classical mechanism) or saturated by activated hydrogen species (per the spillover mechanism). This implies that, before the metal function is able to rehydrogenate/saturate these olefinic cracking products, these fragments are afforded a chance to react with one another, forming large, bulky molecules which deposit as coke, thereby reducing catalyst activity.

It is thus clear that, in future investigations of this nature, it is vital that the catalysts to be utilised be accurately and extensively analysed prior to the commencement of experimentation, so as to ensure that the desired catalyst loading specifications be achieved. Furthermore, it should be noted that this methodology assumes that there is a consistency in the “strength” of the metal and acid sites between all of the loadings. This assumption is justified for the metal in that samples from a single batch of Pt/SiO_2 were utilised in all investigations (see Section 6.1.2.2), but is perhaps not so valid for the zeolites as variations may present due to differences in acid site number and strength interactions or manifestations of various adsorption or diffusion phenomena. As such, it would be far more appropriate to establish a standardised ratio determined on the basis of individual zeolite activity rather than solely on the number of acid sites, with this latter technique perhaps not being as consistent between evaluations as it superficially appeared.

It is no good to try to stop
knowledge from going forward.
Ignorance is never better
than knowledge.
Enrico Fermi (1901 - 1954)

9

Conclusions and Recommendations

This work has shown that acid zeolites with pores smaller than those utilised in the hydrocracking of crude-oil derived feedstocks, such as the medium pore H-MFI, do indeed show potential for the processing of FT wax into middle distillate fuels and that this is predominantly due to the linearity of the FT wax feedstock.

It has been shown that the zeolites with more restrictive medium pores (such as the entire pore system of H-MFI and a portion of the pores of H-BEA) show enhanced overall activity in the hydrocracking of long linear paraffinic feed molecules. This phenomenon is theorised to be due to the more orderly and efficient configuration of the adsorbed molecules within these pores enhancing the activity by strengthening adsorption (through greater adsorbate-zeolite interaction) and maximising contact with the zeolite surface, thereby optimising the usage of available active acid sites.

This adsorption effect appears to be sufficiently influential in promoting the reaction that it is able to surpass the inhibitory effect resulting from the hydrocracking reaction occurring in such medium pores having to proceed via less isomerised reaction intermediates (due to spatial restrictions).

Furthermore, it has been seen that a pore system comprised solely of such medium pores (such as H-MFI) has a definite influence on the product branching selectivity, showing a tendency to produce more linear species than the wider pore zeolites tested (H-USY and H-MOR). It also appears that, for zeolites wherein medium pores intersect with wider pores (such as H-BEA), the pore network thus formed allows for promotion of the overall activity through enhanced adsorption (and more idealistic configuration of adsorbed species) in the medium pores whilst the larger pores allow the zeolite to exhibit a product which shows branching selectivities very similar to those zeolites with only large pores.

It is thus recommended that further research be conducted utilising other medium pore zeolites to verify the promotional effects observed in this study, and possibly confirm the postulation that this promotional effect is indeed due to stronger and more idealistic adsorption. It is also recommended that studies utilising such medium pore zeolites be extended to use longer model feedstocks, or possibly even FT wax, to determine the suitability of such catalysts to the hydrocracking of very long n-paraffins (i.e. those with carbon numbers up to approximately 100).

Given the large variations in the provisional metal and acid co-catalyst property assumptions and the actual analytical values determined during the course of this investigation, which resulted in neither the constant metal:acid site ratio nor the constant active acid site loadings being achieved, it is clear that any future work must begin with a comprehensive analysis of all catalysts to be utilised so as to ensure that the desired loading specifications are met. Furthermore, to ensure the reliability of any such future work, it is recommended that the metal:acid site loading ratio be refined in such a way that the ratio of the overall activities of the metal and acid functions be kept constant as opposed to the number of sites of each. This may, for example, be conducted by studying the effect of metal loading on conversion for each of the zeolites to be evaluated. This data would be anticipated to show an increase in the conversion with increasing metal loading, reaching a maximum conversion at the optimum loading ratio, with this loading ratio being lower for loadings incorporating zeolites with inherently less acid functions and higher for those zeolites with more active acid functions.

Finally, for various reasons the deactivation analyses of the catalysts utilised in this investigation were inconclusive, and it is recommended that, following the refinement of the metal:acid loading ratios, these studies be extended to a detailed analysis, including spent catalyst characterisation, to determine the mechanism(s) of deactivation and its effect on the activity and selectivity of the proposed medium pore zeolites in a potential industrial application.

References

Alvarez, F., Ribeiro, F.R., Perot, G., Thomazeau, C. and Guisnet, M., 1996. *Hydroisomerisation and Hydrocracking of Alkanes: 7. Influence of the Balance Between Acid and Hydrogenating Functions on the Transformation of n-Dodecane on Pt/H-Y Catalysts*. Journal of Catalysis, volume 162, pp. 179–189

AT&T Integer Sequence Research Laboratory, 2005. *The Online Encyclopedia of Integer Sequences*.
Available: http://www.research.att.com/ñjas/sequences/A000602
Accessed: 22/11/2008

Bianchi, D., Lacroix, M., Pajonk, G.M. and Teichner, S.J., 1981. *Spilled-Over Hydrogen Transport from Platinum-on-Alumina Catalyst to Methoxylated Silica Aerogel*. Journal of Catalysis, volume 68, pp. 411–418

Böhringer, W., Kotsiopoulus, A., de Boer, M., Knottenbelt, C. and Fletcher, J.C.Q., 2006. *On the Application of Non-Sulphided Base Metal Catalyst for Normal Paraffin Hydrocracking*. In *SACEC 2006, Durban*

Böhringer, W., Kotsiopoulus, A., de Boer, M., Knottenbelt, C. and Fletcher, J.C.Q., 2007. *Selective Fischer-Tropsch Wax Hydrocracking: Opportunity for Improvement of Overall Gas-to-Liquids Processing*. Studies in Surface Science and Catalysis, volume 163, pp. 345–365

Calinescu, R., 2005. *The Legislation Impact on Current Practices Related to Refinery Flaring*.
Available: http://www.mec.utt.ro/˜tmtar/lucrari_avh05/vol II Pdf/6 Politics pdf/6160 Calinescu Rodica.pdf
Accessed: 01/07/2008

Callahan, F., 1998. *Swagelok Tube Fitter's Manual*. Swagelok Company

CEN (European Committee for Standardization), 2004. *DIN EN 590 : 2004 - Diesel Fuel Requirements and Test Methods*.
Available: http://www.cen.eu
Accessed: 02/12/2008

Chao, K., Wu, H. and Leu, L., 1996. *Hydroisomerization of Light Normal Paraffins over Series of Platinum-Loaded Mordenite and Beta Catalysts*. Applied Catalysis A: General, volume 143, pp. 223–243

Chen, D., Moljord, K., Fuglerud, T. and Holmen, A., 1999. *The Effect of Crystal Size of SAPO-34 on the Selectivity and Deactivation of the MTO Reaction*. Microporous and Mesoporous Materials, volume 29, pp. 191–203

Chevron Corporation, 2006. *Diesel Fuel Refining and Chemistry*.
Available: http://www.chevron.com/products/prodserv/fuels/bulletin/diesel/L2_4_6_rf.htm
Accessed: 30/09/2006

Conner, W. and Falconer, J., 1995. *Spillover in Heterogeneous Catalysis*. Chemical Reviews, volume 95, pp. 759–788

Csicsery, S., 1986. *Catalysis by Shape Selective Zeolites - Science and Technology*. Pure and Applied Chemistry, volume 58, no. 6, pp. 841–856

Daubert, T., Danner, R., Sibul, H., Stebbins, C., Rowley, R., Wilding, W., Oscarson, J., Adams, M. and T.L., M., 1999. *Physical and Thermodynamic Properties of Pur Chemicals - Evaluated Process Design Data*. Taylor & Francis de Klerk, A., 2008. *Hydroprocessing Peculiarities of Fischer-Tropsch Syncrude*. Catalysis Today, volume 130, pp. 439–445

De Meyer, K., Chempath, S., Denayer, J., Martens, J., Snurr, R. and Baron, G., 2003. *Packing Effects in the Liquid-Phase Adsorption of* C_5*-*C_{22} *n-Alkanes on ZSM-5*. Journal of Physical Chemistry B, volume 107, pp. 10760–10766

Denayer, J. and Baron, G., 1997a. *Adsorption of Normal and Branched Paraffins in Faujasite Zeolites NaY, HY, Pt/NaY and USY*. Adsorption, volume 3, pp. 251–265

Denayer, J. and Baron, G., 1997b. *Hydrocracking of n-Alkane Mixtures on Pt/H-Y Zeolite: Chain Length Dependence of the Adsorption and the Kinetic Constants*. Industrial and Engineering Chemistry Research, volume 36, pp. 3242–3247

Denayer, J., Bouyermaouen, A. and Baron, G., 1998a. *Adsorption of Alkanes and Other Organic Molecules in Liquid Phase and in the Dense Vapor Phase: Influence of Polarity, Zeolite Topology, and External Fluid Density and Pressure*. Industrial and Engineering Chemistry Research, volume 37, pp. 3691–3698

Denayer, J., Daems, I. and Baron, G., 2006. *Adsorption and Reaction in Confined Spaces*. Oil and Gas Science and Technology, volume 61, pp. 561–569

Denayer, J., De Jonkheere, B., Hloch, M., Marin, G., Vanbutsele, G., Martens, J. and Baron, G., 2002. *Molecular Competition of* C_7 *and* C_9 *n-Alkanes in Vapor- and Liquid-Phase Hydroconversion over Bifunctional Pt-USY Zeolite Catalysts*. Journal of Catalysis, volume 210, pp. 445–452

Denayer, J., Ocakoglu, A., De Jonkheere, B., Martens, J., Thybaut, J., Marin, G. and Baron, G., 2003. *Adsorption Competition Effects in Hydroconversion of Alkane Mixtures on Zeolites*. International Journal of Chemical Reactor Engineering, volume 1. Article: A36

Denayer, J., Souverijns, W., Jacobs, P., Martens, J. and Baron, G., 1998b. *High-Temperature Low-Pressure Adsorption of Branched* C_5*-*C_8 *Alkanes on Zeolite Beta, ZSM-5, ZSM-22, Zeolite Y, and Mordenite*. Journal of Physical Chemistry B, volume 102, pp. 4588–4597

Djumena, S.T., 2004. *Key Activities of the Global Gas Flaring Reduction Partnership*. In *Methane to Markets Ministerial Meeting*.
Available: http://www.methanetomarkets.org/events/2005/all/docs/djumena.pdf
Accessed: 01/07/2008

Dry, M., 2001. *High Quality Diesel via the Fischer-Tropsch Process - A Review*. Journal of Chemical Technology and Biotechnology, volume 77, pp. 43–50

Dry, M., 2003. *Fischer-Tropsch Synthesis - Industrial*. in Encyclopaedia of Catalysis, volume 3, p. 347

IZA (International Zeolite Association - Structure Commission), 2002. *Database of Zeolite Structures*.
Available: http://www.iza-structure.org/databases/
Accessed: 21/10/2008

Kaldany, R., 2001. *Global Gas Flaring Reduction Initiative*. In *Convening of the Oil, Gas and Chemicals Department of the World Bank Group*.
Available:
http://siteresources.worldbank.org/INTGGFR/64199955-1103819378762/20298989/MarRas.pdf
Accessed: 01/07/2008

Kotrel, S., Knözinger, H. and Gates, B., 2000. *The Haag-Dessau Mechanism of Protolytic Cracking of Alkanes*. Microporous and Mesoporous Materials, volume 35-36, pp. 11–20

Kusakari, T., Tomishige, K. and Fujimoto, K., 2002. *Hydrogen Spillover Effect on Cumene Cracking and n-Pentane Hydroisomerization Over Pt/*SiO_2 *+ H Beta*. Applied Catalysis A: General, volume 224, pp. 219–228

Leckel, D., 2007. *Low-Pressure Hydrocracking of Coal-Derived Fischer-Tropsch Waxes to Diesel*. Energy and Fuels, volume 21, pp. 1425–1431

Levy, R.B. and Boudart, M., 1974. *The Kinetics and Mechanism of Spillover*. Journal of Catalysis, volume 32, pp. 304–314

Martens, J. and Jacobs, P., 1990. *Conceptual Background for the Conversion of Hydrocarbons on Heterogeneous Acid Catalysts*. Theoretical Aspects of Heterogeneous Catalysis, pp. 52–109

Martens, J. and Jacobs, P., 1997. *Reaction Mechanisms of Acid-Catalysed Hydrocarbon Conversions in Zeolites*. in Ertl, G., Knzinger, H. and Weitkamp, J., Handbook of Heterogeneous Catalysis, volume vol. 3

Martens, J. and Jacobs, P., 2001. *Introduction to Acid Catalysis with Zeolites in Hydrocarbon Reactions*. Studies in Surface Science and Catalysis, volume 137, pp. 633–671

Mills, G., Heinemann, H., Milliken, T. and Oblad, A., 1953. *(Houdriforming Reactions) Catalytic Mechanism*. Journal of Industrial and Engineering Chemistry, volume 45, pp. 134–137

Möller, K., Böhringer, W., Schnitzler, A., van Steen, E. and O'Connor, C., 1999. *The Use of a Jet Loop Reactor to Study the Effect of Crystal Size and the Co-feeding of Olefins and Water on the Conversion of Methanol over H-ZSM-5*. Microporous and Mesoporous Materials, volume 29, pp. 127–144

ORNL (Oak Ridge National Laboratory), 2000. *An Emissions Mission: Solving the Sulfur Problem*. Oak Ridge National Laboratory Review, vol. 33.
Available: http://www.ornl.gov/info/ornlreview/v33_3_00/emissions.htm
Accessed: 11/10/2006

Park, K. and Ihm, S., 2000. *Comparison of Pt/zeolite Catalysts for n Hexadecane Hydroisomerization*. Applied Catalysis A: General, volume 203, pp. 201–209

PFC Energy, 2007. *Using Russia's Associated Gas*. World Bank Group.
Available: http://siteresources.worldbank.org/INTGGFR/Resources/pfc_energy_report.pdf
Accessed: 26/08/2008

Pinna, F., 1998. *Supported Metal Catalyst Preparation*. Catalysis Today, volume 41, pp. 129–137

Rastelli, H., Lok, B., Earls, D.J. and J.T., M., 1982. *Characterization of Zeolitic Acidity: The Cracking of 2 mole% n-Butane over A Fixed Zeolite Bed*. Canadian Journal of Chemical Engineering, volume 60, p. 44

Roessner, F. and Roland, U., 1996. *Hydrogen Spillover in Bifunctional Catalysis*. Journal of Molecular Catalysis A: Chemical, volume 112, pp. 401–412

Roland, U., Braunschweig, T. and Roessner, F., 1997. *On the Nature of Spilt Over Hydrogen*. Journal of Molecular Catalysis A, volume 127, pp. 61–84

Rollmann, L. and Walsh, D., 1979. *Shape Selectivity and Carbon Formation in Zeolites*. Journal of Catalysis, volume 56, pp. 139–140

Scherzer, J. and Gruia, A., 1996. *Hydrocracking Science and Technology*, chapter 3. Marcel Dekker Inc., New York, 1st edition

Sie, S., Senden, M. and van Wechem, H., 1991. *Conversion of Natural Gas to Transportation Fuels via the Shell Middle Distillate Synthesis Process (SMDS)*. Catalysis Today, volume 8, pp. 371–394

Sinfelt, J., 1973. *Specificity in Catalytic Hydrogenolysis by Metals*. Advances in Catalysis, volume 23, p. 91

Sinnot, R., 2005. *Coulson and Richardson's Chemical Engineering Series: Chemical Engineering Design*, volume 6. Elsevier Butterworth-Heinemann, 4th edition

Steinberg, K., Mroczek, U. and Roessner, F., 1990. *Aromatization of Ethane on Platinum Containing ZSM-5 Zeolites*. Applied Catalysis, volume 66, pp. 37–44

USA (Senate of the United States of America), 2007. *H.R. 547: Advanced Fuels Infrastructure Research and Development Act*.
Available: http://www.govtrack.us/congress/billtext.xpd?bill=h110-547
Accessed: 03/06/2007

van Bekkum, H., Flanigen, E., Jacobs, P. and Jansen, J. (eds.), 2001. *Introduction to Zeolite Science and Practice*. Elsevier, 2nd edition

Wei, J., 1994. *Nonlinear Phenomena in Zeolite Diffusion and Reaction*. Industrial and Engineering Chemistry Research, volume 33, pp. 2467–2472

Wei, J., 1996. *Adsorption and Cracking of n-Alkanes over ZSM-5: Negative Activation Energy of Reaction*. Chemical Engineering Science, volume 51, no. 11, pp. 2995–2999

Weisz, P. and Prater, C., 1954. *Interpretation of Measurements in Experimental Catalysis*. Advances in Catalysis, volume 6, pp. 143–196

Weisz, P. and Swegler, E., 1957. *Stepwise Reaction on Separate Catalytic Centres: Isomerisation of Saturated Hydrocarbons*. Science, volume 126, pp. 31–32

Weitkamp, J., Jacobs, P. and Martens, J., 1983. *Isomerization and Hydrocracking of C_9 through C_{16} n-Alkanes on Pt/HZSM-5 Zeolite*. Applied Catalysis, volume 8, pp. 123–141

Wheeler, A., 1951. *Reaction Rates and Selectivity in Catalyst Pores*. Advances in Catalysis, volume 3, p. 250

World Bank Group, 2003. *Kyoto Mechanisms for Flaring Reductions*.
Available: http://go.worldbank.org/NIARKC2EC0
Accessed: 01/07/2008

Zhang, W. and Smirniotis, P.G., 1999. *Effect of Zeolite Structure and Acidity on the Product Selectivity and Reaction Mechanism for n-Octane Hydroisomerization and Hydrocracking*. Journal of Catalysis, volume 182, pp. 400–416

Appendices

A

Background Calculations

Herein are contained the various calculations pertaining to the determination of the nitrogen dilution flow rates, the heats of reaction and the mass loadings of the various catalyst components.

A.1 Dilution Flow Rates

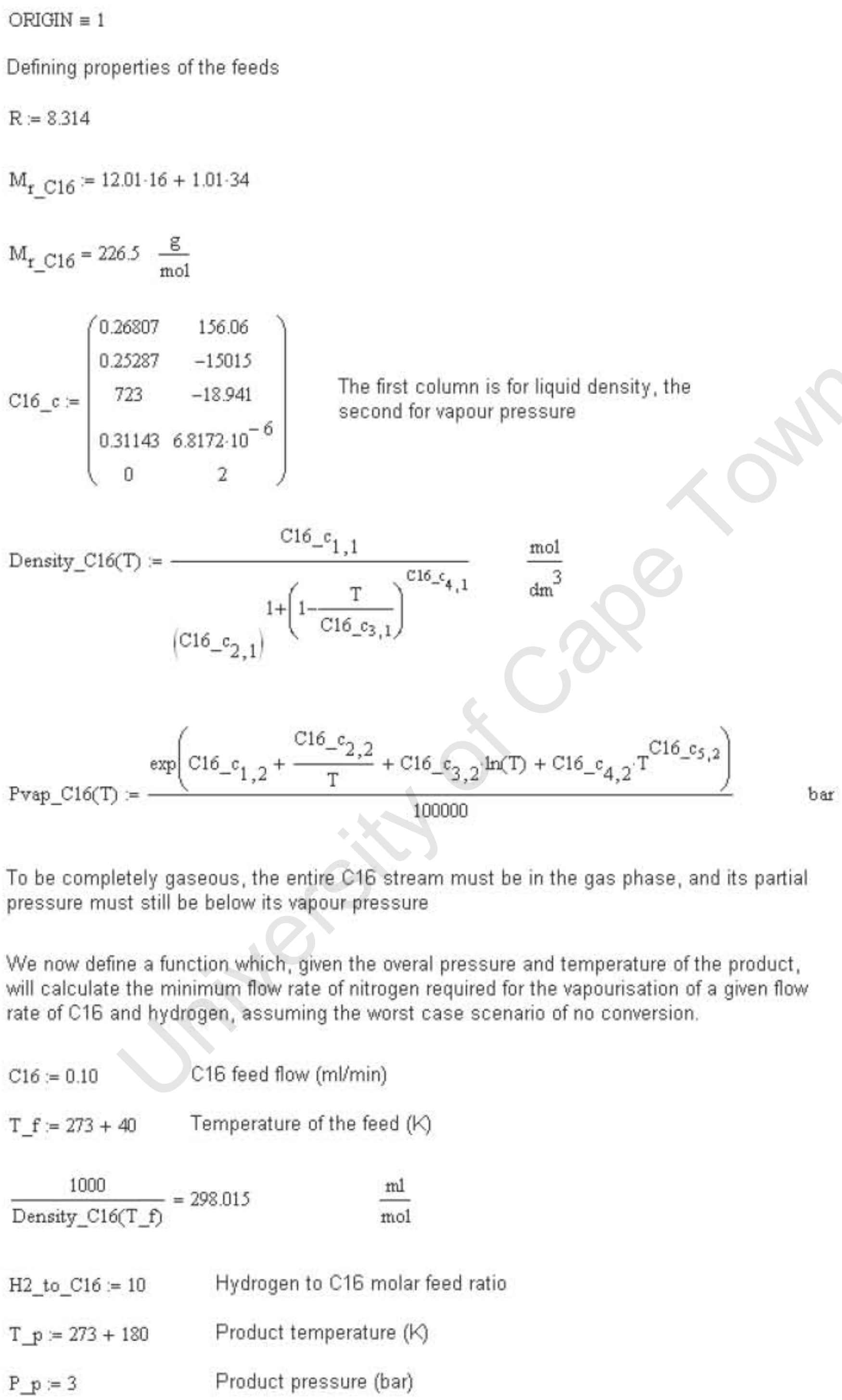

ORIGIN ≡ 1

Defining properties of the feeds

$$R := 8.314$$

$$M_{r\_C16} := 12.01 \cdot 16 + 1.01 \cdot 34$$

$$M_{r\_C16} = 226.5 \quad \frac{g}{mol}$$

$$\text{C16\_c} := \begin{pmatrix} 0.26807 & 156.06 \\ 0.25287 & -15015 \\ 723 & -18.941 \\ 0.31143 & 6.8172 \cdot 10^{-6} \\ 0 & 2 \end{pmatrix}$$

The first column is for liquid density, the second for vapour pressure

$$\text{Density\_C16}(T) := \frac{\text{C16\_c}_{1,1}}{\left(\text{C16\_c}_{2,1}\right)^{1+\left(1-\frac{T}{\text{C16\_c}_{3,1}}\right)^{\text{C16\_c}_{4,1}}}} \qquad \frac{mol}{dm^3}$$

$$\text{Pvap\_C16}(T) := \frac{\exp\left(\text{C16\_c}_{1,2} + \frac{\text{C16\_c}_{2,2}}{T} + \text{C16\_c}_{3,2} \cdot \ln(T) + \text{C16\_c}_{4,2} \cdot T^{\text{C16\_c}_{5,2}}\right)}{100000} \qquad bar$$

To be completely gaseous, the entire C16 stream must be in the gas phase, and its partial pressure must still be below its vapour pressure

We now define a function which, given the overal pressure and temperature of the product, will calculate the minimum flow rate of nitrogen required for the vapourisation of a given flow rate of C16 and hydrogen, assuming the worst case scenario of no conversion.

$\text{C16} := 0.10$ C16 feed flow (ml/min)

$\text{T\_f} := 273 + 40$ Temperature of the feed (K)

$$\frac{1000}{\text{Density\_C16}(\text{T\_f})} = 298.015 \qquad \frac{ml}{mol}$$

$\text{H2\_to\_C16} := 10$ Hydrogen to C16 molar feed ratio

$\text{T\_p} := 273 + 180$ Product temperature (K)

$\text{P\_p} := 3$ Product pressure (bar)

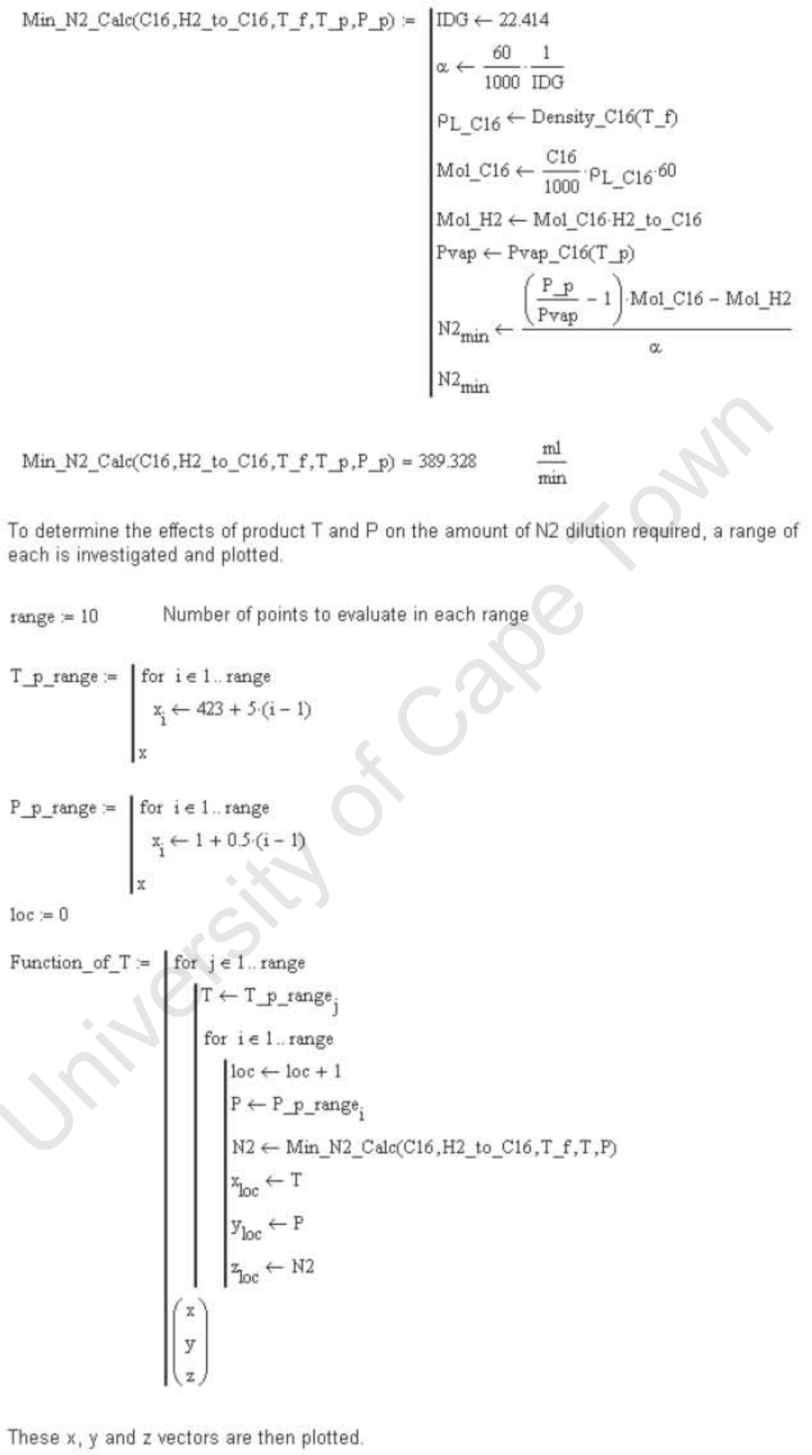

```
Min_N2_Calc(C16,H2_to_C16,T_f,T_p,P_p) := | IDG ← 22.414
                                          | $\alpha \leftarrow \frac{60}{1000}\cdot\frac{1}{IDG}$
                                          | $\rho_{L\_C16} \leftarrow$ Density_C16(T_f)
                                          | $Mol\_C16 \leftarrow \frac{C16}{1000}\cdot\rho_{L\_C16}\cdot 60$
                                          | Mol_H2 ← Mol_C16·H2_to_C16
                                          | Pvap ← Pvap_C16(T_p)
                                          | $N2_{min} \leftarrow \frac{\left(\frac{P\_p}{Pvap}-1\right)\cdot Mol\_C16 - Mol\_H2}{\alpha}$
                                          | $N2_{min}$
```

$$\text{Min\_N2\_Calc(C16,H2\_to\_C16,T\_f,T\_p,P\_p)} = 389.328 \quad \frac{ml}{min}$$

To determine the effects of product T and P on the amount of N2 dilution required, a range of each is investigated and plotted.

range := 10   Number of points to evaluate in each range

```
T_p_range := | for i ∈ 1..range
             |     $x_i \leftarrow 423 + 5\cdot(i-1)$
             | x

P_p_range := | for i ∈ 1..range
             |     $x_i \leftarrow 1 + 0.5\cdot(i-1)$
             | x

loc := 0

Function_of_T := | for j ∈ 1..range
                 |     | T ← $T\_p\_range_j$
                 |     | for i ∈ 1..range
                 |     |     | loc ← loc + 1
                 |     |     | P ← $P\_p\_range_i$
                 |     |     | N2 ← Min_N2_Calc(C16,H2_to_C16,T_f,T,P)
                 |     |     | $x_{loc} \leftarrow T$
                 |     |     | $y_{loc} \leftarrow P$
                 |     |     | $z_{loc} \leftarrow N2$
                 | $\begin{pmatrix} x \\ y \\ z \end{pmatrix}$
```

These x, y and z vectors are then plotted.

A.2 Heats of Reaction

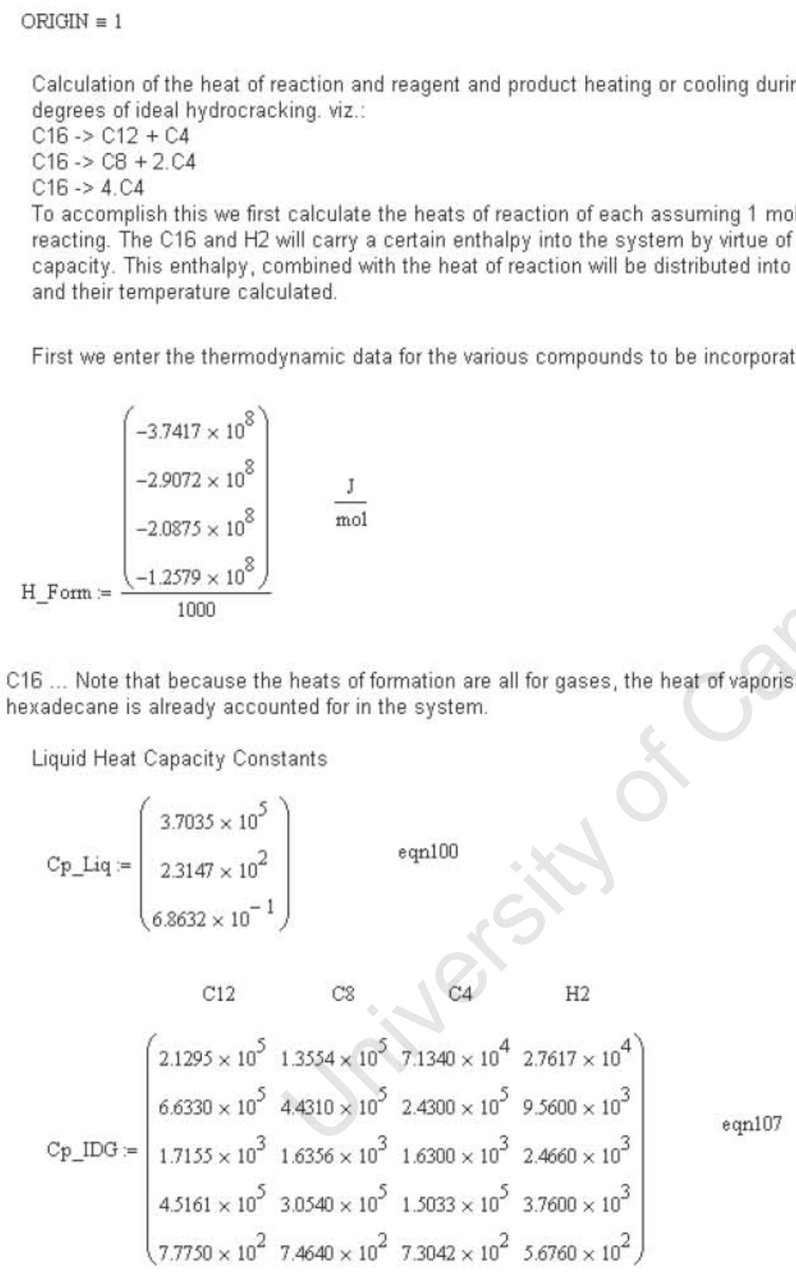

ORIGIN ≡ 1

Calculation of the heat of reaction and reagent and product heating or cooling during three degrees of ideal hydrocracking. viz.:
C16 -> C12 + C4
C16 -> C8 + 2.C4
C16 -> 4.C4
To accomplish this we first calculate the heats of reaction of each assuming 1 mol of C16 reacting. The C16 and H2 will carry a certain enthalpy into the system by virtue of their heat capacity. This enthalpy, combined with the heat of reaction will be distributed into the products and their temperature calculated.

First we enter the thermodynamic data for the various compounds to be incorporated.

$$\mathrm{H\_Form} := \frac{\begin{pmatrix} -3.7417 \times 10^{8} \\ -2.9072 \times 10^{8} \\ -2.0875 \times 10^{8} \\ -1.2579 \times 10^{8} \end{pmatrix}}{1000} \qquad \frac{\mathrm{J}}{\mathrm{mol}}$$

C16 ... Note that because the heats of formation are all for gases, the heat of vaporisation for the hexadecane is already accounted for in the system.

Liquid Heat Capacity Constants

$$\mathrm{Cp\_Liq} := \begin{pmatrix} 3.7035 \times 10^{5} \\ 2.3147 \times 10^{2} \\ 6.8632 \times 10^{-1} \end{pmatrix} \qquad \text{eqn100}$$

$$\mathrm{Cp\_IDG} := \begin{array}{c} \begin{array}{cccc} \text{C12} & \text{C8} & \text{C4} & \text{H2} \end{array} \\ \begin{pmatrix} 2.1295 \times 10^{5} & 1.3554 \times 10^{5} & 7.1340 \times 10^{4} & 2.7617 \times 10^{4} \\ 6.6330 \times 10^{5} & 4.4310 \times 10^{5} & 2.4300 \times 10^{5} & 9.5600 \times 10^{3} \\ 1.7155 \times 10^{3} & 1.6356 \times 10^{3} & 1.6300 \times 10^{3} & 2.4660 \times 10^{3} \\ 4.5161 \times 10^{5} & 3.0540 \times 10^{5} & 1.5033 \times 10^{5} & 3.7600 \times 10^{3} \\ 7.7750 \times 10^{2} & 7.4640 \times 10^{2} & 7.3042 \times 10^{2} & 5.6760 \times 10^{2} \end{pmatrix} \end{array} \qquad \text{eqn107}$$

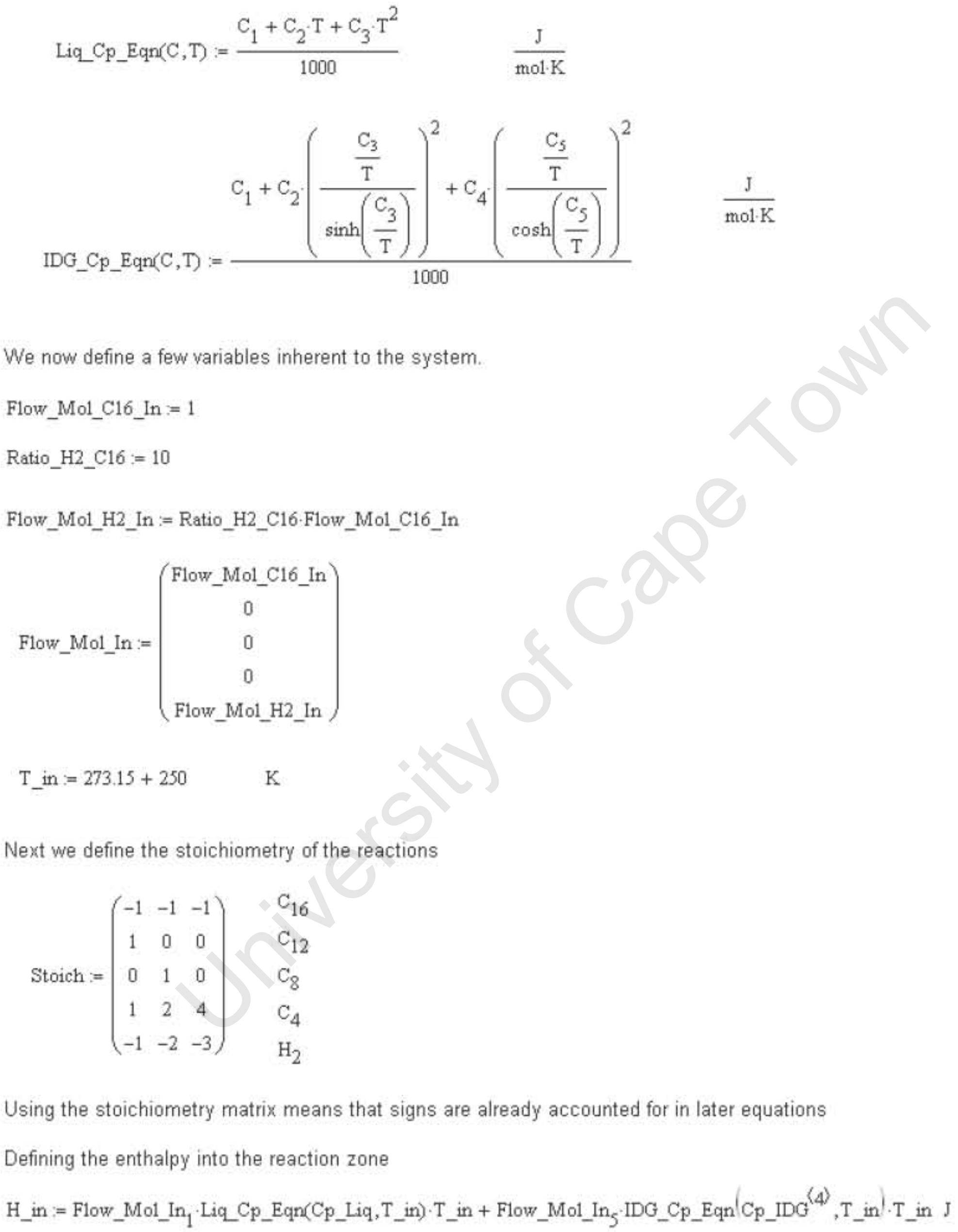

$$\text{Liq\_Cp\_Eqn}(C,T) := \frac{C_1 + C_2 \cdot T + C_3 \cdot T^2}{1000} \qquad \frac{J}{mol \cdot K}$$

$$\text{IDG\_Cp\_Eqn}(C,T) := \frac{C_1 + C_2 \cdot \left(\dfrac{\frac{C_3}{T}}{\sinh\left(\frac{C_3}{T}\right)}\right)^2 + C_4 \cdot \left(\dfrac{\frac{C_5}{T}}{\cosh\left(\frac{C_5}{T}\right)}\right)^2}{1000} \qquad \frac{J}{mol \cdot K}$$

We now define a few variables inherent to the system.

Flow_Mol_C16_In := 1

Ratio_H2_C16 := 10

Flow_Mol_H2_In := Ratio_H2_C16·Flow_Mol_C16_In

$$\text{Flow\_Mol\_In} := \begin{pmatrix} \text{Flow\_Mol\_C16\_In} \\ 0 \\ 0 \\ 0 \\ \text{Flow\_Mol\_H2\_In} \end{pmatrix}$$

$$\text{T\_in} := 273.15 + 250 \qquad K$$

Next we define the stoichiometry of the reactions

$$\text{Stoich} := \begin{array}{cc} \begin{pmatrix} -1 & -1 & -1 \\ 1 & 0 & 0 \\ 0 & 1 & 0 \\ 1 & 2 & 4 \\ -1 & -2 & -3 \end{pmatrix} & \begin{array}{l} C_{16} \\ C_{12} \\ C_8 \\ C_4 \\ H_2 \end{array} \end{array}$$

Using the stoichiometry matrix means that signs are already accounted for in later equations

Defining the enthalpy into the reaction zone

$$\text{H\_in} := \text{Flow\_Mol\_In}_1 \cdot \text{Liq\_Cp\_Eqn}(\text{Cp\_Liq}, \text{T\_in}) \cdot \text{T\_in} + \text{Flow\_Mol\_In}_5 \cdot \text{IDG\_Cp\_Eqn}\left(\text{Cp\_IDG}^{\langle 4 \rangle}, \text{T\_in}\right) \cdot \text{T\_in} \quad J$$

Defining the enthalpies of the various output species

$\mathrm{H\_C12\_out}(T,\mathrm{Mol\_Out}) := \mathrm{Mol\_Out}_2 \cdot \mathrm{IDG\_Cp\_Eqn}\left(\mathrm{Cp\_IDG}^{\langle 1\rangle},T\right)\cdot T \quad \frac{J}{mol}$

$\mathrm{H\_C8\_out}(T,\mathrm{Mol\_Out}) := \mathrm{Mol\_Out}_3 \cdot \mathrm{IDG\_Cp\_Eqn}\left(\mathrm{Cp\_IDG}^{\langle 2\rangle},T\right)\cdot T \quad \frac{J}{mol}$

$\mathrm{H\_C4\_out}(T,\mathrm{Mol\_Out}) := \mathrm{Mol\_Out}_4 \cdot \mathrm{IDG\_Cp\_Eqn}\left(\mathrm{Cp\_IDG}^{\langle 3\rangle},T\right)\cdot T \quad \frac{J}{mol}$

$\mathrm{H\_H2\_out}(T,\mathrm{Mol\_Out}) := \mathrm{Mol\_Out}_5 \cdot \mathrm{IDG\_Cp\_Eqn}\left(\mathrm{Cp\_IDG}^{\langle 4\rangle},T\right)\cdot T \quad \frac{J}{mol}$

Defining a heat of reaction (based solely on the heats of formation) and output flows general solution

$$\mathrm{Vars}(rxn) := \left| \begin{array}{l} \mathrm{Flow\_Out} \leftarrow \mathrm{Flow\_Mol\_In} + \mathrm{Stoich}^{\langle rxn\rangle}\cdot\mathrm{Flow\_Mol\_In}_1 \\ \mathrm{H\_Rxn} \leftarrow \left(\mathrm{Stoich}^{\langle rxn\rangle}\right)_1\cdot\mathrm{Flow\_Mol\_In}_1\cdot\mathrm{H\_Form}_1 + \left(\mathrm{Stoich}^{\langle rxn\rangle}\right)_2\cdot\mathrm{Flow\_Mol\_In}_1\cdot\mathrm{H\_Form}_2 + \left(\mathrm{Stoich}^{\langle rxn\rangle}\right)_3\cdot\mathrm{Flow\_Mol\_In}_1\cdot\mathrm{H\_Form}_3 + \left(\mathrm{Stoich}^{\langle rxn\rangle}\right)_4\cdot\mathrm{Flow\_Mol\_In}_1\cdot\mathrm{H\_Form}_4 \\ \begin{pmatrix} \mathrm{Flow\_Out} \\ \mathrm{H\_Rxn} \end{pmatrix} \end{array} \right.$$

Extracting solution for given stoichiometry

$\mathrm{temp} := \mathrm{Vars}(3) \qquad \mathrm{Flow\_Mol\_Out} := \mathrm{temp}_1 \qquad \mathrm{H\_Rxn} := \mathrm{temp}_2$

Noting that the greatest degree of conversion, i.e. the worst case scenario, is from
hexadecane into butane (i.e. Reaction 3 ... hence the Vars(3)),

Solving for the output temperature of the products assuming **ADIABATIC** operation

$\mathrm{T\_out} := \mathrm{T\_in}$ Initial guess

Given

$\mathrm{H\_C12\_out}(\mathrm{T\_out},\mathrm{Flow\_Mol\_Out}) + \mathrm{H\_C8\_out}(\mathrm{T\_out},\mathrm{Flow\_Mol\_Out}) + \mathrm{H\_C4\_out}(\mathrm{T\_out},\mathrm{Flow\_Mol\_Out}) + \mathrm{H\_H2\_out}(\mathrm{T\_out},\mathrm{Flow\_Mol\_Out}) = \mathrm{H\_Rxn} + \mathrm{H\_in}$

$\mathrm{answer} := \mathrm{Find}(\mathrm{T\_out}) - 273.15$

$\mathrm{answer} = 210.114 \quad ^{\circ}C$ **Output Temperature**

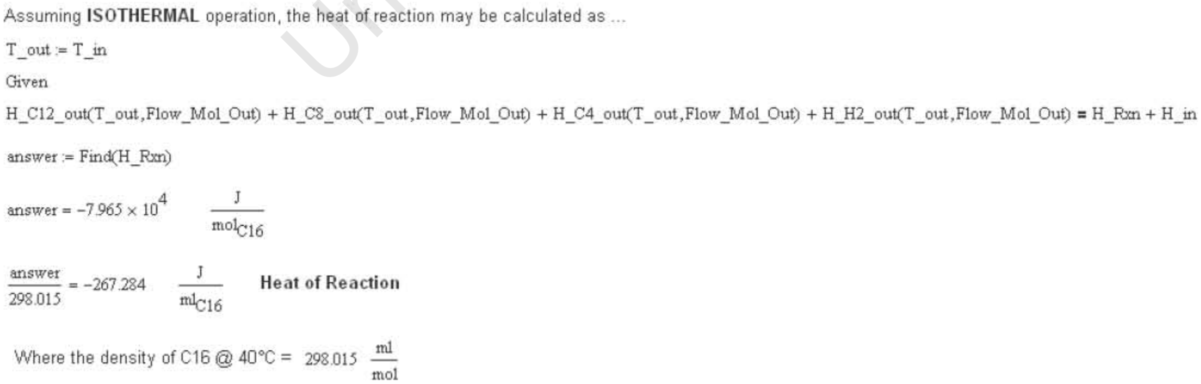

Assuming **ISOTHERMAL** operation, the heat of reaction may be calculated as ...

$\mathrm{T\_out} := \mathrm{T\_in}$

Given

$\mathrm{H\_C12\_out}(\mathrm{T\_out},\mathrm{Flow\_Mol\_Out}) + \mathrm{H\_C8\_out}(\mathrm{T\_out},\mathrm{Flow\_Mol\_Out}) + \mathrm{H\_C4\_out}(\mathrm{T\_out},\mathrm{Flow\_Mol\_Out}) + \mathrm{H\_H2\_out}(\mathrm{T\_out},\mathrm{Flow\_Mol\_Out}) = \mathrm{H\_Rxn} + \mathrm{H\_in}$

$\mathrm{answer} := \mathrm{Find}(\mathrm{H\_Rxn})$

$\mathrm{answer} = -7.965 \times 10^4 \quad \frac{J}{mol_{C16}}$

$\frac{\mathrm{answer}}{298.015} = -267.284 \quad \frac{J}{ml_{C16}}$ **Heat of Reaction**

Where the density of C16 @ 40°C = $298.015 \ \frac{ml}{mol}$

A.3 MATLAB Code for Catalyst Loadings

```
% Reactor Loading Calculation Script - For known dispersion
% Ross Kukard - University of Cape Town
% 2007 - 2008

%===========================================================================

% Utilised for the calculation and optimisation of the loading masses and
% volumes for the bifunctional (metal/acid) hydrocracking of n-alkanes

%===========================================================================

% Script begins with the input of the various properties of the zeolite and
% supported metal to be utilised including the density, particle sizes,
% packing ratios, metal loading, SiO2:Al2O3 ratios, etc.
% Following this, the reactor information must be entered, specifically
% with regards to the isothermal reaction zone.

% This script then continues to calculate the various loadings of supported
% metal and zeolite which would be required to achieve a specified
% metal:acid sites ratio, as well as re-calculate the metal loading which
% would be required to maintain a pre-specified minimum theoretical bed
% height to ensure no adverse hydrodynamic or transport phenomena between
% different runs.

clear
clc
Avogadro = 6.02*10^23; %atoms/mol
R = 8.314;

%===========================================================================
% First the input of the various physical properties
%===========================================================================
% Zeolite
%---------------------------------------------------------------------------
Density_Zeolite = ((33.6365-27.5922)/1000)/(10/100^3); % kg/m^3
% Bulk density from experimental values
```

```
%--------------------------------------------------------------------------
% Supported Metal
%--------------------------------------------------------------------------
%Density_Support = ((31.4020-27.5935)/1000)/(10/100^3); % kg/m^3
% Bulk density
Density_Support = (3.5232/1000)/(10/100^3);
Density_Metal = 21.45/1000 * 100^3; % kg/m^3

%Assuming Platinum
Atoms_Per_Area = 12.5;
Metal_Atoms_Per_Area = Atoms_Per_Area * (10^9)^2; % Atoms/nm^2 -> Atoms/m^2
% This value is a function of the metal used, with 12.5 being that for Pt
Metal_Mr = 195.08; % g/mol ... this being for Pt

Dispersion = 20.0; % %

%==========================================================================
% Reactor Specifications
%==========================================================================

% The reactor diameter and length of the isothermal zone are required to
% determine the total volume of the catalyst bed.

Reactor_Diameter = 0.015; % m
Reactor_Area = (pi * (Reactor_Diameter^2) / 4) * 100^2; %cm^2
Isothermal_Zone_Length = 0.08; % m

% A design factor may be included here, e.g. 90% of the volume, so as to
% allow a little leeway.
Volume_Design_Factor = 1; % Fractional

% A packing ratio is assumed and used to determine the actual volume which
% may be occupied by catalyst particles in the reactor.
% Assuming FCC packing
Packing_Ratio = 0.74; % Fractional

Temp = Bed_Volume_Calculation (Reactor_Diameter, ...
```

```
    Isothermal_Zone_Length, Packing_Ratio, Volume_Design_Factor);
Total_Reaction_Volume = Temp(1);
Particle_Reaction_Volume = Temp(2);

%Save all outputs to file for later viewing and access
Output = fopen('Output.txt','w');

fprintf (Output, '******************************\n');
fprintf (Output, '*** Reactor Specifications ***\n');
fprintf (Output, '******************************\n');
fprintf (Output, 'Reactor Diameter = %1.3f m\n', Reactor_Diameter);
fprintf (Output, 'Isothermal Zone Length = %1.3f m\n', ...
    Isothermal_Zone_Length);
fprintf (Output, ...
    'Reaction Volume (Total bulk including void space) = %3.3f cc\n\n', ...
    Total_Reaction_Volume * 100^3);

%==========================================================================
% Calculation of Unit Masses and Volumes of Loading
%==========================================================================

% A value for the desired metal:acid site ratio is assumed and utilised
% together with the acidity (acid sites per unit mass for the zeolite) and
% metal site number (atoms of exposed metal per unit mass for the metal) to
% calculate the unit masses of each which are required to achieve the
% specified metal:acid ratio.

Metal_To_Acid = 0.12;


%==========================================================================
% Calculation of Required Metal Loading Based on SiO2:Al2O3 Ratios
%==========================================================================

% For the SiO2:Al2O3 ratio and metal loading specified, determine the
% amount of each component required to fill the reactor volume.
% Have unit volumes and have total volume,  so multiply both unit volumes
```

```
% by the total volume so as to obtain the volume required of each
% component. Then compare each of these volumes to the minimum bed volume.
% If a violation is detected, calculate the bed height which would result
% from the amount to be used.

% Tabulate for a vector of SiO2:Al2O3 ratios at a given metal loading and
% calculate the metal loading required to ensure that the smallest bed
% volume (not sure how to detect whether this is metal or acid) can be
% achieved and recalculate to see if the opposite side now fails. Maybe
% even have an optimiser that minimises these shifts.

%SiO2_Al2O3_Ratio = 90;

% Vector of SiO2/Al2O3 ratios
% Using the largest ratio and desired Metal:Acid ratio, find volume or each
% Metal loading will always stay constant if acid sites do, so ...
% Determine number of acid sites
% For each remaining SiO2/Al2O3, determine volume to get desired acids
% site number

Metal_Loading = 5; % wt%
Temp = Metal_Analysis_Dispersion (Density_Support, Metal_Loading, ...
    Metal_Atoms_Per_Area, Metal_Mr, Dispersion, Density_Metal, Avogadro);
Metal_Sites_Molar = Temp (2); % mol(Metal Sites)/g(Supported Metal)
Density_Supported_Metal = Temp (3);
Crystallite_Diameter = Temp(1);

fprintf (Output, '******************************\n');
fprintf (Output, '***    Supported  Metal    ***\n');
fprintf (Output, '******************************\n');
fprintf (Output, 'Metal Loading = %1.2f wt%%\n', Metal_Loading);
fprintf (Output, 'Assumed Exposed Metal Atoms for Pt = %2.1f atoms/nm^2\n', ...
    Atoms_Per_Area);
fprintf (Output, 'Assumed Metal Dispersion = %2.2f %%\n', Dispersion);
fprintf (Output, 'Calculated Metal Crystallite Diameter = %2.2f nm\n', ...
    Crystallite_Diameter * 10^9);
fprintf (Output, 'Silica Support Bulk Density = %3.2f kg/m^3\n', ...
```

```
    Density_Support);
fprintf (Output, 'Supported Metal Bulk Density = %3.2f kg/m^3\n', ...
    Density_Supported_Metal);
fprintf (Output, 'Metal Sites = %2.2e sites/g\n\n', ...
    Metal_Sites_Molar * Avogadro);
fprintf (Output, 'Assumed Metal:Acid Sites Molar Ratio = %1.3f\n\n', Metal_To_Acid);

% Sort ratios -> select highest -> calculate number of acid sites and store
% Run through entire vector using that number of acid sites

SiO2_Al2O3_Ratios = [3 20]; %HUSY ASA Mor Bea MFI MFI MFI
SiO2_Al2O3_Ratios = sort (SiO2_Al2O3_Ratios, 'descend');

Acidity_Molar = Acidity_Calculation (SiO2_Al2O3_Ratios(1));

% The first Acidity_Molar entry represents the highest SiO2/Al2O3 ratio
Temp = Combined_Unit_Mass_And_Volume (Acidity_Molar (1), ...
    Metal_Sites_Molar, Metal_To_Acid, Density_Zeolite, ...
    Density_Supported_Metal);

Unit_Mass_Zeolite = Temp(1);
Unit_Mass_Supported_Metal = Temp(2);
Unit_Volume_Zeolite = Temp(3);
Unit_Volume_Supported_Metal = Temp(4);

Volume_Zeolite = Unit_Volume_Zeolite * Total_Reaction_Volume;
% Note - using total reaction volume as densities are bulk packing densities
Volume_Supported_Metal = Unit_Volume_Supported_Metal * Total_Reaction_Volume;
% Note that all volumes are in cubic meters!!!

Mass_Zeolite = Volume_Zeolite * Density_Zeolite;
Mass_Supported_Metal = Volume_Supported_Metal * Density_Supported_Metal;
Metal_Sites_For_Specified_Loading = Metal_Sites_Molar * Avogadro * ...
    Mass_Supported_Metal * 1000;
% All in kg

Number_of_Sites = Acidity_Molar * Mass_Zeolite * 1000; %mol acid sites
```

```
fprintf (Output, '******************************\n');
fprintf (Output, '*** Highest Silica:Alumina ***\n');
fprintf (Output, '******************************\n');
fprintf (Output, 'Maximum SiO2/Al2O3 = %2.2f \n', SiO2_Al2O3_Ratios(1));
fprintf (Output, 'Associated Acidity = %1.2e sites/g\n', ...
    Acidity_Molar * Avogadro);
fprintf (Output, 'Zeolite Mass = %2.2f g\n', Mass_Zeolite * 1000);
fprintf (Output, 'Zeolite Bulk Density = %3.2f kg/m^3\n', Density_Zeolite);
fprintf (Output, 'Zeolite Volume = %2.2f cc\n', Volume_Zeolite * 100^3);
fprintf (Output, 'Number of Acid Sites = %2.2e sites\n\n', ...
    Number_of_Sites * Avogadro);

fprintf (Output, '*******************************\n');
fprintf (Output, '*** Supported Metal Loading ***\n');
fprintf (Output, '*******************************\n');
fprintf (Output, 'Supported Metal Mass = %2.4f g (constant for all loadings)\n', ...
    Mass_Supported_Metal * 1000);
fprintf (Output, 'Supported Metal Volume = %2.2f cc (constant for all loadings)\n', ...
    Volume_Supported_Metal * 100^3);
fprintf (Output, 'Metal Sites = %2.2e sites (constant for all loadings)\n\n', ...
    Metal_Sites_For_Specified_Loading);

% Now analyse each SiO2/Al2O3 ratio and determine reactor loading

fprintf (Output, '*******************************\n');
fprintf (Output, '*** Variable Silica:Alumina ***\n');
fprintf (Output, '*******************************\n');

fprintf (Output, ...
    'SiO2/Al2O3 \t Molar Acidity (mol/g) \t Mass Zeolite (g) \t Volume Zeolite (cc) \t Vo

for i = 1:length(SiO2_Al2O3_Ratios)
    SiO2_Al2O3_Ratio = SiO2_Al2O3_Ratios(i);
    Acidity_Molar (i) = Acidity_Calculation (SiO2_Al2O3_Ratio);
    Mass_Zeolite (i) = Number_of_Sites / Acidity_Molar (i); %g
    Volume_Zeolite (i) = Mass_Zeolite(i)/1000 / Density_Zeolite; %m^3
```

```
    Volume_Diluent (i) = Total_Reaction_Volume - Volume_Supported_Metal - ...
        Volume_Zeolite (i); %m^3
    Mass_Diluent (i) = Volume_Diluent (i) * Density_Support * 1000; %g
    fprintf (Output, '%2.2f   \t\t %2.2e \t\t\t %2.4f \t\t\t %2.2f \t\t\t %2.2f
        SiO2_Al2O3_Ratio, Acidity_Molar (i) * Avogadro, ...
        Mass_Zeolite (i), Volume_Zeolite (i) * 100^3, Volume_Diluent (i) * ...
        100^3, Mass_Diluent (i));
end

%==========================================================================
% Calculation of The Space Velocities and Linear Velocities
%==========================================================================
%Where SHSV = Mole flow feed / Moles total active sites with the reactor
Total_Sites = Number_of_Sites + Metal_Sites_For_Specified_Loading/Avogadro;

%First a vector of the pump flow rates is provided
Pump_Flows = 0.01:0.01:0.15; %ml/min

%Various operating parameters are provided
H2_HC_Molar_Ratio = 10;
T_f_HC = 273 + 30;
T_f_Gases = 273 + 25;
P_f = 101325; %Pa
T_rxn = 273 + 250;
T_p = 273 + 180;
P_p = 1*10^5; %Pa
P_rxn = 40 * 10^5; %Pa
Mr_C16 = 12.01*16+1.01*34; %g/mol
IDG = 22.414; %dm^3/mol
C16_Density_f = C16_stats(T_f_HC); %mol/dm^3
C16_Density_rxn = C16_stats(T_rxn);

fprintf (Output, '\n*********************************\n');
fprintf (Output, '***** Site Space Velocities *****\n');
fprintf (Output, '*********************************\n');
fprintf (Output, 'Hydrogen:C16 Molar Feed Ratio = %2.2f\n', ...
    H2_HC_Molar_Ratio);
```

```
fprintf (Output, 'Volume of Catalyst Bed = %2.2f cc\n', ...
    Total_Reaction_Volume * 100^3);
fprintf (Output, 'Total Active Sites (Metal + Acid) in Reactor = %2.2e moles\n\n', ...
    Total_Sites);
fprintf (Output, ...
    'Pump Rate (ml/min) \t Molar Flow C16 (mol/hr) \t Molar Flow H2 (mol/hr) \t Site Hc

fprintf (Output, '\n* Where Site Hourly Space Velocity = Moles C16 fed / Mole active si

fprintf (Output, '\n***********************************\n');
fprintf (Output, '***** Weight Space Velocities *****\n');
fprintf (Output, '***********************************\n');

fprintf (Output, 'Vol. Flow of C16 (ml/min)\t');
fprintf (Output, '%1.2f \t\t', Pump_Flows);
fprintf (Output, '\nMass Flow of C16 (g/hr)\t\t');
fprintf (Output, '%1.2f \t\t', C16_Mass_Flow);
fprintf (Output, '\nTotal Catalyst Mass (g)\t\tWeight Hourly Space Velocity (/hr)');
%Calculating WHSV for each catalyst loading
for j = 1:length(Pump_Flows)
    C16_flow = C16_Mass_Flow(j);

    for i = 1:length(SiO2_Al2O3_Ratios)
        Mass_Total_Catalyst(i) = Mass_Zeolite(i) + Mass_Supported_Metal * 1000; %g
        WHSV(i,j) = C16_flow / Mass_Total_Catalyst(i);
    end

end

for i = 1:length(SiO2_Al2O3_Ratios)
    fprintf (Output, '\n\t%2.4f\t', Mass_Total_Catalyst(i));
    fprintf (Output, '\t\t%3.2f', WHSV(i,:));
    %fprintf (Output, '\n');
end

fclose(Output);
```

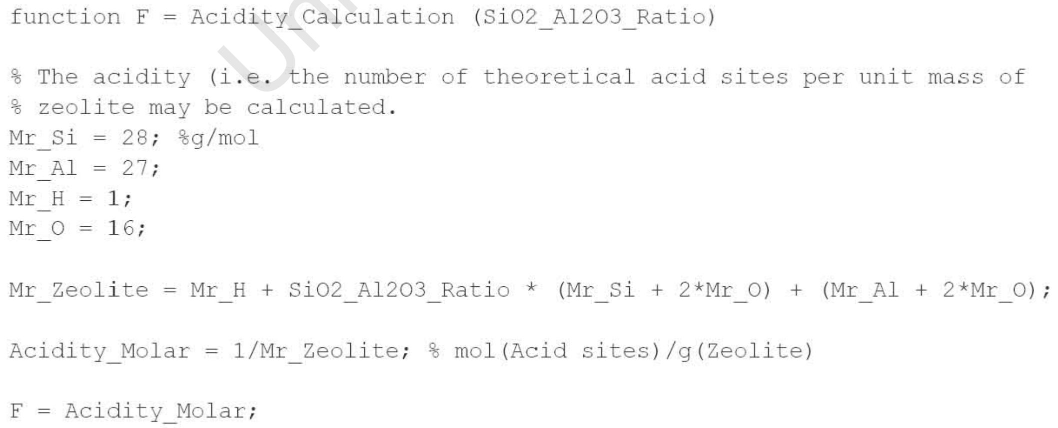

```
function F = Acidity_Calculation (SiO2_Al2O3_Ratio)

% The acidity (i.e. the number of theoretical acid sites per unit mass of
% zeolite may be calculated.
Mr_Si = 28; %g/mol
Mr_Al = 27;
Mr_H = 1;
Mr_O = 16;

Mr_Zeolite = Mr_H + SiO2_Al2O3_Ratio * (Mr_Si + 2*Mr_O) + (Mr_Al + 2*Mr_O);

Acidity_Molar = 1/Mr_Zeolite; % mol(Acid sites)/g(Zeolite)

F = Acidity_Molar;
```

```
function F = Bed_Volume_Calculation (D, H, Packing, Safety)

Total_Reaction_Volume = pi * D^2 * 1/4 * H;

Safe_Reaction_Volume = Total_Reaction_Volume * Safety;

Particle_Reaction_Volume = Safe_Reaction_Volume * Packing;

F = [Total_Reaction_Volume, Particle_Reaction_Volume];
```

```
function F = C16_stats (T)

%First define the constants
C = [0.26807 0.25287 723 0.31143 0; 156.06 -15015 -18.941 6.8172*10^-6 2];

%Now the density equation
Density = C(1,1) / (C(1,2)^(1 + (1 - T/(C(1,3)))^(C(1,4))));

F = Density;
```

```
function F = Combined_Unit_Mass_And_Volume (Acidity_Molar, ...
    Metal_Sites_Molar, Metal_To_Acid, Density_Zeolite, ...
    Density_Supported_Metal)

Temp = Simul_Unit_Mass (Acidity_Molar, Metal_Sites_Molar, Metal_To_Acid);

Unit_Mass_Zeolite = Temp(1);
Unit_Mass_Supported_Metal = Temp(2);

% By incorporating the densities, these unit masses may be converted to
% unit volumes too.

Temp = Unit_Mass_to_Unit_Volume (Unit_Mass_Zeolite, Density_Zeolite, ...
    Unit_Mass_Supported_Metal, Density_Supported_Metal);
Unit_Volume_Zeolite = Temp(1);
Unit_Volume_Supported_Metal = Temp(2);

F = [Unit_Mass_Zeolite, Unit_Mass_Supported_Metal, Unit_Volume_Zeolite, ...
    Unit_Volume_Supported_Metal];
```

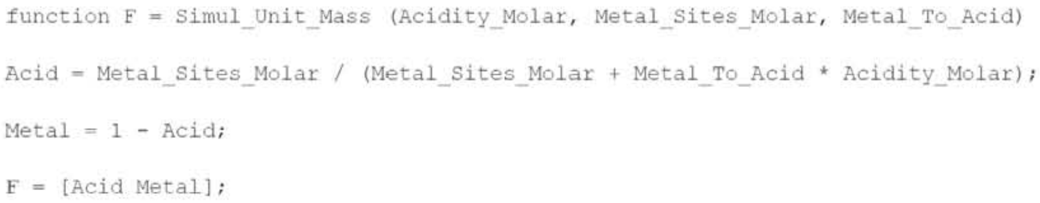

```
function F = Simul_Unit_Mass (Acidity_Molar, Metal_Sites_Molar, Metal_To_Acid)

Acid = Metal_Sites_Molar / (Metal_Sites_Molar + Metal_To_Acid * Acidity_Molar);

Metal = 1 - Acid;

F = [Acid Metal];
```

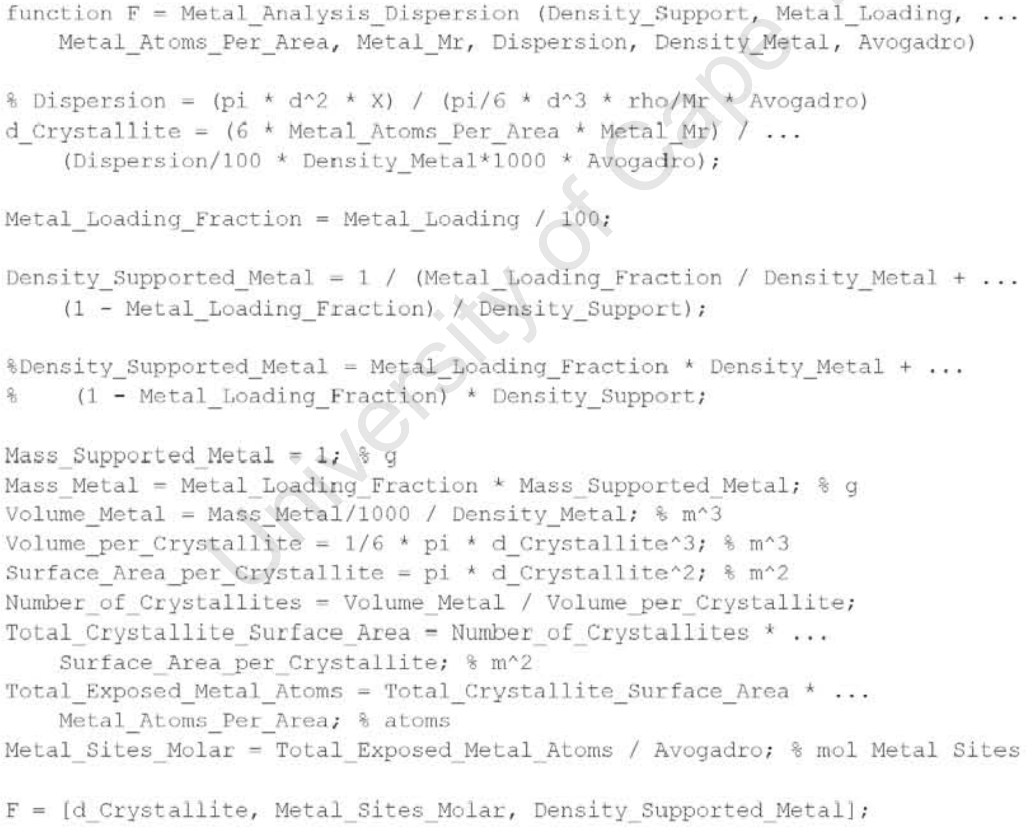

```
function F = Metal_Analysis_Dispersion (Density_Support, Metal_Loading, ...
    Metal_Atoms_Per_Area, Metal_Mr, Dispersion, Density_Metal, Avogadro)

% Dispersion = (pi * d^2 * X) / (pi/6 * d^3 * rho/Mr * Avogadro)
d_Crystallite = (6 * Metal_Atoms_Per_Area * Metal_Mr) / ...
    (Dispersion/100 * Density_Metal*1000 * Avogadro);

Metal_Loading_Fraction = Metal_Loading / 100;

Density_Supported_Metal = 1 / (Metal_Loading_Fraction / Density_Metal + ...
    (1 - Metal_Loading_Fraction) / Density_Support);

%Density_Supported_Metal = Metal_Loading_Fraction * Density_Metal + ...
%    (1 - Metal_Loading_Fraction) * Density_Support;

Mass_Supported_Metal = 1; % g
Mass_Metal = Metal_Loading_Fraction * Mass_Supported_Metal; % g
Volume_Metal = Mass_Metal/1000 / Density_Metal; % m^3
Volume_per_Crystallite = 1/6 * pi * d_Crystallite^3; % m^3
Surface_Area_per_Crystallite = pi * d_Crystallite^2; % m^2
Number_of_Crystallites = Volume_Metal / Volume_per_Crystallite;
Total_Crystallite_Surface_Area = Number_of_Crystallites * ...
    Surface_Area_per_Crystallite; % m^2
Total_Exposed_Metal_Atoms = Total_Crystallite_Surface_Area * ...
    Metal_Atoms_Per_Area; % atoms
Metal_Sites_Molar = Total_Exposed_Metal_Atoms / Avogadro; % mol Metal Sites

F = [d_Crystallite, Metal_Sites_Molar, Density_Supported_Metal];
```

B

Experimental Data

Herein are presented the tabulated datasets corresponding to the temperature profile analyses and the various catalytic investigations.

B.1 Temperature Profiles

Table B.13: Experimental Temperature Profile Data

Reactor Assembly Zone	Distance from Top of Reactor (cm)	Measured Internal Temperature (°C)			
		SiC Loading		Catalyst Loading	
		Reactor 1	Reactor 2	Reactor 1	Reactor 2
Below Brass Housing	50	167.8	177.4	179.5	162.8
Heating Band 4 (Setpoint = 233°C)	48	234.4	233.3	235.4	226.2
	46	248.2	248.1	247.4	245.6
	44	249.8	249.9	249.4	248.8
	42	250.2	250.2	249.9	249.4
Heating Band 3 (Setpoint = 230°C)	40	250.4	250.3	250.0	249.6
	38	250.7	250.4	250.1	249.6
	36	250.8	250.5	250.0	249.6
	34	250.9	250.5	250.0	249.5
	32	250.8	250.5	250.0	249.5
	30	250.9	250.5	249.9	249.4
Heating Band 2 (Setpoint = 235°C)	28	251.0	250.5	249.7	249.2
	26	251.2	250.6	249.5	249.0
	24	251.2	250.5	249.2	248.8
	22	251.0	250.1	248.8	248.5
Heating Band 1 (Setpoint = 235°C)	20	250.3	249.3	248.1	247.8
	18	249.2	248.2	247.4	247.0
	16	247.0	246.2	245.5	244.9
	14	237.0	234.1	236.4	237.2
Above Brass Housing	12	Not Measured	Not Measured	207.7	204.2
	10			160.4	156.0
	8			119.5	115.6
	6			88.7	85.4
	4			71.6	69.6

B.2 Reactor Comparison

Table B.14: Experimental Data for Side-by-Side Comparison of H-MFI-90 (with both reactors loaded with 0.800 g H-MFI-90, 0.119 g 5 wt% Pt/SiO_2, 0.667 g SiO_2 diluent and operated at a temperature of 250°C, total pressure of 40 bar, H_2:n-C_{16} molar feed ratio of 10:1 and a space velocity of 76.1 $mol_{n\text{-}C16}/(mol_{Total\_Sites} \times hr)$)

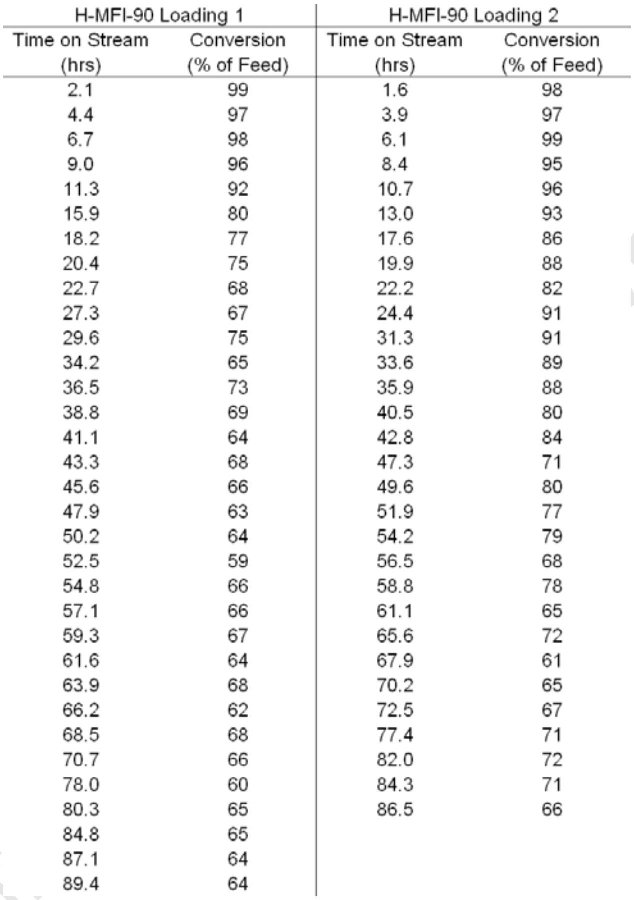

H-MFI-90 Loading 1		H-MFI-90 Loading 2	
Time on Stream (hrs)	Conversion (% of Feed)	Time on Stream (hrs)	Conversion (% of Feed)
2.1	99	1.6	98
4.4	97	3.9	97
6.7	98	6.1	99
9.0	96	8.4	95
11.3	92	10.7	96
15.9	80	13.0	93
18.2	77	17.6	86
20.4	75	19.9	88
22.7	68	22.2	82
27.3	67	24.4	91
29.6	75	31.3	91
34.2	65	33.6	89
36.5	73	35.9	88
38.8	69	40.5	80
41.1	64	42.8	84
43.3	68	47.3	71
45.6	66	49.6	80
47.9	63	51.9	77
50.2	64	54.2	79
52.5	59	56.5	68
54.8	66	58.8	78
57.1	66	61.1	65
59.3	67	65.6	72
61.6	64	67.9	61
63.9	68	70.2	65
66.2	62	72.5	67
68.5	68	77.4	71
70.7	66	82.0	72
78.0	60	84.3	71
80.3	65	86.5	66
84.8	65		
87.1	64		
89.4	64		

B.3 H-MFI-90

Table B.15: Experimental Data for H-MFI-90 at 0.06 ml/min n-C_{16} Feed

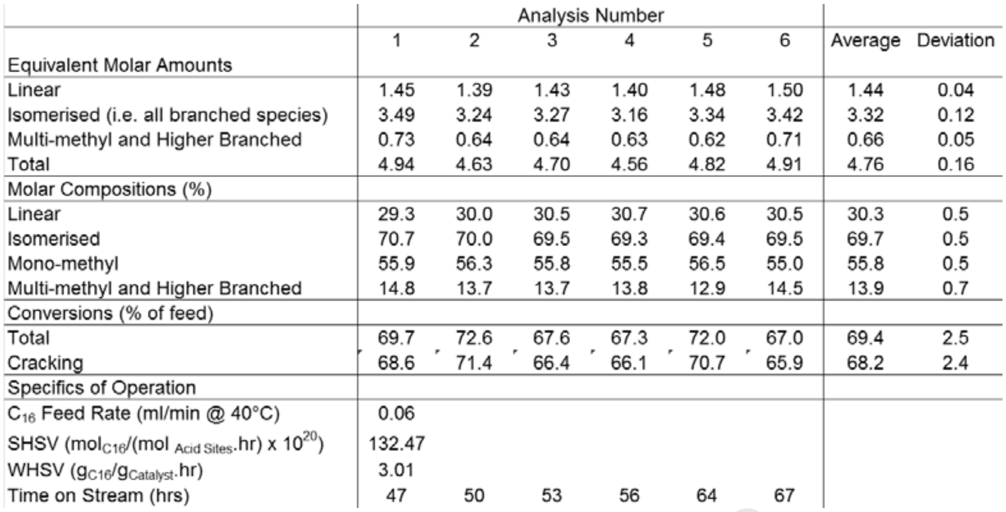

	Analysis Number							
	1	2	3	4	5	6	Average	Deviation
Equivalent Molar Amounts								
Linear	1.45	1.39	1.43	1.40	1.48	1.50	1.44	0.04
Isomerised (i.e. all branched species)	3.49	3.24	3.27	3.16	3.34	3.42	3.32	0.12
Multi-methyl and Higher Branched	0.73	0.64	0.64	0.63	0.62	0.71	0.66	0.05
Total	4.94	4.63	4.70	4.56	4.82	4.91	4.76	0.16
Molar Compositions (%)								
Linear	29.3	30.0	30.5	30.7	30.6	30.5	30.3	0.5
Isomerised	70.7	70.0	69.5	69.3	69.4	69.5	69.7	0.5
Mono-methyl	55.9	56.3	55.8	55.5	56.5	55.0	55.8	0.5
Multi-methyl and Higher Branched	14.8	13.7	13.7	13.8	12.9	14.5	13.9	0.7
Conversions (% of feed)								
Total	69.7	72.6	67.6	67.3	72.0	67.0	69.4	2.5
Cracking	68.6	71.4	66.4	66.1	70.7	65.9	68.2	2.4
Specifics of Operation								
C_{16} Feed Rate (ml/min @ 40°C)	0.06							
SHSV (mol_{C16}/(mol $_{Acid\ Sites}$.hr) x 10^{20})	132.47							
WHSV ($g_{C16}/g_{Catalyst}$.hr)	3.01							
Time on Stream (hrs)	47	50	53	56	64	67		

Table B.16: Experimental Data for H-MFI-90 at 0.08 ml/min n-C_{16} Feed

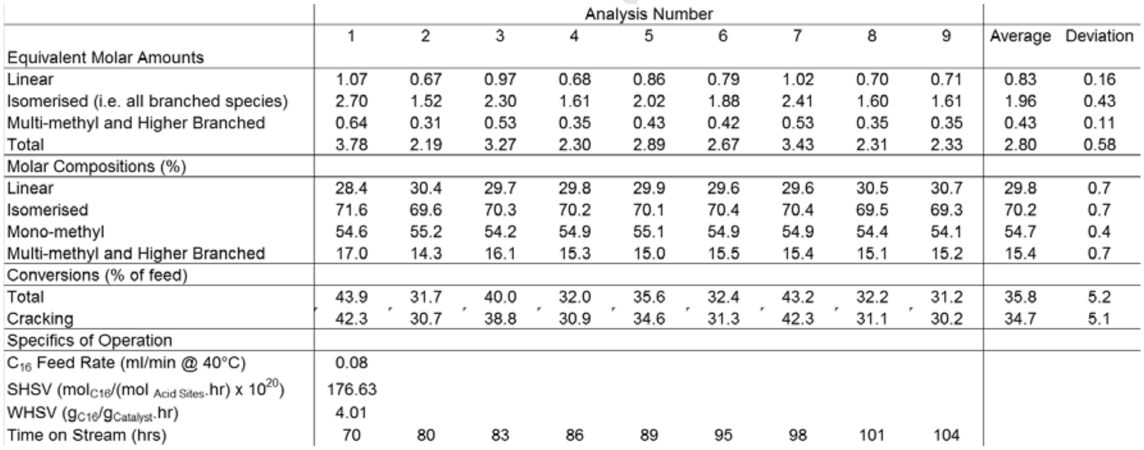

	Analysis Number										
	1	2	3	4	5	6	7	8	9	Average	Deviation
Equivalent Molar Amounts											
Linear	1.07	0.67	0.97	0.68	0.86	0.79	1.02	0.70	0.71	0.83	0.16
Isomerised (i.e. all branched species)	2.70	1.52	2.30	1.61	2.02	1.88	2.41	1.60	1.61	1.96	0.43
Multi-methyl and Higher Branched	0.64	0.31	0.53	0.35	0.43	0.42	0.53	0.35	0.35	0.43	0.11
Total	3.78	2.19	3.27	2.30	2.89	2.67	3.43	2.31	2.33	2.80	0.58
Molar Compositions (%)											
Linear	28.4	30.4	29.7	29.8	29.9	29.6	29.6	30.5	30.7	29.8	0.7
Isomerised	71.6	69.6	70.3	70.2	70.1	70.4	70.4	69.5	69.3	70.2	0.7
Mono-methyl	54.6	55.2	54.2	54.9	55.1	54.9	54.9	54.4	54.1	54.7	0.4
Multi-methyl and Higher Branched	17.0	14.3	16.1	15.3	15.0	15.5	15.4	15.1	15.2	15.4	0.7
Conversions (% of feed)											
Total	43.9	31.7	40.0	32.0	35.6	32.4	43.2	32.2	31.2	35.8	5.2
Cracking	42.3	30.7	38.8	30.9	34.6	31.3	42.3	31.1	30.2	34.7	5.1
Specifics of Operation											
C_{16} Feed Rate (ml/min @ 40°C)	0.08										
SHSV (mol_{C16}/(mol $_{Acid\ Sites}$.hr) x 10^{20})	176.63										
WHSV ($g_{C16}/g_{Catalyst}$.hr)	4.01										
Time on Stream (hrs)	70	80	83	86	89	95	98	101	104		

Table B.17: Experimental Data for H-MFI-90 at 0.10 ml/min n-C_{16} Feed

	Analysis Number									
Equivalent Molar Amounts	1	2	3	4	5	6	7	8	Average	Deviation
Linear	0.68	0.58	0.70	0.71	0.67	0.67	0.65	0.74	0.68	0.05
Isomerised (i.e. all branched species)	1.59	1.35	1.64	1.64	1.49	1.60	1.50	1.69	1.56	0.11
Multi-methyl and Higher Branched	0.35	0.33	0.37	0.35	0.33	0.38	0.33	0.36	0.35	0.02
Total	2.27	1.94	2.34	2.36	2.15	2.27	2.16	2.44	2.24	0.16
Molar Compositions (%)										
Linear	29.9	30.1	30.0	30.3	30.9	29.4	30.3	30.5	30.2	0.4
Isomerised	70.1	69.9	70.0	69.7	69.1	70.6	69.7	69.5	69.8	0.4
Mono-methyl	54.8	53.0	54.2	54.7	53.6	53.9	54.4	54.7	54.2	0.6
Multi-methyl and Higher Branched	15.3	16.9	15.8	15.0	15.5	16.7	15.3	14.8	15.7	0.8
Conversions (% of feed)										
Total	28.0	26.0	28.1	30.0	26.6	27.0	26.8	31.0	27.9	1.8
Cracking	27.0	25.0	27.3	29.2	25.8	26.1	26.1	30.4	27.1	1.8
Specifics of Operation										
C_{16} Feed Rate (ml/min @ 40°C)	0.10									
SHSV (mol_{C16}/(mol $_{Acid\ Sites}$.hr) x 10^{20})	220.79									
WHSV ($g_{C16}/g_{Catalyst}$.hr)	5.01									
Time on Stream (hrs)	106	118	121	124	126	129	132	135		

Table B.18: Experimental Data for H-MFI-90 Repeat of 0.06 ml/min n-C_{16} Feed

	Analysis Number							
Equivalent Molar Amounts	1	2	3	4	5	6	Average	Deviation
Linear	0.98	1.14	1.06	0.86	1.06	0.94	1.01	0.10
Isomerised (i.e. all branched species)	2.18	2.68	2.49	1.95	2.43	2.16	2.31	0.27
Multi-methyl and Higher Branched	0.44	0.66	0.57	0.44	0.57	0.48	0.53	0.09
Total	3.17	3.81	3.56	2.81	3.49	3.10	3.32	0.36
Molar Compositions (%)								
Linear	31.1	29.8	29.9	30.7	30.5	30.5	30.4	0.5
Isomerised	68.9	70.2	70.1	69.3	69.5	69.5	69.6	0.5
Mono-methyl	55.0	52.9	54.1	53.8	53.3	54.0	53.8	0.7
Multi-methyl and Higher Branched	14.0	17.4	16.0	15.5	16.2	15.5	15.8	1.1
Conversions (% of feed)								
Total	41.4	48.5	39.3	35.8	48.4	37.8	41.8	5.4
Cracking	40.5	47.5	38.2	34.8	47.4	36.8	40.9	5.4
Specifics of Operation								
C_{16} Feed Rate (ml/min @ 40°C)	0.06							
SHSV (mol_{C16}/(mol $_{Acid\ Sites}$.hr) x 10^{20})	132.47							
WHSV ($g_{C16}/g_{Catalyst}$.hr)	3.01							
Time on Stream (hrs)	139	142	145	161	170	172		

Table B.19: Projection of H-MFI-90 Data to 20% Conversion

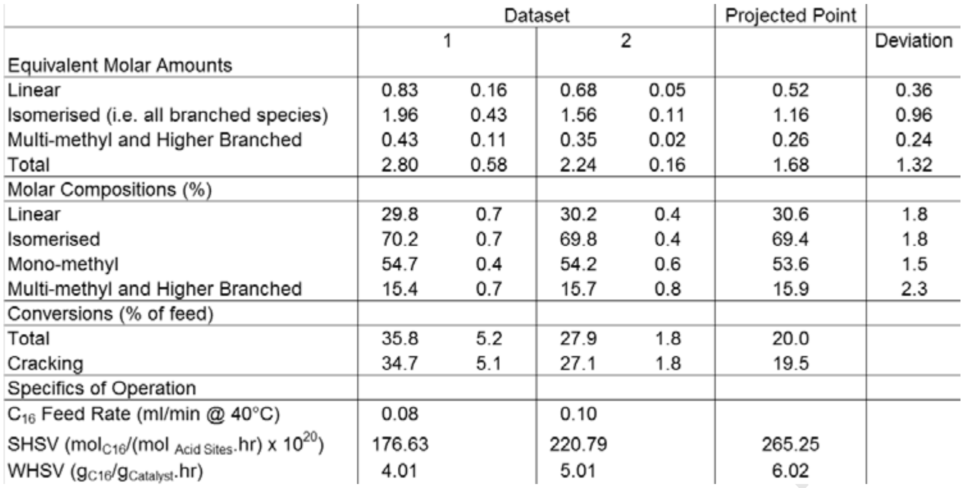

	Dataset				Projected Point	
	1		2			Deviation
Equivalent Molar Amounts						
Linear	0.83	0.16	0.68	0.05	0.52	0.36
Isomerised (i.e. all branched species)	1.96	0.43	1.56	0.11	1.16	0.96
Multi-methyl and Higher Branched	0.43	0.11	0.35	0.02	0.26	0.24
Total	2.80	0.58	2.24	0.16	1.68	1.32
Molar Compositions (%)						
Linear	29.8	0.7	30.2	0.4	30.6	1.8
Isomerised	70.2	0.7	69.8	0.4	69.4	1.8
Mono-methyl	54.7	0.4	54.2	0.6	53.6	1.5
Multi-methyl and Higher Branched	15.4	0.7	15.7	0.8	15.9	2.3
Conversions (% of feed)						
Total	35.8	5.2	27.9	1.8	20.0	
Cracking	34.7	5.1	27.1	1.8	19.5	
Specifics of Operation						
C_{16} Feed Rate (ml/min @ 40°C)	0.08		0.10			
SHSV ($mol_{C16}/(mol_{Acid\ Sites}.hr) \times 10^{20}$)	176.63		220.79		265.25	
WHSV ($g_{C16}/g_{Catalyst}.hr$)	4.01		5.01		6.02	

Table B.20: Product Composition Associated with Projection of H-MFI-90 Data to 20% Conversion

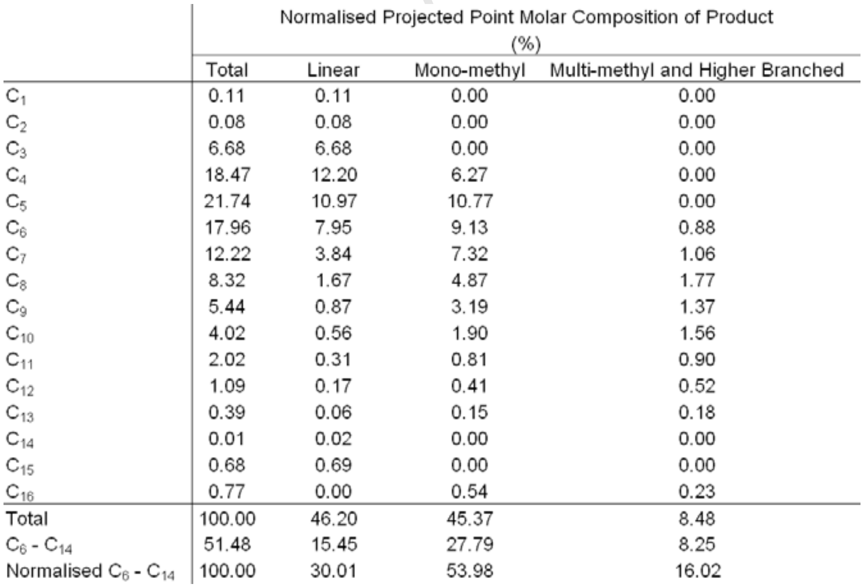

	Normalised Projected Point Molar Composition of Product (%)			
	Total	Linear	Mono-methyl	Multi-methyl and Higher Branched
C_1	0.11	0.11	0.00	0.00
C_2	0.08	0.08	0.00	0.00
C_3	6.68	6.68	0.00	0.00
C_4	18.47	12.20	6.27	0.00
C_5	21.74	10.97	10.77	0.00
C_6	17.96	7.95	9.13	0.88
C_7	12.22	3.84	7.32	1.06
C_8	8.32	1.67	4.87	1.77
C_9	5.44	0.87	3.19	1.37
C_{10}	4.02	0.56	1.90	1.56
C_{11}	2.02	0.31	0.81	0.90
C_{12}	1.09	0.17	0.41	0.52
C_{13}	0.39	0.06	0.15	0.18
C_{14}	0.01	0.02	0.00	0.00
C_{15}	0.68	0.69	0.00	0.00
C_{16}	0.77	0.00	0.54	0.23
Total	100.00	46.20	45.37	8.48
C_6 - C_{14}	51.48	15.45	27.79	8.25
Normalised C_6 - C_{14}	100.00	30.01	53.98	16.02

B.4 H-BEA-25

Table B.21: Experimental Data for H-BEA-25 at 0.01 ml/min n-C_{16} Feed

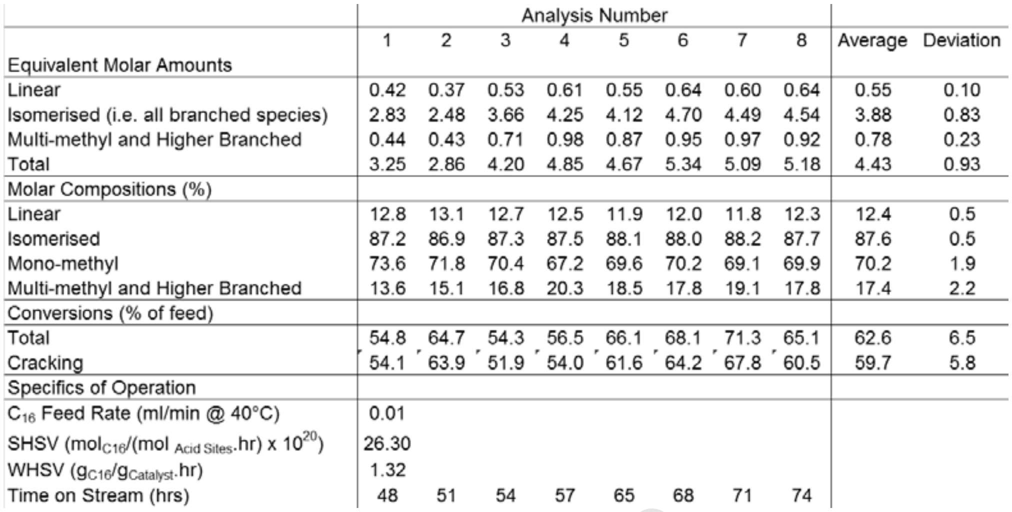

	Analysis Number									
Equivalent Molar Amounts	1	2	3	4	5	6	7	8	Average	Deviation
Linear	0.42	0.37	0.53	0.61	0.55	0.64	0.60	0.64	0.55	0.10
Isomerised (i.e. all branched species)	2.83	2.48	3.66	4.25	4.12	4.70	4.49	4.54	3.88	0.83
Multi-methyl and Higher Branched	0.44	0.43	0.71	0.98	0.87	0.95	0.97	0.92	0.78	0.23
Total	3.25	2.86	4.20	4.85	4.67	5.34	5.09	5.18	4.43	0.93
Molar Compositions (%)										
Linear	12.8	13.1	12.7	12.5	11.9	12.0	11.8	12.3	12.4	0.5
Isomerised	87.2	86.9	87.3	87.5	88.1	88.0	88.2	87.7	87.6	0.5
Mono-methyl	73.6	71.8	70.4	67.2	69.6	70.2	69.1	69.9	70.2	1.9
Multi-methyl and Higher Branched	13.6	15.1	16.8	20.3	18.5	17.8	19.1	17.8	17.4	2.2
Conversions (% of feed)										
Total	54.8	64.7	54.3	56.5	66.1	68.1	71.3	65.1	62.6	6.5
Cracking	54.1	63.9	51.9	54.0	61.6	64.2	67.8	60.5	59.7	5.8
Specifics of Operation										
C_{16} Feed Rate (ml/min @ 40°C)	0.01									
SHSV (mol_{C16}/(mol $_{Acid\ Sites}$.hr) x 10^{20})	26.30									
WHSV (g_{C16}/$g_{Catalyst}$.hr)	1.32									
Time on Stream (hrs)	48	51	54	57	65	68	71	74		

Table B.22: Experimental Data for H-BEA-25 at 0.02 ml/min n-C_{16} Feed

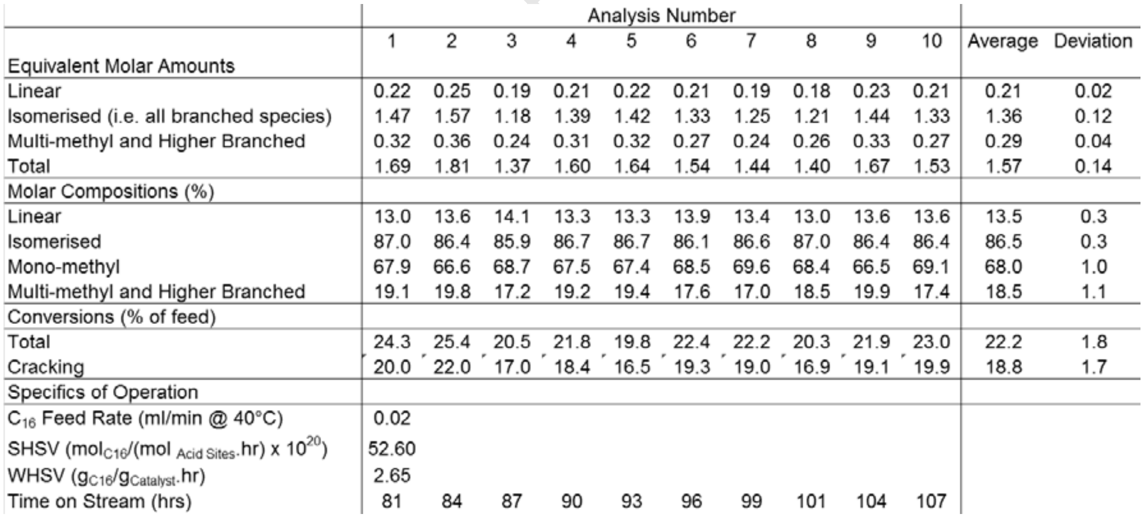

	Analysis Number											
Equivalent Molar Amounts	1	2	3	4	5	6	7	8	9	10	Average	Deviation
Linear	0.22	0.25	0.19	0.21	0.22	0.21	0.19	0.18	0.23	0.21	0.21	0.02
Isomerised (i.e. all branched species)	1.47	1.57	1.18	1.39	1.42	1.33	1.25	1.21	1.44	1.33	1.36	0.12
Multi-methyl and Higher Branched	0.32	0.36	0.24	0.31	0.32	0.27	0.24	0.26	0.33	0.27	0.29	0.04
Total	1.69	1.81	1.37	1.60	1.64	1.54	1.44	1.40	1.67	1.53	1.57	0.14
Molar Compositions (%)												
Linear	13.0	13.6	14.1	13.3	13.3	13.9	13.4	13.0	13.6	13.6	13.5	0.3
Isomerised	87.0	86.4	85.9	86.7	86.7	86.1	86.6	87.0	86.4	86.4	86.5	0.3
Mono-methyl	67.9	66.6	68.7	67.5	67.4	68.5	69.6	68.4	66.5	69.1	68.0	1.0
Multi-methyl and Higher Branched	19.1	19.8	17.2	19.2	19.4	17.6	17.0	18.5	19.9	17.4	18.5	1.1
Conversions (% of feed)												
Total	24.3	25.4	20.5	21.8	19.8	22.4	22.2	20.3	21.9	23.0	22.2	1.8
Cracking	20.0	22.0	17.0	18.4	16.5	19.3	19.0	16.9	19.1	19.9	18.8	1.7
Specifics of Operation												
C_{16} Feed Rate (ml/min @ 40°C)	0.02											
SHSV (mol_{C16}/(mol $_{Acid\ Sites}$.hr) x 10^{20})	52.60											
WHSV (g_{C16}/$g_{Catalyst}$.hr)	2.65											
Time on Stream (hrs)	81	84	87	90	93	96	99	101	104	107		

Table B.23: Experimental Data for H-BEA-25 at 0.03 ml/min n-C_{16} Feed

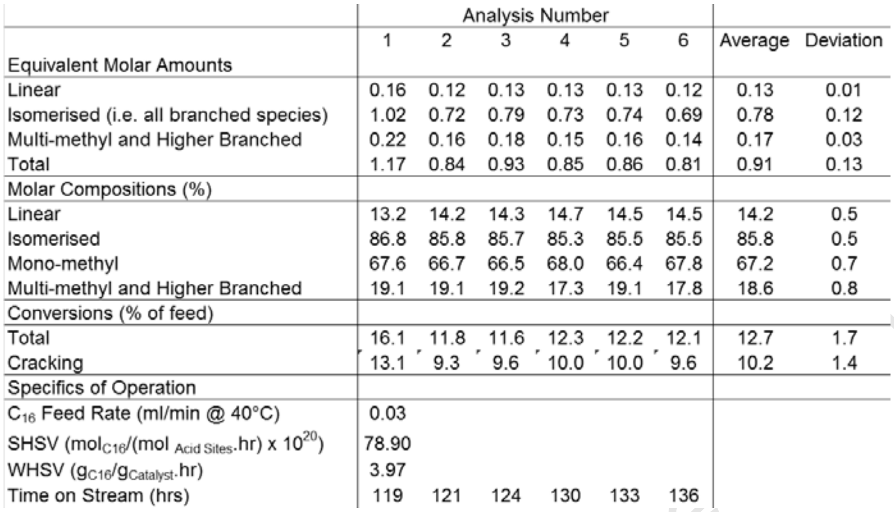

	Analysis Number							
Equivalent Molar Amounts	1	2	3	4	5	6	Average	Deviation
Linear	0.16	0.12	0.13	0.13	0.13	0.12	0.13	0.01
Isomerised (i.e. all branched species)	1.02	0.72	0.79	0.73	0.74	0.69	0.78	0.12
Multi-methyl and Higher Branched	0.22	0.16	0.18	0.15	0.16	0.14	0.17	0.03
Total	1.17	0.84	0.93	0.85	0.86	0.81	0.91	0.13
Molar Compositions (%)								
Linear	13.2	14.2	14.3	14.7	14.5	14.5	14.2	0.5
Isomerised	86.8	85.8	85.7	85.3	85.5	85.5	85.8	0.5
Mono-methyl	67.6	66.7	66.5	68.0	66.4	67.8	67.2	0.7
Multi-methyl and Higher Branched	19.1	19.1	19.2	17.3	19.1	17.8	18.6	0.8
Conversions (% of feed)								
Total	16.1	11.8	11.6	12.3	12.2	12.1	12.7	1.7
Cracking	13.1	9.3	9.6	10.0	10.0	9.6	10.2	1.4
Specifics of Operation								
C_{16} Feed Rate (ml/min @ 40°C)	0.03							
SHSV (mol_{C16}/($mol_{Acid\ Sites}$.hr) x 10^{20})	78.90							
WHSV (g_{C16}/$g_{Catalyst}$.hr)	3.97							
Time on Stream (hrs)	119	121	124	130	133	136		

Table B.24: Experimental Data for H-BEA-25 Repeat of 0.01 ml/min n-C_{16} Feed

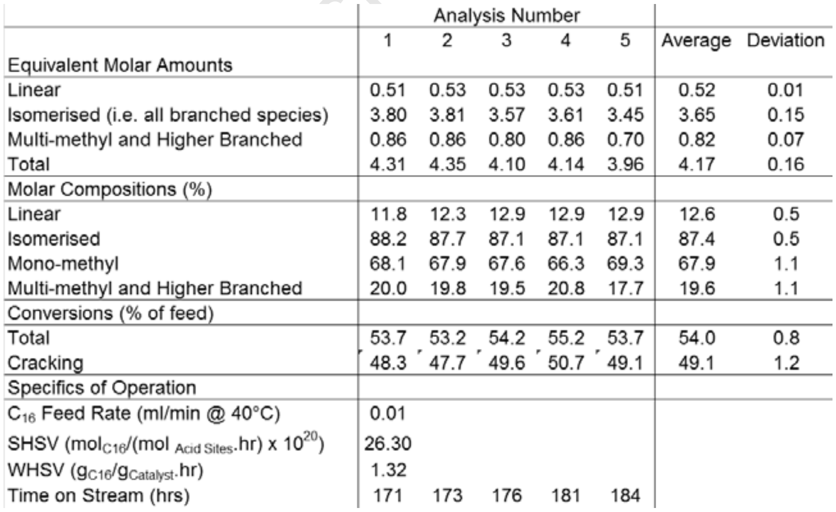

	Analysis Number						
Equivalent Molar Amounts	1	2	3	4	5	Average	Deviation
Linear	0.51	0.53	0.53	0.53	0.51	0.52	0.01
Isomerised (i.e. all branched species)	3.80	3.81	3.57	3.61	3.45	3.65	0.15
Multi-methyl and Higher Branched	0.86	0.86	0.80	0.86	0.70	0.82	0.07
Total	4.31	4.35	4.10	4.14	3.96	4.17	0.16
Molar Compositions (%)							
Linear	11.8	12.3	12.9	12.9	12.9	12.6	0.5
Isomerised	88.2	87.7	87.1	87.1	87.1	87.4	0.5
Mono-methyl	68.1	67.9	67.6	66.3	69.3	67.9	1.1
Multi-methyl and Higher Branched	20.0	19.8	19.5	20.8	17.7	19.6	1.1
Conversions (% of feed)							
Total	53.7	53.2	54.2	55.2	53.7	54.0	0.8
Cracking	48.3	47.7	49.6	50.7	49.1	49.1	1.2
Specifics of Operation							
C_{16} Feed Rate (ml/min @ 40°C)	0.01						
SHSV (mol_{C16}/($mol_{Acid\ Sites}$.hr) x 10^{20})	26.30						
WHSV (g_{C16}/$g_{Catalyst}$.hr)	1.32						
Time on Stream (hrs)	171	173	176	181	184		

Table B.25: Projection of H-BEA-25 Data to 20% Conversion

	Dataset				Projected Point	
	1		2			Deviation
Equivalent Molar Amounts						
Linear	0.21	0.02	0.13	0.01	0.19	0.05
Isomerised (i.e. all branched species)	1.36	0.12	0.78	0.12	1.23	0.36
Multi-methyl and Higher Branched	0.29	0.04	0.17	0.03	0.26	0.11
Total	1.57	0.14	0.91	0.13	1.42	0.41
Molar Compositions (%)						
Linear	13.5	0.3	14.2	0.5	13.6	1.2
Isomerised	86.5	0.3	85.8	0.5	86.4	1.2
Mono-methyl	68.0	1.0	67.2	0.7	67.8	2.8
Multi-methyl and Higher Branched	18.5	1.1	18.6	0.8	18.5	3.1
Conversions (% of feed)						
Total	22.2	1.8	12.7	1.7	20.0	5.2
Cracking	18.8	1.7	10.2	1.4	16.9	4.8
Specifics of Operation						
C_{16} Feed Rate (ml/min @ 40°C)	0.02		0.03			
SHSV ($mol_{C16}/(mol_{Acid\ Sites}.hr) \times 10^{20}$)	52.60		78.90		58.61	
WHSV ($g_{C16}/g_{Catalyst}.hr$)	2.65		3.97		2.95	

Table B.26: Product Composition Associated with Projection of H-BEA-25 Data to 20% Conversion

	Normalised Projected Point Molar Composition of Product (%)			
	Total	Linear	Mono-methyl	Multi-methyl and Higher Branched
C_1	0.39	0.39	0.00	0.00
C_2	0.17	0.17	0.00	0.00
C_3	3.60	3.60	0.00	0.00
C_4	23.82	3.46	20.37	0.00
C_5	18.81	2.84	15.97	0.00
C_6	12.76	2.17	10.48	0.10
C_7	10.93	1.42	8.67	0.84
C_8	7.71	0.85	4.91	1.96
C_9	4.80	0.45	2.68	1.67
C_{10}	3.77	0.29	1.77	1.71
C_{11}	3.14	0.21	1.42	1.51
C_{12}	1.89	0.14	0.71	1.04
C_{13}	0.00	0.00	0.00	0.00
C_{14}	0.00	0.00	0.00	0.00
C_{15}	3.53	1.05	2.29	0.19
C_{16}	4.68	0.00	2.63	2.05
Total	100.00	17.04	71.89	11.07
C_6 - C_{14}	45.00	5.53	30.64	8.83
Normalised C_6 - C_{14}	100.00	12.29	68.08	19.63

B.5 H-USY

B.5.1 Initial Loading

Table B.27: Experimental Data for Initial H-USY Testing at 0.01 ml/min n-C_{16} Feed

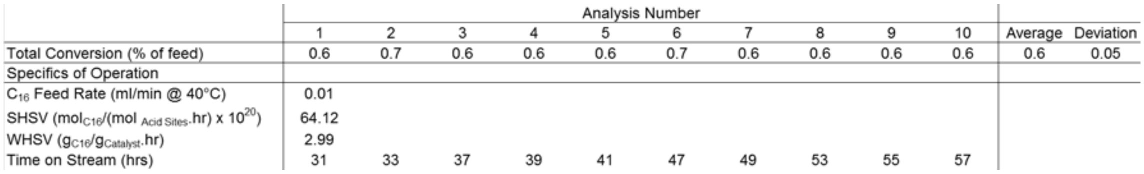

	Analysis Number											
	1	2	3	4	5	6	7	8	9	10	Average	Deviation
Total Conversion (% of feed)	0.6	0.7	0.6	0.6	0.6	0.7	0.6	0.6	0.6	0.6	0.6	0.05
Specifics of Operation												
C_{16} Feed Rate (ml/min @ 40°C)	0.01											
SHSV (mol_{C16}/(mol $_{Acid\ Sites}$.hr) x 10^{20})	64.12											
WHSV ($g_{C16}/g_{Catalyst}$.hr)	2.99											
Time on Stream (hrs)	31	33	37	39	41	47	49	53	55	57		

Table B.28: Experimental Data for Initial H-USY Testing at 0.02 ml/min n-C_{16} Feed

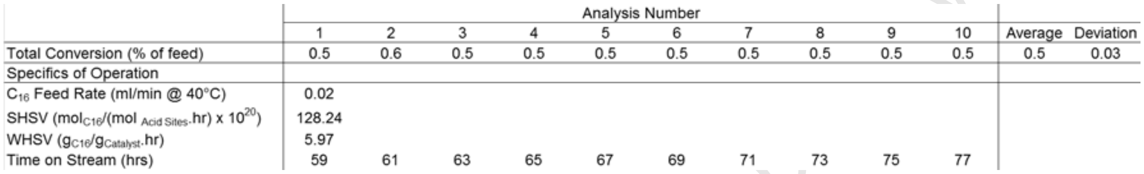

	Analysis Number											
	1	2	3	4	5	6	7	8	9	10	Average	Deviation
Total Conversion (% of feed)	0.5	0.6	0.5	0.5	0.5	0.5	0.5	0.5	0.5	0.5	0.5	0.03
Specifics of Operation												
C_{16} Feed Rate (ml/min @ 40°C)	0.02											
SHSV (mol_{C16}/(mol $_{Acid\ Sites}$.hr) x 10^{20})	128.24											
WHSV ($g_{C16}/g_{Catalyst}$.hr)	5.97											
Time on Stream (hrs)	59	61	63	65	67	69	71	73	75	77		

Table B.29: Experimental Data for Initial H-USY Testing at 0.03 ml/min n-C_{16} Feed

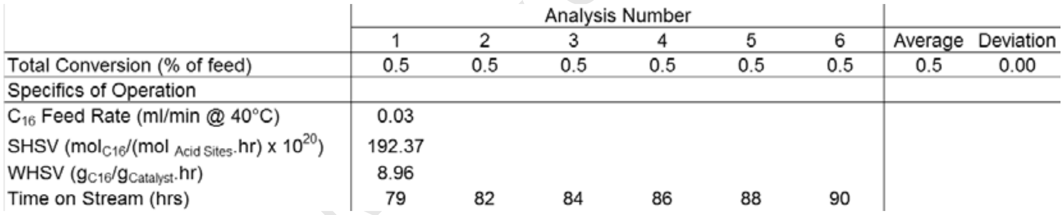

	Analysis Number							
	1	2	3	4	5	6	Average	Deviation
Total Conversion (% of feed)	0.5	0.5	0.5	0.5	0.5	0.5	0.5	0.00
Specifics of Operation								
C_{16} Feed Rate (ml/min @ 40°C)	0.03							
SHSV (mol_{C16}/(mol $_{Acid\ Sites}$.hr) x 10^{20})	192.37							
WHSV ($g_{C16}/g_{Catalyst}$.hr)	8.96							
Time on Stream (hrs)	79	82	84	86	88	90		

B.5.2 Second Loading

Table B.30: Experimental Data for H-USY at 0.05 ml/min n-C_{16} Feed

	Analysis Number						
Equivalent Molar Amounts	1	2	3	4	5	Average	Deviation
Linear	0.12	0.11	0.12	0.12	0.11	0.11	0.00
Isomerised (i.e. all branched species)	1.00	0.94	1.03	0.98	0.91	0.97	0.05
Multi-methyl and Higher Branched	0.18	0.17	0.18	0.18	0.17	0.18	0.01
Total	1.12	1.05	1.14	1.09	1.01	1.08	0.05
Molar Compositions (%)							
Linear	10.4	10.9	10.3	10.6	10.5	10.5	0.2
Isomerised	89.6	89.1	89.7	89.4	89.5	89.5	0.2
Mono-methyl	73.1	72.6	73.7	72.9	73.1	73.1	0.4
Multi-methyl and Higher Branched	16.5	16.5	16.0	16.5	16.3	16.4	0.2
Conversions (% of feed)							
Total	14.6	14.0	14.8	14.2	13.8	14.3	0.4
Cracking	11.5	11.0	11.8	11.2	10.8	11.3	0.4
Specifics of Operation							
C_{16} Feed Rate (ml/min @ 40°C)	0.05						
SHSV (mol_{C16}/($mol_{Acid\ Sites}$.hr) x 10^{20})	14.21						
WHSV (g_{C16}/$g_{Catalyst}$.hr)	0.66						
Time on Stream (hrs)	35	38	42	45	49		

Table B.31: Experimental Data for H-USY at 0.03 ml/min n-C_{16} Feed

	Analysis Number							
Equivalent Molar Amounts	1	2	3	4	5	6	Average	Deviation
Linear	0.16	0.17	0.19	0.19	0.18	0.17	0.18	0.01
Isomerised (i.e. all branched species)	1.52	1.72	1.93	1.93	1.77	1.66	1.75	0.16
Multi-methyl and Higher Branched	0.26	0.29	0.31	0.34	0.31	0.32	0.30	0.03
Total	1.68	1.90	2.12	2.11	1.95	1.82	1.93	0.17
Molar Compositions (%)								
Linear	9.5	9.1	9.2	8.9	9.1	9.2	9.2	0.2
Isomerised	90.5	90.9	90.8	91.1	90.9	90.8	90.8	0.2
Mono-methyl	74.8	75.7	76.4	74.8	74.9	73.3	75.0	1.1
Multi-methyl and Higher Branched	15.6	15.2	14.4	16.3	15.9	17.5	15.8	1.1
Conversions (% of feed)								
Total	20.8	23.9	26.6	25.9	24.6	21.2	23.8	2.4
Cracking	17.8	20.3	22.7	22.1	20.9	17.3	20.2	2.2
Specifics of Operation								
C_{16} Feed Rate (ml/min @ 40°C)	0.03							
SHSV (mol_{C16}/($mol_{Acid\ Sites}$.hr) x 10^{20})	8.53							
WHSV (g_{C16}/$g_{Catalyst}$.hr)	0.40							
Time on Stream (hrs)	57	61	63	66	69	72		

Table B.32: Experimental Data for H-USY at 0.02 ml/min n-C_{16} Feed

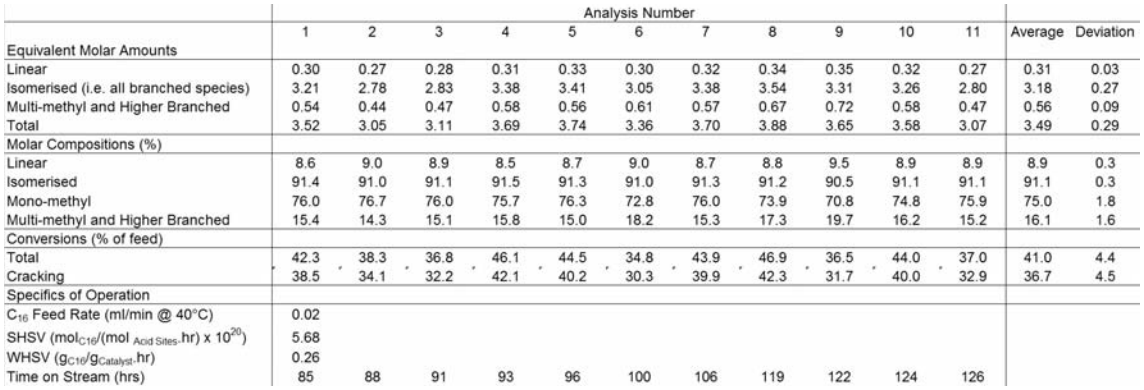

	Analysis Number												
	1	2	3	4	5	6	7	8	9	10	11	Average	Deviation
Equivalent Molar Amounts													
Linear	0.30	0.27	0.28	0.31	0.33	0.30	0.32	0.34	0.35	0.32	0.27	0.31	0.03
Isomerised (i.e. all branched species)	3.21	2.78	2.83	3.38	3.41	3.05	3.38	3.54	3.31	3.26	2.80	3.18	0.27
Multi-methyl and Higher Branched	0.54	0.44	0.47	0.58	0.56	0.61	0.57	0.67	0.72	0.58	0.47	0.56	0.09
Total	3.52	3.05	3.11	3.69	3.74	3.36	3.70	3.88	3.65	3.58	3.07	3.49	0.29
Molar Compositions (%)													
Linear	8.6	9.0	8.9	8.5	8.7	9.0	8.7	8.8	9.5	8.9	8.9	8.9	0.3
Isomerised	91.4	91.0	91.1	91.5	91.3	91.0	91.3	91.2	90.5	91.1	91.1	91.1	0.3
Mono-methyl	76.0	76.7	76.0	75.7	76.3	72.8	76.0	73.9	70.8	74.8	75.9	75.0	1.8
Multi-methyl and Higher Branched	15.4	14.3	15.1	15.8	15.0	18.2	15.3	17.3	19.7	16.2	15.2	16.1	1.6
Conversions (% of feed)													
Total	42.3	38.3	36.8	46.1	44.5	34.8	43.9	46.9	36.5	44.0	37.0	41.0	4.4
Cracking	38.5	34.1	32.2	42.1	40.2	30.3	39.9	42.3	31.7	40.0	32.9	36.7	4.5
Specifics of Operation													
C_{16} Feed Rate (ml/min @ 40°C)	0.02												
SHSV (mol_{C16}/($mol_{\text{Acid Sites}}$.hr) x 10^{20})	5.68												
WHSV (g_{C16}/$g_{Catalyst}$.hr)	0.26												
Time on Stream (hrs)	85	88	91	93	96	100	106	119	122	124	126		

Table B.33: Experimental Data for H-USY Repeat of 0.05 ml/min n-C_{16} Feed

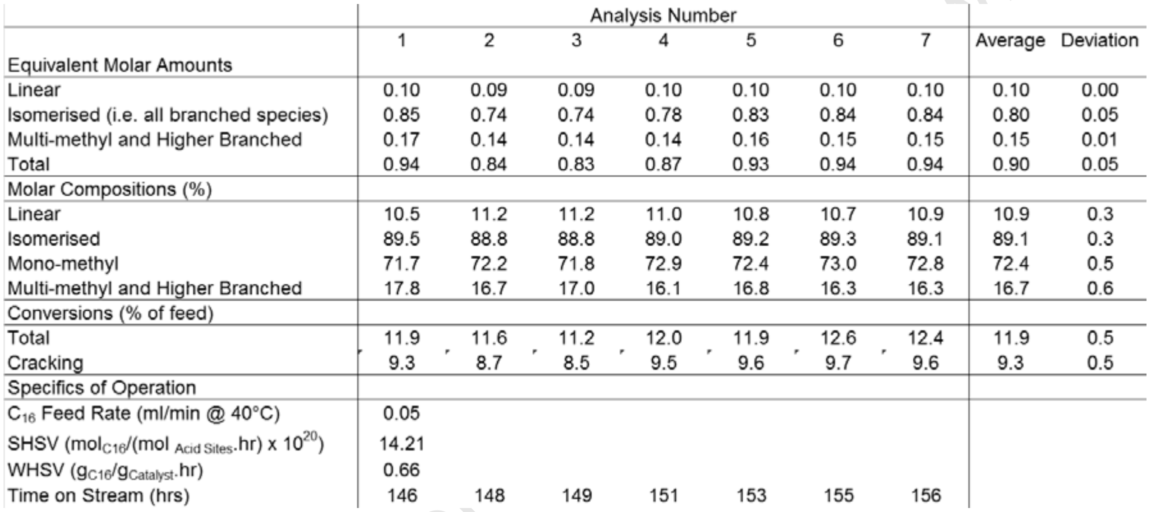

	Analysis Number								
	1	2	3	4	5	6	7	Average	Deviation
Equivalent Molar Amounts									
Linear	0.10	0.09	0.09	0.10	0.10	0.10	0.10	0.10	0.00
Isomerised (i.e. all branched species)	0.85	0.74	0.74	0.78	0.83	0.84	0.84	0.80	0.05
Multi-methyl and Higher Branched	0.17	0.14	0.14	0.14	0.16	0.15	0.15	0.15	0.01
Total	0.94	0.84	0.83	0.87	0.93	0.94	0.94	0.90	0.05
Molar Compositions (%)									
Linear	10.5	11.2	11.2	11.0	10.8	10.7	10.9	10.9	0.3
Isomerised	89.5	88.8	88.8	89.0	89.2	89.3	89.1	89.1	0.3
Mono-methyl	71.7	72.2	71.8	72.9	72.4	73.0	72.8	72.4	0.5
Multi-methyl and Higher Branched	17.8	16.7	17.0	16.1	16.8	16.3	16.3	16.7	0.6
Conversions (% of feed)									
Total	11.9	11.6	11.2	12.0	11.9	12.6	12.4	11.9	0.5
Cracking	9.3	8.7	8.5	9.5	9.6	9.7	9.6	9.3	0.5
Specifics of Operation									
C_{16} Feed Rate (ml/min @ 40°C)	0.05								
SHSV (mol_{C16}/($mol_{\text{Acid Sites}}$.hr) x 10^{20})	14.21								
WHSV (g_{C16}/$g_{Catalyst}$.hr)	0.66								
Time on Stream (hrs)	146	148	149	151	153	155	156		

Table B.34: Projection of H-USY Data to 20% Conversion

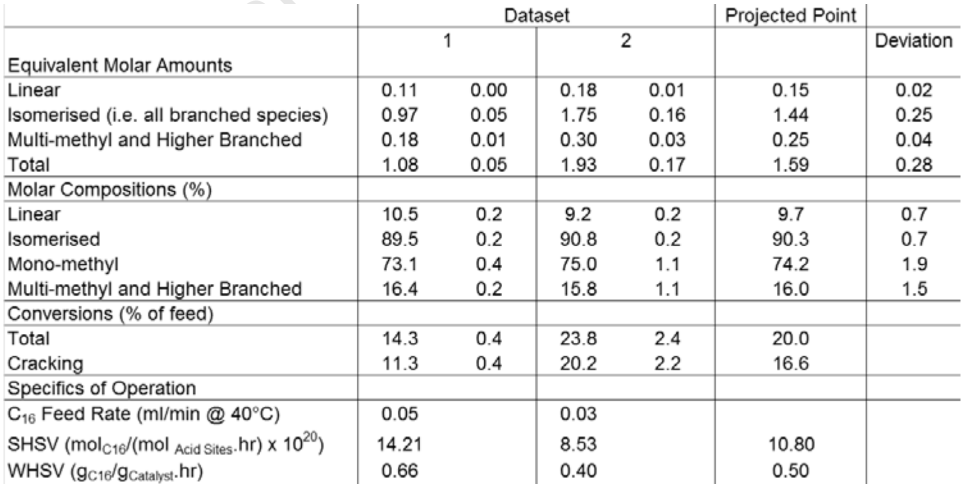

	Dataset				Projected Point	
	1		2			Deviation
Equivalent Molar Amounts						
Linear	0.11	0.00	0.18	0.01	0.15	0.02
Isomerised (i.e. all branched species)	0.97	0.05	1.75	0.16	1.44	0.25
Multi-methyl and Higher Branched	0.18	0.01	0.30	0.03	0.25	0.04
Total	1.08	0.05	1.93	0.17	1.59	0.28
Molar Compositions (%)						
Linear	10.5	0.2	9.2	0.2	9.7	0.7
Isomerised	89.5	0.2	90.8	0.2	90.3	0.7
Mono-methyl	73.1	0.4	75.0	1.1	74.2	1.9
Multi-methyl and Higher Branched	16.4	0.2	15.8	1.1	16.0	1.5
Conversions (% of feed)						
Total	14.3	0.4	23.8	2.4	20.0	
Cracking	11.3	0.4	20.2	2.2	16.6	
Specifics of Operation						
C_{16} Feed Rate (ml/min @ 40°C)	0.05		0.03			
SHSV (mol_{C16}/($mol_{\text{Acid Sites}}$.hr) x 10^{20})	14.21		8.53		10.80	
WHSV (g_{C16}/$g_{Catalyst}$.hr)	0.66		0.40		0.50	

Table B.35: Product Composition Associated with Projection of H-USY Data to 20% Conversion

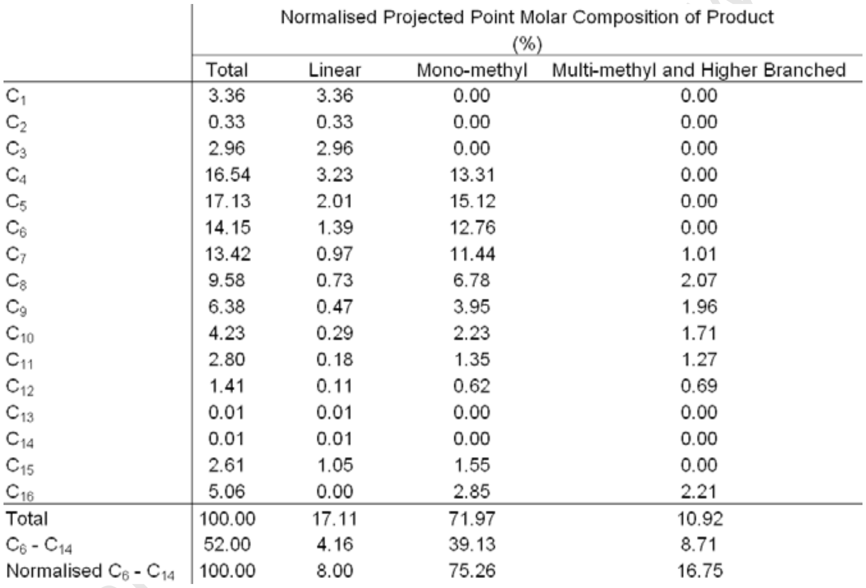

	Normalised Projected Point Molar Composition of Product (%)			
	Total	Linear	Mono-methyl	Multi-methyl and Higher Branched
C_1	3.36	3.36	0.00	0.00
C_2	0.33	0.33	0.00	0.00
C_3	2.96	2.96	0.00	0.00
C_4	16.54	3.23	13.31	0.00
C_5	17.13	2.01	15.12	0.00
C_6	14.15	1.39	12.76	0.00
C_7	13.42	0.97	11.44	1.01
C_8	9.58	0.73	6.78	2.07
C_9	6.38	0.47	3.95	1.96
C_{10}	4.23	0.29	2.23	1.71
C_{11}	2.80	0.18	1.35	1.27
C_{12}	1.41	0.11	0.62	0.69
C_{13}	0.01	0.01	0.00	0.00
C_{14}	0.01	0.01	0.00	0.00
C_{15}	2.61	1.05	1.55	0.00
C_{16}	5.06	0.00	2.85	2.21
Total	100.00	17.11	71.97	10.92
C_6 - C_{14}	52.00	4.16	39.13	8.71
Normalised C_6 - C_{14}	100.00	8.00	75.26	16.75

B.6 H-MOR-20

B.6.1 Initial Loading

Table B.36: Experimental Data for Initial H-MOR-20 Testing at 0.01 ml/min n-C_{16} Feed

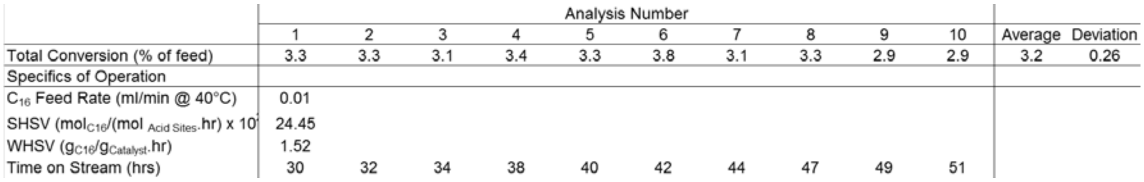

	Analysis Number											
	1	2	3	4	5	6	7	8	9	10	Average	Deviation
Total Conversion (% of feed)	3.3	3.3	3.1	3.4	3.3	3.8	3.1	3.3	2.9	2.9	3.2	0.26
Specifics of Operation												
C_{16} Feed Rate (ml/min @ 40°C)	0.01											
SHSV (mol_{C16}/($mol_{Acid\ Sites}$.hr) x 10	24.45											
WHSV (g_{C16}/$g_{Catalyst}$.hr)	1.52											
Time on Stream (hrs)	30	32	34	38	40	42	44	47	49	51		

Table B.37: Experimental Data for Initial H-MOR-20 Testing at 0.02 ml/min n-C_{16} Feed

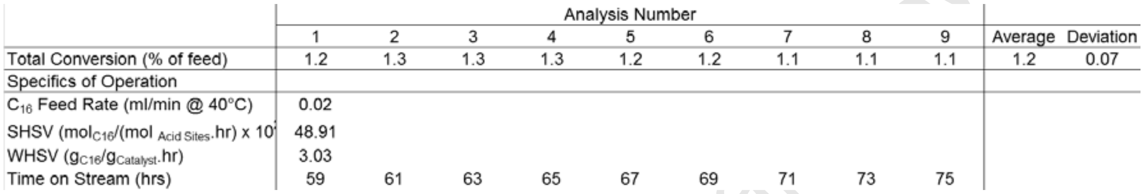

	Analysis Number										
	1	2	3	4	5	6	7	8	9	Average	Deviation
Total Conversion (% of feed)	1.2	1.3	1.3	1.3	1.2	1.2	1.1	1.1	1.1	1.2	0.07
Specifics of Operation											
C_{16} Feed Rate (ml/min @ 40°C)	0.02										
SHSV (mol_{C16}/($mol_{Acid\ Sites}$.hr) x 10	48.91										
WHSV (g_{C16}/$g_{Catalyst}$.hr)	3.03										
Time on Stream (hrs)	59	61	63	65	67	69	71	73	75		

Table B.38: Experimental Data for Initial H-MOR-20 Testing at 0.03 ml/min n-C_{16} Feed

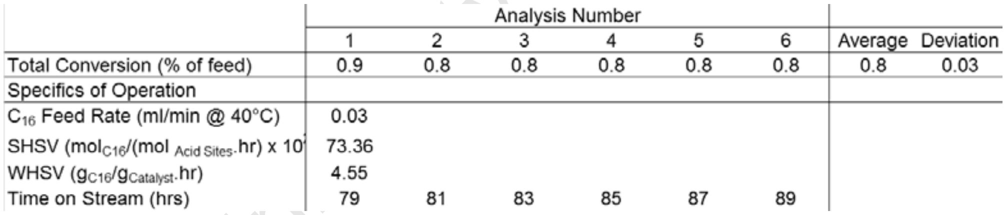

	Analysis Number							
	1	2	3	4	5	6	Average	Deviation
Total Conversion (% of feed)	0.9	0.8	0.8	0.8	0.8	0.8	0.8	0.03
Specifics of Operation								
C_{16} Feed Rate (ml/min @ 40°C)	0.03							
SHSV (mol_{C16}/($mol_{Acid\ Sites}$.hr) x 10	73.36							
WHSV (g_{C16}/$g_{Catalyst}$.hr)	4.55							
Time on Stream (hrs)	79	81	83	85	87	89		

B.6.2 Second Loading

Table B.39: Experimental Data for H-MOR-20 at 0.05 ml/min n-C_{16} Feed

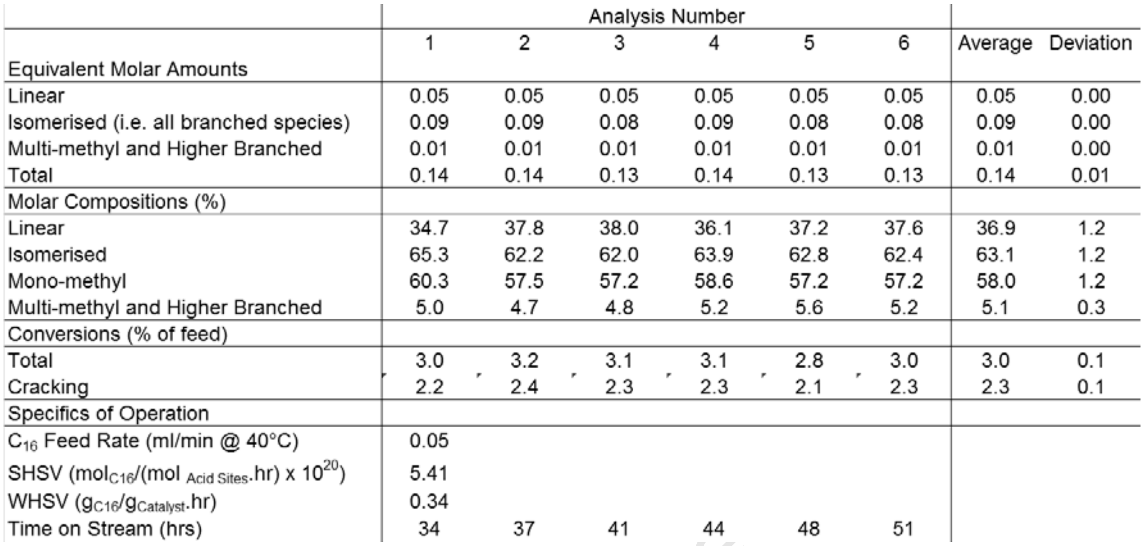

	Analysis Number							
Equivalent Molar Amounts	1	2	3	4	5	6	Average	Deviation
Linear	0.05	0.05	0.05	0.05	0.05	0.05	0.05	0.00
Isomerised (i.e. all branched species)	0.09	0.09	0.08	0.09	0.08	0.08	0.09	0.00
Multi-methyl and Higher Branched	0.01	0.01	0.01	0.01	0.01	0.01	0.01	0.00
Total	0.14	0.14	0.13	0.14	0.13	0.13	0.14	0.01
Molar Compositions (%)								
Linear	34.7	37.8	38.0	36.1	37.2	37.6	36.9	1.2
Isomerised	65.3	62.2	62.0	63.9	62.8	62.4	63.1	1.2
Mono-methyl	60.3	57.5	57.2	58.6	57.2	57.2	58.0	1.2
Multi-methyl and Higher Branched	5.0	4.7	4.8	5.2	5.6	5.2	5.1	0.3
Conversions (% of feed)								
Total	3.0	3.2	3.1	3.1	2.8	3.0	3.0	0.1
Cracking	2.2	2.4	2.3	2.3	2.1	2.3	2.3	0.1
Specifics of Operation								
C_{16} Feed Rate (ml/min @ 40°C)	0.05							
SHSV (mol_{C16}/(mol $_{Acid\ Sites}$.hr) x 10^{20})	5.41							
WHSV ($g_{C16}/g_{Catalyst}$.hr)	0.34							
Time on Stream (hrs)	34	37	41	44	48	51		

Table B.40: Experimental Data for H-MOR-20 at 0.03 ml/min n-C_{16} Feed

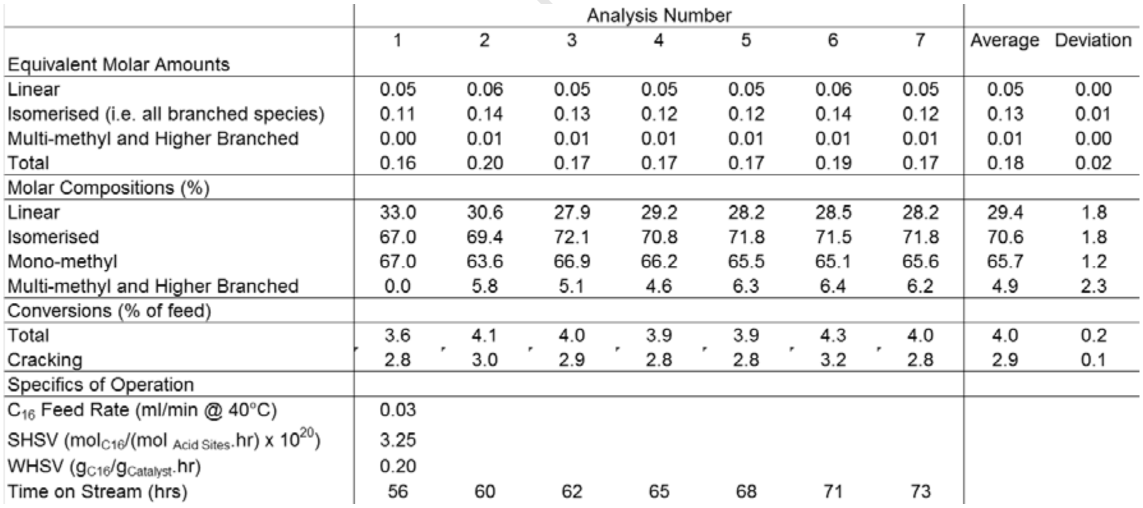

	Analysis Number								
Equivalent Molar Amounts	1	2	3	4	5	6	7	Average	Deviation
Linear	0.05	0.06	0.05	0.05	0.05	0.06	0.05	0.05	0.00
Isomerised (i.e. all branched species)	0.11	0.14	0.13	0.12	0.12	0.14	0.12	0.13	0.01
Multi-methyl and Higher Branched	0.00	0.01	0.01	0.01	0.01	0.01	0.01	0.01	0.00
Total	0.16	0.20	0.17	0.17	0.17	0.19	0.17	0.18	0.02
Molar Compositions (%)									
Linear	33.0	30.6	27.9	29.2	28.2	28.5	28.2	29.4	1.8
Isomerised	67.0	69.4	72.1	70.8	71.8	71.5	71.8	70.6	1.8
Mono-methyl	67.0	63.6	66.9	66.2	65.5	65.1	65.6	65.7	1.2
Multi-methyl and Higher Branched	0.0	5.8	5.1	4.6	6.3	6.4	6.2	4.9	2.3
Conversions (% of feed)									
Total	3.6	4.1	4.0	3.9	3.9	4.3	4.0	4.0	0.2
Cracking	2.8	3.0	2.9	2.8	2.8	3.2	2.8	2.9	0.1
Specifics of Operation									
C_{16} Feed Rate (ml/min @ 40°C)	0.03								
SHSV (mol_{C16}/(mol $_{Acid\ Sites}$.hr) x 10^{20})	3.25								
WHSV ($g_{C16}/g_{Catalyst}$.hr)	0.20								
Time on Stream (hrs)	56	60	62	65	68	71	73		

Table B.41: Experimental Data for H-MOR-20 at 0.01 ml/min n-C_{16} Feed

	Analysis Number												
Equivalent Molar Amounts	1	2	3	4	5	6	7	8	9	10	11	Average	Deviation
Linear	0.11	0.13	0.13	0.15	0.14	0.15	0.13	0.11	0.16	0.16	0.15	0.14	0.02
Isomerised (i.e. all branched species)	0.39	0.55	0.61	0.59	1.07	0.67	0.62	0.47	0.83	0.61	0.73	0.65	0.18
Multi-methyl and Higher Branched	0.00	0.00	0.03	0.04	0.40	0.06	0.10	0.03	0.12	0.07	0.07	0.08	0.11
Total	0.50	0.69	0.74	0.74	1.21	0.82	0.75	0.58	0.98	0.78	0.88	0.79	0.19
Molar Compositions (%)													
Linear	21.6	19.4	17.2	20.3	11.4	18.0	17.3	18.9	15.9	21.0	16.7	18.0	2.8
Isomerised	78.4	80.6	82.8	79.7	88.6	82.0	82.7	81.1	84.1	79.0	83.3	82.0	2.8
Mono-methyl	78.4	80.6	78.7	74.4	55.9	74.7	68.9	76.0	71.9	69.9	75.5	73.2	6.8
Multi-methyl and Higher Branched	0.0	0.0	4.0	5.3	32.7	7.3	13.8	5.1	12.2	9.1	7.9	8.8	9.0
Conversions (% of feed)													
Total	9.8	13.3	14.4	12.9	19.1	15.7	15.0	12.4	17.6	13.5	16.3	14.6	2.6
Cracking	9.1	12.6	13.2	11.3	16.7	12.8	12.2	8.2	13.3	9.4	12.0	11.9	2.4
Specifics of Operation													
C_{16} Feed Rate (ml/min @ 40°C)	0.01												
SHSV (mol_{C16}/($mol_{Acid\ Sites}$.hr) x 10^{20})	1.08												
WHSV (g_{C16}/$g_{Catalyst}$.hr)	0.07												
Time on Stream (hrs)	84	87	90	92	95	99	105	108	121	123	125		

Table B.42: Experimental Data for H-MOR-20 Repeat of 0.05 ml/min n-C_{16} Feed

	Analysis Number								
Equivalent Molar Amounts	1	2	3	4	5	6	7	Average	Deviation
Linear	0.04	0.04	0.04	0.04	0.04	0.04	0.04	0.04	0.00
Isomerised (i.e. all branched species)	0.07	0.07	0.07	0.06	0.07	0.07	0.07	0.07	0.00
Multi-methyl and Higher Branched	0.01	0.01	0.01	0.00	0.00	0.01	0.01	0.01	0.00
Total	0.11	0.11	0.12	0.11	0.11	0.11	0.11	0.11	0.00
Molar Compositions (%)									
Linear	37.8	38.3	36.0	39.0	37.2	36.3	37.3	37.4	1.1
Isomerised	62.2	61.7	64.0	61.0	62.8	63.7	62.7	62.6	1.1
Mono-methyl	57.2	57.1	58.1	56.7	58.6	58.0	56.9	57.5	0.7
Multi-methyl and Higher Branched	5.1	4.6	5.8	4.2	4.2	5.7	5.8	5.1	0.7
Conversions (% of feed)									
Total	2.7	2.5	2.5	2.4	2.4	2.5	2.4	2.5	0.1
Cracking	1.9	1.8	1.7	1.7	1.7	1.8	1.7	1.8	0.1
Specifics of Operation									
C_{16} Feed Rate (ml/min @ 40°C)	0.05								
SHSV (mol_{C16}/($mol_{Acid\ Sites}$.hr) x 10^{20})	5.41								
WHSV (g_{C16}/$g_{Catalyst}$.hr)	0.34								
Time on Stream (hrs)	145	147	149	150	152	154	156		

Table B.43: Projection of H-MOR-20 Data to 20% Conversion

	Dataset				Projected Point	
Equivalent Molar Amounts	1		2			Deviation
Linear	0.05	0.00	0.14	0.02	0.18	0.03
Isomerised (i.e. all branched species)	0.13	0.01	0.65	0.18	0.91	0.21
Multi-methyl and Higher Branched	0.01	0.00	0.08	0.11	0.12	0.12
Total	0.18	0.02	0.79	0.19	1.09	0.22
Molar Compositions (%)						
Linear	29.4	1.8	18.0	2.8	12.2	6.5
Isomerised	70.6	1.8	82.0	2.8	87.8	6.5
Mono-methyl	65.7	1.2	73.2	6.8	76.9	9.2
Multi-methyl and Higher Branched	4.9	2.3	8.8	9.0	10.8	13.5
Conversions (% of feed)						
Total	4.0	0.2	14.6	2.6	20.0	
Cracking	2.9	0.1	11.9	2.4	16.4	
Specifics of Operation						
C_{16} Feed Rate (ml/min @ 40°C)	0.03		0.01			
SHSV (mol_{C16}/($mol_{Acid\ Sites}$.hr) x 10^{20})	3.25		1.08		0.000	
WHSV (g_{C16}/$g_{Catalyst}$.hr)	0.20		0.07		0.000	

Table B.44: Product Composition Associated with Projection of H-MOR-20 Data to 20% Conversion

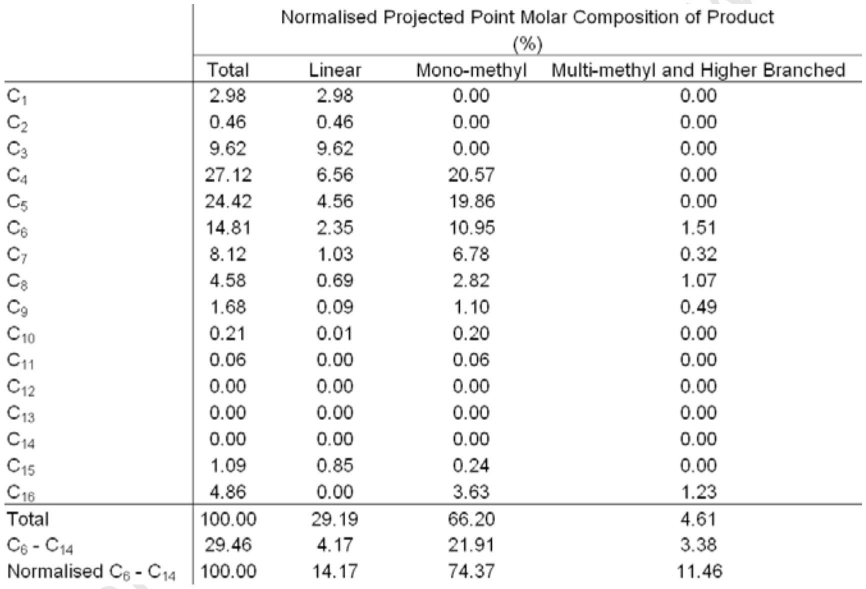

	Normalised Projected Point Molar Composition of Product (%)			
	Total	Linear	Mono-methyl	Multi-methyl and Higher Branched
C_1	2.98	2.98	0.00	0.00
C_2	0.46	0.46	0.00	0.00
C_3	9.62	9.62	0.00	0.00
C_4	27.12	6.56	20.57	0.00
C_5	24.42	4.56	19.86	0.00
C_6	14.81	2.35	10.95	1.51
C_7	8.12	1.03	6.78	0.32
C_8	4.58	0.69	2.82	1.07
C_9	1.68	0.09	1.10	0.49
C_{10}	0.21	0.01	0.20	0.00
C_{11}	0.06	0.00	0.06	0.00
C_{12}	0.00	0.00	0.00	0.00
C_{13}	0.00	0.00	0.00	0.00
C_{14}	0.00	0.00	0.00	0.00
C_{15}	1.09	0.85	0.24	0.00
C_{16}	4.86	0.00	3.63	1.23
Total	100.00	29.19	66.20	4.61
C_6 - C_{14}	29.46	4.17	21.91	3.38
Normalised C_6 - C_{14}	100.00	14.17	74.37	11.46